

Direct Numerical Simulation of Noise-Generation Mechanisms in the Mixing Layer of a Jet

A thesis accepted by the Faculty of
Aerospace Engineering and Geodesy of the Universität Stuttgart
in partial fulfilment of the requirements for the degree of
Doctor of Engineering Sciences (Dr.-Ing.)

by

Andreas Babucke

born in Heidenheim an der Brenz

main-referee : apl. Prof. Dr.-Ing. Ulrich Rist
co-referee : Prof. Neil Sandham, PhD
Date of defence : May 28th, 2009

Institut für Aerodynamik und Gasdynamik
Universität Stuttgart

2009

The Guide is definitive. Reality is frequently inaccurate.

(D. Adams: The Hitchhiker's Guide to the Galaxy)

Vorwort / Preface

Die vorliegende Arbeit entstand während meiner Tätigkeit als wissenschaftlicher Mitarbeiter am Institut für Aerodynamik und Gasdynamik (IAG) der Universität Stuttgart.

Mein Doktorvater Ulrich Rist hat mir die Arbeit in diesem spannenden Themenbereich ermöglicht und mich stets tatkräftig unterstützt. Bei ihm möchte ich mich herzlich für das entgegengebrachte Vertrauen, die eingeräumten Freiheiten und die hervorragende Betreuung bedanken.

Ebenso gebührt mein Dank Markus Kloker für die vielen Diskussionen und Anregungen zur Arbeit. Insbesondere bei der Entwicklung des DNS-Codes waren seine Ratschläge unersetzlich.

I would like to thank Prof. Neil Sandham from the University of Southampton for his interest in my work and participating in the evaluation committee. His thorough review and comments definitely improved this manuscript.

All meinen Kollegen am IAG gilt ein besonderes Dankeschön für die fachlichen Diskussionen und die hervorragende Atmosphäre ohne die die Arbeit nur halb soviel Spass gemacht hätte. Daneben möchte ich mich bei den Mitarbeitern vom HLRS und NEC für die Unterstützung bei diversen Computerproblemen bedanken.

Lats but not least, I would like to thank all members of the DFG-CNRS research group *Noise Generation in Turbulent Flows* for the scientific exchange and the friendly atmosphere throughout the years.

Stuttgart, im Juni 2009

Andreas Babucke

Contents

Abstract	v
Kurzfassung	vii
Nomenclature	ix
1 Introduction	1
1.1 Jet Noise	1
1.2 Characterization of Sound	6
1.3 Computational Aeroacoustics	7
1.4 Noise Reduction Technology	10
1.5 Scope of the Work	12
2 Physical Model	15
2.1 Notation	15
2.2 Governing Equations	17
2.3 Properties of the Fluid	19
3 Numerical Method	21
3.1 Code Development at IAG	21
3.2 Simulation Framework	22
3.3 DNS Code	23
3.3.1 Spatial Discretization	23
3.3.2 Time Integration	31
3.3.3 Boundary Conditions	36
3.3.4 Parallelization	48
3.4 Linear Stability Theory	53
3.4.1 Fundamentals	53
3.4.2 Boundary Conditions	55
3.4.3 Matrix Solver	56
3.4.4 Wielandt Iteration	60
3.5 Initial Conditions	62
3.5.1 Grid Generation	62
3.5.2 Flow Field	63
3.6 Pre- and Postprocessing	67

4	Fundamentals of Mixing-Layer Noise	69
4.1	Flow Parameters	69
4.2	Linear Stability Analysis	71
4.3	Two-Dimensional Simulation	74
4.4	Three-Dimensional Simulation	81
5	Mixing Layer with Splitter Plate	87
5.1	Flow Parameters	87
5.2	Linear Stability Analysis	90
5.3	Simulation Results	93
6	Serrated Trailing Edge	101
6.1	Reference Case	103
6.2	Rectangular Serration	106
6.3	Non-symmetric Serration	110
6.4	Comparison of Sound Emission	115
7	Turbulent Mixing Layer	119
7.1	Generation of Inflow Data	119
7.2	Results for the Turbulent Mixing Layer	128
8	Conclusions and Outlook	139
	Appendix	143
A	Finite Differences on Non-Uniform Grids	143
A.1	Modified-Wavenumber Analysis	144
A.2	One-dimensional Numerical Investigation	156
A.3	Summary	164
B	Coefficients of the LST Matrix Solver	167
C	Computational Aspects	173
C.1	Computational Performance	173
C.2	Scaling	175
C.3	Different Domain Sizes	177
D	Coupling with Acoustic Solver	179
D.1	Numerical Example	179
D.2	Computational Performance	184
	References	187

Abstract

The present work deals with the process of flow-induced noise generation in a mixing layer. The term mixing layer describes a flow field with two different velocities in the streamwise direction and serves as a model for the initial part of a jet. Due to the inflection point in the streamwise-velocity profile, disturbances are strongly amplified by hydrodynamic instability, leading to a roll-up of the mixing layer and the generation of Kelvin-Helmholtz vortices. Their pairing is one of the dominant noise sources in a jet.

Direct numerical simulation of the noise-generating flow and the acoustic farfield is difficult because of the different scales of hydrodynamic fluctuations and emitted sound. This requires a highly accurate numerical method with appropriate boundary conditions in order not to spoil the sensitive acoustic field. For this, a new code for direct numerical simulation of the compressible Navier-Stokes equations is presented. It is based on compact finite differences and a spectral ansatz in spanwise direction. In combination with linear stability theory and postprocessing this forms a comprehensive framework for the simulation of unsteady compressible flows.

The fundamentals of flow-induced noise generation in a mixing layer with S-shaped velocity profile are investigated by means of two- and three-dimensional simulations with defined disturbances. The combination of vortex pairing and notable amplitude of the respective subharmonic yields the dominant sound emission in downstream direction. Since the growth of low-frequency disturbances is driven by subharmonic resonance, the strength of the acoustic source can be influenced by phase shifts of the introduced disturbances. An additional spanwise disturbance can prevent the resonance mechanism which results in upstream directed sound. In contrast to tonal acoustic emissions due to two-dimensional Kelvin-Helmholtz vortices, three-dimensional effects lead to broad band noise.

A more realistic configuration for jet noise is achieved by including a splitter plate, representing the nozzle end. Downstream of the plate, a combination of wake and mixing layer develops. Due to the splitter plate, the flow is only quasi deterministic. This indicates a feedback loop where upstream traveling acoustic sources induce new instability waves at the trailing edge. Accord-

ingly, higher amplitudes of non-introduced low-frequency disturbances can be observed for a splitter plate with increased thickness. A serrated trailing edge leads to a spanwise deformation of the Kelvin-Helmholtz vortices, followed by longitudinal vortex tubes. These lead to a breakdown of the large coherent structures. In the considered case, this reduces the noise emission substantially.

Finally, a turbulent mixing layer is considered where the fast-stream boundary layer is already turbulent. This is done by prescribing unsteady data of a previous simulation at the inflow. The turbulent mixing layer is made of small-scale structures with the generation of first large-scale Kelvin-Helmholtz vortices. Despite similar scales, their growth is due to the inflection point of the mean velocity profile. The dominant sound is due to a downstream-traveling acoustic source in the turbulent boundary layer. When reaching the trailing edge, a pulse-like noise is emitted in the low-speed stream. Between the periodic appearance of the source, the noise generation at the trailing edge is weak. Thus the geometrical unsteadiness of the trailing edge itself does not contribute substantially to the generated noise, here.

Kurzfassung

Die vorliegende Arbeit behandelt die strömungsinduzierte Schallerzeugung in freien Scherschichten. Der Begriff Scherschicht bezeichnet ein Strömungsfeld mit zwei ungleichen Geschwindigkeiten in Längsrichtung und dient als Modell für den anfänglichen Bereich eines Freistrahls. Aufgrund des Wendepunktes im Geschwindigkeitsprofil werden Störungen stark angefacht, was zu einem Aufrollen der Scherschicht und Auswerfen von Kelvin-Helmholtz-Wirbeln führt. Deren Verschmelzung weiter stromab ist eine der dominanten Schallquellen in einem Freistrah.

Die Schwierigkeit bei der Direkten Numerischen Simulation von schallerzeugender Strömung und akustischem Fernfeld liegt in den unterschiedlichen Skalen von hydrodynamischen Schwankungen und abgestrahltem Lärm. Dies erfordert ein hochgenaues numerisches Verfahren mit passenden Randbedingungen, um das empfindliche akustische Feld nicht zu verfälschen. Hierzu wird ein neues Verfahren zur Direkten Numerischen Simulation der kompressiblen Navier-Stokes-Gleichungen, basierend auf kompakten Finiten Differenzen und einem Spektralansatz in Spannweitenrichtung, vorgestellt. In Kombination mit Linearer Stabilitätstheorie und Auswertung ergibt dies eine umfangreiche Simulationsumgebung für instationäre kompressible Strömungen.

Die Grundlagen der strömungsinduzierten Schallentstehung in Scherschichten mit einem S-förmigen Geschwindigkeitsprofil werden mittels zwei- und dreidimensionalen Simulationen unter kontrollierter Störungseingabe untersucht. Die Kombination von Wirbelverschmelzung und merklicher Amplitude der jeweiligen subharmonischen Störung verursacht die dominante Schallabstrahlung in Stromabrichtung. Da das Wachstum von niederfrequenten Fluktuationen durch subharmonische Resonanz bestimmt ist, kann die Stärke der akustischen Quelle durch die relativen Phasenlagen der Störungsanregung beeinflusst werden. Eine zusätzliche spannweitige Störung kann den Resonanzmechanismus unterbinden, was sich in der Generierung von stromaufgerichtetem Schall widerspiegelt. Im Gegensatz zur tonalen Schallabstrahlung von zweidimensionalen Kelvin-Helmholtz-Wirbeln führen dreidimensionale Effekte zu Breitbandlärm.

Eine realistischere Konfiguration zur Untersuchung von Strahlärm ergibt sich durch das Einbeziehen des Düsenendes, welches durch eine endliche ebene

Platte repräsentiert wird. Stromab der Trennplatte entwickelt sich eine Kombination aus Scherschicht und Nachlauf. Aufgrund der Trennplatte ist das Strömungsfeld nunmehr quasi deterministisch, was auf die Existenz einer Rückkopplung schließen lässt, bei der stromauf abgestrahlter Schall neue Instabilitätswellen an der Hinterkante erzeugt. Entsprechend ergeben sich bei einem dickeren Düsenende höhere Amplituden für nicht eingebrachte niederfrequente Störungen. Einkerbungen an der Hinterkante führen zu einer spannweitigen Verformung der Kelvin-Helmholtz-Wirbel mit anschließenden Längswirbeln, welche stromab zum Zusammenbruch der großen Strukturen führen. Im betrachteten Fall kann dadurch der abgestrahlte Lärm deutlich verringert werden.

Abschließend wird eine turbulente Scherschicht untersucht, bei der eine der beiden Grenzschichten entlang der Trennplatte bereits turbulent ist. Hierzu werden instationäre Daten aus einer vorhergehenden Simulation am Einströmrand vorgeschrieben. Die turbulente Scherschicht besteht aus kleinskaligen Strukturen, wobei die Bildung von größeren Kelvin-Helmholtz-Wirbeln erkennbar ist. Trotz ähnlicher Skalen ist deren Entstehen durch den Wendepunkt des mittleren Geschwindigkeitsprofils verursacht. Die dominante Schallabstrahlung hat ihre Ursache in einer akustischen Quelle in der turbulenten Grenzschicht, die stromab läuft. Bei Erreichen der Hinterkante wird ein Schallpuls in den unteren Bereich des Fernfeldes abgestrahlt. Zwischen dem periodischen Auftreten der Quelle ist die Schallerzeugung am Plattenende gering, so dass im vorliegenden Fall die geometrische Unstetigkeit der Hinterkante selbst nicht dominant zur Schallerzeugung beiträgt.

Nomenclature

Latin Letters

$a - g$	coefficients of finite differences
a	speed of sound
A, B	coefficient matrices for linear stability theory
AP_{mod}	amplitude ratio after one period
$c_1 - c_5$	characteristic variables
c	convection speed
c_f	friction coefficient = $\tau_w / (1/2 \cdot \rho_\infty u_\infty^2)$
c_{ph}	phase speed $c_{ph} = \omega_r / \alpha_r$
c_p, c_v	heat capacities at constant pressure, volume
d	diffusion, damping rate
D₁, D₂	matrices for 1 st and 2 nd derivatives, respectively
e	efficiency
E	total energy
f	frequency = $\omega / 2\pi$
F, G, H	flux vectors in x - y - and z -direction, respectively
h	index of frequencies
h_{TE}	thickness of trailing edge
H_{12}	shape factor = δ_1 / δ_2
i	imaginary unit = $\sqrt{-1}$
J	determinant of the Jacobian matrix
j	index of grid point
k	index of spanwise modes
K	number of spanwise modes
k^*	non-dimensional wave number, normalized with step size
\tilde{L}	reference length [m]
L_p	sound pressure level [dB]
l	equidistant time level, iteration number
Ma	Mach number
N	number of grid-points or time steps

\mathcal{O}	order of approximation
p	pressure
Pr	Prandtl number
q_x, q_y, q_z	heat flux density in x -, y - and z -direction, respectively
\hat{q}	eigenvector of compressible LST
\mathbf{Q}	solution vector with conservative variables
Re	Reynolds number
SU	speed-up of parallelization
t	time
Δt	time step
T	temperature
\tilde{T}_S	Sutherland temperature = 110.4K
TF	transfer function of filter
\mathbf{u}	velocity vector = $[u, v, w]^T$
u, v, w	velocity components in x -, y - and z -direction, respectively
u^+	velocity normalized with wall friction velocity = u/u_τ
u_τ	wall friction velocity for turbulent flows = $\sqrt{\langle \bar{\tau}_w \rangle} / \rho$
x_0	streamwise coordinate at the inflow
x, y, z	streamwise, normal and spanwise coordinate
$\Delta x, \Delta y, \Delta z$	stepsizes in x -, y - and z -direction, respectively
y^+	wall length scale for turbulent flows = $(u_\tau \cdot \rho / \mu) \cdot y$

Greek Letters

α, β, γ	wave numbers in streamwise, normal and spanwise direction, respectively
$\tilde{\delta}_\Omega$	vorticity thickness (mixing layer)
$\tilde{\delta}_1$	displacement thickness
$\tilde{\delta}_2$	momentum thickness
δ_{99}	boundary layer thickness where $u = 0.99 \cdot u_\infty$
ζ	arbitrary direction in computational space
$\Delta \zeta$	arbitrary stepsize in computational space
ϑ	heat conductivity
Θ	phase
κ	adiabatic index (heat-capacity ratio)
λ	wavelength
Λ_2	vortex criterion by Jeong & Hussain
μ	dynamic viscosity
μ_B	coefficient of secondary viscosity (volume viscosity)

ξ, η	computational space in x - y -plane
$\Delta\xi, \Delta\eta$	stepsizes in equidistant computational space
π	circular constant ≈ 3.1415927
ρ	density
σ	ramping function
$\tau_{xx}, \tau_{yy}, \tau_{zz}$	normal stresses
$\tau_{xy}, \tau_{xz}, \tau_{yz}$	shear stresses
φ	directivity angle of sound (relative to x -axis)
Φ	any flow quantity
Ψ	wave angle = $\text{atan}(\gamma/\alpha)$
ω	angular frequency = $2\pi \cdot f$
Ω_x, Ω_z	streamwise and spanwise vorticity, respectively

Symbols

'	fluctuation $\Phi' = \Phi - \Phi_0$
‡	filtered value
\sim	dimensional quantity
$\hat{}$	quantity in Fourier space
$\bar{}$	time-averaged quantity
$\langle \rangle$	averaged along multiple directions
$\langle \rangle$	spanwise-averaged values
$ $	absolute value of a quantity
$()^T$	transposed vector
(h, k)	mode with frequency $h \cdot \omega_0$ and spanwise wavenumber $k \cdot \gamma_0$
\mathfrak{p}	degree of derivation, e.g. $\mathfrak{p}=2$: second derivative
∇	nabla operator: $\nabla = \left[\frac{\partial}{\partial x}, \frac{\partial}{\partial y}, \frac{\partial}{\partial z} \right]^T$
$\arg\{ \}$	argument of a complex number, $\in [0, 2\pi[$
$\mathcal{E}\mathcal{V}()$	an eigenvalue of a matrix

Subscripts

∞	freestream condition
$+,-$	forward and backward biased FD, respectively
0	fundamental quantity, baseflow
I, II	upper and lower stream, respectively
an	analytically computed
bc	boundary condition
lhs	left-hand side coefficients

<i>max</i>	maximum value
<i>mod</i>	modified wave number
<i>num</i>	numerically computed
<i>rms</i>	root mean square of fluctuations
<i>r, i</i>	real and imaginary parts, respectively
<i>w</i>	quantity at the wall

Abbreviations

BL	boundary layer
c.c.	complex conjugate
CFL	Courant-Friedrichs-Lewy number
CPU	central processing unit
dB	decibel
DNS	direct numerical simulation
EAS3	Ein-Ausgabe-System 3
EPNL	effective perceived noise level
FD	finite difference
FLOP/s	floating point operations per second
HLRS	High Performance Computing Center Stuttgart
IAG	Institut für Aerodynamik und Gasdynamik
I/O	Input/Output of files
LST	linear stability theory
MPI	message passing interface
RANS	Reynolds-averaged Navier-Stokes equations
RK	Runge-Kutta
SPL	sound pressure level
TS	Tollmien-Schlichting
TCP/IP	Transmission Control Protocol/Internet Protocol

1 Introduction

1.1 Jet Noise

Noise reduction is of great interest for a variety of technical applications. This is especially the case in the aeronautics branch. Most airports are located in highly populated areas and thus, many people are exposed to aircraft noise emission. High acoustic loads may cause stress to people affected permanently, reduce the quality of life and even be the origin of illness. This is reflected in increasing regulations: e.g. in Germany, the nightly emission is restricted to 55 dB(A) in residential areas near commercial airports [18]. Additionally, airport operators are urged to provide funding for acoustic insulation of apartments. Since landing fees depend on the noise emission and because of the passengers' comfort, airlines and aircraft manufacturers are interested in noise reduction, too. Beyond the civil market, also military aircraft are requested to have a smaller acoustic signature to be less detectable.

Aircraft noise can be decomposed into two fundamental sources: one being caused by the airframe itself, e.g. landing gears or flaps, and the other due to the engine. Engine noise is generated by the fan, combustion, the turbine and the exhaust of the primary and secondary stream. The latter is denoted as jet noise. According to NASA [78], the engine noise is the major acoustic source of a civil aircraft. During the approach of the aircraft, the main acoustic load is due to the compressor (fan), generating high-frequency screech tones which are directed towards the nose of the aircraft. Behind air frame noise, the acoustic emissions of the jet is the third largest noise source of a landing commercial aircraft. Jet noise is even more important during take-off where it is by far the dominant acoustic source.

Compared to early jet planes, today's commercial aircrafts are up to 20 dB more quiet. As shown in figure 1.1 this recent reduction of jet noise has been achieved mainly by an increased bypass ratio. However, technical limits like the engine's diameter prevent higher bypass ratios. Thus, the reduction of jet noise is stuck at some 90 dB (EPNL) nowadays and new concepts for noise reduction are required.

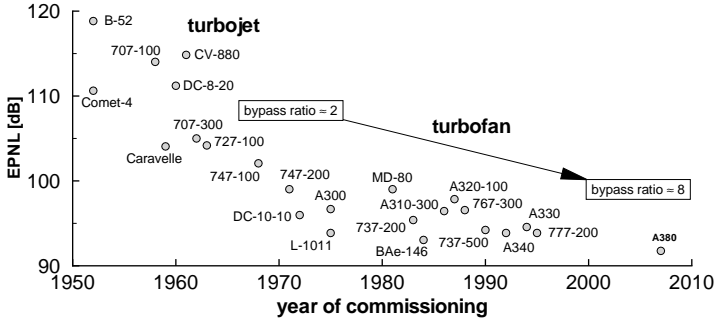


Figure 1.1: Progress in noise reduction during lift-off for various transportation aircrafts according to Michel [70]. The effective perceived noise level (EPNL) is taken at the sideline (distance of 450m) and normalized with respect to a constant thrust of 446 kN.

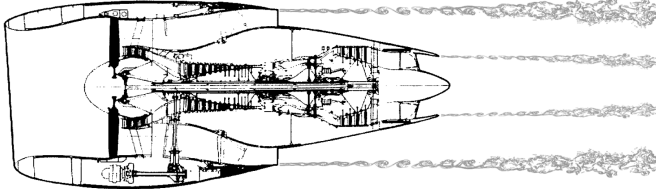


Figure 1.2: Mixing layers behind the jet engine of a commercial aircraft.

In the initial part of the jet, the generated sound is caused by the mixing layer surrounding the potential core. The term mixing layer or free shear layer describes a flow field composed of two streams with unequal velocities. Their locations behind a typical jet engine for commercial aircrafts are illustrated in figure 1.2. Mixing layers occur between the primary and the bypass stream as well as between the bypass stream and the freestream. For jets with large diameters, the mixing layer is known to be the source of the most audible high-frequency noise with frequencies in the range of 1 to 4 kHz. A further acoustic source is located at the end of the potential core where the spatially growing mixing layers merge. Compared to the mixing layer, its sound emission is of lower frequencies.

Since computational resources are limited and because of the complexity of the problem, highly accurate numerical investigations require to use a simplified configuration. One possibility is the simulation of low-Reynolds-number jets as done by Avital et al. [3] or Freund [34]. Due to the small diameter of the jet the end of the potential core is included. However, the Reynolds similarity is not valid for large-diameter jets and thus, the transfer of the results to real jet engines is questionable. Hence, the focus within this work is set on the mixing layer behind the nozzle end, sketched in figure 1.3. This can be done by prescribing an S-shaped velocity profile at the inflow [15, 25] or by including the trailing edge of the nozzle [6]. The first is denoted as pure mixing layer, here. The latter provides a more realistic configuration since it accounts for the finite boundary-layer thicknesses which yield a combination of wake and mixing layer behind the trailing edge. Furthermore, actuators for flow control can be included in the investigation.

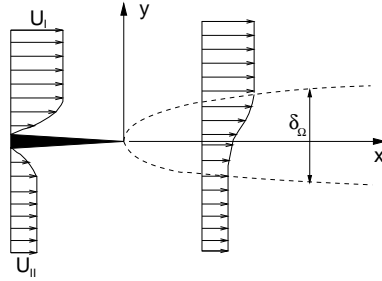


Figure 1.3: Simplified model of the initial part of a jet: mixing layer past a splitter plate with unequal velocities u_I and u_{II} .

Flow Field

A laminar mixing layer can be viewed as steady only in its initial region. If the splitter plate is not taken into account, a similarity solution exists, see White [106]. This solution of the boundary-layer equations is called Blasius mixing layer and its vorticity thickness δ_Ω grows with \sqrt{x} . According to Rayleigh [82], the inflection point in the velocity profile leads to inviscid instability and with large amplification rates, the mixing layer is highly unstable. Michalke [68] investigated the stability of a hyperbolic-tangent velocity profile using linear stability theory (LST). Maximum amplification is found for frequency $f_0 \approx 0.132 \cdot u_{mean}/\delta_\Omega$ with u_{mean} being the arithmetic mean of both

freestream velocities. Later he could show that two-dimensional waves are more amplified than three-dimensional ones [69]. Monkewitz & Huerre [72] extended the stability computations to Blasius mixing layers and found the maximum amplification rate of a self-similar mixing layer to be roughly proportional to the velocity ratio. The combination of wake and mixing layer was considered by Zhuang & Dimotakis [110]. Their inviscid linear stability theory revealed the existence of an additional wake mode due to the existence of two inflection points.

The unsteady free shear layer is predominantly two-dimensional in its initial stages. This is also found in experiments, e.g. by Miksad [71]. The mixing layer rolls up to Kelvin-Helmholtz vortices with subsequent vortex pairing. Typically, the three-dimensional development towards a turbulent flow sets in with streamwise vortices which are bended around their spanwise counterparts. In their experiments, Bernal & Roshko [13] found these longitudinal vortices to be pairwise counter rotating. They interact with the spanwise vortices, leading to a breakdown to small-scale structures. Hipp-Kalthoff [43] could show in his incompressible simulations that secondary instability (translative instability) plays a major role in the origin of three-dimensional structures. Once the mixing layer is turbulent, its mean flow field grows linearly with respect to the streamwise coordinate. The spreading rate is approximately proportional to the velocity ratio, see Ho & Huerre [44]. With increasing compressibility, the growth rate of the averaged mixing layer decreases as shown by Vreman et al. [102]. The end of the jet's potential core is dominated by small-scale turbulent structures and enhanced mixing, illustrated by a Schlieren photograph in figure 1.4.

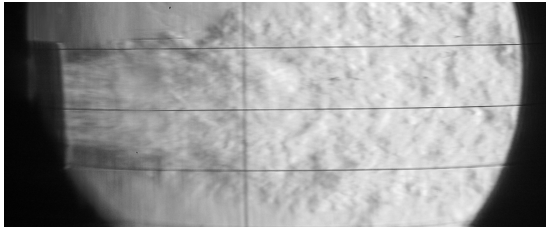


Figure 1.4: Schlieren picture of a low-Reynolds-number jet (hairdryer) with $Re \approx 18000$, showing the end of the potential core.¹

¹Thanks to Birgit Lenz and Anne-Marie Schreyer for taking the photograph.

One should keep in mind that the above transition mechanism strongly depends on the disturbance spectrum. If the introduced disturbances are predominantly oblique modes, it is possible to bypass the two-dimensional Kelvin-Helmholtz mechanism and reach turbulence directly. Alternatively, the flow parameters may inhibit large coherent structures. For mixing layers with a non-zero sweep angle, oblique modes are most amplified and an early breakdown can be observed, see e.g. Kamoun [48]. This is also the case in two-dimensional mixing layers with large compressibility effects. Sandham & Reynolds [86] showed by means of LST and temporal DNS that oblique waves grow more rapidly than two-dimensional instabilities for high Mach numbers. The resulting Λ -vortices are staggered in streamwise direction.

Acoustic Field

When sound is caused by the flow and not by mechanical vibrations of a structure, one speaks of aeroacoustics. Commonly, one distinguishes between the unsteady flow field where the sound is generated and the acoustic farfield in which the acoustic wave propagates. The acoustic field is coupled with the generating flow field in frequency space. For example every time when two vortices collide, an acoustic fluctuation is generated and thus, the frequency of the emitted sound is the one of the vortex pairing. On the other hand, the emitted sound may generate new instability waves in the presence of solid surfaces, thus forming a feedback loop between flow field and acoustics.

A first connection between the flow field and the generated sound was developed by Lighthill [59, 60]. His analogy predicts quadrupole sources and the main sound emission in downstream direction for the mixing layer. Although acoustic sources are generated by downstream-convected disturbances, their location is fixed with respect to the nozzle end as shown experimentally by Laufer & Yen [57]. They found the sources to be associated with the saturation of instability waves and the corresponding vortex positions. The sound caused by large turbulent structures like Kelvin-Helmholtz vortices is known to propagate mainly in downstream direction while the acoustic emission due to small scale structures is less directive, see Tam & Auriault [97]. The effect of large structures in a mixing layer is confirmed by various numerical simulations [15, 25] which showed good agreement with acoustic analogies. The simulation of a jet with $Re = 3600$ by Freund [34] provided the main sound emission from the end of the potential core. However, a direct relation between vortex pairing and sound generation can not be established: the flow field of the noise-controlled mixing layer by Wei & Freund [105] does not differ fundamentally from the uncontrolled case with larger sound emission.

In supersonic jets, the interaction of shock cells with the mixing layer acts as an additional source of sound, see e.g. Schulze et al. [89]. Furthermore the phase velocity of instability waves may become supersonic depending on the temperature and the Mach number of the jet. The resulting instability waves show a linear phase distribution in normal direction [91]. Hence, these waves travel not only in streamwise but also in normal direction and the instability itself is an acoustic wave. For details on supersonic jet noise, the reader is referred to the review by Tam [96].

1.2 Characterization of Sound

Sound is one of the characteristic waves in compressible flows, traveling with the vector sum of the local flow velocity and the speed of sound. Since acoustic waves are usually of small amplitude with respect to the ambient flow field, sound is a linear wave. It can be described by frequency $f = \omega/(2\pi)$ and amplitude. Due to the wide range of acoustic fluctuations along several orders of magnitude, the sound pressure level (SPL) is given in logarithmic scale:

$$L_p = 20 \cdot \log_{10} \left(\frac{\tilde{p}'_{rms}}{\tilde{p}'_{ref}} \right), \quad (1.1)$$

where the subscript $_{rms}$ denotes the root-mean-square. The reference pressure is $\tilde{p}'_{ref} = 2 \cdot 10^{-5} Pa$, being the threshold of hearing at a frequency of $f = 1 kHz$. According to equation (1.1), an increase of sound pressure by a factor of two corresponds to +6 dB. The sound pressure level scales inversely with the distance to an acoustic point source. Exemplary noise sources with their typical SPL values are listed in table 1.1.

source	\tilde{p}'_{rms} [Pa]	SPL [dB]
jet engine at 30m	630	150
gun shot at 1m	200	140
threshold of pain	100	133
jack hammer at 1m	2	100
traffic noise	$2 \cdot 10^{-1}$	80
normal talking	$2 \cdot 10^{-2}$	60
library	$2 \cdot 10^{-3}$	40
auditory threshold at 1 kHz	$2 \cdot 10^{-5}$	0

Table 1.1: Sound pressure levels in air and rms-values of the pressure fluctuation for various acoustic sources.

Beyond the physical quantification of sound, various psycho-acoustic models exist to obtain a better agreement with the sensitivity of the human ear. The so-called A-weighted filter is used especially in the field of technical acoustics and for regulations. It is denoted by dB(A) and emphasizes frequencies between 3 and 6 kHz. For example sound with a frequency of 95 Hz is reduced by -20 while the one with $f = 3$ kHz increases by $+1.27$ in the dB(A)-scale. The effect of aircraft noise is often characterized by the effective perceived noise level (EPNL) which is used by the Federal Aviation Administration [31] and includes the duration of the emitted sound as well. As investigations are done in non-dimensional quantities, pressure fluctuations are given simply in logarithmic scales, within this work.

1.3 Computational Aeroacoustics

Compared to other disciplines in the range of computational fluid dynamics, aeroacoustic simulations are a relatively new field, facing several difficulties. The main problem are the different scales of the hydrodynamic² fluctuations and the emitted sound, forming a multiscale problem sketched in figure 1.5. The actual flow field, e.g. a mixing or a boundary layer, is dominated by high frequencies with short wave lengths. For turbulent flows, large fluctuations occur and the size of the structures ranges down to the Kolmogorov scale. On the other hand, the emitted sound has relatively small amplitudes. Up to moderate Mach numbers, the propagation speed of acoustic waves is significantly larger than the flow speed. Furthermore, larger scales of the flow like Kelvin-Helmholtz vortices in a mixing layer are known to be the dominant acoustic sources. Since acoustic emissions are triggered by the frequencies of the flow, the wavelengths of the sound are large with respect to the hydrodynamic fluctuations.

Two principal methods exist to deal with aeroacoustic problems: direct acoustic simulations, where the flow field and the generated sound are obtained by one single simulation, and hybrid computations, where the acoustic field is derived by sources taken from a previous simulation of the flow field. A time-accurate coupling of flow and acoustic solver as given in appendix D and [4] may be classified somewhere between both methods.

²The term *hydrodynamic* denotes the actual flow field in contrary to the acoustic field. It does not imply incompressible flow, here.

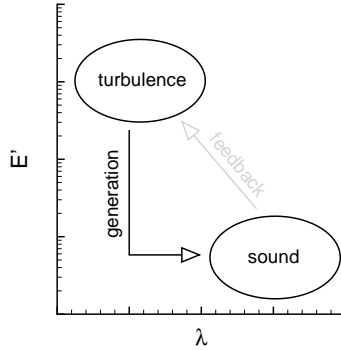


Figure 1.5: Intensity and wavelength of hydrodynamic fluctuations (e.g. turbulence) and the emitted sound.

Hybrid Simulation

In the hybrid approach, the flow field is simulated separately from the acoustic field. Depending on the requested accuracy and the Reynolds number, this can be based on direct numerical simulations (DNS), large-eddy simulations (LES) or unsteady Reynolds-averaged Navier-Stokes equations (RANS). Since sound is not yet considered in this step, the simulation may be compressible or incompressible. In a second step, the unsteady data of the flow field is used to compute the acoustic far field based on acoustic theories. The one developed first is the acoustic analogy by Lighthill [59]. He transformed the compressible Navier-Stokes equations into a linear wave equation. Non-linear terms and viscous effects are represented by a source term which is taken from the unsteady flow field computed before. Solid surfaces were included in the acoustic analogy by Ffowks-Williams & Hawkings [33]. Lilley [61] derived an extension of Lighthill's analogy which accounts for sound propagation in a non-uniform mean flow. Yet the acoustic field in a sheared baseflow can be subject to hydrodynamic instabilities as well. These are avoided by the acoustic perturbation equations derived by Ewert & Schröder [29] which were shown to be hydrodynamically stable. When less accurate solutions of the flow field are used, the acoustic sources due to the missing fine scales can be modelled by semi-empirical theories like the one of Tam & Auriault [97].

With the computation of the sound being some kind of postprocessing, flow and acoustic simulations are completely decoupled. The hybrid approach resolves some major difficulties of the multiscale problem and hence may be applied to

higher Reynolds numbers. Yet numerical approximations of the source terms must be done thoroughly since small errors may affect the acoustic field severely, see e.g. Avital et al. [3]. Up to now it is difficult to separate the source terms from linear acoustic perturbations in spreading shear flows. Thus, Wang et al. [103] classify acoustic analogies as modeling which should be applied with caution.

Direct Acoustic Simulation

Commonly, direct acoustic simulations are based on direct numerical simulation which resolves all relevant scales, or large-eddy simulation where dissipative scales are described by a sub-grid-scale model. In principle this may be done also by means of unsteady RANS. However, noise due to turbulence is not included and its dissipative behavior may handicap an adequate wave propagation. Examples of successful simulations are given by Colonius et al. [25] and Freund [34] for DNS and by Bogey et al. [15] and Keiderling & Kleiser [49] for LES. Since modeling is avoided, direct computation based on DNS seems to be the most promising method to study the mechanisms of sound generation and for the development of flow-control techniques. Unlike acoustic analogies, possible feedback of acoustics on the noise-generating flow field as sketched in figure 1.5 is included in this approach.

Direct aeroacoustic simulations have high demands on the numerical scheme. In order to represent the mechanisms of sound generation correctly, a well-resolved mesh is required. Since the relevant portion of the acoustic farfield must be included as well, non-uniform grids are necessary to perform efficient computations. To ensure that the discretization itself does not act as a source of sound, a highly-accurate numerical scheme is compulsory. This is especially the case for low Mach-number flows where the magnitude of the generated sound is very small, e.g. see Wang et al. [103].

Success or failure of DNS with direct sound computation is directly related to the choice of boundary conditions. At the freestream boundaries, outgoing acoustic waves must be allowed to leave the computational domain. Due to their small amplitudes, linearized boundary conditions can be employed, here. Usually this is some characteristic boundary condition as described by Thompson [98] or Giles [36] where the Euler equations are linearized about a given baseflow. Based on an eigenvalue analysis, incoming disturbances are set to zero and outgoing waves are computed from the interior flow field. By combining them with a small damping zone, reflections due to oblique waves can be reduced significantly.

The most crucial part is the outflow boundary where reflections due to high-amplitude fluctuations of the flow must be prevented. In incompressible flows, ramping the vorticity vector to a reference condition was shown to work properly by Kloker & Konzelmann [53]. However, this can not be applied to compressible flow quantities in direct acoustic simulations since the continuity equation is not satisfied, hence generating large acoustic reflections. Colonius et al. [24] proposed a combination of grid stretching and spatial filtering. Disturbances are less resolved as they propagate through the sponge region and are successively removed by the filter. Since the complete set of equations is solved in the damping zone, the continuity equation is not violated and hence acoustic reflections are sufficiently small. In the zonal approach of Sandberg & Sandham [85] incoming characteristics are smoothly ramped to zero inside a buffer zone. A further method is the perfectly matched layer (PML) which was developed by Berenger [11] for electromagnetic waves and extended to fluid dynamics by Hu [45]. The PML technique reduces reflections by adding an additional advection velocity and damping inside the layer. A characterization of various boundary conditions for aeroacoustic simulations has been summarized by Colonius [23].

1.4 Noise Reduction Technology

Currently, different approaches towards quiet aircraft are considered. One possibility is to optimize the flight path such that the acoustic burden near airports is reduced. This may yield a reduction of 1 to 3 dB [74]. Another approach is the modification of the complete configuration of an aircraft. The blended wing concept is a flying wing with its engines on top. With this design, the noise emission towards the ground is shielded, e.g. Hileman et al. [42]. However, these concepts do not tackle the origin of sound generation.

Probably more promising is the application of flow control where flow structures in the mixing layer are modified in order to decrease their acoustic emissions. A reasonable approach is to alter the geometry of the nozzle end. The Chevron nozzle consists of serrations at the trailing edge and is known to affect the noise generation positively. As shown in figure 1.6, this is already applied to commercial aircraft. The effect is often explained by enhanced mixing but this is rather a description than an explanation. Thus, the physical mechanisms of non-uniform nozzle ends are only partly understood.

The experimental study of various chevron nozzles by Callender et al. [20] reveals a noise reduction of 3 – 6 dB for the lower frequencies and a slightly

increased generation of high-frequency sound. With the improvement strongly depending on the velocity difference of the mixing layer, they state that chevron nozzles should be operated near the design point. Bridges & Brown [17] investigated a hot $Ma = 0.9$ jet with various nozzle shapes. The number of chevrons was a dominant parameter while their length appeared to be less important. The decreased generation of low-frequency noise is also observed in RANS simulations by Engblom et al. [28]. Birch et al. [14] explain this by a reduction of turbulence production due to an increased thickness of the mixing layer. Yet this is contrary to the stronger generation of high-frequency noise. Gudmundsson & Colonius [38] applied linear stability theory to the time-averaged chevron flow field taken from [17]. Compared to a straight trailing edge, spatial amplification rates are reduced and their maxima are shifted to lower frequencies. Kit et al. [50] investigated the mixing layer past a trailing edge with triangular chevrons experimentally. They found streamwise vortices and a spanwise deformation of the Kelvin-Helmholtz vortices. Similar results were obtained in the DNS by Babucke et al. [7, 8], leading to an early breakdown of the spanwise vortices and a notable reduction of low-frequency noise. A slit trailing edge can reduce airfoil trailing-edge noise as shown by Herr [41]. In her experimental study, generated sound was decreased furthermore by using a flexible material which might be an option for jet-noise reduction as well.



Figure 1.6: Chevron nozzle on a Boeing 787's jet engine.³

A further approach is fluid injection in the mixing layer of a jet. Arakeri et al. [2] studied the effect of microjets on a Mach 0.9 jet by means of particle image

³Image by M.J. Handel from <http://en.wikipedia.org/wiki/Image:Boeing-787-engine-chevrons.jpg>.

velocimetry. Its flow field shows a reduced peak vorticity and the noise field was reduced by 2 dB. A similar reduction is found by Harrison et al. [39] for optimized angles of injection and in the LES by Gröschel et al. [37].

Beyond steady modifications of the flow, active actuation may be used to affect the sound generation of a jet's mixing layer. Due to the complexity of the flow field, the shape of a proper actuation is an open question. A method to deal with the large number of unknown is based on adjoint analysis. The adjoint Navier-Stokes equations are computed backward in time and provide the sensitivity of the flow to disturbances. They are linearized about a given solution of the Navier-Stokes equations at the respective time instances. Such sensitivity analyses have been performed by Cervino et al. [22] for a low-Reynolds-number jet and by Spagnoli & Airiau [93] for a compressible mixing layer. The backward-in-time integration leads to a broadening of the adjoint spectrum at the inflow. Hence, it is possible to control high-frequency noise with low-frequency actuation.

The adjoint solution directly provides the gradient of the acoustic emission allowing an optimization of the control parameters. The minimum of the cost function can be found using a gradient algorithm. Yet one should keep in mind that gradient-based methods provide a local minimum. Since the adjoint equations are linear with respect to the time-evolving Navier-Stokes solution, several iterations of DNS and adjoint computation need to be performed. The resulting computational effort limits this approach to two-dimensional investigations up to now. Wei & Freund [105] applied such control to a randomly excited mixing layer, leading to a noise reduction of 11 dB. Since the flow field of the controlled and uncontrolled case do not differ significantly, vortex pairing does not act automatically as an acoustic source. The optimized control is found to make the flow more uniform. In a harmonically excited mixing layer, the flow is less chaotic and hence, Spagnoli [92] achieved a slightly lower noise reduction, there. These results show that actuation requires only little energy. However, the resulting control is quite complex in space and time and thus, the actual design of an active control device for jet-noise reduction remains unclear.

1.5 Scope of the Work

Despite the achieved progress in recent decades, jet noise is still an open issue and the underlying mechanisms are not well understood. Acoustic sources often correlate with vortex pairing but the origin of sound generation can not be referred to a specific flow feature yet. It is also unclear in which way the emitted

sound may generate new hydrodynamic instability waves and hence may form a feedback loop of acoustic and flow field. However, profound knowledge seems to be unavoidable to achieve significant jet-noise reduction in the future. In this context, the present work is intended to provide a detailed insight into the process of sound generation in a mixing layer. To avoid modeling, spatial direct numerical simulation is used to compute the flow and relevant portions of the acoustic farfield. The topics worked on are the following:

- development of a highly-accurate DNS code for aeroacoustic simulations
- identification of the fundamental mechanisms of flow-induced noise generation in a mixing layer
- determination of the influence of the nozzle end
- investigation of the mechanisms of serrated nozzle ends and their effect on sound generation
- simulation of a mixing layer with a turbulent boundary layer upstream of the nozzle end

The first objective is the development of a new DNS code for aeroacoustic simulations based on unsteady compressible Navier-Stokes equations, given in chapter 2. The numerical scheme including appropriate boundary conditions for aeroacoustic simulations is presented in chapter 3. The discretization is designed with great care, including an accuracy analysis on non-uniform grids (appendix A). Beyond accuracy and computational efficiency (appendix C), emphasis is set on the flexibility of the code, allowing a wide range of applications like the trailing edge of a nozzle or a complete airfoil. The DNS code is part of a complete framework including linear stability theory, pre- and post-processing. A new approach to deal with multiscale problems is the coupling of DNS with an acoustic solver whose principal functionality is shown in appendix D.

The numerical method is verified by comparing its results of a mixing layer with a reference case and spatial linear stability theory (chapter 4). Additionally, this rather generic case serves to determine the flow features which are relevant for noise generation. A more realistic configuration is achieved by adding the nozzle end to the simulation. The effects of thickness and spanwise shape are considered in chapters 5 and 6, respectively. In chapter 7, the focus is set on a mixing layer at higher Reynolds number, emanating from a turbulent boundary layer at the nozzle. A final conclusion (chapter 8) summarizes the findings and provides an outlook on future research.

2 Physical Model

Direct numerical simulations are intended to be an exact representation of the reality. However, modeling takes place by defining the integration domain and the partial differential equations to be solved. In the following, this mathematical representation is described.

2.1 Notation

The Cartesian reference system (x, y, z) for the computations is sketched in figures 2.1 and 2.2 for two exemplary configurations. The x -axis is normal to the leading or trailing edge of the geometry pointing in streamwise direction. For a flat plate, the x -axis is aligned to the wall and in case of a vanishing sweep angle, it corresponds to the flow direction of the freestream. The y -axis is aligned in vertical direction with the x - y plane being normal to the spanwise z -direction, forming a right-handed coordinate system with periodicity in spanwise direction. The corresponding velocity components are u , v and w for x -, y - and z -direction, respectively.

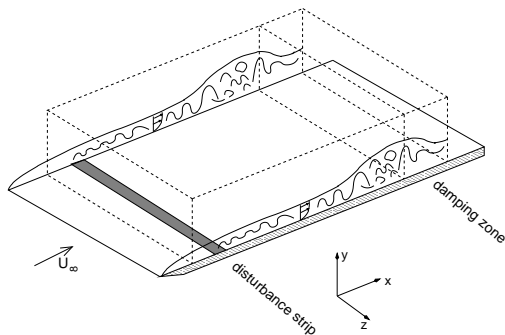


Figure 2.1: Sketch of a typical integration domain for the simulation of a boundary layer along a flat plate with disturbance strip and damping zone.

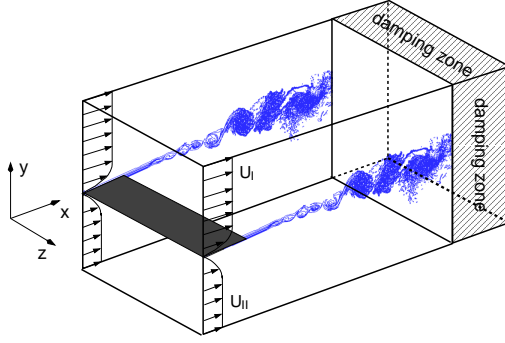


Figure 2.2: Integration domain for the mixing layer behind a splitter plate with the fast stream u_I on top and the slow stream u_{II} below the splitter plate.

All computations are performed in non-dimensional quantities. Velocities are normalised by the reference velocity \tilde{u}_∞ , temperature \tilde{T} and density $\tilde{\rho}$ with their corresponding free-stream values being marked with the subscript ∞ . The tilde denotes dimensional quantities. Length scales are made non-dimensional with the reference length \tilde{L} and time \tilde{t} with $\tilde{L}/\tilde{u}_\infty$:

$$\begin{aligned} u &= \frac{\tilde{u}}{\tilde{u}_\infty}, & v &= \frac{\tilde{v}}{\tilde{u}_\infty}, & w &= \frac{\tilde{w}}{\tilde{u}_\infty}, \\ \rho &= \frac{\tilde{\rho}}{\tilde{\rho}_\infty}, & T &= \frac{\tilde{T}}{\tilde{T}_\infty}, \\ x &= \frac{\tilde{x}}{\tilde{L}_\infty}, & y &= \frac{\tilde{y}}{\tilde{L}_\infty}, & z &= \frac{\tilde{z}}{\tilde{L}_\infty}, & t &= \tilde{t} \cdot \frac{\tilde{u}_\infty}{\tilde{L}}. \end{aligned} \quad (2.1)$$

With the above quantities, we obtain the normalised pressure and heat capacities to:

$$p = \frac{\tilde{p}}{\tilde{\rho}_\infty \tilde{u}_\infty^2}, \quad c_p = \tilde{c}_p \cdot \frac{\tilde{T}_\infty}{\tilde{u}_\infty^2}, \quad c_v = \tilde{c}_v \cdot \frac{\tilde{T}_\infty}{\tilde{u}_\infty^2}. \quad (2.2)$$

Using their free-stream values to normalise viscosity $\tilde{\mu}$ and thermal conductivity $\tilde{\vartheta}$ yields the Reynolds number

$$Re = \frac{\tilde{\rho}_\infty \tilde{u}_\infty \tilde{L}}{\tilde{\mu}_\infty} \quad (2.3)$$

and the Prandtl number

$$Pr = \frac{\tilde{c}_p \tilde{\mu}_\infty}{\tilde{\vartheta}_\infty}. \quad (2.4)$$

Compressibility effects are described by the global Mach number, being the ratio of the free-stream velocity and the speed of sound at reference conditions:

$$Ma_\infty = \frac{\tilde{u}_\infty}{\tilde{a}_\infty} \quad (2.5)$$

In case of a mixing layer, two freestream conditions exist which are marked by the subscripts I and II for the upper and lower stream, respectively. Within this work, the quantities at the upper stream are used for normalization ($\infty = I$).

2.2 Governing Equations

The three-dimensional unsteady compressible Navier-Stokes equations are given in conservative formulation with the solution vector

$$\mathbf{Q} = (\rho, \rho u, \rho v, \rho w, E)^T \quad (2.6)$$

containing the density, the three mass fluxes and the total energy per volume E which is generally defined as

$$E = \rho \int c_v dT + \frac{\rho}{2} (u^2 + v^2 + w^2). \quad (2.7)$$

The compressible Navier-Stokes equations can be written in vector notation

$$\frac{\partial \mathbf{Q}}{\partial t} + \frac{\partial \mathbf{F}}{\partial x} + \frac{\partial \mathbf{G}}{\partial y} + \frac{\partial \mathbf{H}}{\partial z} = 0 \quad (2.8)$$

with the flux vectors \mathbf{F} , \mathbf{G} and \mathbf{H} :

$$\mathbf{F} = \begin{bmatrix} \rho u \\ \rho u^2 + p - \tau_{xx} \\ \rho uv - \tau_{xy} \\ \rho uw - \tau_{xz} \\ u(E + p) + q_x - u\tau_{xx} - v\tau_{xy} - w\tau_{xz} \end{bmatrix} \quad (2.9)$$

$$\mathbf{G} = \begin{bmatrix} \rho v \\ \rho w v - \tau_{xy} \\ \rho v^2 + p - \tau_{yy} \\ \rho v w - \tau_{yz} \\ v(E + p) + q_y - u\tau_{xy} - v\tau_{yy} - w\tau_{yz} \end{bmatrix} \quad (2.10)$$

$$\mathbf{H} = \begin{bmatrix} \rho w \\ \rho w w - \tau_{xz} \\ \rho v w - \tau_{yz} \\ \rho w^2 + p - \tau_{zz} \\ w(E + p) + q_z - u\tau_{xz} - v\tau_{yz} - w\tau_{zz} \end{bmatrix}, \quad (2.11)$$

containing normal stresses

$$\tau_{xx} = \frac{\mu}{Re} \left(\frac{4}{3} \frac{\partial u}{\partial x} - \frac{2}{3} \frac{\partial v}{\partial y} - \frac{2}{3} \frac{\partial w}{\partial z} \right) \quad (2.12)$$

$$\tau_{yy} = \frac{\mu}{Re} \left(\frac{4}{3} \frac{\partial v}{\partial y} - \frac{2}{3} \frac{\partial u}{\partial x} - \frac{2}{3} \frac{\partial w}{\partial z} \right) \quad (2.13)$$

$$\tau_{zz} = \frac{\mu}{Re} \left(\frac{4}{3} \frac{\partial w}{\partial z} - \frac{2}{3} \frac{\partial u}{\partial x} - \frac{2}{3} \frac{\partial v}{\partial y} \right), \quad (2.14)$$

shear stresses

$$\tau_{xy} = \frac{\mu}{Re} \left(\frac{\partial u}{\partial y} + \frac{\partial v}{\partial x} \right) \quad (2.15)$$

$$\tau_{xz} = \frac{\mu}{Re} \left(\frac{\partial u}{\partial z} + \frac{\partial w}{\partial x} \right) \quad (2.16)$$

$$\tau_{yz} = \frac{\mu}{Re} \left(\frac{\partial v}{\partial z} + \frac{\partial w}{\partial y} \right) \quad (2.17)$$

and the heat flux

$$q_x = -\frac{\vartheta}{(\kappa - 1)RePrMa_\infty^2} \cdot \frac{\partial T}{\partial x} \quad (2.18)$$

$$q_y = -\frac{\vartheta}{(\kappa - 1)RePrMa_\infty^2} \cdot \frac{\partial T}{\partial y} \quad (2.19)$$

$$q_z = -\frac{\vartheta}{(\kappa - 1)RePrMa_\infty^2} \cdot \frac{\partial T}{\partial z}. \quad (2.20)$$

2.3 Properties of the Fluid

The fluid is assumed to be a non-reacting ideal gas with the equation of state providing closure of the equation system:

$$p = \frac{\rho \cdot T}{\kappa Ma_\infty^2} \quad (2.21)$$

Hence, the speed of sound in non-dimensional quantities is

$$a = \frac{\sqrt{T}}{Ma_\infty}. \quad (2.22)$$

The heat capacities for constant pressure and volume are considered to be constant:

$$c_p = \frac{1}{(\kappa - 1) \cdot Ma_\infty^2}, \quad c_v = \frac{1}{\kappa (\kappa - 1) \cdot Ma_\infty^2} \quad (2.23)$$

Thus, the adiabatic index $\kappa = c_p/c_v$ is fixed as well and the integral in equation (2.7) simplifies to the product $c_v \cdot T$. The heat capacity ratio $\kappa = 1.4$ used throughout the simulations is the theoretical value for a diatomic gas and corresponds well to the thermodynamical properties of air.

Temperature dependence of viscosity is modelled by the Sutherland law [95] for temperatures above the Sutherland temperature $\tilde{T}_s = 110.4K$:

$$\tilde{\mu}(T) = \tilde{\mu}_0(\tilde{T}_0) \cdot T^{3/2} \cdot \frac{1 + T_s}{T + T_s}, \quad (2.24)$$

where $T_s = \tilde{T}_s/\tilde{T}_\infty$ is the nondimensional Sutherland temperature and $\tilde{\mu}_0(\tilde{T}_0 = 280K) = 1.735 \cdot 10^{-5} kg/(ms)$. For temperatures below T_s , a linear temperature dependence of the viscosity is assumed. The Prandtl number is fixed to $Pr = 0.71$ being a typical value for air at moderate conditions.

3 Numerical Method

In this chapter, the numerical methods used for the solution are described. The following sections provide an outline of the developed simulation framework for compressible flows based on the DNS code NS3D. The set of tools includes linear stability theory, initial conditions and postprocessing.

3.1 Code Development at IAG

The history of direct numerical simulations at IAG¹ ranges back to the first spatial simulations of instability waves by Fasel [30]. In 1991, Rist & Fasel [83] presented the first spatial simulations of three-dimensional non-linear transition. The numerical scheme for incompressible flows was further developed by Kloker [52] et al. [53], allowing stable long-time simulations by implementing alternating biased finite differences and a special buffer zone at the outflow boundary. Later, the spatial discretization was extended to compact finite differences [55]. Despite being specialized to boundary layers along a flat plate, special modifications of the incompressible code allowed the computation of other flow configurations: for example, Hipp-Kalthoff [43] applied it to incompressible mixing layers.

DNS of the compressible Navier-Stokes equations was initiated at IAG by Thumm [99]. His numerical scheme was based on explicit finite differences and a second-order time integration scheme. The spectral ansatz allowed cases which are symmetric in spanwise direction. Eissler [27] applied it to supersonic boundary layers with the following improvements: alternating compact finite differences in streamwise direction and the 4th-order Runge-Kutta scheme for time integration. By its adaptation to conical coordinates, Fezer & Kloker [32] simulated the supersonic boundary layers along a cone. The numerical scheme was extended to curvilinear grids by Pagella et al. [79], allowing the computation of a supersonic boundary layer along a compression ramp.

With the NEC-SX6 and SX8 [12], new supercomputers were installed at HLRS in 2004 and 2005, respectively. Due to the new architecture with multiple

¹Up to 1990, the transition research group was affiliated to the Institut A für Mechanik of the Universität Stuttgart.

shared-memory nodes, the previously used purely shared-memory parallelization showed to be no more sufficient. Additionally, one may expect aeroacoustic simulations of mixing layers including the nozzle end to be quite difficult using a DNS code which is specialized on boundary layers. Therefore, the new DNS-code NS3D has been developed, satisfying the scientific and computational requirements.

3.2 Simulation Framework

Obtaining DNS results does not only require the simulation itself, it also includes pre- and postprocessing as well as stability analysis of the considered baseflow. By far, most computer resources are required by the DNS code. Nevertheless the user spends a lot of time in setup of the problem and analysis of the computed data. Therefore, a complete framework of tools with a common structure of in- and output files, based on the EAS3 tool set [75], has been developed. This not only leads to a more efficient work for the scientist, it also provides reproducibility of the complete set of results. The typical workflow for a DNS is illustrated in figure 3.1.

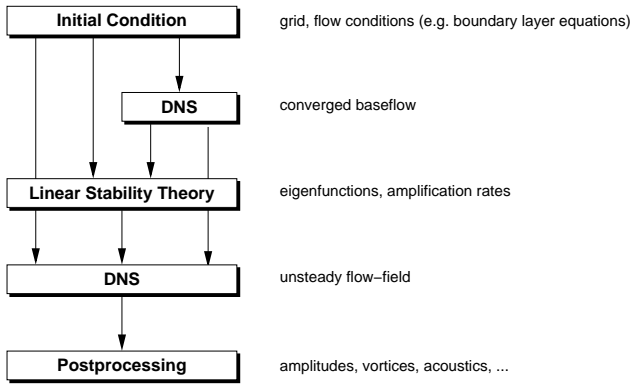


Figure 3.1: Workflow for DNS including pre- and postprocessing as well as stability analysis.

The first step is the definition of the problem itself. Here, the flow conditions, the grid and a possible domain decomposition are specified, providing initial data for the DNS. Of course, this step strongly depends on the problem to be investigated, resulting in specific tools. If the problem allows a steady-state solution, the DNS code may be used already here to get a converged

solution of the Navier-Stokes equations. The initial condition or a converged solution obtained from the previous step can be used in linear stability theory, providing amplification rates and eigenfunctions. This information is used to define disturbance generation for the actual simulation performed by the DNS code. The resulting output is raw binary data with the flow variables given on the computational grid for several time steps. To get a better understanding of the flow physics, postprocessing is used to compute e.g. spectra and amplitudes or vortex criteria.

3.3 DNS Code

The newly developed DNS code NS3D is the core of the simulation framework, solving the unsteady compressible Navier-Stokes equations from section 2.2. On the one hand, the implemented domain decomposition in the x - y plane fulfills the parallelization requirements. On the other hand, its combination with grid transformation allows the application of the numerical scheme to a wide range of geometrical configurations.

3.3.1 Spatial Discretization

The spatial discretization in x - and y -direction is based on compact finite differences (FD) of 6th order. With the non-linear terms generating higher harmonics, dealiasing is necessary to stabilize the numerical scheme. This is achieved by using a high-order McCormack-type scheme with alternating up- and downwind biased finite differences for the convective terms. As shown by Kloker [55], this provides damping of high-wavenumber modes regardless of the flow direction. Thereby, the biasing of the finite differences changes with every sub-cycle of the time integration scheme, given in section 3.3.2.

The classical analysis of finite differences is based on the modified wavenumber [55, 58]. For a simple wave with wavenumber k , the first and second spatial derivatives are complex proportional to the wavenumber and its square, respectively. Accordingly, the modified wavenumber k_{mod}^* and the modified wavenumber square k_{mod}^{*2} are defined as the ratio between the numerically computed spatial derivative and the wave itself:

$$k_{mod}^* = -i \cdot \Delta\zeta \cdot \frac{(\partial\Phi/\partial\zeta)_{num.}}{\Phi} \quad (3.1)$$

$$k_{mod}^{*2} = -\Delta\zeta^2 \cdot \frac{(\partial^2\Phi/\partial\zeta^2)_{num.}}{\Phi}, \quad (3.2)$$

where Φ is an arbitrary flow variable and $i = \sqrt{-1}$. Thus, the exact expressions of equations (3.1) and (3.2) are the wavenumber k^* and its square k^{*2} , respectively. The superscript $*$ indicates that the wavenumber k is normalized with the step size $\Delta\zeta$ by $k^* = k \cdot \Delta\zeta$. The above equation reveals that $k^* = \pi$ corresponds to the least resolved wave with two points per wave length and $k^* = 0$ means an arbitrarily fine resolution of the wave. The deviation of the real part from the exact solution corresponds to an amplitude error while the imaginary part indicates the phase shift which is due to a non-symmetric stencil.

Different compact finite differences with varying dissipation properties are implemented and may be used according to the flow parameters of the simulation. For example, high Mach numbers will cause relevant triple products requiring more dissipation than a low Mach-number flow with marginal density fluctuations. For the simulations of subsonic flows considered within this work, the following alternating stencils (D1) are used for convective terms [54]:

$$\begin{aligned} \frac{1}{5} \cdot \frac{\partial\Phi}{\partial\zeta} \Big|_{j-1,+} &+ \frac{3}{5} \cdot \frac{\partial\Phi}{\partial\zeta} \Big|_{j,+} + \frac{1}{5} \cdot \frac{\partial\Phi}{\partial\zeta} \Big|_{j+1,+} \\ &= \frac{-1 \cdot \Phi_{j-2} - 19 \cdot \Phi_{j-1} + 11 \cdot \Phi_j + 9 \cdot \Phi_{j+1}}{30 \cdot \Delta\zeta} \end{aligned} \quad (3.3)$$

$$\begin{aligned} \frac{1}{5} \cdot \frac{\partial\Phi}{\partial\zeta} \Big|_{j-1,-} &+ \frac{3}{5} \cdot \frac{\partial\Phi}{\partial\zeta} \Big|_{j,-} + \frac{1}{5} \cdot \frac{\partial\Phi}{\partial\zeta} \Big|_{j+1,-} \\ &= \frac{-9 \cdot \Phi_{j-1} - 11 \cdot \Phi_j + 19 \cdot \Phi_{j+1} + 1 \cdot \Phi_{j+2}}{30 \cdot \Delta\zeta} \end{aligned} \quad (3.4)$$

The subscripts $+$ and $-$ denote up- and downwind biasing, respectively and j is the index of the corresponding grid point. The stepsize $\Delta\zeta$ in equidistant computational space is $\Delta\xi$ or $\Delta\eta$, depending on the direction ζ of the spatial derivative. The convective terms are discretized in conservative formulation, meaning that derivatives of the products like (ρu) or (ρuv) and not of the primitive variables are computed by the above stencils. The coefficients of additionally implemented biased compact finite differences are listed in table 3.1.

First derivatives of viscous terms are computed using the standard 6th-order compact FD:

$$\begin{aligned} 1 \cdot \frac{\partial\Phi}{\partial\zeta} \Big|_{j-1} &+ 3 \cdot \frac{\partial\Phi}{\partial\zeta} \Big|_j + 1 \cdot \frac{\partial\Phi}{\partial\zeta} \Big|_{j+1} \\ &= \frac{-1 \cdot \Phi_{j-2} - 28 \cdot \Phi_{j-1} + 28 \cdot \Phi_{j+1} + 1 \cdot \Phi_{j+2}}{12 \cdot \Delta\zeta} \end{aligned} \quad (3.5)$$

	\mathbf{b}_{lhs}	\mathbf{c}_{lhs}	\mathbf{d}_{lhs}	\mathbf{a}	\mathbf{b}	\mathbf{c}	\mathbf{d}	\mathbf{e}
D1 ₊	$\frac{1}{5}$	$\frac{3}{5}$	$\frac{1}{5}$	$-\frac{1}{30 \cdot \Delta \zeta}$	$-\frac{19}{30 \cdot \Delta \zeta}$	$\frac{11}{30 \cdot \Delta \zeta}$	$\frac{9}{30 \cdot \Delta \zeta}$	
D1 ₋					$-\frac{9}{30 \cdot \Delta \zeta}$	$-\frac{11}{30 \cdot \Delta \zeta}$	$\frac{19}{30 \cdot \Delta \zeta}$	$\frac{1}{30 \cdot \Delta \zeta}$
D2 ₊	$\frac{1}{5}$	$\frac{3}{5}$	$\frac{1}{5}$	$-\frac{3}{30 \cdot \Delta \zeta}$	$-\frac{19}{30 \cdot \Delta \zeta}$	$\frac{15}{30 \cdot \Delta \zeta}$	$\frac{9}{30 \cdot \Delta \zeta}$	$-\frac{2}{30 \cdot \Delta \zeta}$
D2 ₋				$\frac{2}{30 \cdot \Delta \zeta}$	$-\frac{9}{30 \cdot \Delta \zeta}$	$-\frac{15}{30 \cdot \Delta \zeta}$	$\frac{19}{30 \cdot \Delta \zeta}$	$\frac{3}{30 \cdot \Delta \zeta}$
D3 ₊	$\frac{1}{5}$	$\frac{3}{5}$	$\frac{1}{5}$	$-\frac{9}{60 \cdot \Delta \zeta}$	$-\frac{38}{60 \cdot \Delta \zeta}$	$\frac{36}{60 \cdot \Delta \zeta}$	$\frac{18}{60 \cdot \Delta \zeta}$	$-\frac{7}{60 \cdot \Delta \zeta}$
D3 ₋				$\frac{7}{60 \cdot \Delta \zeta}$	$-\frac{18}{60 \cdot \Delta \zeta}$	$-\frac{36}{60 \cdot \Delta \zeta}$	$\frac{38}{60 \cdot \Delta \zeta}$	$\frac{9}{60 \cdot \Delta \zeta}$

Table 3.1: Coefficients of the implemented biased FDs D1 to D3 for convective terms [54]. The coefficients \mathbf{a} - \mathbf{e} correspond to the grid points $j - 2$ to $j + 2$ and coefficients of the left-hand-side are marked with the subscript lhs .

The real part $k_{mod,r}^*$ for all up- and downwind biased stencils is the same as for the standard 6th-order compact scheme given by equation (3.5). The dispersion relation given by the real part of the modified wavenumber is shown in figure 3.2 a). Comparing the 6th-order compact scheme (solid line) with the explicit schemes of up to the same order reveals a better agreement with the exact solution $k_{mod}^* = k^*$ in case of a compact discretization. Since the group velocity is proportional to $\partial k_{mod,r}^* / \partial k^*$, aliasing occurs from the maximum of $k_{mod,r}^*$ onwards. The aliasing limit for the 6th-order compact scheme is $k^* = 2.267$. This is an improvement compared to explicit finite differences of 4th and 6th order by 25% and 17%, respectively. The generation of higher-harmonics by the non-linear terms in the Navier-Stokes equations as well as aliasing of the finite differences themselves requires artificial damping of high wave-number fluctuations to stabilize the numerical scheme.

The imaginary part of the modified wavenumber is responsible for the numerical damping and is shown for the downwind-biased finite differences D1 to D3 in figure 3.2 b). With upwind-biased stencils being orientated in the opposite direction, their imaginary parts differ only by their algebraic sign ($k_{mod,i,+}^* = -k_{mod,i,-}^*$). The higher the absolute value of $k_{mod,i}^*$, the stronger is the artificial damping by the forward-backward alternating scheme. Since a quantitative estimation depends on the time step, it is discussed in section 3.3.2.

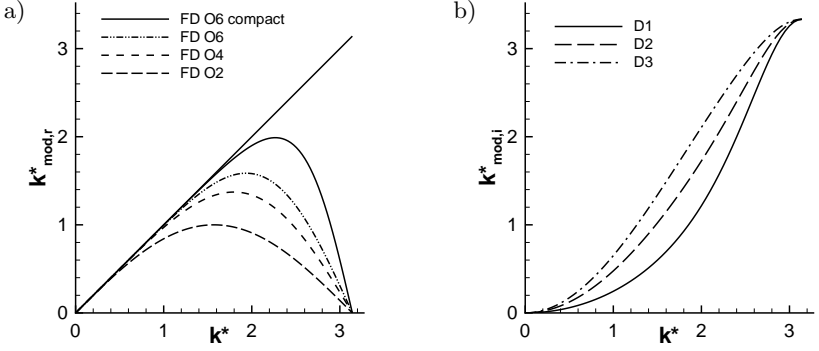


Figure 3.2: a) Real part $k_{mod,r}^*$ of the modified wavenumber for 6^{th} -order compact scheme compared with explicit FDs.
b) Imaginary part $k_{mod,i}^*$ of the downwind biased FDs of table 3.1. The solid line corresponds to the compact FD given by equation (3.4).

The second derivative is computed directly using a central stencil since biasing would cause artificial advection. To provide a consistent order of all spatial derivatives, the standard compact FD of 6^{th} order is used:

$$\begin{aligned}
& 2 \cdot \left. \frac{\partial^2 \Phi}{\partial \zeta^2} \right|_{j-1} + 11 \cdot \left. \frac{\partial^2 \Phi}{\partial \zeta^2} \right|_j + 2 \cdot \left. \frac{\partial^2 \Phi}{\partial \zeta^2} \right|_{j+1} \\
& = \frac{3 \cdot \Phi_{j-2} + 48 \cdot \Phi_{j-1} - 102 \cdot \Phi_j + 48 \cdot \Phi_{j+1} + 3 \cdot \Phi_{j+2}}{4 \cdot \Delta \zeta^2} \quad (3.6)
\end{aligned}$$

With this stencil, the second derivative is computed directly and not by applying the first derivative twice as done by Eissler [27] for example. This provides a better agreement with the exact solution up to high wavenumbers. The improvement is illustrated in 3.3 for explicit and compact FDs of 4^{th} and 6^{th} order respectively. First of all, the direct computation yields a better accordance with the exact solution k^{*2} . Additionally, the modified wavenumber square k_{mod}^{*2} does not vanish for the least resolved wave ($k^* = \pi$). The finite value of the second derivative for the saw-tooth mode provides a markedly more stable and consistent numerical scheme. This is especially important for non-linear computations as high-wavenumber waves are damped by viscous terms, now.

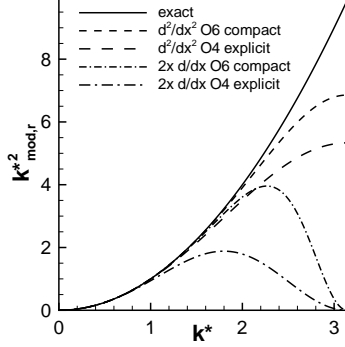


Figure 3.3: Modified wavenumber square k_{mod}^{*2} for direct calculation of the second derivative versus applying the first derivative twice (4^{th} and 6^{th} order).

The above stencils require two neighboring points at both sides. Thus, one sided and biased finite differences are necessary at the boundaries and at the next point, respectively. Directly at the boundaries, a one-sided explicit stencil of the form

$$\left. \frac{\partial^b \Phi}{\partial \zeta^b} \right|_{j=1} = \frac{\mathbf{a} \cdot \Phi_{j=1} + \mathbf{b} \cdot \Phi_{j=2} + \mathbf{c} \cdot \Phi_{j=3} + \mathbf{d} \cdot \Phi_{j=4} + \mathbf{e} \cdot \Phi_{j=5}}{\Delta \zeta^b} \quad (3.7)$$

is used for the first ($b=1$) and the second derivatives ($b=2$). The coefficients of the corresponding stencil are denoted as $\mathbf{a} - \mathbf{e}$. The above equation can be applied directly to the left and the lower boundary, respectively. For the right and upper boundaries, the derivative at $j=N$ is computed with the stencil ranging from $j=N-4$ to the last grid point $j=N$.

The spatial derivatives at the point next to the boundary are computed by the following biased compact finite difference

$$\begin{aligned} \mathbf{b}_{lhs} \cdot \left. \frac{\partial^b \Phi}{\partial \zeta^b} \right|_{j=2} + \mathbf{c}_{lhs} \cdot \left. \frac{\partial^b \Phi}{\partial \zeta^b} \right|_{j=3} &= \frac{\mathbf{a} \cdot \Phi_{j=1} + \mathbf{b} \cdot \Phi_{j=2} + \mathbf{c} \cdot \Phi_{j=3}}{\Delta \zeta^b} \\ &+ \frac{\mathbf{d} \cdot \Phi_{j=4} + \mathbf{e} \cdot \Phi_{j=5} + \mathbf{f} \cdot \Phi_{j=6} + \mathbf{g} \cdot \Phi_{j=7}}{\Delta \zeta^b}, \end{aligned} \quad (3.8)$$

where the coefficients of the left-hand side are marked with the subscript lhs . Again, the above stencil is given exemplarily for the left and lower boundaries.

For the right and upper boundaries the direction of the stencil needs to be reversed as it is the case for the one-sided finite difference.

Depending on the used boundary conditions, different coefficients for FDs of first and second derivatives can be chosen. Thus, the actual stencils for the respective boundary conditions are given in section 3.3.3. In case of neighbors, the tridiagonal equation system due to the compact finite differences ranges along multiple domains. Its solution is based on a pipelined version of the Thomas algorithm. As this affects mainly the parallelization, it is explained in section 3.3.4.

Grid Transformation

With the necessity to capture relevant portions of the acoustic far field, non-uniform grids are essential to perform aeroacoustic computations efficiently. Grid stretching is also necessary to construct appropriate outflow boundary conditions for aeroacoustic simulations, as done by Colonius et al. [24] for example. Additionally, grid transformation is implemented to extend the application of the DNS code beyond a flat plate geometry. Grid transformation is achieved by mapping the generally non-uniform curvilinear x - y mesh to the perpendicular computational space ξ - η with uniform spacing $\Delta\xi$ and $\Delta\eta$. According to Anderson [1], the first spatial derivatives in physical space are computed as

$$\frac{\partial}{\partial x} = \frac{1}{J} \left[\left(\frac{\partial}{\partial \xi} \right) \left(\frac{\partial y}{\partial \eta} \right) - \left(\frac{\partial}{\partial \eta} \right) \left(\frac{\partial y}{\partial \xi} \right) \right] \quad (3.9)$$

$$\frac{\partial}{\partial y} = \frac{1}{J} \left[\left(\frac{\partial}{\partial \eta} \right) \left(\frac{\partial x}{\partial \xi} \right) - \left(\frac{\partial}{\partial \xi} \right) \left(\frac{\partial x}{\partial \eta} \right) \right] \quad (3.10)$$

$$J = \begin{vmatrix} \frac{\partial x}{\partial \xi} & \frac{\partial y}{\partial \xi} \\ \frac{\partial x}{\partial \eta} & \frac{\partial y}{\partial \eta} \end{vmatrix} = \frac{\partial x}{\partial \xi} \cdot \frac{\partial y}{\partial \eta} - \frac{\partial y}{\partial \xi} \cdot \frac{\partial x}{\partial \eta}, \quad (3.11)$$

with J being the Jacobi determinant. The grid transformation is defined by the metric coefficients $\partial x/\partial \xi$, $\partial x/\partial \eta$, $\partial y/\partial \xi$ and $\partial y/\partial \eta$. In general the metrics are a function of ξ and η as well. Second and mixed derivatives are obtained by applying equations (3.9) and (3.10) twice. Together with the expansion of the Navier-Stokes equations, which is necessary to obtain the direct computation of second derivatives, grid transformation causes huge terms. While the evaluation of the continuity equation may be done still by hand, the other conservation equations require an automated code generation: e.g. the source code for the energy equation alone ranges along more than 140 lines and its file size is almost 9 KByte. Thus, the computer algebra system Maple [56] was used

for the expansion of the Navier-Stokes equations and the subsequent export to Fortran source code.

The combination of grid transformation and domain decomposition allows rather complex configurations. An example of a more sophisticated configuration is an airfoil shown in figure 3.4. The construction of such a C-grid is realized by a decomposition into four domains and an appropriate grid transformation.

With the metric terms being derivatives of the coordinates in computational space, two possible methods exist for their evaluation. The first way is to use the same discretization method as for regular flow quantities which can be applied for all cases. The second possibility is an analytical derivation of the metric terms if the grid transformation is given as an analytical function. Although one would assume analytical metric coefficients to be the best choice, it was found to be less accurate than numerical grid transformation, if the same discretization is used for both metric and flow quantities. A theoretical analysis and numerical experiments considering the accuracy on non-uniform grids is given in appendix A and by Babucke and Kloker [5].

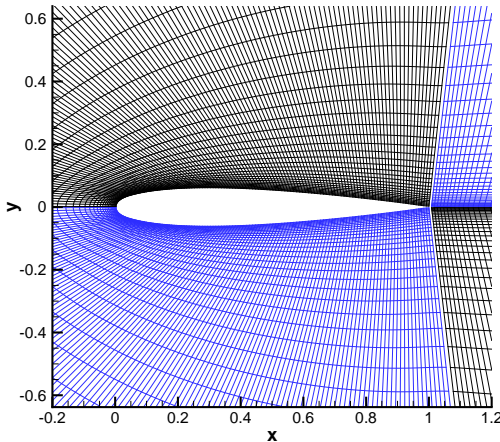


Figure 3.4: Exemplary grid configuration for an airfoil by Schneider [88]. The domain decomposition is illustrated by black and blue colours.

Spanwise Discretization

A spectral discretization for the z -direction has been chosen due to the periodicity in spanwise direction:

$$\Phi(x, y, z, t) = \sum_{k=0}^K \hat{\Phi}_k(x, y, t) \cdot e^{i(k \cdot \gamma_0 \cdot z)} \quad (3.12)$$

with Φ being any flow variable, $\hat{\Phi}_k$ its complex Fourier coefficient and K the number of spanwise modes. Since all flow variables are real values, the modes $k < 0$ are complex conjugate to their corresponding modes $k > 0$

$$\hat{\Phi}_{-k} = c.c. \left\{ \hat{\Phi}_k \right\}. \quad (3.13)$$

Accordingly, only the modes $k \geq 0$ are considered in equation (3.12). The fundamental spanwise wavenumber γ_0 is given by the spanwise extent of the integration domain λ_z :

$$\gamma_0 = \frac{2\pi}{\lambda_z} \quad (3.14)$$

If a two-dimensional initial condition is used and disturbances of u , v , ρ , T , p are symmetric and disturbances of w are antisymmetric, all flow quantities are symmetric/antisymmetric with respect to $z = 0$. This transforms equation (3.12) to

$$\Phi(x, y, z, t) = \Phi_{0,r}(x, y, z, t) + 2 \cdot \sum_{k=1}^K \hat{\Phi}_{k,r}(x, y, t) \cdot \cos(k \cdot \gamma_0 \cdot z) \quad (3.15)$$

for $\Phi \in [u, v, \rho, T, p]$

$$\Phi(x, y, z, t) = -2 \cdot \sum_{k=1}^K \hat{\Phi}_{k,i}(x, y, t) \cdot \sin(k \cdot \gamma_0 \cdot z) \quad (3.16)$$

for $\Phi \in [w]$.

In this case, only half of the spanwise extent needs to be considered ($0 \leq z \leq \lambda_z/2$ instead of $0 \leq z < \lambda_z$). This reduces the amount of grid points in z -direction to half the points plus one.

In previous implementations at the IAG, the main part of the computation was done in Fourier space and flow variables were transformed to physical space only for the computation of non-linear terms. This is favorable for the incompressible Navier-Stokes equations since it allows to solve the Poisson equation independently for each mode. For the compressible case, no elliptic equation occurs. Furthermore, the compressible Navier-Stokes equations solely consist of

non-linear terms. To avoid unnecessary transformations, all computations are performed in physical space and the Fourier-transformation to spectral space is only carried out to compute the spanwise derivatives. For this reason it is relatively easy to allow both symmetric and non-symmetric simulations. The latter is used for the non-symmetric serration (section 6.3) and was applied to a mixing layer with sweep angle by Kamoun [48].

According to equation (3.12), first and second derivatives can be obtained easily by multiplying the spectral components Φ_k with their corresponding wavenumber ($i \cdot k\gamma_0$) or its square $-(k\gamma_0)^2$, respectively. The following inverse Fourier transformation provides the spanwise derivatives in physical space. For the symmetric case, the proper inverse transformation has to be chosen according to symmetry/antisymmetry of the corresponding derivatives:

- symmetric derivatives: $\partial w/\partial z, \partial^2\Phi/\partial z^2$ for $\Phi \in [u, v, \rho, T, p]$
- antisymmetric derivatives: $\partial\Phi/\partial z$ for $\Phi \in [u, v, \rho, T, p], \partial^2 w/\partial z^2$

To suppress aliasing, only $2/3$ of the maximum number of modes for a specific z -resolution are used [21]. Primarily, this is done by setting the higher harmonics $k > (2/3 \cdot K)$ to zero before transforming the derivatives back to physical space. Since other products which are not affected by spanwise derivatives generate higher harmonics as well, an additional filter with the same cut-off wavenumber as above is required. Since the initial condition is usually two-dimensional or at least well resolved in spanwise direction, it is sufficient to filter the time derivatives $\partial\mathbf{Q}/\partial t$ of the solution vector (2.6). For some cases, e.g. the wake behind a blunt body [51], non-linear boundary conditions may generate higherharmonics in spanwise direction. In such cases, the filter can be applied directly to the conservative variables.

3.3.2 Time Integration

For time integration, the classical four-step Runge-Kutta (RK) scheme has been chosen. This method is of high accuracy ($\mathcal{O}4$) and robust with respect to oscillation and diffusion problems as shown in figure 3.5 a). Based on equidistant time levels marked with the superscript l , it consists of four substeps where Δt is the time step from level l to $l + 1$. The conservative variables listed in the solution vector \mathbf{Q} are integrated in time:

$$\mathbf{Q}_k^{l+\frac{1}{2}*} = \mathbf{Q}_k^l + \frac{1}{2}\Delta t \cdot \left. \frac{\partial \mathbf{Q}}{\partial t} \right|_{+/-}^l \quad (3.17)$$

$$\mathbf{Q}_k^{l+\frac{1}{2}} = \mathbf{Q}_k^l + \frac{1}{2}\Delta t \cdot \left. \frac{\partial \mathbf{Q}}{\partial t} \right|_{-/+}^{l+\frac{1}{2}*} \quad (3.18)$$

$$\mathbf{Q}_k^{l+1*} = \mathbf{Q}_k^l + \Delta t \cdot \left. \frac{\partial \mathbf{Q}}{\partial t} \right|_{+/-}^{l+\frac{1}{2}} \quad (3.19)$$

$$\begin{aligned} \mathbf{Q}_k^{l+1} = \mathbf{Q}_k^l + \Delta t \cdot & \left(\frac{1}{6} \cdot \left. \frac{\partial \mathbf{Q}}{\partial t} \right|_{+/-}^l + \frac{1}{3} \cdot \left. \frac{\partial \mathbf{Q}}{\partial t} \right|_{-/+}^{l+\frac{1}{2}*} \right. \\ & \left. + \frac{1}{3} \cdot \left. \frac{\partial \mathbf{Q}}{\partial t} \right|_{+/-}^{l+\frac{1}{2}} + \frac{1}{6} \cdot \left. \frac{\partial \mathbf{Q}}{\partial t} \right|_{-/+}^{l+1*} \right) \quad (3.20) \end{aligned}$$

At each intermediate level, the time derivatives $\partial \mathbf{Q}/\partial t$ and hence, the spatial derivatives have to be recomputed. The direction of the finite differences (3.3) and (3.4) for convective terms changes with every substep, indicated by the subscript $+/-$. To avoid any preferred direction of the spatial discretization, the alternation differs at each time step including all forward-backward combinations in x - and y -direction.

Numerical Dissipation

The actual damping rate is not only a function of the imaginary part of the modified wavenumber but of the time step Δt as well. Therefore, the time integration needs to be considered as well to get quantitative information about numerical damping of the scheme. For this, we consider a linear advection problem transporting a wave with constant speed c . The first spatial derivative can be expressed by the modified wavenumber and the actual value according to equation 3.1. Inserting this to the Runge-Kutta scheme of equations (3.17) to (3.20), we obtain after some algebra the solution at the new time step $l+1$:

$$\begin{aligned} \frac{\Phi^{l+1}}{\Phi^l} = & 1 - i \cdot CFL \cdot k_{mod,r}^* - \frac{1}{2} \cdot CFL^2 \cdot k_{mod,r}^{*2} \\ & + i \cdot \frac{1}{6} \cdot CFL^3 \cdot k_{mod,r}^{*3} + \frac{1}{24} \cdot CFL^4 \cdot k_{mod,r}^{*4} \\ & - \frac{1}{2} \cdot CFL^2 \cdot k_{mod,i}^{*2} + i \cdot \frac{1}{6} \cdot CFL^3 \cdot k_{mod,r}^* k_{mod,i}^{*2} \\ & + \frac{1}{12} \cdot CFL^4 \cdot k_{mod,r}^{*2} k_{mod,i}^{*2} + \frac{1}{24} \cdot CFL^4 \cdot k_{mod,i}^{*4} \quad (3.21) \end{aligned}$$

where CFL is the Courant-Friedrichs-Lewy number:

$$CFL = \frac{c \cdot \Delta t}{\Delta \zeta} \quad (3.22)$$

The first two lines of equation (3.21) are the Taylor expansion in time containing only the real part of the modified wavenumber. Hence, only the following lines are responsible for numerical damping due to the spatial discretization. The leading term of $k_{mod,i}^*$ is of order CFL^2 , so damping is mainly proportional to the square of the time step and independently of the flow direction. The amplitude ratio after one time step is given by the absolute value of equation (3.21). A more significant quantity is the amplitude's change after one period of the considered wave, see Kloker [55]. The number of time steps per period is $2\pi / (CFL \cdot k^*)$ and thus, the amplitude ratio after one period is

$$AP_{mod} = \left| \frac{\Phi^{l+1}}{\Phi^l} \right|^{\frac{2\pi}{CFL \cdot k^*}}. \quad (3.23)$$

The behavior of AP_{mod} based on the Runge-Kutta scheme and the alternating compact finite differences D1 of equations (3.3) and (3.4) is illustrated for different CFL numbers in figure 3.5 b).

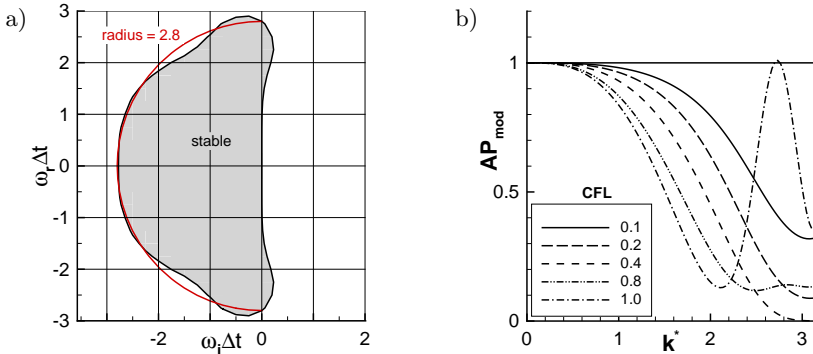


Figure 3.5: a) Stability diagram of the 4th-order Runge-Kutta scheme and the simplified stability limit (half-circle with radius 2.8).

b) Amplitude ratio after one period of the linear advection problem for various CFL numbers: RK4 – $\mathcal{O}4$ time integration with alternating compact FDs D1.

For small *CFL* numbers, only high wavenumbers are damped. For larger time steps (*CFL* ≥ 0.8), damping is no longer continuously increasing with the non-dimensional wavenumber k^* and for *CFL* = 1 the stability limit is already exceeded.

Time-step Limit

With an explicit time integration, the time-step limit has to be hold. Considering computational efficiency, a time step as large as possible is favorable since less iterations are necessary to compute a specific period of time. Additionally, the numerical damping due to the biased finite differences decreases for small *CFL* numbers and dealiasing in the *x-y* plane is no more ensured. Hence, computations may crash even because of Δt being too small. In case the numerical damping of the biased finite differences is no more sufficient because of a rigorous time-step limit, the computation can be stabilized by applying a spatial filter.

To estimate the maximum time step, a mixed convection/diffusion equation is considered:

$$\begin{aligned} \frac{\partial \Phi}{\partial t} &+ (|u| + a) \cdot \frac{\partial \Phi}{\partial x} + (|v| + a) \cdot \frac{\partial \Phi}{\partial y} + (|w| + a) \cdot \frac{\partial \Phi}{\partial z} \\ &= d \cdot \left(\frac{\partial^2 \Phi}{\partial x^2} + \frac{\partial^2 \Phi}{\partial y^2} + \frac{\partial^2 \Phi}{\partial z^2} \right), \end{aligned} \quad (3.24)$$

where the largest convection speed in each direction is taken into account. The fastest propagation is given by the downstream running acoustic wave with its velocity being the sum of the flow speed and the speed of sound a .

The second constraint of the time step is the strongest viscous term d which may be either viscosity or heat conductivity:

$$d = \max \left\{ \frac{\mu}{\rho \cdot Re}, \frac{\vartheta}{\rho(\kappa-1)Ma_\infty^2 Pr Re} \right\} \quad (3.25)$$

The highest occurring frequencies $\omega_{r,max} = c \cdot k_{mod,max}^* / \Delta \zeta$ and temporal decay rates $\omega_{i,max}$ for equation (3.24) are given by the largest values of the first and second spatial derivatives. Considering only one spatial direction with a uniform step size, these are

$$\omega_{r,max} = \frac{c \cdot k_{mod,max}^*}{\Delta \zeta}, \quad \omega_{i,max} = \frac{d \cdot k_{mod,max}^{*2}}{\Delta \zeta^2} \quad (3.26)$$

where $c \in (|u| + a), (|v| + a), (|w| + a)$ is the velocity of the downstream running acoustic wave for the respective spatial direction. As illustrated by figure 3.5 a), the stability limit of the 4th-order Runge-Kutta scheme may be estimated by $|\omega \cdot \Delta t|_{max} = 2.8$. Thus, the maximum time step is given by

$$\Delta t_{max} = \frac{2.8}{\sqrt{|\omega_{max}|^2}} \quad (3.27)$$

where $|\omega_{max}|^2 = \max \{\omega_r^2 + \omega_i^2\}$ is the maximum along all grid points. In figure 3.5 a), this corresponds to the distance from the origin divided by the time step. For the orthogonal uniform grid, it is computed as follows:

$$\begin{aligned} |\omega_{max}|^2 &= \left[\frac{(|u| + a) \cdot k_{mod,max,x}^*}{\Delta x} + \frac{(|v| + a) \cdot k_{mod,max,y}^*}{\Delta y} \right. \\ &\quad \left. + \frac{(|w| + a) \cdot k_{mod,max,z}^*}{\Delta z} \right]^2 \\ &\quad + \left[d \cdot \left(\frac{k_{mod,max,x}^{*2}}{\Delta x^2} + \frac{k_{mod,max,y}^{*2}}{\Delta y^2} + \frac{k_{mod,max,z}^{*2}}{\Delta z^2} \right) \right]^2 \end{aligned} \quad (3.28)$$

In case of non-uniform curvilinear grids, first derivatives in physical space may be replaced easily by their counterparts in equidistant computational space according to equations 3.9 and 3.10. For second derivatives, the evolving terms would be too large for a pure estimation of the time step limit. Therefore, only effective step sizes are considered for the viscous terms:

$$\begin{aligned} |\omega_{max}|^2 &= \left[\frac{(|u| + a) \cdot \frac{\partial y}{\partial \eta} - (|v| + a) \cdot \frac{\partial x}{\partial \eta}}{J} \cdot \frac{k_{mod,max,\xi}^*}{\Delta \xi} \right. \\ &\quad \left. + \frac{(|v| + a) \cdot \frac{\partial x}{\partial \xi} - (|u| + a) \cdot \frac{\partial y}{\partial \xi}}{J} \cdot \frac{k_{mod,max,\eta}^*}{\Delta \eta} \right. \\ &\quad \left. + \frac{(|w| + a) \cdot k_{mod,max,z}^*}{\Delta z} \right]^2 \\ &\quad + \left[d \cdot \left(\frac{k_{mod,max,\xi}^{*2}}{\left(\frac{\partial x}{\partial \xi} \cdot \Delta \xi \right)^2 + \left(\frac{\partial y}{\partial \xi} \cdot \Delta \xi \right)^2} \right. \right. \\ &\quad \left. \left. + \frac{k_{mod,max,\eta}^{*2}}{\left(\frac{\partial x}{\partial \eta} \cdot \Delta \eta \right)^2 + \left(\frac{\partial y}{\partial \eta} \cdot \Delta \eta \right)^2} + \frac{k_{mod,max,z}^{*2}}{\Delta z^2} \right) \right]^2 \end{aligned} \quad (3.29)$$

Disturbance Computation

Apart from a regular simulation, the code allows a disturbance computation where the baseflow given by the initial condition is assumed to be a steady-state solution of the Navier-Stokes equations, e.g. used in [5]. Due to their non-linearity, an actual disturbance formulation of the Navier-Stokes equations does not seem to be feasible. The approach implemented here goes back to Thumm [99] and does not require a new formulation of the equations. Instead, the time derivatives of the conservative variables are computed for the baseflow for each combination of the forward-backward biased discretization. During a simulation in disturbance mode, the stored values $\partial\mathbf{Q}_0/\partial t$ are subtracted from the computed time derivatives. Thus, the time derivatives of the baseflow serve as a source term, forcing the prescribed baseflow to be a steady solution. By using exactly the same discretization for the source term and the actual computation, this is equivalent to an original disturbance formulation.

In case of boundary conditions which prescribe time derivatives, this procedure is applied in the same way to the respective boundary. If flow quantities are prescribed, the deviation of the baseflow is stored and subsequently subtracted from the newly computed values.

3.3.3 Boundary Conditions

To allow rather complex geometrical configurations, boundary conditions must be applicable to each boundary which has no neighboring subdomain. Additionally, future extensions of the code will mostly affect the boundary conditions, e.g. disturbance generation, suction or blowing at the wall. Thus, a modular implementation is necessary, meaning that each boundary condition acts independently from neighboring domains or other boundary conditions. To avoid conflicts at the corners of the subdomains, a ranking of boundary conditions is introduced so that the code can allocate the respective corner to the boundary condition which is more restrictive. For the algorithm, two principal boundary conditions exist:

- prescribing the values themselves, this may be steady or unsteady
- giving time derivatives so that time integration is applied to the respective boundary.

According to the property of the boundary conditions, the spatial extent of the Runge-Kutta scheme is determined automatically.

Up to now, a variety of boundary conditions and extensions of them have been implemented by people using the code, e.g. [62]. With boundary conditions

being a crucial point for the success of aeroacoustic simulations, special emphasis was set on non-reflecting boundary conditions, mainly for the outflow. The following pages describe the boundary conditions used within this work.

3.3.3.1 Supersonic Inflow

The supersonic inflow is one of the simplest boundary conditions where all flow variables are prescribed. Apart from using the steady values of the baseflow, it is possible to add periodic disturbances, given by amplitude and phase distribution along the inflow boundary. This allows a direct assignment of the eigenfunctions from linear stability theory (see 3.4) at the inflow. The time-dependent values of a flow variable Φ are obtained by adding the number of disturbances N to the steady baseflow Φ_0 :

$$\Phi(y, t) = \Phi_0(y) + \sum_{j=1}^N \hat{\Phi}_j(y) \cdot \cos(\theta_j(y) + \gamma_j \cdot z - \omega_j \cdot t) \quad (3.30)$$

In case of a symmetric computation, both left- and right-traveling waves related to the symmetry plane $z = 0$ are introduced. Thus, all disturbances with a spanwise wavenumber γ have a counterpart with the spanwise wavenumber $-\gamma$ and the values at the boundary are given by

$$\Phi(y, t) = \Phi_0(y) + \sum_{j=1}^N \hat{\Phi}_j(y) \cdot \cos(\Theta_j(y) - \omega_j \cdot t) \cdot \cos(\gamma_j \cdot z). \quad (3.31)$$

To satisfy the equation of state, temperature fluctuations are not taken from the eigenfunctions but computed by the equation of state (2.21). Especially when large domains are used, e.g. to compute the acoustic farfield, the eigenfunctions are typically not given along the whole boundary. To avoid artificial noise generation at the tail of the given eigenfunction, amplitude- and phase distributions are extrapolated. According to LST, amplitudes are extrapolated using an exponential ansatz. With decreasing amplitudes, the phase becomes less relevant and thus, a linear extrapolation of Θ is sufficient.

Near the boundary, the following finite differences are used for spatial discretization:

$$\frac{8}{15} \cdot \frac{\partial \Phi}{\partial \zeta} \Big|_{j=2} + \frac{6}{15} \cdot \frac{\partial \Phi}{\partial \zeta} \Big|_{j=3} = \frac{-25 \cdot \Phi_{j=1} - 104 \cdot \Phi_{j=2} + 114 \cdot \Phi_{j=3}}{180 \cdot \Delta \zeta} + \frac{16 \cdot \Phi_{j=4} - 1 \cdot \Phi_{j=5}}{180 \cdot \Delta \zeta} \quad (3.32)$$

$$2 \cdot \frac{\partial^2 \Phi}{\partial \zeta^2} \Big|_{j=2} + 15 \cdot \frac{\partial^2 \Phi}{\partial \zeta^2} \Big|_{j=3} = \frac{79 \cdot \Phi_{j=1} + 3126 \cdot \Phi_{j=2} - 6810 \cdot \Phi_{j=3}}{180 \cdot \Delta \zeta^2} + \frac{3940 \cdot \Phi_{j=4} - 345 \cdot \Phi_{j=5} + 6 \cdot \Phi_{j=6} + 4 \cdot \Phi_{j=7}}{180 \cdot \Delta \zeta^2} \quad (3.33)$$

Equation (3.33) is a linear combination of a 6th- and 5th-order formula to overcome the illness of the pure 6th-order scheme [54, 104]. Contrary to its name, the supersonic inflow can be used for subsonic flows as well. However, upstream propagating acoustic waves may not leave the domain.

3.3.3.2 Subsonic Inflow

The implementation of the subsonic inflow is based on the work of Giles [36], allowing upstream traveling acoustic waves to leave the domain. Based on the one-dimensional linearized Euler equations, the disturbances can be transformed to the characteristic variables $c_1 - c_5$:

$$\begin{pmatrix} c_1 \\ c_2 \\ c_3 \\ c_4 \\ c_5 \end{pmatrix} = \begin{pmatrix} -a_0^2 & 0 & 0 & 0 & 1 \\ 0 & 0 & \rho_0 \cdot a_0 & 0 & 0 \\ 0 & 0 & 0 & \rho_0 \cdot a_0 & 0 \\ 0 & \rho_0 \cdot a_0 & 0 & 0 & 1 \\ 0 & -\rho_0 \cdot a_0 & 0 & 0 & 1 \end{pmatrix} \cdot \begin{pmatrix} \rho' \\ u' \\ v' \\ w' \\ p' \end{pmatrix} \quad (3.34)$$

Quantities of the baseflow are marked by the subscript $_0$ and the superscript $'$ denotes fluctuations where the baseflow quantities are subtracted from the corresponding flow variables. According to equation (3.34), c_1 corresponds to an entropy disturbance and c_2 as well as c_3 are vorticity fluctuations Ω'_z in spanwise and Ω'_x streamwise direction, respectively. The up- and downstream travelling acoustic waves are represented by c_4 and c_5 , respectively. While the first three characteristic fluctuations are propagating with the velocity u_0 , the sound waves are convected with $(u_0 - a_0)$ and $(u_0 + a_0)$. Thus, we obtain one outgoing and four incoming disturbances at the subsonic inflow, since $u_0 < a_0$ for subsonic flows. Upstream running acoustic waves are capable to pass the inflow by setting only the incoming fluctuations $c_1 - c_4$ to zero. The characteristic variable $c_{5(j=1)}$ at the inflow is obtained by extrapolating its value from the interior grid points with a second order stencil:

$$c_{5(j=1)} = 3 \cdot c_{5(j=2)} - 3 \cdot c_{5(j=3)} + c_{5(j=4)} \quad (3.35)$$

With the characteristic disturbances being determined, they are transformed back to get the primitive variables:

$$\begin{pmatrix} \rho' \\ u' \\ v' \\ w' \\ p' \end{pmatrix} = \begin{pmatrix} -\frac{1}{a_0^2} & 0 & 0 & \frac{1}{2 \cdot a_0^2} & \frac{1}{2 \cdot a_0^2} \\ 0 & 0 & 0 & \frac{1}{2 \cdot \rho_0 \cdot a_0^2} & \frac{1}{2 \cdot \rho_0 \cdot a_0^2} \\ 0 & \frac{1}{\rho_0 \cdot a_0^2} & 0 & 0 & 0 \\ 0 & 0 & \frac{1}{\rho_0 \cdot a_0^2} & 0 & 0 \\ 0 & 0 & 0 & \frac{1}{2} & \frac{1}{2} \end{pmatrix} \cdot \begin{pmatrix} c_1 \\ c_2 \\ c_3 \\ c_4 \\ c_5 \end{pmatrix} \quad (3.36)$$

These are added to their corresponding values of the baseflow giving the set of primitive variables at the inflow. Like for the supersonic inflow, it is possible to introduce disturbances via amplitude and phase distributions. The fluctuations are simply added after applying the characteristic boundary condition. This implementation showed the eigenfunctions to be less affected by the characteristic boundary condition than introducing them before the characteristic boundary condition is applied. The spatial derivatives near the subsonic inflow are computed the same way as done for the supersonic inflow.

3.3.3.3 Turbulent Inflow

The turbulent inflow allows using unsteady DNS data as inflow condition. This allows investigations in a turbulent flow field by computing laminar-turbulent transition only once. The required inflow data can be taken directly from a localized output of a previous simulation. Usually high temporal resolution is required so even with a small spatial extent of the data, large files of several GB can occur. This data is assumed to be periodic in time and is interpolated to the time steps used within the current simulation. In the proximity of the inflow, a successive passage from prescribed flow quantities Φ_{input} to their computed values $\Phi_{comp.}$ is provided by

$$\Phi = \sigma \cdot \Phi_{input} + (1 - \sigma) \cdot \Phi_{comp.}, \quad (3.37)$$

where σ is the weighting function of the inflow

$$\sigma = 1 - 6 \cdot x^{*5} + 15 \cdot x^{*4} - 10 \cdot x^{*3} \quad (3.38)$$

$$x^* = \frac{x - x_0}{\Delta x_{ramp}}. \quad (3.39)$$

Here, x^* denotes the coordinate in streamwise direction normalized with the length of the forcing region Δx_{ramp} . The polynomial of 5th order has been chosen such that its first and second derivatives are zero at the beginning and at the end of the ramping region. This guarantees a smooth change-over between prescribed and computed values as shown in figure 3.6. Additionally,

the flush ramping function can act as a damping zone for upstream traveling acoustic waves. In case that the prescribed values are not given along the whole boundary, a similar weighting function is applied in y -direction towards the free stream. For the spatial discretization at the grid point next to the boundary, the same finite differences are used as for the super- and subsonic inflow. A detailed description of the implementation, including test computations can be found in the work of Meister [65].

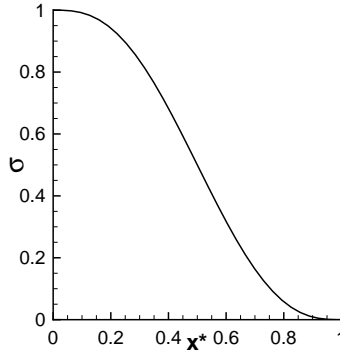


Figure 3.6: Weighting function σ for a smooth change-over from prescribed to computed values.

3.3.3.4 Wall Boundary Condition

At the wall, no-slip ($u = w = 0$) and impermeability conditions ($v = 0$) are applied. Within this work, the wall temperature is assumed to be constant with its values taken from the initial condition. Alternatively, it is possible to apply an adiabatic wall where the wall-normal temperature gradient vanishes. In this case, the temperature at the wall is computed by a one-sided finite difference. In the implementation of Eissler [27], the pressure at the wall was obtained by solving the wall-normal momentum equation. However, this requires second derivatives at the wall whose computation by a one-sided finite difference yields bad results and causes additional computational costs. Thus, the general implementation is the extrapolation of the pressure by a polynomial of 4th order:

$$p_{j=1} = 5 \cdot p_{j=2} - 10 \cdot p_{j=3} + 10 \cdot p_{j=4} - 5 \cdot p_{j=5} + p_{j=6} \quad (3.40)$$

Since a high-order extrapolation may cause artificial oscillations, an alternative formulation is implemented as well (e.g. for turbulent flows), setting the wall-normal derivative of the pressure to zero. This is achieved by an optimized 5th-order finite difference [55]:

$$p_{j=1} = \left(\begin{aligned} &415.98004386001 \cdot p_{j=2} - 49.33319115624 \cdot p_{j=3} \\ &+ 801.54477983974 \cdot p_{j=4} - 725.61937450295 \cdot p_{j=5} \\ &+ 467.51854160051 \cdot p_{j=6} - 203.30695291712 \cdot p_{j=7} \\ &+ 53.39737032908 \cdot p_{j=8} - 6.37538573229 \cdot p_{j=9} \end{aligned} \right) \cdot \frac{1}{153.80583132074} \quad (3.41)$$

This additional constraint is not introduced arbitrarily. Various results show this to be a valid assumption: a steady flow field and eigenfunctions from linear stability theory have a vanishing wall-normal pressure gradient at the wall. Also DNS results using equation (3.40) confirm this approach [10].

Again, the discretization is given exemplarily for the left and lower boundaries ($j = 1, 2$). The first derivative in the wall-normal direction is discretized by an explicit 4th-order biased finite difference

$$\left. \frac{\partial \Phi}{\partial \zeta} \right|_{j=2} = \frac{-3 \cdot \Phi_{j=1} - 10 \cdot \Phi_{j=2} + 18 \cdot \Phi_{j=3} - 6 \cdot \Phi_{j=4} + 1 \cdot \Phi_{j=5}}{12 \cdot \Delta \zeta} \quad (3.42)$$

and the second derivative is computed according to equation (3.33). While this stencil provides good results for the flat-plate boundary layer, the non-central discretization of second derivatives may cause problems for other configurations. This has been observed for the flow around an airfoil by Schneider [88] and the wake behind a flat plate with larger thickness by Kleine [51]. In such cases, the second derivative at the gridpoint next to the wall is computed by a central stencil of 2nd order:

$$\left. \frac{\partial^2 \Phi}{\partial \zeta^2} \right|_{j=2} = \frac{\Phi_{j=1} - 2 \cdot \Phi_{j=2} + \Phi_{j=3}}{\Delta \zeta^2} \quad (3.43)$$

With actuators usually being mounted on a solid structure, a variety of extensions are implemented for the wall boundary conditions up to now. Examples are a disturbance strip [10] or blowing/suction through holes or slits by Linn & Kloker [62]. One of these add-ons is the serrated trailing edge where the end of the splitter plate is no longer constant along the spanwise direction. As grid transformation is only implemented for the x - y plane, the spanwise varying trailing edge is achieved by modifying the connectivity of the affected domains above and below the splitter plate. Instead of prescribing the wall boundary

condition along the whole border of the respective domains, an area without wall can be defined. At these grid points, the wall-normal derivatives are re-computed using the values from both sides of the splitter plate. This is done at the quasi-boundary and the next gridpoint, overwriting the spatial derivatives which are computed regularly by one-sided (3.7) or biased stencils (3.8). To fulfill the requirements of a modular boundary condition, not interfering with other components of the code, explicit finite differences are applied. In order to have similar numerical properties in the notch as in the flow field, the order of the explicit finite differences is raised to eight. First derivatives of viscous terms

$$\begin{aligned} \left. \frac{\partial \Phi}{\partial \zeta} \right|_j &= \frac{3 \cdot \Phi_{j-4} - 32 \cdot \Phi_{j-3} + 168 \cdot \Phi_{j-2} - 672 \cdot \Phi_{j-1}}{840 \cdot \Delta \zeta} \\ &+ \frac{672 \cdot \Phi_{j+1} - 168 \cdot \Phi_{j+2} + 32 \cdot \Phi_{j+3} - 3 \cdot \Phi_{j+4}}{840 \cdot \Delta \zeta} \end{aligned} \quad (3.44)$$

and second derivatives

$$\begin{aligned} \left. \frac{\partial^2 \Phi}{\partial \zeta^2} \right|_j &= \frac{-9 \cdot \Phi_{j-4} + 128 \cdot \Phi_{j-3} - 1008 \cdot \Phi_{j-2} + 8064 \cdot \Phi_{j-1} - 14350 \cdot \Phi_j}{5040 \cdot \Delta \zeta^2} \\ &+ \frac{8064 \cdot \Phi_{j+1} - 1008 \cdot \Phi_{j+2} + 128 \cdot \Phi_{j+3} - 9 \cdot \Phi_{j+4}}{5040 \cdot \Delta \zeta^2} \end{aligned} \quad (3.45)$$

are computed by standard central finite differences. This pushes $k_{mod,r}^*$ and $k_{mod,r}^{*2}$ towards the compact scheme which is shown in figures 3.7 a) and b), respectively.

For convective terms, the alternating up- and downwind biased finite differences are designed such that the imaginary part of the modified wavenumber is similar to the one of the compact scheme used within the flow field. Keeping the favorable dispersion relation of the 8th-order scheme yields the difference between two corresponding coefficients (e.g. $j + 1$ and $j - 1$) to be the same as for the central stencil [55]. The constraint for the central coefficient at grid point j is the sum of all coefficients being zero. The four unknowns are determined by requesting $k_{mod,i}^*$ to be the same as scheme D1 at $k^* = 0.5$, $k^* = 1$, $k^* = 1.5$ and $k^* = \pi$. The resulting up- and downwind-biased finite differences are given by equations (3.46) and (3.47), respectively. Figure 3.7 a) shows the good agreement of the dissipation properties between explicit and compact finite differences. Thus, the different discretization in the notch should not affect the simulation results.

$$\begin{aligned}
\left. \frac{\partial \Phi}{\partial \zeta} \right|_{j,+} &= \frac{13.335153682 \cdot \Phi_{j-4} - 93.7757329 \cdot \Phi_{j-3} + 377.07560362 \cdot \Phi_{j-2}}{840 \cdot \Delta \zeta} \\
&+ \frac{-1310.2242671 \cdot \Phi_{j-1} + 961.1784854 \cdot \Phi_j}{840 \cdot \Delta \zeta} \\
&+ \frac{33.7757329 \cdot \Phi_{j+1} + 41.07560362 \cdot \Phi_{j+2}}{840 \cdot \Delta \zeta} \\
&+ \frac{-29.7757329 \cdot \Phi_{j+3} + 7.335153682 \cdot \Phi_{j+4}}{840 \cdot \Delta \zeta} \quad (3.46)
\end{aligned}$$

$$\begin{aligned}
\left. \frac{\partial \Phi}{\partial \zeta} \right|_{j,-} &= \frac{-7.335153682 \cdot \Phi_{j-4} + 29.7757329 \cdot \Phi_{j-3} - 41.07560362 \cdot \Phi_{j-2}}{840 \cdot \Delta \zeta} \\
&+ \frac{-33.7757329 \cdot \Phi_{j-1} - 961.1784854 \cdot \Phi_j}{840 \cdot \Delta \zeta} \\
&+ \frac{1310.2242671 \cdot \Phi_{j+1} - 377.07560362 \cdot \Phi_{j+2}}{840 \cdot \Delta \zeta} \\
&+ \frac{93.7757329 \cdot \Phi_{j+3} - 13.335153682 \cdot \Phi_{j+4}}{840 \cdot \Delta \zeta} \quad (3.47)
\end{aligned}$$

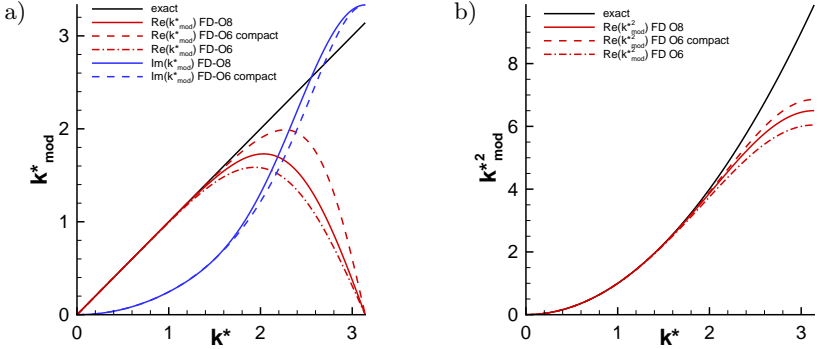


Figure 3.7: a) Real and imaginary parts of $k_{mod,r}^*$ for 8th-order explicit finite differences compared to the compact scheme D1.

b) Real part of k_{mod}^{*2} of the second derivative for 6th- and 8th-order explicit stencils versus compact discretization of 6th order.

3.3.3.5 Characteristic Freestream

The characteristic boundary condition at the freestream is similar to the subsonic inflow given (section 3.3.3.2). Due to the orientation of the boundary, the normal velocity v_0 and not the streamwise component u_0 of the baseflow is used to determine the characteristic disturbances. According to the subsonic inflow, incoming disturbances are set to zero while outgoing disturbances are extrapolated from the interior of the flow field. Since the boundary condition is based on a one-dimensional decomposition of the Euler equations, it works well for waves impinging normally to the boundary. To avoid reflections due to oblique acoustic waves, an additional damping zone in front of the boundary is implemented. There, the conservative flow variables are drawn to the baseflow by adding a source term which is proportional to the fluctuation of the respective quantity:

$$\frac{\partial \mathbf{Q}}{\partial t} = \frac{\partial \mathbf{Q}}{\partial t} \Big|_{NS} - d \cdot \sigma(y) \cdot (\mathbf{Q} - \mathbf{Q}_0) \quad (3.48)$$

The subscript NS denotes the time derivatives from the Navier-Stokes equations and d defines the magnitude of the damping. Using a polynomial of 5th order similar to equation (3.39) for $\sigma(y)$ provides a smooth transition from no damping within the flow field to the maximum damping rate d at the boundary. With oblique waves covering a longer distance in the damping zone, the problematic non-normal waves are affected strongly by the damping zone.

3.3.3.6 Supersonic Outflow

For supersonic flows, a boundary condition similar to the implementation of Eissler [27] is used. By setting the second derivatives in streamwise direction to zero, the Navier-Stokes equations can be integrated directly at the outflow as it is done for the rest of the domain. First derivatives are computed by a one-sided stencil of 2nd order at the boundary and a 4th-order compact finite difference at the previous grid point:

$$\frac{\partial \Phi}{\partial \zeta} \Big|_j = \frac{\Phi_{j-2} - 4 \cdot \Phi_{j-1} + 3 \cdot \Phi_j}{2 \cdot \Delta \zeta} \quad (3.49)$$

$$\frac{\partial \Phi}{\partial \zeta} \Big|_{j-1} + 4 \cdot \frac{\partial \Phi}{\partial \zeta} \Big|_j + \frac{\partial \Phi}{\partial \zeta} \Big|_{j+1} = \frac{-6 \cdot \Phi_{j-1} + 6 \cdot \Phi_{j+1}}{2 \cdot \Delta \zeta} \quad (3.50)$$

A compact stencil of 4th order is used as well for second derivatives directly in front of the outflow boundary. Including the neglected second derivative on

the left-hand side yields the stencil for the second last grid point:

$$\left. \frac{\partial^2 \Phi}{\partial \zeta^2} \right|_{j-1} + 10 \cdot \left. \frac{\partial^2 \Phi}{\partial \zeta^2} \right|_j = \frac{12 \cdot \Phi_{j-1} - 24 \cdot \Phi_j + 12 \cdot \Phi_{j+1}}{\Delta \zeta^2} \quad (3.51)$$

Of course, this procedure is not applicable to simulations with high-amplitude disturbances. For such cases, a damping zone similar to Kloker et al. [53] can be used, ramping the fluctuations towards the baseflow. Smooth ramping is provided by a polynomial of 5th order analogous to equation 3.38. Since this is applied to all flow quantities, the continuity equation is not fulfilled. Thus, this method causes huge acoustic reflections in the subsonic regime and it is not recommended for aeroacoustic simulations.

3.3.3.7 Subsonic Outflow

For flow speeds below the speed of sound, a stronger boundary condition is necessary. Spatial discretization is done in the same way as for the supersonic outflow. However, its values directly in front of the boundary are used for the outflow as well:

$$\left. \frac{\partial \mathbf{Q}}{\partial t} \right|_N = \left. \frac{\partial \mathbf{Q}}{\partial t} \right|_{N-1} \quad (3.52)$$

This allows the flow field to change while specifying that it does not vary in streamwise direction. Of course, this boundary condition requires fluctuations to be removed before they reach the outflow boundary. The construction of such a sponge zone is probably the most crucial part of aeroacoustic simulations since reflections must be smaller than the hydrodynamic fluctuations in order not to spoil the sensitive acoustic field. This is achieved by a combination of grid stretching and spatial low-pass filtering as proposed by Colonius et al. [24]. With the mesh being stretched smoothly towards the outflow, disturbances become increasingly badly resolved as they propagate downstream. With the effect of the spatial filter depending on the stepsize, perturbations are continuously dissipated before they reach the outflow boundary. The filter may be used either explicit or compact, depending on the filter parameter \mathbf{b}_{lhs} :

$$\begin{aligned} \mathbf{b}_{lhs} \cdot \Phi_{j-1}^\ddagger + \Phi_j^\ddagger + \mathbf{b}_{lhs} \cdot \Phi_{j+1}^\ddagger \\ = \mathbf{a} \cdot \Phi_{j-2} + \mathbf{b} \cdot \Phi_{j-1} + \mathbf{c} \cdot \Phi_j + \mathbf{b} \cdot \Phi_{j+1} + \mathbf{a} \cdot \Phi_{j+2} \end{aligned} \quad (3.53)$$

where the superscript \ddagger denotes filtered values. The coefficients of a filter of 4th-order accuracy are given by Lele [58]:

$$\mathbf{a} = -\frac{1 - 2 \cdot \mathbf{b}_{lhs}}{16}, \quad \mathbf{b} = \frac{1 + 2 \cdot \mathbf{b}_{lhs}}{4}, \quad \mathbf{c} = \frac{5 + 6 \cdot \mathbf{b}_{lhs}}{8}. \quad (3.54)$$

For the above stencil of the filter, the transfer function \mathcal{TF} which is the ratio of the filtered and unfiltered values depending on the non-dimensional wavenumber k^* :

$$\mathcal{TF} = \frac{2\mathbf{a} \cdot \cos(2 \cdot k^*) + 2\mathbf{b} \cdot \cos(k^*) + \mathbf{c}}{1 + 2\mathbf{b}_{l_{hs}} \cdot \cos(k^*)} \quad (3.55)$$

Depending on the chosen filter parameter $\mathbf{b}_{l_{hs}}$, the resulting transfer function is shown in figure 3.8. Independently of $\mathbf{b}_{l_{hs}}$, the wobble mode ($k^* = \pi$) is completely removed by the filter operation. For the explicit filter ($\mathbf{b}_{l_{hs}} = 0$), the amplitude of a wave with 5 points per wave length already reduces to 90% of its initial value. By increasing the filter parameter, less resolved waves are longer preserved, e.g. an amplitude reduction of 10% occurs at 2.7 points per wave length in case of $\mathbf{b}_{l_{hs}} = 0.475$. Note that the $\mathbf{b}_{l_{hs}}$ needs to be smaller than 0.5 to avoid amplification ($\mathcal{TF} > 1$).

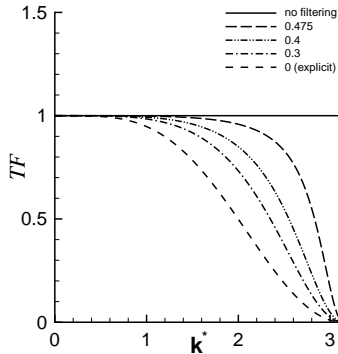


Figure 3.8: Transfer function \mathcal{TF} of the filter in dependency of the non-dimensional wavenumber k^* for different filter parameters $\mathbf{b}_{l_{hs}}$.

Since non-central filters may cause amplification and phase shifts, the left-hand side uses non-filtered quantities at the beginning and the end of the filtering region. A smooth change-over from unfiltered values to filtered quantities is ensured by ramping the spatial filter with a polynomial according to equation (3.38). Besides grid stretching and filter parameter, the dissipation in the sponge region can be controlled by the number of time steps between two filtering operations.

3.3.3.8 Coupling with Acoustic Solver

Since the emitted sound is smaller than the hydrodynamic fluctuations by several magnitudes, the idea arose to compute the acoustic farfield with a different code using linearized equations. Additionally, the acoustic field is assumed to be less affected by viscous terms. Therefore, the linearized Euler equations are used for the acoustic farfield, within the coupling examples. The code Hydsol, chosen to compute the sound propagation, is an unstructured Discontinuous Galerkin method developed at the IAG. Thus, we have a coupling of different equations, different discretization techniques and different time steps.

To keep the DNS code and the acoustic solver separated, data transmission is done via the regular network using TCP/IP [80]. Apart from avoiding the effort to merge two completely different codes, the chosen data exchange allows to run each code on different machines. While the DNS code is fully vectorized, the unstructured acoustic code runs best on scalar machines. Of course, this requires a data transformation from little to big endian and vice versa [73]. In both codes, the network connection is done only by one MPI process which collects and distributes the data to the other ones. Thus, each side does not have to care about the parallelization of the other code.

The acoustic code is started first since the DNS code is subject to the queuing system on the vector computer. After the DNS code connects to the acoustic code, initializing data, listed in table 3.2, is exchanged. After that, both parts know when to send and receive which amount of data. The disturbances of the primitive variables (ρ' , u' , v' , w' , p') are exchanged on a structured grid at the corresponding time levels. While the DNS code sends only the data of the current time step, the acoustic code hands over the fluctuations at all time levels up to the following data exchange, including the Runge-Kutta subcycles. The quantities at these points in time are computed by the acoustic solver using a Taylor expansion in time [100]. At the actual time step, the spatial derivatives normal to the coupling plane are computed by explicit 6th-order finite differences:

$$\begin{aligned} \left. \frac{\partial \Phi}{\partial \zeta} \right|_j &= \frac{-1 \cdot \Phi_{j-3} + 9 \cdot \Phi_{j-2} - 45 \cdot \Phi_{j-1}}{180 \cdot \Delta \zeta} \\ &+ \frac{45 \cdot \Phi_{j+1} - 9 \cdot \Phi_{j+2} + 1 \cdot \Phi_{j+3}}{180 \cdot \Delta \zeta} \end{aligned} \quad (3.56)$$

$$\begin{aligned} \left. \frac{\partial^2 \Phi}{\partial \zeta^2} \right|_j &= \frac{2 \cdot \Phi_{j-3} - 27 \cdot \Phi_{j-2} + 270 \cdot \Phi_{j-1} - 490 \cdot \Phi_j}{180 \cdot \Delta \zeta^2} \\ &+ \frac{270 \cdot \Phi_{j+1} - 27 \cdot \Phi_{j+2} + 2 \cdot \Phi_{j+3}}{180 \cdot \Delta \zeta^2} \end{aligned} \quad (3.57)$$

The above stencils are used at the coupling plane and the grid points in front of it, overwriting the spatial derivatives usually computed by one-sided or biased finite differences. Since only small-amplitude waves are assumed to pass the coupling plane to the acoustic solver, the convective terms are discretized by central stencils as well. A detailed description on the coupling mechanism including the implementation in the acoustic code is provided by Babucke, Dumbser and Utzmann [4]. Results of a test case are given in appendix D.

packet	direction	data
1	Hydsol \rightarrow NS3D	width of Hydsol ghost cells, sequence of data exchange
2	NS3D \rightarrow Hydsol	array sizes for data exchange, time step Δt , overall number of time steps, time steps per period $\lambda_{t,0}$
3, 4	NS3D \rightarrow Hydsol	coordinates of Hydsol ghost cells at upper and lower coupling interfaces
5, 6	NS3D \rightarrow Hydsol	baseflow in Hydsol ghost cells at upper and lower coupling interface
7, 8	NS3D \rightarrow Hydsol	coordinates of DNS ghost points at upper and lower coupling interface
9	Hydsol \rightarrow NS3D	time step ratio $\Delta t_{Hydsol}/\Delta t_{DNS}$

Table 3.2: Data exchange for initialization of coupling the DNS code NS3D with the acoustic code Hydsol.

3.3.4 Parallelization

An efficient parallelization is essential to perform large simulations on modern super-computers. For the NS3D code, a hybrid parallelization of both MPI [77] and shared memory parallelization is chosen. Due to the fact that the Fourier transformation requires data over the whole spanwise direction, a domain decomposition in z -direction would have caused high overhead. Hence, shared memory parallelization is implemented along the spanwise direction, using Microtasking [12] on the vector machines at HLRS. Yet the more important part is the domain decomposition in the x - y plane with data exchange using MPI. First of all, it is not limited to shared memory architectures but allows to run a simulation on multiple nodes. Additionally, domain decomposition enables more complex geometrical configurations as discussed above.

Communication between neighboring domains is only required for computing spatial derivatives normal to the catenation of two domains. All other operations are local for each domain. The right-hand side of a finite difference is computed easily by exchanging the current flow quantities near the interface. The crucial part for an efficient parallelization is the solution of the tridiagonal equation system

$$\mathfrak{b}_{lhs,j} \cdot \Phi_{\zeta,j-1} + \mathfrak{c}_{lhs,j} \cdot \Phi_{\zeta,j} + \mathfrak{d}_{lhs,j} \cdot \Phi_{\zeta,j+1} = \mathcal{RHS}_j \quad (3.58)$$

with \mathcal{RHS} being the right-hand side of the compact finite difference (see section 3.3.1). This linear equation system needs to be solved for the spatial derivatives Φ_{ζ} at all grid points $j = 1, \dots, N$, ranging along multiple domains. The common algorithm for solving this is the Thomas algorithm, e.g. [81]. It is made up of three recursive loops:

1. forward loop of left-hand side:

$$\begin{aligned} \mathfrak{c}_{lhs,1}^* &= \mathfrak{c}_{lhs,1} \\ \mathfrak{c}_{lhs,j}^* &= \mathfrak{c}_{lhs,j} - \mathfrak{b}_{lhs,j} \cdot \frac{\mathfrak{d}_{lhs,j-1}}{\mathfrak{c}_{lhs,j-1}^*}, \quad j \in [2, N] \end{aligned} \quad (3.59)$$

2. forward loop of right-hand side:

$$\begin{aligned} \Phi_{\zeta,1}^* &= \frac{\mathcal{RHS}_1}{\mathfrak{c}_{lhs,1}^*} \\ \Phi_{\zeta,j}^* &= \frac{-\mathfrak{b}_{lhs,j} \cdot \Phi_{\zeta,j-1}^* + \mathcal{RHS}_j}{\mathfrak{c}_{lhs,j}^*}, \quad j \in [2, N] \end{aligned} \quad (3.60)$$

3. backward loop of right-hand side:

$$\begin{aligned} \Phi_{\zeta,N} &= \Phi_{\zeta,N}^* \\ \Phi_{\zeta,j} &= \Phi_{\zeta,j}^* - \frac{\mathfrak{d}_{lhs,j}}{\mathfrak{c}_{lhs,j}^*} \cdot \Phi_{\zeta,j+1}, \quad j \in [(N-1), 1] \end{aligned} \quad (3.61)$$

Since the first step involves only the coefficients of the left-hand side, it has to be done only once at the initialization of the simulation. The forward and backward loop of the right hand side have to be computed at every intermediate Runge-Kutta step. The inherent difficulty regarding a parallel implementation is that both loops require values from the previous step: $\Phi_{\zeta,j-1}^*$ for the forward loop and $\Phi_{\zeta,j+1}$ for the backward loop (note that equation (3.61) goes from $[N-1]$ to 1). An ad-hoc implementation would lead to large dead times because each process has to wait until the previous domain has finished. To avoid a serialization of this part of the code, we make use of the fact that we have to

compute not only one, but 21 and 25 spatial derivatives in ξ - and η -direction, respectively. The so-called pipelining works as follows: the first domain starts with the forward loop of derivative 1. After its completion, the intermediate value Φ_{ξ}^* at the last grid point of domain 1 is sent to domain number 2. While the second domain continues with derivative 1, the first domain continues with the computation of derivative 2. The subsequent backward loop works in the reverse direction accordingly. The resulting pipelining is illustrated in figure 3.9 exemplarily for four derivatives and three domains.

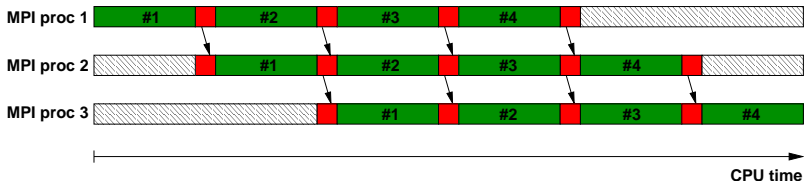


Figure 3.9: Illustration of the pipelined Thomas algorithm for four derivatives (#1 to #4) on three domains, showing the forward loop of the right-hand side. The horizontal axis represents computational time, green denotes the actual computation, red MPI communication and hatched areas correspond to dead times.

Neglecting communication time yields the theoretical speedup and the parallel efficiency of the pipelined Thomas algorithm:

$$SU = \frac{m \cdot n}{m + n - 1} \quad (3.62)$$

$$e = \frac{m}{m + n - 1}, \quad (3.63)$$

where n denotes the number of domains in a row or column and m the number of derivatives in the corresponding direction. For the maximum of $m = 25$ spatial derivatives, the theoretical speed-up and the efficiency of the pipelined Thomas algorithm are shown in figure 3.10 a). Indeed, the efficiency of the parallelization decreases to less than 50% for 30 domains in a row, but this holds only for the solution of the tridiagonal equation system. Since all other computations are local for each MPI process, the decrease of the parallel efficiency is less distinctive for the complete simulation. If we assume the spatial derivatives in ξ - and η -direction to require 15% of the CPU time (appendix C shows this to be a reasonable value), the overall efficiency stays well above 70% for 100 domains and beyond, as one can see in figure 3.10 b). Furthermore,

shared memory parallelization allows to compute each domain with multiple processes. Each MPI process and hence, each domain reads and writes its own files with the data being stored in the binary EAS3 file format [75]. This allows parallel file I/O and an arbitrary alignment of the domains.

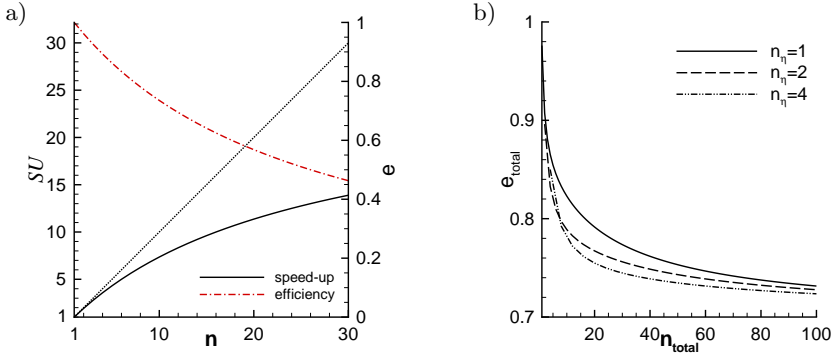


Figure 3.10: a) Speed-up SU and efficiency e of the pipelined Thomas algorithm versus the number of domains in a row/column (for 25 spatial derivatives).
 b) Overall parallel efficiency versus the number of MPI processes for a rectangular domain aligned in 1, 2 and 4 rows.

Periodicity

Of course, it is possible to specify the domain decomposition such that periodicity in a direction may occur. Using compact finite differences at the periodic boundary as well would result in a pentadiagonal equation system. Since we focus on spatial simulations, less emphasis was placed on the numerical properties of the periodic interface compared to the engrailed trailing edge for example. Hence, standard explicit finite differences are used at the periodic interface and the next/previous grid points:

$$\left. \frac{\partial \Phi}{\partial \zeta} \right|_j = \frac{\Phi_{j-2} - 8 \cdot \Phi_{j-1} + 8 \cdot \Phi_{j+1} - \Phi_{j+2}}{12 \cdot \Delta \zeta} \quad (3.64)$$

$$\left. \frac{\partial^2 \Phi}{\partial \zeta^2} \right|_j = \frac{-\Phi_{j-2} + 16 \cdot \Phi_{j-1} - 30 \cdot \Phi_j + 16 \cdot \Phi_{j+1} - \Phi_{j+2}}{12 \cdot \Delta \zeta^2} \quad (3.65)$$

The 4th-order stencils have been chosen since they require the same number of ghost points as the compact scheme.

Index Inversion

The combination of domain decomposition and grid transformation allows a wide range of geometries to compute. However, some geometrical configurations require a special conjunction of two domains. One example is the flow around an airfoil, discretized by a C-grid (see figure 3.4 for example). Assuming a regular connectivity past the airfoil (the same x -indices are connected behind the trailing edge), the first domains on top and below the airfoil need to be combined at the leading edge. As illustrated in figure 3.11, the combination of two left boundaries leads to a flip of the mesh indices. Below the airfoil, the grid point directly at the wall is the last point in wall-normal direction (index N). For the upper domain, the first grid points (index 1) are located on the surface of the airfoil.

Besides that, these two domains are connected at their left boundaries, unlike the usual combination of a left boundary with a right one. This is not captured by the Thomas algorithm for the tridiagonal equation system since it requires a left boundary condition to determine in which domain to start. Hence, this particular case is implemented like a boundary condition with data exchange between the two affected domains. For the spatial discretization, the explicit finite differences of equations (3.44)-(3.47) are used. As discussed in section 3.3.3.4, this provides similar numerical properties as the compact scheme which is used in the rest of the flow field.

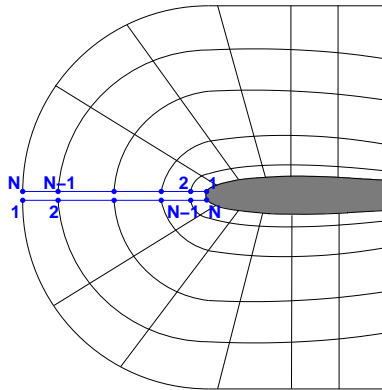


Figure 3.11: Illustration of grid indices within the connection of two domains at the leading edge of an airfoil.

3.4 Linear Stability Theory

Linear stability theory is the primary method to gain information on amplified disturbances depending on their frequencies. Hence, it is an important tool to determine the disturbance generation for the DNS code. Furthermore, LST can be used for verification and data analysis by comparing its amplification rates with those obtained from the simulation. For a detailed description of LST including its historical development, please refer to Mack [63].

3.4.1 Fundamentals

In analogy to the incompressible case, the compressible stability equations are obtained by splitting each flow variable in a steady baseflow (subscript $_0$) and a fluctuation (marked with $'$):

$$\Phi = \Phi_0 + \Phi', \quad \Phi \in (u, v, w, \rho, T, p, \mu, \vartheta) \quad (3.66)$$

This is done for the set of primitive variables (u, v, w, ρ, T, p) as well as for viscosity μ , second viscosity μ_B and heat conductivity ϑ . The additional second viscosity, also known as volume viscosity, is only included to validate the solver with results from Mack [63] who uses μ_B for hypersonic flow regimes. Since moderate Mach numbers are considered within this work, the second viscosity is set to zero.

The first assumption of LST is the given baseflow to be a steady solution of the Navier-Stokes equations. Therewith, all terms which contain only baseflow quantities vanish. The second step is to consider the baseflow to be parallel which neglects the widening of a boundary/mixing layer. Due to the continuity equation, the normal velocity component v_0 of the baseflow is zero:

$$\begin{aligned} v_0(y) &= 0, \\ \Phi_0 &= \Phi_0(y), \quad \Phi_0 \in (\bar{u}_0, \bar{w}_0, \bar{\rho}_0, \bar{T}_0, \bar{p}_0) \end{aligned} \quad (3.67)$$

So linear stability theory is a local theory where each x -position is considered separately. Assuming the disturbances to be small, products of the disturbances can be neglected:

$$\Phi' \ll 1 \quad \Rightarrow \quad \Phi'^2 \approx 0, \quad \Phi' \in (u', v', w', \rho', T', p') \quad (3.68)$$

Accordingly, the equation of state (2.21) can be linearized. This allows to express the pressure disturbances by the fluctuations of density and temperature:

$$\frac{p'}{p_0} = \frac{\rho'}{\rho_0} \cdot \frac{T'}{T_0} \quad (3.69)$$

With viscosity being a function of temperature, its y -derivative can be expressed by the spatial derivative of the temperature. Here, this is shown exemplarily for the y -direction:

$$\begin{aligned}\frac{\partial \mu}{\partial y} &= \frac{\partial \mu_0}{\partial y} + \frac{\partial}{\partial y} \left(\left. \frac{d\mu}{dT} \right|_{T_0} \cdot T' \right) \\ &= \frac{\partial \mu_0}{\partial y} + \frac{\partial}{\partial y} \left(\left. \frac{d\mu}{dT} \right|_{T_0} \right) \cdot T' + \left. \frac{d\mu}{dT} \right|_{T_0} \cdot \frac{\partial T'}{\partial y},\end{aligned}\quad (3.70)$$

Substituting

$$\frac{\partial}{\partial y} = \frac{\partial T}{\partial y} \cdot \frac{\partial}{\partial T} = \left(\frac{\partial T_0}{\partial y} + \frac{\partial T'}{\partial y} \right) \cdot \frac{\partial}{\partial T} \quad (3.71)$$

to equation (3.70) and disregarding products of the fluctuations yields

$$\frac{\partial \mu}{\partial y} = \left. \frac{d\mu}{dT} \right|_{T_0} \cdot \frac{\partial T_0}{\partial y} + \left. \frac{d^2 \mu}{dT^2} \right|_{T_0} \cdot \frac{\partial T_0}{\partial y} \cdot T' + \left. \frac{d\mu}{dT} \right|_{T_0} \cdot \frac{\partial T'}{\partial y}, \quad (3.72)$$

where derivatives with respect to temperature are taken from the Sutherland law of equation (2.24). The secondary viscosity μ_B is taken proportional to the dynamic viscosity μ . Due to a constant Prandtl number, the heat conductivity ϑ is proportional to μ as well.

Fluctuations are considered in wave form

$$\Phi'(x, y, z, t) = \hat{\Phi}(y) \cdot e^{i \cdot (\alpha x + \gamma z - \omega t)}, \quad (3.73)$$

where α and γ are the wavenumbers in streamwise and spanwise direction, respectively, and ω denotes the frequency of the particular wave. The complex amplitude $\hat{\Phi}(y)$ defines the physical amplitude and phase distribution along the normal direction: the amplitude is the absolute value $|\hat{\Phi}(y)|$ and its argument $\arg\{\hat{\Phi}(y)\}$ corresponds to the phase distribution of fluctuation Φ' . Assuming periodicity in z -direction, the spanwise wavenumber is real, preventing disturbances to grow in spanwise direction. Depending on whether we allow the frequency ω or the streamwise wavenumber α to be complex, it is called temporal or spatial problem, respectively. In the temporal case, the amplitude of a disturbance may grow or decay in time with ω_i being the temporal amplification rate. However for most flow conditions, the spatial problem is more realistic since disturbances are convected downstream. Here, amplitudes grow in space with the spatial amplification rate being $-\alpha_i$. Due to equation (3.73), negative values of α_i correspond to amplification while positive values denote damping.

Unlike the incompressible case, where the continuity equation can be used to reduce the number of equations to two (Orr-Sommerfeld and Squire equations), all five equations need to be solved: the continuity equation, three momentum equations and the energy equation. With the ansatz of equation (3.73), time and spatial derivatives in streamwise and spanwise direction are given analytically by

$$\frac{\partial \Phi'}{\partial t} = -i \cdot \omega \cdot \Phi' \tag{3.74}$$

$$\frac{\partial \Phi'}{\partial x} = i \cdot \alpha \cdot \Phi' \tag{3.75}$$

$$\frac{\partial \Phi'}{\partial z} = i \cdot \gamma \cdot \Phi' \tag{3.76}$$

and accordingly for the second derivatives. Thus, only derivatives in y -direction need to be discretized.

3.4.2 Boundary Conditions

With first and second y -derivatives of temperature and the three velocity components, it is obvious that these quantities require two boundary conditions, respectively. To determine whether the density requires an additional boundary condition, we take a look at the continuity equation:

$$\frac{\partial \rho'}{\partial t} + \rho_0 \left(\frac{\partial u'}{\partial x} + \frac{\partial v'}{\partial y} + \frac{\partial w'}{\partial z} \right) + \left(\frac{\partial \rho_0}{\partial y} \right) v' + u_0 \frac{\partial \rho'}{\partial x} + w_0 \frac{\partial \rho'}{\partial z} = 0 \tag{3.77}$$

With the wave ansatz and the corresponding derivatives (3.74) - (3.76), the continuity equation can be solved for the complex amplitude of the density:

$$\hat{\rho} = \frac{1}{\alpha \cdot u_0 + \gamma \cdot w_0 - \omega} \cdot \left[i \left(\frac{\partial \rho_0}{\partial y} \right) \cdot \hat{v} + i \rho_0 \cdot \frac{\partial \hat{v}}{\partial y} - \rho_0 \cdot (\alpha \cdot u_0 + \gamma \cdot w_0) \right] \tag{3.78}$$

Since $\hat{\rho}$ can be expressed analytically without solving a differential equation, no further boundary condition for the density is required. This is consistent with the transformation to an eighth-order system used for a shooting method [63].

At the wall, the boundary condition of the velocity components is the no-slip condition. Due to relatively high frequencies of the instability waves, it is assumed that the temperature at the wall does not follow the temperature fluctuations of the flow. Thus, its disturbance is set to zero, too, and the boundary conditions at the wall are:

$$\hat{u}_w = 0, \quad \hat{v}_w = 0, \quad \hat{w}_w = 0, \quad \hat{T}_w = 0 \tag{3.79}$$

At the freestream, the boundary condition is based on the solution for a uniform mean flow where amplitudes decay along the normal direction. Accordingly, the disturbances vanish far away and we may state at the freestream boundary

$$\hat{u}(y) = 0, \quad \hat{v}(y) = 0, \quad \hat{w}(y) = 0, \quad \hat{T}(y) = 0, \quad y \rightarrow \pm\infty, \quad (3.80)$$

where the coordinates $y = +\infty$ and $y = -\infty$ correspond to an upper and lower free stream, respectively. Since boundary conditions at infinity can not be prescribed numerically at infinity, the complex amplitudes are set to zero directly at the free stream boundary. Of course, this requires the spatial extent of the domain to be large enough to avoid wrong results.

3.4.3 Matrix Solver

Two fundamental ways exist to solve the stability equations numerically: i) a shooting method and ii) a matrix solver. The shooting method is very fast and can be applied directly to temporal and spatial problems. However, such a solver requires initial values whose guessing can be difficult, especially for higher Mach numbers. Despite being more costly in terms of computational resources, a matrix solver was developed since it provides the full spectrum containing all modes. Furthermore, it can be applied directly to boundary layers and mixing layers.

While the stability equations are linear with respect to ω , the square of the streamwise wavenumber α occurs due to the second derivatives in x -direction. Thus, only the temporal problem is a linear eigenvalue problem which can be written as

$$\mathbf{A}_0 \cdot \hat{q} + \mathbf{A}_1 \cdot \frac{\partial \hat{q}}{\partial y} + \mathbf{A}_2 \cdot \frac{\partial^2 \hat{q}}{\partial y^2} = \omega \cdot \mathbf{B} \cdot \hat{q} \quad (3.81)$$

with the complex frequency $\omega \in \mathbb{C}$ being the eigenvalue. The eigenvector \hat{q} contains the complex amplitude of the different flow quantities at each grid point y_j :

$$\hat{q} = \left(\hat{\rho}_j, \hat{u}_j, \hat{v}_j, \hat{w}_j, \hat{T}_j \right)^T, \quad \hat{q} \in \mathbb{C}, \quad j \in [1, N] \quad (3.82)$$

The coefficient matrices \mathbf{A}_0 , \mathbf{A}_1 and \mathbf{A}_2 contain the prefactors of the complex amplitudes and their first and second y -derivatives, respectively. Prefactors of the eigenvalue ω are included in matrix \mathbf{B} . The size of these matrices is five times the number of grid points in normal direction since five equations are

solved. Accordingly, the matrix structure is made of 5x5 submatrices, e.g.:

$$\mathbf{A}_0 = \begin{bmatrix} \mathbf{A}0_{11} & \mathbf{A}0_{12} & \mathbf{A}0_{13} & \mathbf{A}0_{14} & \mathbf{A}0_{15} \\ \mathbf{A}0_{21} & \mathbf{A}0_{22} & \mathbf{A}0_{23} & \mathbf{A}0_{24} & \mathbf{A}0_{25} \\ \mathbf{A}0_{31} & \mathbf{A}0_{32} & \mathbf{A}0_{33} & \mathbf{A}0_{34} & \mathbf{A}0_{35} \\ \mathbf{A}0_{41} & \mathbf{A}0_{42} & \mathbf{A}0_{43} & \mathbf{A}0_{44} & \mathbf{A}0_{45} \\ \mathbf{A}0_{51} & \mathbf{A}0_{52} & \mathbf{A}0_{53} & \mathbf{A}0_{54} & \mathbf{A}0_{55} \end{bmatrix} \quad (3.83)$$

With the coefficients affecting only the current grid point, each of the submatrix $\mathbf{A}0_{k,l}$ is a diagonal matrix containing the coefficients at the respective grid points:

$$\mathbf{A}0_{k,l} = \begin{bmatrix} a0_{kl}(y_2) & 0 & \cdots & 0 & 0 \\ 0 & a0_{kl}(y_3) & \cdots & 0 & 0 \\ \vdots & \vdots & \ddots & \vdots & \vdots \\ 0 & 0 & 0 & a0_{kl}(y_{N-2}) & 0 \\ 0 & 0 & 0 & 0 & a0_{kl}(y_{N-1}) \end{bmatrix} \quad (3.84)$$

With the boundary conditions prescribing the eigenvector to zero at the boundaries at y_1 and y_N , the stability equations do not need to be solved there. Thus, the boundaries are not included in the equation system. Accordingly, the index in normal direction ranges from 2 to $N - 1$.

k	equation	l	$a0_{j,k}, b_{j,k}$	$a1_{j,k}$	$a2_{j,k}$
1	continuity eq.	1	$\hat{\rho}$	$\frac{\partial \hat{\rho}}{\partial y}$	$\frac{\partial^2 \hat{\rho}}{\partial y^2}$
2	x -momentum eq.	2	\hat{u}	$\frac{\partial \hat{u}}{\partial y}$	$\frac{\partial^2 \hat{u}}{\partial y^2}$
3	y -momentum eq.	3	\hat{v}	$\frac{\partial \hat{v}}{\partial y}$	$\frac{\partial^2 \hat{v}}{\partial y^2}$
4	z -momentum eq.	4	\hat{w}	$\frac{\partial \hat{w}}{\partial y}$	$\frac{\partial^2 \hat{w}}{\partial y^2}$
5	energy eq.	5	\hat{T}	$\frac{\partial \hat{T}}{\partial y}$	$\frac{\partial^2 \hat{T}}{\partial y^2}$

Table 3.3: Notation for the indices of the coefficient submatrices: the first index k corresponds to the equation (left) and the second index l represents the particular quantity (right).

The above structure is the same for the coefficient matrices of the first (\mathbf{A}_1) and second y -derivatives (\mathbf{A}_2) and for matrix \mathbf{B} . With this notation, the first index k corresponds to the particular equation and the second index l denotes

the individual quantities as provided by table 3.3. For example, $a_{12,3}$ is the prefactor of $\partial v/\partial y$ in the x -momentum equation. The complete set of the matrix coefficients $a_{0k,l}$, $a_{1k,l}$, $a_{2k,l}$ and $b_{k,l}$ is listed in appendix B.

The y -derivatives of the complex amplitudes are discretized by explicit finite differences. Since this is a linear combination of the neighboring grid points, derivatives in normal direction can be expressed as matrix operation:

$$\frac{\partial \hat{q}}{\partial y} = \mathbf{D}_1 \cdot \hat{q}, \quad \frac{\partial^2 \hat{q}}{\partial y^2} = \mathbf{D}_2 \cdot \hat{q}, \quad (3.85)$$

with \mathbf{D}_1 and \mathbf{D}_2 being the derivative matrices of the first and second derivatives in normal direction, respectively.

Since the derivatives of a specific quantity depend only on its values and not on those of other variables, only the main diagonals of \mathbf{D}_1 and \mathbf{D}_2 are filled with submatrices:

$$\mathbf{D}_1 = \begin{bmatrix} \mathbf{D1} & 0 & 0 & 0 & 0 \\ 0 & \mathbf{D1}_{bc} & 0 & 0 & 0 \\ 0 & 0 & \mathbf{D1}_{bc} & 0 & 0 \\ 0 & 0 & 0 & \mathbf{D1}_{bc} & 0 \\ 0 & 0 & 0 & 0 & \mathbf{D1}_{bc} \end{bmatrix} \quad (3.86)$$

$$\mathbf{D}_2 = \begin{bmatrix} \mathbf{D2} & 0 & 0 & 0 & 0 \\ 0 & \mathbf{D2}_{bc} & 0 & 0 & 0 \\ 0 & 0 & \mathbf{D2}_{bc} & 0 & 0 \\ 0 & 0 & 0 & \mathbf{D2}_{bc} & 0 \\ 0 & 0 & 0 & 0 & \mathbf{D2}_{bc} \end{bmatrix} \quad (3.87)$$

The submatrices $\mathbf{D1}$ and $\mathbf{D2}$ contain the coefficients of the finite differences used for discretization. The subscript bc denotes that the boundary conditions are included in the stencils near the boundaries. Thus, velocity and temperature fluctuations are discretized using $\mathbf{D1}_{bc}$ and $\mathbf{D2}_{bc}$. Having no boundary condition for the density, the corresponding derivatives are computed using one-sided and biased finite differences near the boundaries.

Within the domain, standard explicit finite differences of 4th order are used for all quantities:

$$\left. \frac{\partial \hat{\Phi}}{\partial y} \right|_j = \frac{\hat{\Phi}_{j-2} - 8 \cdot \hat{\Phi}_{j-1} + 8 \cdot \hat{\Phi}_{j+1} - \hat{\Phi}_{j+2}}{12 \cdot \Delta y} \quad (3.88)$$

$$\left. \frac{\partial^2 \hat{\Phi}}{\partial y^2} \right|_j = \frac{-\hat{\Phi}_{j-2} + 16 \cdot \hat{\Phi}_{j-1} - 30 \cdot \hat{\Phi}_j + 16 \cdot \hat{\Phi}_{j+1} - \hat{\Phi}_{j+2}}{12 \cdot \Delta y^2} \quad (3.89)$$

$$j \in [4, N - 3]$$

Thus, the coefficients from the lower to the upper tertiary diagonal of the submatrices are allocated by the finite differences given above. For disturbances requiring a boundary condition, the above stencils can be applied one grid point further using $\hat{\Phi}_1 = \hat{\Phi}_N = 0$. At the grid points next to the boundaries, 4th-order biased FDs are used for velocity and temperature fluctuations:

$$\left. \frac{\partial \hat{\Phi}}{\partial y} \right|_2 = \frac{-10 \cdot \hat{\Phi}_2 + 18 \cdot \hat{\Phi}_3 - 6 \cdot \hat{\Phi}_4 + 1 \cdot \hat{\Phi}_5}{12 \cdot \Delta y} \quad (3.90)$$

$$\left. \frac{\partial^2 \hat{\Phi}}{\partial y^2} \right|_2 = \frac{-20 \cdot \hat{\Phi}_2 + 6 \cdot \hat{\Phi}_3 + 4 \cdot \hat{\Phi}_4 - 1 \cdot \hat{\Phi}_5}{12 \cdot \Delta y^2} \quad (3.91)$$

$$\hat{\Phi} \in [\hat{u}, \hat{v}, \hat{w}, \hat{T}]$$

The stencils are given here at grid point $j = 2$. For the upper boundary, this corresponds to biased FDs with the opposite orientation, ranging from $j = (N - 4)$ to $j = (N - 1)$. In case of the density, no boundary condition is applied and the grid points $j = 1$ and $j = N$ are not included in the stencil. The used one-sided finite differences are

$$\left. \frac{\partial \hat{\Phi}}{\partial y} \right|_2 = \frac{-25 \cdot \hat{\rho}_2 + 48 \cdot \hat{\rho}_3 - 36 \cdot \hat{\rho}_4 + 16 \cdot \hat{\rho}_5 - 3 \cdot \hat{\rho}_6}{12 \cdot \Delta y} \quad (3.92)$$

$$\left. \frac{\partial \hat{\Phi}}{\partial y} \right|_3 = \frac{-3 \cdot \hat{\rho}_2 - 10 \cdot \hat{\rho}_3 + 18 \cdot \hat{\rho}_4 - 6 \cdot \hat{\rho}_5 + 1 \cdot \hat{\rho}_6}{12 \cdot \Delta y} \quad (3.93)$$

and

$$\left. \frac{\partial^2 \hat{\Phi}}{\partial y^2} \right|_2 = \frac{35 \cdot \hat{\rho}_2 - 104 \cdot \hat{\rho}_3 + 114 \cdot \hat{\rho}_4 - 56 \cdot \hat{\rho}_5 + 11 \cdot \hat{\rho}_6}{12 \cdot \Delta y^2} \quad (3.94)$$

$$\left. \frac{\partial^2 \hat{\Phi}}{\partial y^2} \right|_3 = \frac{11 \cdot \hat{\rho}_2 - 20 \cdot \hat{\rho}_3 + 6 \cdot \hat{\rho}_4 + 4 \cdot \hat{\rho}_5 - 1 \cdot \hat{\rho}_6}{12 \cdot \Delta y^2} \quad (3.95)$$

at the lower boundary for the first and second derivatives, respectively. The stencils of the upper boundary are of analogous shape in opposite direction.

With the derivatives in normal direction being implemented by the matrices \mathbf{D}_1 and \mathbf{D}_2 , equation (3.81) can be recast to

$$\mathbf{A} = \mathbf{A}_0 + \mathbf{A}_1 \mathbf{D}_1 + \mathbf{A}_2 \mathbf{D}_2 \quad (3.96)$$

$$\mathbf{A} \cdot \hat{q} = \omega \cdot \mathbf{B} \cdot \hat{q}, \quad (3.97)$$

being a generalized eigenvalue problem with eigenvalue ω and eigenvector \hat{q} . This is solved using the QZ algorithm provided by the LAPACK package [76].

3.4.4 Wielandt Iteration

The matrix solver described above is capable of solving the temporal problem with $\omega \in \mathbb{C} \wedge \alpha \in \mathbb{R}$. However, most of the relevant flow problems are of convective nature where disturbances grow or decay in space while being transported by the local flow speed ($\omega \in \mathbb{R} \wedge \alpha \in \mathbb{C}$). In order to obtain spatial amplification rates, α_i is iterated such that the temporal amplification rate of one selected eigenvalue vanishes. Each iteration step causes a slightly modified matrix \mathbf{A} due to the variation of α_i . The resulting eigenvalue is obtained using the Wielandt iteration [107] which works as follows:

First, the generalized eigenvalue problem (3.97) is changed to an ordinary eigenvalue problem by $\mathbf{M} = \mathbf{A} \cdot \mathbf{B}^{-1}$. Let ω_I be the known eigenvalue of matrix \mathbf{M}_I and ω_{II} be the unknown eigenvalue of matrix \mathbf{M}_{II} . Subtracting both matrices yields $\mathbf{M}_\Delta = [\mathbf{M}_{II} - \mathbf{M}_I]$. Since we assume \mathbf{M}_{II} to be only a marginal variation of the original \mathbf{M}_I , one of its eigenvalues is very small:

$$\mathcal{E}\mathcal{V}(\mathbf{M}_\Delta) \approx \omega_{II} - \omega_I \ll 1 \quad (3.98)$$

Hence, the corresponding eigenvalue of the inverse matrix is

$$\mathcal{E}\mathcal{V}(\mathbf{M}_\Delta^{-1}) = \Lambda \approx \frac{1}{\omega_{II} - \omega_I} \gg 1. \quad (3.99)$$

Since Λ is the largest eigenvalue of \mathbf{M}_Δ^{-1} , applying the inverse matrix to any arbitrary vector $\vec{\Phi}$ causes the strongest amplification of the eigenvector which corresponds to the eigenvalue Λ . This assumes that $\vec{\Phi}$ is a linear combination of all eigenvectors of matrix \mathbf{M}_Δ^{-1} :

$$\vec{\Phi} = \sum_j c_j \cdot e\vec{v}_{j, \mathbf{M}_\Delta^{-1}}, \quad c_j \neq 0 \quad (3.100)$$

In principle, some prefactors c_j may be zero. However in a numerical implementation, $\vec{\Phi}$ will contain all eigenvalues due to round-off errors. For example, a simple vector like $\vec{\Phi} = (1, 1, \dots, 1)^T$ works fine within this algorithm. After enough iterations, the strongest amplified eigenvector prevails:

$$\mathbf{M}_\Delta^{-1} \cdot \vec{\Phi} = \Lambda \cdot \vec{\Phi} \tag{3.101}$$

The iteration is aborted when all components of $[\mathbf{M}_\Delta^{-1} \cdot \vec{\Phi}]$ and $\vec{\Phi}$ differ by the same factor Λ with an accuracy of $\epsilon = 10^{-10}$. Hence, the new eigenvalue is

$$\omega_{II} = \frac{1 - \Lambda \cdot \omega_I}{\Lambda}. \tag{3.102}$$

Being able to compute the eigenvalue of a slightly modified matrix, the Newton iteration is used to get from the temporal to the spatial solution. The necessary gradient is obtained by a small variation of the spatial amplification rate. Depending on $\partial\omega_i/\partial\alpha_i$, large changes of α_i may occur. However, the Wielandt iteration requires variations of the matrix to be small. Thus, the modification of the spatial amplification rate is limited to $\Delta\alpha_{i,max}$ as illustrated in figure 3.12. Unfortunately, the value of $\Delta\alpha_{i,max}$ cannot be determined directly. Thus, one has to rely on empirical values to guarantee convergence without requiring too many iterations.

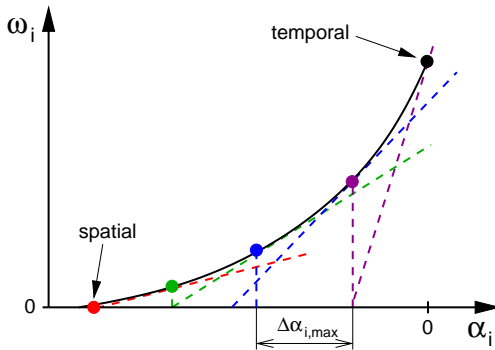


Figure 3.12: Illustration of the Newton iteration, transforming the temporal to the spatial solution. The colors denote different iteration steps. Since the Wielandt iteration allows only small variations of the matrix, the step size is limited to $\Delta\alpha_{i,max}$.

Since the type of matrix variation is not fixed, this procedure can also be used for changing other parameters. So it is possible to cover a range of streamwise wavenumbers α_r and x -positions to compute a stability diagram. Since the value of ω_r is part of the result, the frequency range of a stability diagram is determined indirectly by the range of streamwise wavenumbers. Again, the Wielandt iteration requires the variation of x and α_r to be small.

3.5 Initial Conditions

The first step of a numerical investigation according to figure 3.1 is the definition of the initial condition including the mesh. Since this may differ strongly for various flow problems and configurations, separate programs specialized on the respective problem are used.

3.5.1 Grid Generation

The grid generation is based on a common module containing a variety of grid transformations. The module is included in the different tools for the initial conditions and in the DNS-code. This provides the same grid transformations for all programs and allows the DNS-code to perform simulations with analytical metric coefficients, recognizing the particular grid transformation. Within this work, the following grid transformations are used:

To cover the relevant part of the acoustic farfield efficiently, the mesh is stretched continuously in normal direction:

$$y = a_3 \cdot (\eta - \eta_0)^3 + (\eta - \eta_0) \quad (3.103)$$

The 3rd-order polynomial was chosen since it allows stretching in both positive and negative direction. The strength of the grid coarsening in normal direction is defined by the parameter a_3 . The value of η_0 specifies the center of the stretching being the location with the finest resolution in normal direction.

In streamwise direction, the mesh is typically equidistant in the region of interest. However, the damping zone for the subsonic outflow requires the grid to become coarser (section 3.3.3.7). In the damping zone, the grid is stretched continuously in streamwise direction according to Colonius et al. [24]:

$$s_x = \frac{\xi_{max} \cdot \left(1 + \frac{\Delta x_{max}}{\Delta \xi}\right) - (x_{max} - x_0)}{\frac{\Delta x_{max}}{\Delta \xi}} \quad (3.104)$$

$$\sigma_x = \frac{\ln\left(\frac{\Delta x_{max}}{\Delta \xi} \cdot \frac{1}{\delta_x}\right)}{s_x - x_p} \quad (3.105)$$

$$x = x_0 + \xi + \frac{\Delta x_{max}}{\Delta \xi} \cdot \frac{1}{\sigma_x} \cdot \ln\left(e^{\sigma_x(\xi - s_x)} + 1\right) \quad (3.106)$$

The transformation is defined by four parameters. The coarsening of the grid begins at x_p with the initial stretching given by $\delta_x = \Delta x_{(x_p)}/\Delta \xi - 1$. The final x -coordinate is x_{max} , having the step size ratio $\Delta x_{max}/\Delta \xi$, there.

The mesh used to investigate the numerical properties on non-uniform grids is stretched and coarsened in streamwise direction almost instantaneously. This is done by a hyperbolic tangent distribution of the metric coefficient x_ξ being

$$x = x_0 + \frac{1 + r_x}{2} \cdot \xi + \frac{r_x - 1}{2 \cdot b_x} \ln [\cosh(b_x \cdot (\xi - \xi_1))] - \frac{r_x - 1}{2 \cdot b_x} \ln [\cosh(-b_x \cdot \xi_1)] \quad (3.107)$$

for the coarsening of the mesh. At the beginning, the regular stepsize is used ($\Delta x = \Delta \xi$). Past the position of coarsening ξ_1 , the resolution is decreased by the factor $r_x = \Delta x_{(\xi > \xi_1)}/\Delta x_{(\xi < \xi_1)}$. The additional parameter b_x controls how rapidly the resolution changes. Small values of b_x provide a smooth transition from fine to coarse spacing and large values may cause an almost unsteady change of the resolution in x -direction. The subsequent refinement is done accordingly.

Of course, the above transformations are rather simple. Thus, one has to rely on grid-generation software to obtain the mesh for more complex geometries like the airfoil shown in figure 3.4. For further details, the reader is referred to the work of Schneider [88].

3.5.2 Flow Field

The flow condition is the actual definition of the problem to be solved by DNS. Since boundary conditions like the inflow or the characteristic freestream

are based on the initial condition, appropriate initial flow quantities are required. Therefore, the solution of the boundary-layer equations is an appropriate method.

Blasius Boundary Layer

For the boundary layer (BL) along a flat plate, the self-similar solution of the BL-equations is used. The module PROFKOM [19] provides all flow quantities of a compressible Blasius boundary layer as a function of the wall-normal similarity coordinate

$$\eta = y \cdot \sqrt{\frac{Re}{x}}, \quad (3.108)$$

where $x = 0$ denotes the streamwise coordinate of the trailing edge of the flat plate. The self-similar solution is then mapped to the chosen mesh using a quadratic interpolation.

Self-similar Mixing Layer

In case of a mixing layer without any wall, the initial condition is made of two self-similar boundary layers with their free-stream velocities, being the two different flow speeds above and below the mixing layer, see White [106]. The two BLs are attached to each other at their former walls. The velocity and the temperature of this virtual wall, forming the center of the mixing layer at $y = 0$, are adjusted such that the wall-normal derivatives of the streamwise velocity and of the temperature are equal. As the flow quantities and thus their derivatives are given along the similarity coordinate, the η -derivatives need to be rescaled:

$$\sqrt{\frac{u_{\infty,I}}{\mu_{\infty,I}}} \cdot \left. \frac{\partial u}{\partial \eta} \right|_{I,y=0} = \sqrt{\frac{u_{\infty,II}}{\mu_{\infty,II}}} \cdot \left. \frac{\partial u}{\partial \eta} \right|_{II,y=0} \quad (3.109)$$

$$\sqrt{\frac{u_{\infty,I}}{\mu_{\infty,I}}} \cdot \left. \frac{\partial T}{\partial \eta} \right|_{I,y=0} = \sqrt{\frac{u_{\infty,II}}{\mu_{\infty,II}}} \cdot \left. \frac{\partial T}{\partial \eta} \right|_{II,y=0} \quad (3.110)$$

The upper and lower streams are marked with I and II , respectively and the subscript ∞ denotes the corresponding free-stream values. In a physical sense, the above condition means that no shear stress and heat flux is transferred to the virtual wall. The quantities at $y = 0$ are determined by a Newton iteration. Finally, the two self-similar BL-solutions are interpolated on the grid, taking the different scaling of the two boundary layers into account.

Mixing Layer with Splitter Plate

If a splitter plate is included in the simulation, the two boundary layers above and below the flat plate are taken from the similarity solution. From the trailing edge of the plate onwards, the x -derivatives from the boundary-layer equations

$$\frac{\partial \rho}{\partial x} = -\frac{v \cdot \frac{\partial \rho}{\partial y}}{u} - \frac{2\mu \cdot \left(\frac{\partial \rho}{\partial y}\right)^2}{\rho^2 u \cdot c_p (\kappa - 1) \cdot Re \cdot Pr \cdot Ma_\infty^2} + \frac{\mu \cdot \frac{\partial^2 \rho}{\partial y^2}}{\rho u \cdot c_p (\kappa - 1) \cdot Re \cdot Pr \cdot Ma_\infty^2} - \frac{\rho \cdot \mu \cdot \left(\frac{\partial u}{\partial y}\right)^2}{u \cdot c_p \cdot Re} \quad (3.111)$$

$$\frac{\partial u}{\partial x} = \frac{v \cdot \frac{\partial u}{\partial y}}{u} - \frac{\frac{\partial \mu}{\partial y} \cdot \frac{\partial u}{\partial y}}{Re} - \frac{\mu}{\rho u} \cdot \frac{\partial^2 u}{\partial y^2} \quad (3.112)$$

are integrated in downstream direction. The normal velocity v is obtained by integrating

$$\frac{\partial v}{\partial y} = \frac{\frac{\partial \rho}{\partial x} \cdot u + \frac{\partial \rho}{\partial y} \cdot v}{\rho} \quad (3.113)$$

in both directions, starting at the center $v(y = 0) = 0$. For boundary layers with a non-zero sweep angle ($w_{\infty, I} \neq 0$ or $w_{\infty, II} \neq 0$), the self-similar streamwise-velocity profile is rotated. Due to the 3-d boundary layers, the integration in x -direction has to consider the spanwise velocity component now. The extension of equations (3.111)-(3.113) for the 3-d BL-solution can be found in [48].

The numerical integration is implemented in a rather simple way. In the downstream direction, the 1st-order Adams predictor-corrector method is used:

$$\Phi_{j+1}^* = \Phi_j + \Delta x \cdot \left. \frac{\partial \Phi}{\partial x} \right|_j \quad (3.114)$$

$$\Phi_{j+1} = \Phi_j + \Delta x \cdot \left. \frac{\partial \Phi}{\partial x} \right|_{j+1}^* \quad (3.115)$$

The integration of the normal-velocity component is done by the method of Heun:

$$v_{k+1}^* = v_k + \Delta y \cdot \left. \frac{\partial v}{\partial y} \right|_k \quad (3.116)$$

$$v_{k+1} = v_k + \frac{\Delta y}{2} \cdot \left(\left. \frac{\partial v}{\partial y} \right|_k + \left. \frac{\partial v}{\partial y} \right|_{k+1}^* \right) \quad (3.117)$$

Here, j and k denote the indices in streamwise and normal direction, respectively. In order to stay within the stability limit, integration of the BL-equations is done on an equidistant grid. While the y -resolution in the middle of the domain appeared to be sufficiently fine, the spacing in streamwise direction typically needs to be decreased.

As the second x -derivatives are not negligible near the trailing edge, it is somehow problematic to use the BL-equations, here. Accordingly, the discontinuity of the geometry causes a jump in the wall-normal velocity. In order to provide a smooth distribution, necessary for the free-stream boundary condition, the normal velocity of the previous x -position is used and then filtered in normal direction:

$$v_{j,k} = \left(\frac{1}{Re \cdot \Delta x} \right) \cdot \frac{v_{j-1,k+1} + v_{j-1,k-1}}{2} + \left(1 - \frac{1}{Re \cdot \Delta x} \right) \cdot v_{j-1,k} \quad (3.118)$$

The 1st-order filter actually averages the neighboring values, modeling the successive smoothing of the v -profile. Since the strength of the filtering should be effected neither by the streamwise resolution nor by the reference length \tilde{L} , the averaging is weighted with the factor $1/Re\Delta x$. Of course, this does not fulfill the continuity equation. However, the flow field showed to be sufficient as initial condition. Note that equation (3.118) is applied after the complete integration of the BL-equations. Thus, all other flow quantities are not affected by the smoothing. Since the normal velocity is not used in LST, its results are not distorted by the modification of the normal velocity component.

Figure 3.13 shows the difference between the original v -distribution (left) and smoothing (right). The original solution of the BL-equation generates an instantaneous increase of the wall-normal velocity directly behind the splitter plate. With values ranging from $v = -0.77$ to $v = -0.9$, a rather unphysical flow field emerges. Yet, a rather reasonable distribution is achieved by applying equation (3.118) and the initial condition is directly applicable to the characteristic free-stream boundary condition whose linearization requires a valid mean flow.

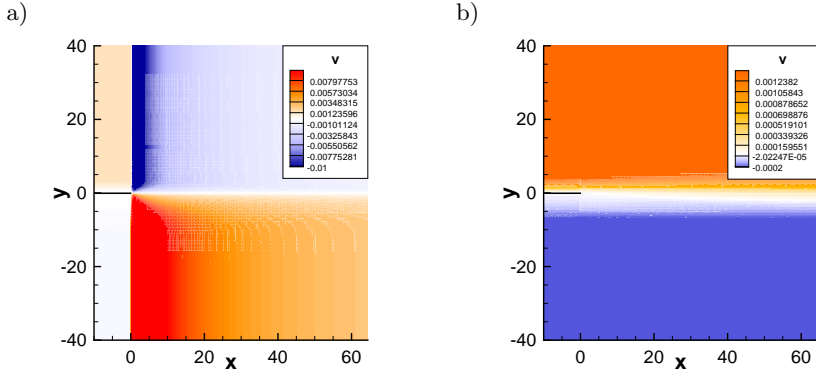


Figure 3.13: Comparison of the wall-normal velocity component for the mixing layer past a splitter plate of case 5A:

- a) original solution of the BL-equations,
- b) additional smoothing of v according to equation (3.118).

3.6 Pre- and Postprocessing

The DNS code is run via a shell script which gathers all information required for the simulation, compiles the code with the respective array sizes and submits the job to the queuing system. With all input files and the source code being saved, the complete simulation is fully reproducible. Additional tools complete the work flow like time-step estimation or combining eigenfunctions from LST for disturbance generation. The latter also normalizes the amplitude with respect to the maximum of $|\hat{u}|$ and shifts the phase such that $\theta_u = 0$ at the location where the amplitude of u has its maximum. Thus, the phase shift is given relatively to the maximum of $|\hat{u}|$.

With the DNS producing a huge amount of data, postprocessing is vital for data analysis. For this purpose the EAS3 toolset [75] is used which provides a variety of data operations via the command-line interface and allows postprocessing to be triggered by a bunch of shell scripts. Thus, postprocessing of multiple files can be done in parallel, simply by adding a “&” to respective call. Examples of the implemented functionality are double Fourier transformation in time and spanwise direction, the Λ_2 vortex criterion of Jeong and Hussain [46] and the dilatation $\nabla \mathbf{u}$ to visualize the acoustic field.

4 Fundamentals of Mixing-Layer Noise

The pure mixing layer, also denoted as free shear layer is a generic and rather simple configuration for jet-noise investigations. Unlike the mixing layer behind a splitter plate (chapter 5), the inflow is made of an S-shaped velocity profile here. Having no walls in the domain, the origin of the two different streams is not included in the simulation. However, the fundamental sound-generation mechanisms due to vortex interaction can be investigated with this setup.

4.1 Flow Parameters

The flow configuration has been closely matched to the case of Colonius et al. [25]. This allows to verify the numerical scheme for aeroacoustic simulations. The Mach numbers of the upper and lower stream are $Ma_I = 0.5$ and $Ma_{II} = 0.25$, respectively. As both free stream temperatures are equal ($\tilde{T}_I = \tilde{T}_{II} = 280K$), the ratio of the streamwise velocities is $u_I/u_{II} = 2$. The Reynolds number $Re = \rho_I u_I \delta_\Omega(x_0)/\mu = 500$ is based on the vorticity thickness at the inflow which is used to normalize length scales:

$$\delta_\Omega(x_0) = \left(\frac{\Delta U}{|\partial u / \partial y|_{max}} \right)_{x=x_0}, \quad (4.1)$$

with $\Delta U = u_I - u_{II}$ being the difference between the two free-stream velocities. The origin of the streamwise coordinate is the singularity of the Blasius mixing layer at its beginning. Here, the initial coordinate $x_0 = 30$ is chosen such that the vorticity thickness of the boundary layer solution is one at the inflow. By that length scales are made dimensionless with $\delta_\Omega(x_0)$. The solution of the boundary-layer equations provides the Blasius mixing layer, shown in figure 4.1 for the inflow $x_0 = 30$.

A cartesian grid is used with 2500x850 grid points in x - and y -direction, respectively. In streamwise direction, the grid is uniform with spacing $\Delta x = 0.157$ up to the sponge region where the grid is highly stretched. In normal direction, the grid is continuously stretched with the smallest stepsize $\Delta y = 0.15$ in the middle of the mixing layer and the largest spacing $\Delta y = 1.06$ at the upper and lower boundaries. The grid stretching and the domain decomposition for parallelization are illustrated in figure 4.1.

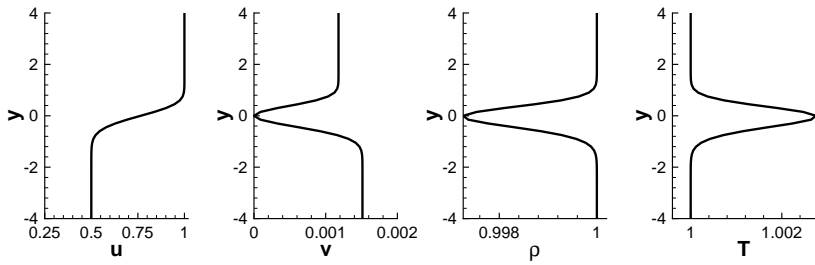


Figure 4.1: Initial condition at the inflow $x_0 = 30$, obtained from the boundary-layer equations.

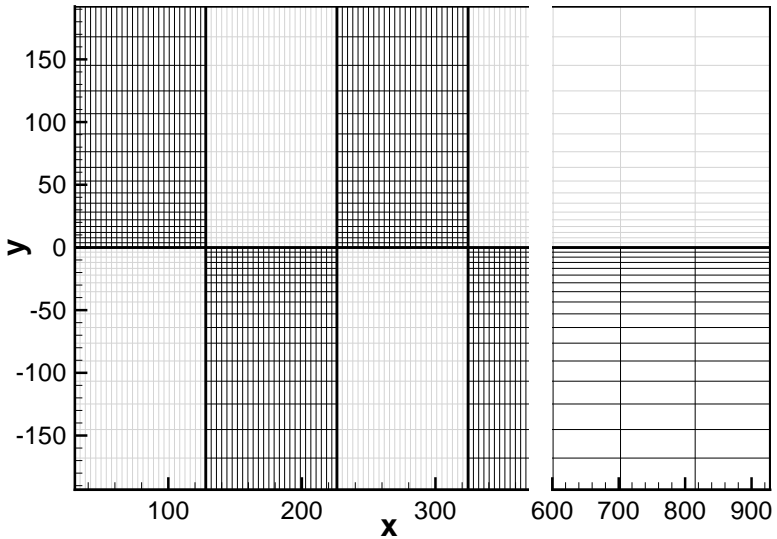


Figure 4.2: Grid in the x - y -plane showing every 25th gridline. The domain decomposition is indicated by black and grey lines.

4.2 Linear Stability Analysis

Linear stability analysis is based on the solution of the boundary-layer equations, here. This is done on an equidistant version of the grid with 301 points in y -direction and a spacing of $\Delta y = 0.15$, ranging from $y = -22.5$ to $y = 22.5$. Figure 4.2 shows the temporal spectrum at the inflow for a streamwise wave number $\alpha_r = 0.1$. One amplified eigenvalue exists with $\omega_r = 0.075$, $\omega_i = 0.019$, being the Kelvin-Helmholtz mode of the mixing layer. Its phase speed $c_{ph} = \omega_r/\alpha_r = 0.75$ is the meanvalue of the two freestream velocities. Moreover, two continuous spectra exist with phase speeds of $c_{ph} = 1.0$ and $c_{ph} = 0.5$. They correspond to freestream disturbances of the upper and lower stream, respectively.

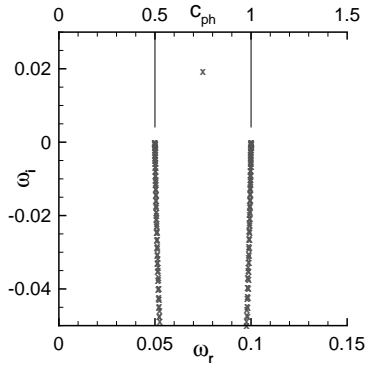


Figure 4.3: Temporal spectrum of the mixing layer for streamwise wave number $\alpha_r = 0.1$ at $x_0 = 30$.

The spatial amplification rates of the most amplified eigenvalue are given in figure 4.4 a) as a function of the angular frequency $\omega = 2\pi \cdot f$. The fundamental frequency $\omega_0 = 0.6293$ is defined by the highest amplification rate. Downstream of the inflow, spatial amplification decreases and its maximum moves towards lower frequencies. A comparison with the inviscid instability solution reveals that the growth rates differ by up to 10%. Figure 4.4 b) shows that the amplification of oblique waves decreases for larger values of γ while its maximum stays at the same frequency.

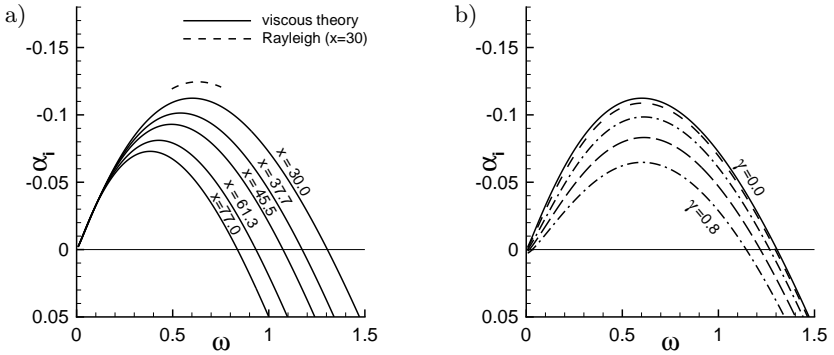


Figure 4.4: a) Stability diagram of the mixing layer for 2-d disturbances at various streamwise positions, including inviscid theory.

b) Spatial Amplification rates at the inflow $x_0 = 30$ in dependence of the spanwise wave number; $\gamma = 0.0$ to $\gamma = 0.8$ with $\Delta\gamma = 0.2$.

The eigenfunctions for the two-dimensional Kelvin-Helmholtz mode and an oblique wave with a spanwise wave number $\gamma = 0.8$ are shown in figures 4.5 and 4.6, respectively. For comparison, the amplitudes of both eigenfunctions are scaled such that the maximum amplitude of the streamwise velocity is one. The maximum of $|\hat{u}|$ surrounded by two local extrema and with phase jumps between them is the characteristic shape of the eigenfunction in a mixing layer. Being a two-dimensional disturbance, the eigenfunction for $\gamma = 0$ does not have fluctuations of the spanwise velocity. The amplitudes of the other flow quantities possess only one maximum which is located in the center of the mixing layer. With $\gamma = 0.8$ and $\alpha_r = 0.83$, the oblique instability has a wave angle $\Psi \approx 45^\circ$. The profile of $|\hat{u}|$ is narrower in the three-dimensional case and the v -amplitude is shifted to the spanwise velocity. The amplitudes of the thermodynamic quantities ρ , T and p are reduced by a factor of more than two compared to the two-dimensional eigenfunction.

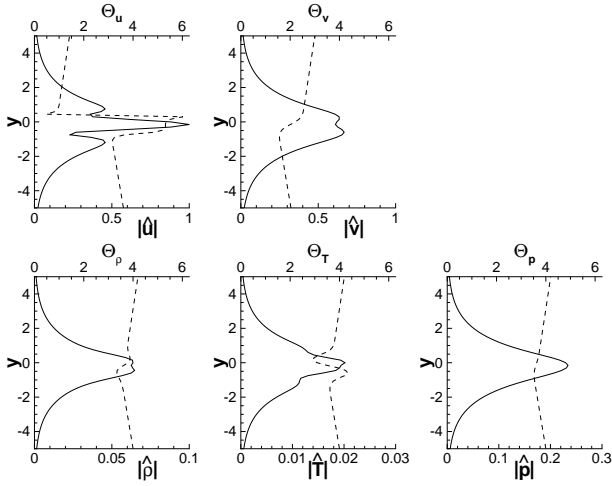


Figure 4.5: Amplitude (solid line) and phase distribution (dashed line) of the two-dimensional eigenfunction with fundamental frequency $\omega_0 = 0.6293$.

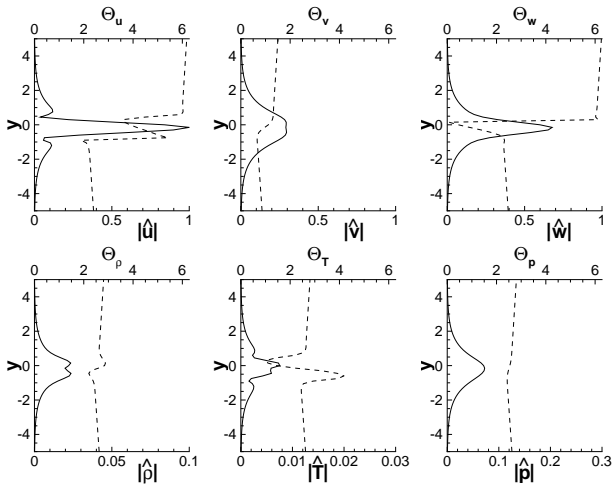


Figure 4.6: Eigenfunction of an oblique wave with frequency $\omega_0 = 0.6293$ and spanwise wave number $\gamma = 0.8$ (lines according to figure 4.5).

4.3 Two-Dimensional Simulation

To introduce defined disturbances, the flow is forced at the subsonic inflow with eigenfunctions from linear stability theory. The eigenfunctions of the fundamental frequency $\omega_0 = 0.6293$ and its first three subharmonics are used with the maximum of $|\hat{u}| = 0.001$ for all disturbances. In simulation 4A, the phase shift is $\Delta\Theta = -0.028$ for $(1/2, 0)$, $\Delta\Theta = 0.141$ for $(1/4, 0)$ and $\Delta\Theta = 0.391$ for $(1/8, 0)$ as done by Colonius et al. [25]. However it is not clear how the phase shift is specified by them since the phase distribution varies along the normal direction (see figures 4.5 and 4.6). Here, the phase is defined with respect to the maximum of $|\hat{u}|$ such that $\Theta = 0$ at the location of $|\hat{u}|_{max}$ in case of no phase shift. To investigate the influence of the phase, a second simulation (case 4B) with an alternative phase shift $\Delta\Theta = 3.141$ of mode $(1/4, 0)$ has been performed. At the upper and lower boundaries, a characteristic boundary condition with a damping zone is used. The buffer zone in front of the subsonic outflow covers 400 points in x -direction with spatial filtering.

case	4A, 4B	
number of grid points ($N_x \times N_y$)	2500 \times 850	
Δx	0.157 - 4.761	
Δy	0.150 - 1.062	
time step Δt	0.0133	
computed time steps	57000	
fundamental frequency ω_0	0.6293	
periods of ω_0 for analysis	8	
subsonic inflow:	$ \hat{u} _{max}$	$\Delta\Theta$
(1, 0)	0.001	0.000
(1/2, 0)	0.001	-0.028
(1/4, 0)	0.001	0.141, 3.141
(1/8, 0)	0.001	0.391
characteristic free stream:		
damping parameter d	0.01	
grid points in damping zone	40	
subsonic outflow:		
beginning of filtering (x -position)	359.71	
filtering sequence (time steps)	5	
ramping of filter (grid points)	5	

Table 4.1: Parameters for the two-dimensional simulations 4A and 4B: pure mixing layer with $Ma_I = 0.5$, $Ma_{II} = 0.25$ and $Re = 500$.

The time step is $\Delta t = 0.0133$ which corresponds to 750 time steps per period of the fundamental frequency. An overall number of 57000 time steps has been computed of which 80 time steps during eight fundamental periods are used for data analysis. The parameters of the simulation are summarized in table 4.1.

The spanwise vorticity Ω_z is shown in figure 4.7 after 76 periods of the fundamental frequency for case 4A. The solution is in good agreement with the result of Colonius et al. [25]. Yet the roll-up of Kelvin-Helmholtz vortices and the subsequent pairing occurs a bit earlier, here. Unlike the reference solution where forcing is done with eigenfunctions from the inviscid Rayleigh equations, eigenfunctions from viscous linear stability theory are used here to excite the flow. As shown in [9], the viscous and inviscid eigenfunctions differ by up to 15%. Thus, the more accurate viscous eigenfunctions seem to be slightly more efficient for disturbance generation. The last merging which ejects vortices with frequency $f = (\omega_0/4)/(2\pi)$ is in an earlier stage compared to Colonius et al. This is due to the unclear definition of the phase shift mentioned above. Again, the final vortex at $x \approx 290$ looks the same as in the reference solution.

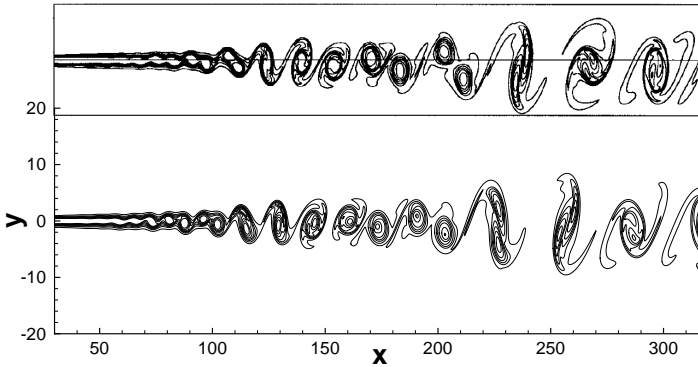


Figure 4.7: Snapshot of the spanwise vorticity Ω_z after 76 fundamental periods for case 4A with $\Delta\Theta(\omega_0/4) = 0.141$. Contour levels range from -0.26 to 0.02 with an increment of 0.04 . The reference solution of Colonius et al. [25] is shown above.

The time-averaged streamwise velocity is computed as

$$\bar{u} = \frac{1}{j_2 - j_1} \cdot \sum_{j=j_1}^{j_2} u(t_j), \quad (4.2)$$

where all 6000 time steps within the analysis time frame $[(j_2 - j_1) \cdot \Delta t] = 2\pi/(\omega_0/8)$ are used. As shown in figure 4.8, the thickness of the mixing layer strongly increases at the positions of vortex pairing $x = 130$ and $x = 240$. Moreover, good agreement with the reference solution can be observed.

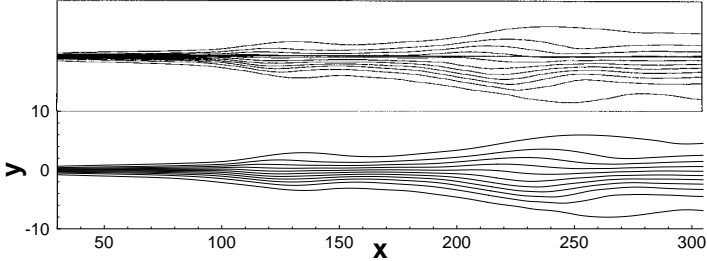


Figure 4.8: Mean streamwise velocity contours from case 4A with the reference solution [25] of the corresponding domain above. Contour levels range from 0.52 to 0.98.

The amplitudes of v are shown in figure 4.9 a) with their maximum taken along the normal direction. The velocity component in normal direction is chosen since its streamwise development is mainly associated with vorticity. The modes are denoted as (h, k) , with h and k being the multiple of the fundamental frequency ω_0 and the spanwise wavenumber γ_0 , respectively. The corresponding amplification rates

$$\alpha_i = -\frac{\partial}{\partial x} \left\{ \ln(|\hat{\Phi}|_{max}) \right\} \quad (4.3)$$

are compared with linear stability theory in figure 4.9 b). In the initial region of the integration domain amplitudes grow exponentially. Despite α_i being a very sensitive value, the amplification rates correspond well to those from linear stability theory. Further downstream, modes $(1, 0)$, $(1/2, 0)$, $(1/4, 0)$ saturate at positions $x = 90$, $x = 130$ and $x = 240$, respectively. These streamwise locations correlate well with the positions where the respective vortices are fully developed (see figure 4.7).

For case 4B with $\Delta\Theta(\omega_0/4) = 3.141$, the amplitudes of the normal velocity are shown in figure 4.10 a). For comparison, the result for $\Delta\Theta(\omega_0/4) = 0.141$ is included by dotted lines. In the initial part of the flow field, the amplitudes grow independently of the phase shift.

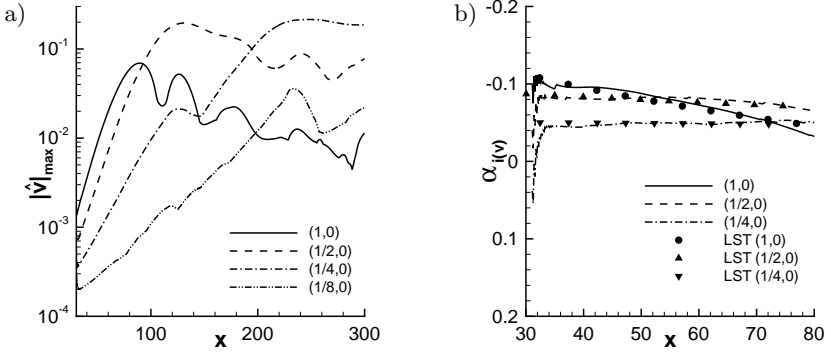


Figure 4.9: a) Maximum amplitudes of the normal velocity v along y -direction for simulation 4A.
 b) Corresponding amplification rates compared with LST (symbols).

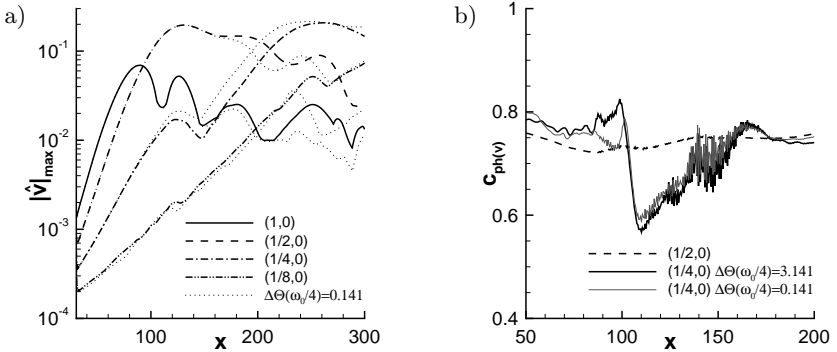


Figure 4.10: a) Maximum amplitudes of the normal velocity v along y -direction for simulation 4B ($\Delta\Theta(\omega_0/4) = 3.141$). Dotted lines denote the respective modes for $\Delta\Theta(\omega_0/4) = 0.141$ (case 4A).
 b) Phase velocities c_{ph} of normal-velocity modes at $y = 0$.

Yet the development of the second subharmonic differs from $x \approx 120$ onwards. There, its phase is adjusted to the one of the first subharmonic. This can be seen in figure 4.10 b) showing the phase speed

$$c_{ph} = \frac{\omega}{\partial\Theta/\partial x} \quad (4.4)$$

of the first two subharmonics at $y = 0$. From $x = 100$ onwards, the phase speed decreases and then adapts to the one of the first subharmonic. During this process, the amplitudes reduce before they grow again. Phase adjustment is found for both cases, but for $\Delta\Theta(\omega_0/4) = 3.141$, the phase speed varies more and subharmonic resonance of mode $(1/4, 0)$ is achieved with a slightly reduced amplitude compared to $\Delta\Theta(\omega_0/4) = 0.141$. Accordingly, its saturation at $x = 260$ is further downstream and the phase shift between $(1/8, 0)$ and the maximum of $(1/4, 0)$ differs. This provides faster resonance and increases the amplitude of $(1/8, 0)$ by a factor of almost four downstream of $x \geq 270$.

The resulting difference of the vortical structures is shown in figure 4.11 for time level $t = 758.1$. Apparently, the merged vortices look the same and only their relative orientation differs. For phase shift $\Delta\Theta(\omega_0/4) = 0.141$, the angle between both vortex axes is smaller than the one observed for $\Delta\Theta(\omega_0/4) = 3.141$. This is the only visible difference in the flow field between both cases. Note that the actual alignment of the vortices is time dependent.

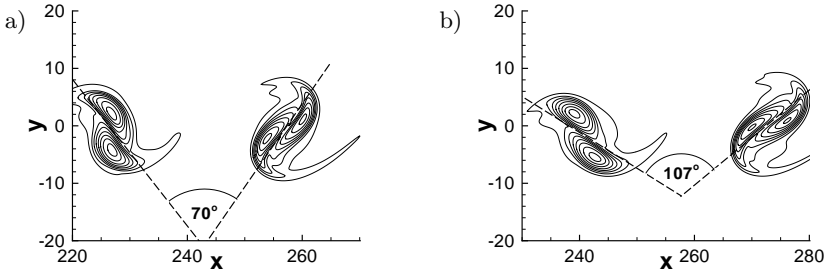


Figure 4.11: Comparison of the spanwise vorticity Ω_z at $t = 758.1$ for different phase shifts of the second subharmonic:

a) case 4A ($\Delta\Theta(\omega_0/4) = 0.141$), b) case 4B ($\Delta\Theta(\omega_0/4) = 3.141$).

The acoustic field is visualized by the dilatation being the divergence of the velocity field $\nabla \mathbf{u}$. In the freestream, the steady solution is $\nabla \mathbf{u} = 0$. Since vorticity and entropy fluctuations propagate with the flow speed and thus in x -direction here, non-zero values of $\nabla \mathbf{u}$ in the freestream represent the emitted sound. Selected frequencies can be visualized by the real part of the Fourier-transformed dilatation field. Beyond this, acoustic emission can be characterized by their directivity which is defined as the angle of noise propagation versus the streamwise direction:

$$\tan(\varphi) = \frac{dy}{dx} \tag{4.5}$$

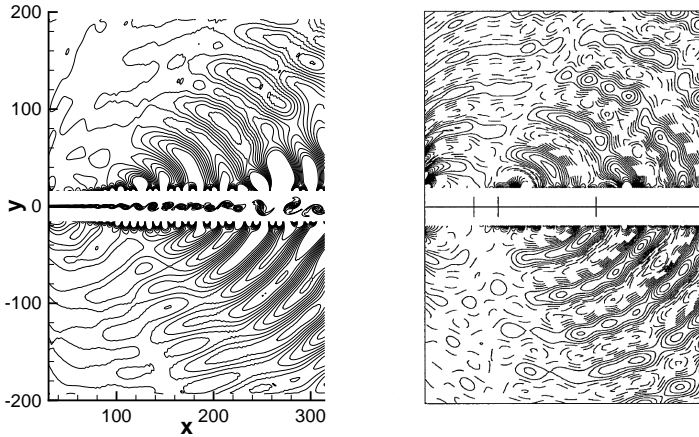


Figure 4.12: Real part of the Fourier-transformed dilatation field for frequency $\omega_0/2$ with contour levels ranging from $-8 \cdot 10^{-7}$ to $8 \cdot 10^{-7}$ (case 4B). In the middle, an instantaneous snapshot of the spanwise vorticity is shown. The corresponding reference solution of Colonius et al. [25] is shown on the right side.

Figure 4.12 shows the real part of the Fourier-transformed dilatation field of the first subharmonic for case 4B. The main acoustic source is located at $x \approx 130$ with a directivity of $\varphi = -40^\circ$ to $+50^\circ$. The emitted sound is enhanced by an additional source at $x \approx 200$, where the amplitude of the second subharmonic exceeds mode $(1/2, 0)$. Since the amplitudes do not differ that much up to the second vortex pairing, the acoustic field of the first subharmonic is very similar in case of $\Delta\Theta(\omega_0/4) = 0.141$. Despite the ambiguity in the phase shift definition, the result is in good agreement with the reference solution of Colonius et

al., given on the right half of figure 4.12. Unlike their result, no artificial sound due to the forcing at the inflow can be observed in the upper half of the domain.

In case 4A, sound with frequency $\omega_0/4$ is emitted mainly perpendicular to the flow direction as shown in figure 4.13 a). This differs to [9, 25] where the emitted sound with frequency $\omega_0/4$ is directed mainly downstream. This result is achieved by the alternative phase shift of case 4B for which a stronger noise generation can be observed. Sound with frequency $\omega_0/4$ is emitted from $x \approx 240$ in downstream direction ($\varphi = -70^\circ$ to $+60^\circ$) which corresponds to the reference solution of Colonius et al. [25]. The acoustic waves propagating in normal direction are only weakly affected by the different phase shift of the second subharmonic.

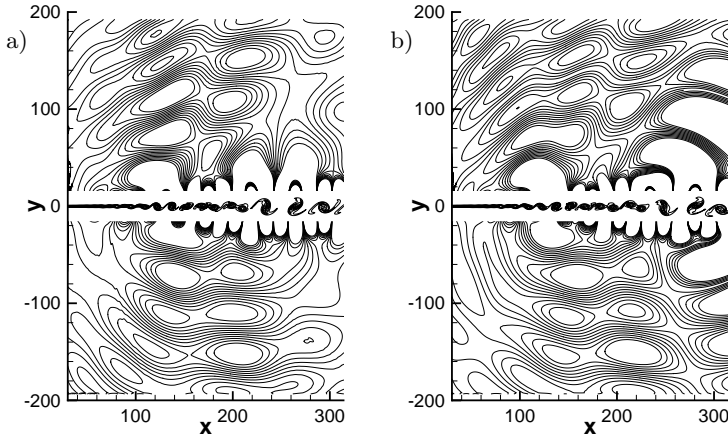


Figure 4.13: Emitted sound with frequency $\omega_0/4$, visualized by the real part of the Fourier-transformed dilatation with contour levels ranging from $-2 \cdot 10^{-6}$ to $2 \cdot 10^{-6}$:

a) $\Delta\Theta(\omega_0/4) = 0.141$ (case 4A), b) $\Delta\Theta(\omega_0/4) = 3.141$ (case 4B).

The two-dimensional results show that a notable subharmonic of a merged vortex causes the main acoustic emission of a mixing layer. With resonance determining the growth of low-frequency disturbances, it is possible to reduce or inhibit the emitted sound by a varied phase shift of the introduced particular subharmonic. This confirms the conclusion of Wei and Freund [105] that vortex pairing per se is not responsible for generating tonal noise. Since the acoustic

emission strongly depends on phase and amplitudes, any statistical approach may hardly capture the mechanisms of aeroacoustic sound generation correctly.

4.4 Three-Dimensional Simulation

Although two-dimensional disturbances are most amplified in the plane mixing layer, three-dimensional effects play an important role in fluid dynamics since turbulence is a three-dimensional phenomenon. The three-dimensional simulation contains an additional 1% steady disturbance with a spanwise wave number $\gamma = 0.8$. It is introduced at the inflow using the eigenfunction of mode (1, 1) shown in figure 4.6. The high amplitude of the steady disturbance has been chosen to allow two-dimensional unsteady disturbances to interact with mode (0, 1), generating unsteady oblique waves. The spanwise direction is resolved by five modes (de-aliased) which corresponds to 9 grid points in the symmetric case. Except the additional steady disturbance, the boundary conditions are the same as in section 4.3. The simulation parameters are summarized in table 4.2.

case	4C	
number of grid points ($N_x \times N_y \times N_z$)	2500 \times 850 \times 9	
Δx	0.157 - 4.761	
Δy	0.150 - 1.062	
Δz	0.491	
number of spanwise modes	5	
fund. spanwise wave number γ_0	0.8	
time step Δt	0.00998	
computed time steps	76000	
fundamental frequency ω_0	0.6293	
periods of ω_0 for analysis	8	
subsonic inflow:	$ \hat{u} _{max}$	$\Delta\Theta$
(1, 0)	0.001	0.000
(1/2, 0)	0.001	-0.028
(1/4, 0)	0.001	3.141
(1/8, 0)	0.001	0.391
(0, 1)	0.010	0.000

Table 4.2: Parameters for the three-dimensional simulation 4C of the mixing layer with $Ma_I = 0.5$, $Ma_{II} = 0.25$, $Re = 500$. Quantities of the free-stream and outflow boundaries are those from table 4.1.

The spanwise vorticity Ω_z is shown in figure 4.14. The initial region is similar to the corresponding two-dimensional simulation: the mixing layer rolls up into vortices and the first pairing takes place at $x \approx 120$. Further downstream three-dimensional effects increase and the vortical structures differ. The Kelvin-Helmholtz vortices break up into small-scale structures for $x > 150$. Compared to the two-dimensional simulations of section 4.3, large scales almost disappear.

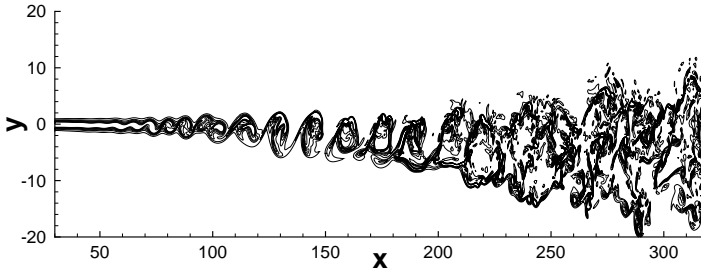


Figure 4.14: Snapshot of the spanwise vorticity Ω_z at $z = 0$ after 76 fundamental periods for case 4C. Contour levels -0.26 to 0.02 correspond to those of figure 4.7.

A three-dimensional impression of the vortical structures is given by the Λ_2 -criterion by Jeong and Hussain [46], shown in figure 4.15. In order to see all structures completely, the iso-surfaces $\Lambda_2 = -0.005$ are given along two spanwise periods. In the initial region of the mixing layer, S-shaped streamwise vortices are bended around the spanwise vortices. These are counter-rotating vortices as shown in figure 4.16 for an exemplary cross-section at $x = 137.4$.

With increasing streamwise position, their intensity grows and a pairwise approach in spanwise direction is visible. Their shape is reminiscent of the Λ -vortices known from boundary-layer transition, see e.g. Meyer [67]. Furthermore, Ω -shaped vortices can be found on top of the Λ -type vortices. The interaction of spanwise and streamwise vortices leads to a breakdown in small scale structures. Despite the flow field is dominated by small vortices for $x > 200$, accumulations with the wavelength of the second subharmonic are visible (see also figure 4.14).

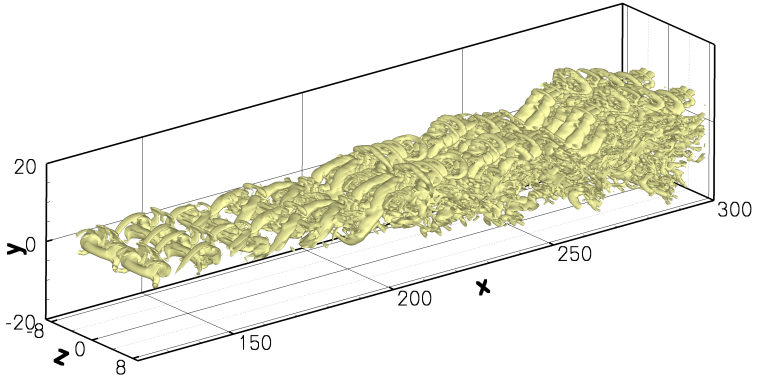


Figure 4.15: Perspective view of the iso-surface $\Lambda_2 = -0.005$ in the range of two spanwise periods at $t = 758.81$.

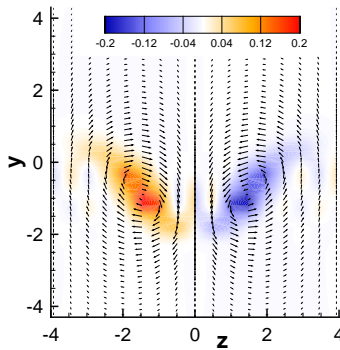


Figure 4.16: Streamwise vorticity Ω_x and velocity field at streamwise position $x = 137.4$ and time $t = 758.81$.

The spectral decomposition is given in figures 4.17 a) and b) for two- and three-dimensional modes, respectively. For comparison, the maximum amplitudes of the corresponding 2-d case 4B are plotted as dotted lines as well.

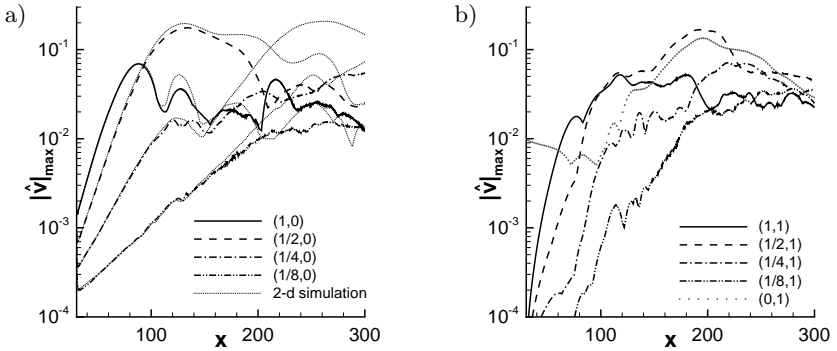


Figure 4.17: Maximum amplitudes of the normal velocity along y -direction:
 a) two-dimensional disturbances $(h, 0)$ of case 4C compared with 2-d simulation 4B (dotted lines),
 b) three-dimensional disturbances $(h, 1)$ with $\gamma_0 = 0.8$.

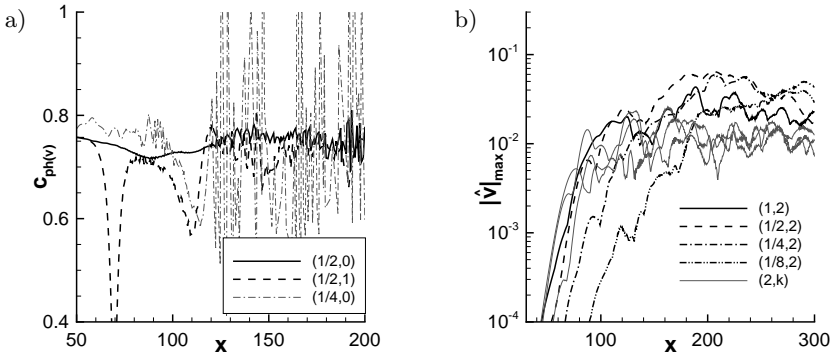


Figure 4.18: a) Phase velocities of the first two subharmonics: 2-d and 3-d disturbances, computed from the normal velocity at $y = 0$.
 b) Spanwise and temporal higherharmonics of the normal velocity component v , based on the maximum along y .

Up to $x \approx 110$, the two-dimensional disturbances grow as in the two-dimensional case 4B and the saturation of the first subharmonic differs only slightly. The excited steady mode $(0, 1)$ slowly decays up to $x = 100$. However, its large amplitude generates unsteady oblique modes $(h, 1)$. From $x = 100$ onwards, the non-linear generation of mode $(0, 1)$ exceeds the initial disturbance. The initial increase of disturbances $(1, 1)$ and $(1/2, 1)$ ends where the first subharmonic $(1/2, 0)$ saturates. Figure 4.18 a) shows the adaptation of the oblique subharmonic to its two-dimensional counterpart. Downstream of $x = 150$, both disturbances are in phase and the oblique mode $(1/2, 1)$ grows again. Driven by the oblique subharmonic the amplitude of the steady disturbance $(0, 1)$ increases as well. It is clearly visible that the phase speed of the second subharmonic $(1/4, 0)$ is unable to match that of mode $(1/2, 0)$. Thus, the subharmonic resonance known from the two-dimensional simulation of case 4B is suppressed by the oblique modes $(1/2, 1)$ and $(0, 1)$. The last third of the domain is dominated by the generation of spanwise higher harmonics, shown in figure 4.18 b). These correspond to the small-scale structures shown above. Temporal higher harmonics $(2, k)$ are limited to $|\hat{v}| \approx 10^{-2}$ which is reached at the saturation of the first subharmonic.

The acoustic emission is illustrated in figure 4.19 for the first and second subharmonics. The sound with frequency $\omega_0/4$ is generated among others in the range of $x = 200 - 240$ which is a bit upstream compared to the two-dimensional simulation. In the upper half of the acoustic field, the directivity is in the range of $\varphi = 60^\circ$ to 80° being narrower compared to figure 4.13 b). The amplitude itself is not reduced significantly. Below the mixing layer, the intensity is reduced by a factor of roughly two with a directivity $\varphi = -35^\circ$ to -90° . Further upstream, an additional source is located at $x \approx 130$. This is the position where the original subharmonic resonance of mode $(1/4, 0)$ is suppressed. Thus, the inability to adapt the phase velocity causes the noise generation in the direction of $\varphi \approx 125^\circ$. The sound with the frequency of the first subharmonic is shown in figure 4.19 b). The major source exists at $x \approx 210$ with a directivity mainly in the range of $\varphi = 0^\circ$ to -60° . Less intense noise is emitted in various directions in the upper part of the acoustic field with a second source at $x \approx 160$.

Sound is also generated for unforced frequencies, given for example for $3/8 \cdot \omega_0$ and $3/4 \cdot \omega_0$ in figures 4.19 c) and d), respectively. While the lower unexcited frequency contributes only a little to the emitted sound, a large noise source with downstream directivity is observed at $x = 210$. Its position corresponds clearly with the saturation of the spanwise higher harmonics, shown in figure 4.18 b). The combination of various frequencies yields a broadband noise source where lower frequencies are directed more perpendicular to the flow speed.

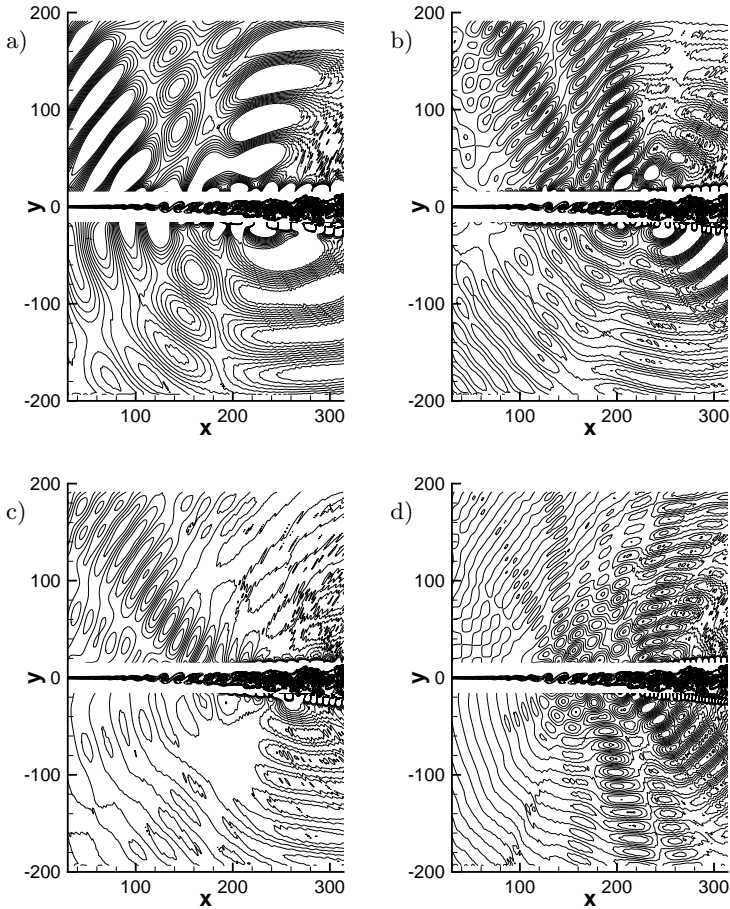


Figure 4.19: Real parts of the Fourier-transformed dilatation field at the symmetry plane $z = 0$: a) $\omega_0/4$, b) $\omega_0/2$, c) $3/8 \cdot \omega_0$, d) $3/4 \cdot \omega_0$. Contour levels range from $-2 \cdot 10^{-6}$ to $2 \cdot 10^{-6}$.

5 Mixing Layer with Splitter Plate

The pure mixing layer considered above allows the investigation of the fundamental mechanisms of sound generation. However, it is a rather academic case since the mixing layer of a jet has its origin at the nozzle end as sketched in figure 1.3. The thicknesses of the boundary layers on both sides of the nozzle end cause a combination of wake and mixing layer past the trailing edge. Apart from being a more realistic configuration, including the nozzle end will allow the investigation of physical actuators placed at the wall (see chapter 6).

5.1 Flow Parameters

In order to investigate the influence of the splitter plate, two different thicknesses are considered. In the first case 5A, the thickness $h_{TE} = 0.15$ is equal to the stepsize in normal direction at $y = 0$. The splitter plate is implemented using the domain decomposition a sketched in figure 5.1. As shown in the detailed view, the normal stepsize Δy is the smallest thickness of the flat plate which can be computed by the NS3D code. With this setup, wall boundary conditions are given only at the upper and lower side of the flat plate and no special treatment of corner points is required. The other configuration (case 5B) contains a thick splitter plate with $h_{TE} = 5.4$ ¹. This is achieved by adding a row of domains behind the trailing edge with the first one having a wall-boundary condition on its left side. Again, the possible corner point is considered to be no boundary condition. As shown in figure 5.3 a), this is equivalent to a chamfered edge whose spatial extent is below the resolution of the grid.

The origin of the coordinate system is located at the upper trailing edge of the splitter plate. In streamwise direction, the mesh is uniform up to the damping zone where the stepsize increases smoothly from $\Delta x = 0.15$ to $\Delta x = 14.7$ using equation (3.106). The spacing in normal direction is $\Delta y = 0.15$ in the middle of the flow field and $\Delta y = 1.06$ at the freestream boundary with a distribution of the grid points according to equation (3.103). The additional domains in case of $h_{TE} = 5.4$ are discretized with an equidistant spacing in y -direction. The domains above and below the splitter plate each contain 650 and 425 grid points in streamwise and normal direction, respectively. The additional

¹Thanks to Vitor Kleine [51] for performing the simulation with thick splitter plate.

domains behind the thick trailing edge are discretized with 35 grid points in y -direction.

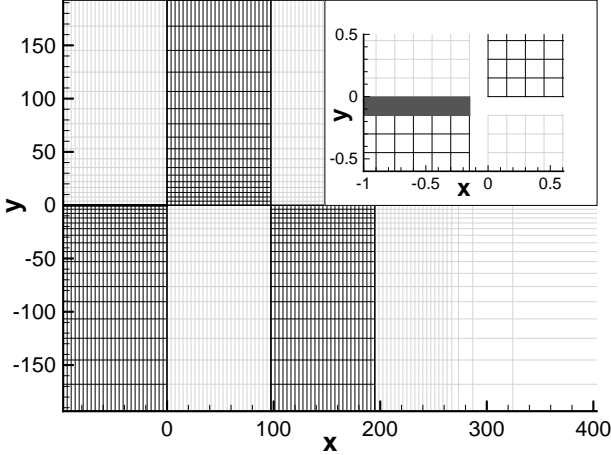


Figure 5.1: Grid for the thin splitter plate showing every 25th gridline. The domain decomposition is indicated by black and grey lines. The detailed view illustrates the trailing edge of the splitter plate (every gridline).

The flow field is made of two boundary layers above and below the splitter plate which represents the nozzle end. The fast stream with $Ma_I = 0.8$ is placed on top and the slow-speed stream with $Ma_{II} = 0.2$ underneath the flat plate. With both streams having the same free-stream temperature $\tilde{T}_\infty = 280K$, the velocity ratio is $u_{II}/u_I = 4$. Since thermal conduction inside the splitter plate is not included in the simulation, the temperature of the wall is fixed to $\tilde{T}_w = 296K$. This value has been selected since it is the mean value of the adiabatic wall temperatures of the two streams. The Reynolds number $Re = \rho_\infty u_I \delta_{1,I} / \mu_\infty = 1000$ is based on the displacement thickness [87]

$$\delta_1 = \int_0^{\delta_{99}} \left(1 - \frac{\rho u}{\rho_\infty u_\infty} \right) dy \quad (5.1)$$

of the upper stream at the inflow $x_0 = -97.5$. With $\delta_{1,I}(x_0) = 1$, length scales are normalized with the displacement thickness of the fast stream at the inflow. The boundary layer of the lower stream corresponds to the same origin of the

flat plate. The profiles of the streamwise velocity at the inflow are shown in figure 5.2 a). Behind the trailing edge, a combination of wake and mixing layer occurs. As one can see in figure 5.2 b), the flow field keeps its wake-like shape for a long range. With high amplifications due to the inflection points in the velocity profile, the flow is already unsteady before a pure mixing layer can develop.

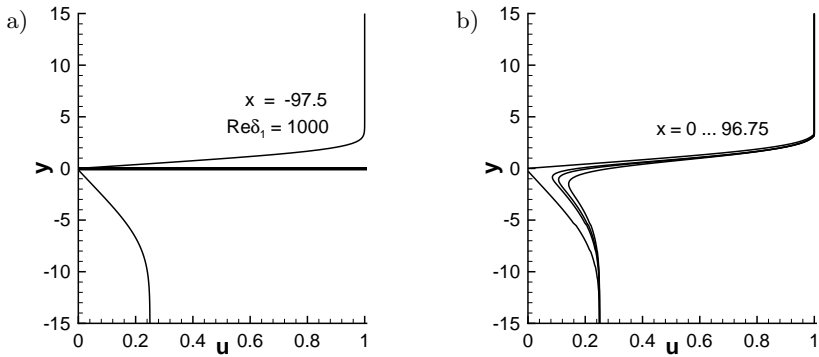


Figure 5.2: Streamwise velocity profiles of the baseflow:

- a) upper and lower boundary layer at the inflow $x = -97.5$
- b) combination of wake and mixing layer behind the thin splitter plate with $h_{TE} = 0.15$ (case 5A).

Due to separation behind the trailing edge, it is not possible to derive a baseflow from the boundary-layer equations in case of the thick splitter plate. Thus, a time-averaged solution is given in figure 5.3 b) to estimate the properties of the flow. Behind the end of the splitter plate, a separation zone with $u < 0$ exists. It is located past the upper half of the flat plate and ranges up to $x \approx 27$. In the lower part of the separation, the streamwise velocity adapts rapidly to the lower freestream velocity. This leads to an S-shaped velocity profile much earlier, compared to figure 5.2 b). However, the flow field is already unsteady there as shown in figure 5.7 b).

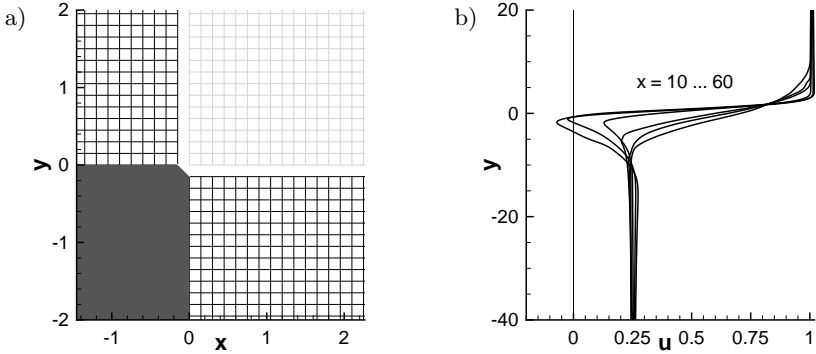


Figure 5.3: a) Detailed view of the mesh at the trailing edge with $h_{TE} = 5.4$.
 b) Streamwise velocity profiles of the baseflow behind the thick splitter plate (time-averaged-solution of 5B).

5.2 Linear Stability Analysis

The spatial stability diagram of the upper boundary layer is given in figure 5.4 a). The maximum amplification $\alpha_i = -0.004$ of two-dimensional waves is relatively independent of the streamwise position. Accordingly, the fundamental frequency for disturbance generation is chosen to $\omega_0 = 0.0688$. For the thin splitter plate, the amplification rates behind the splitter plate are shown in figure 5.4 b). Due to the inflection points in the velocity profile, high amplification rates occur. With values of up to $\alpha_i = -0.267$, the exponential growth of disturbances is approximately 60 times stronger behind the trailing edge, compared to the upper boundary layer. The highest amplification is achieved for frequencies which are 3 to 3.5 the value of the fundamental frequency ω_0 .

In case of the splitter plate with thickness $h_{TE} = 5.4$ two amplified eigenvalues exist shortly behind the trailing edge. This is shown in figure 5.5 a), where the temporal spectrum is given for $\alpha = 0.2$, $\gamma = 0$. As for the pure mixing layer, two continuous spectra exist. With phase speeds of $c_{ph} = 1.0$ and $c_{ph} = 0.25$, these eigenvalues are fluctuations in the upper and lower freestream, respectively. The most amplified eigenvalue is located between both continuous spectra. The eigenvalue of the second unstable mode with $\omega_r = 0.0133$ is only weakly amplified.

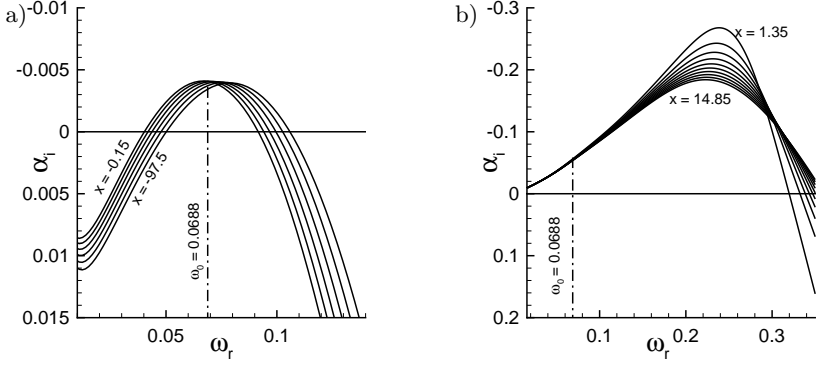


Figure 5.4: Spatial amplification rates for two-dimensional disturbances:
 a) upper boundary layer ($x < 0$), b) mixing wake behind the thin splitter plate ($h_{TE} = 0.15$)

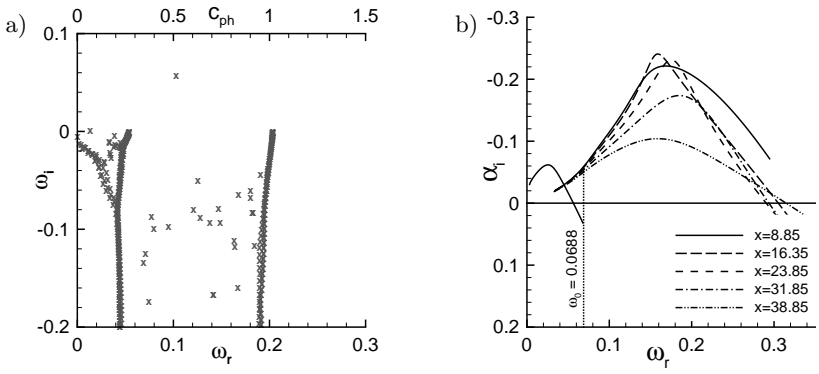


Figure 5.5: a) Temporal spectrum behind the thick trailing edge ($h_{TE} = 5.4$). Spanwise wave number $\alpha_r = 0.2$, position $x = 16.35$.
 b) Spatial amplification rates of two-dimensional waves ($\gamma = 0$) past the splitter plate with $h_{TE} = 5.4$.

The corresponding temporal eigenfunctions in figure 5.6 reveal the physical meaning of both solutions. For comparison, the eigenfunctions are normalized such that the maximum amplitude of u is one. With its maximum amplitudes located at $y = 0$, the most amplified eigenvalue $\omega_r = 0.1027$, $\omega_i = 0.0574$ corresponds to the Kelvin-Helmholtz instability of the upper mixing layer. For the velocity components and the pressure, its amplitude distribution is quite similar to the one of the pure mixing layer of figure 4.5. As the eigenfunction of the second amplified eigenvalue has its maximum amplitude for negative values of y , it is an additional wake mode as found by Zhuang & Dimotakis [110]. Accordingly, the peaks of the amplitudes cover a wider range in normal direction.

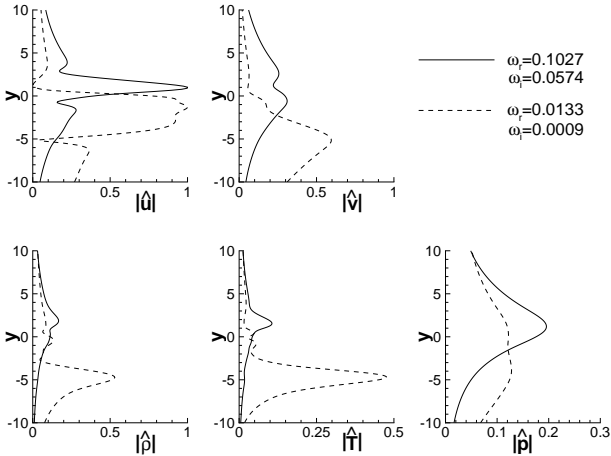


Figure 5.6: Temporal amplitude distributions for $\alpha_r = 0.2$ at streamwise position $x = 16.35$. The solid and dashed lines correspond to the two amplified eigenvalues in figure 5.5 a).

The spatial amplification rates past the thick splitter plate are given in figure 5.5 b) for both amplified solutions. Because the lower mixing layer is dissipated rapidly, relevant amplification due to the second eigenvalue is only given directly behind the trailing edge. The largest amplification is $\alpha_i = -0.06$ for the first subharmonic of the fundamental frequency. Growth of disturbances is mainly dominated by the upper mixing layer at $y = 0$. Compared to the thin splitter plate, maximum amplification is found for lower frequencies.

5.3 Simulation Results

As for the baseflow an isothermal boundary condition with pressure extrapolation is used at the wall. The subsonic inflow is used along the complete left boundary of the domain. Additionally, the upper boundary layer is forced with the eigenfunction of its two-dimensional TS-wave with frequency $\omega_0 = 0.0688$. The maximum amplitude of the streamwise-velocity fluctuation is $|\hat{u}| = 0.005$. The characteristic freestream BC is used on the upper and lower boundaries. The buffer zone in front of the outflow boundary contains the last 370 grid points along which the solution is filtered every 5th time step. With a time step of $\Delta t = 0.02283$, the fundamental period is resolved with 4000 time steps. The analysis is based on 16 periods of the fundamental frequency. Furthermore the acoustic emission is analyzed along 64 periods of ω_0 . See table 5.1 for a summary of the simulation parameters.

case	5A	5B
splitter-plate thickness h_{TE}	0.15	5.4
total number of grid points	2210000	2278250
computed time steps	556000	488000
Δx	0.15 - 14.738	
Δy	0.15 - 1.062	
fund. frequency ω_0	0.0688	
time step Δt	0.02283	
periods of ω_0 for analysis	16/64	
subsonic inflow:	$ \hat{u} _{max}$	$\Delta\Theta$
(1, 0)	$5 \cdot 10^{-3}$	0
characteristic freestream:		
damping parameter d	0.01	
grid points in damping zone	40	
subsonic outflow:		
beginning of filtering (x -position)	250	
filtering sequence (time steps)	5	
ramping of filter (grid points)	5	

Table 5.1: Parameters of the simulation of the mixing layer past a splitter plate. $Ma_I = 0.8$, $Ma_{II} = 0.2$, $Re = 1000$.

Figure 5.7 shows a snapshot of the spanwise vorticity Ω_z for splitter-plate thicknesses $h_{TE} = 0.15$ and $h_{TE} = 5.4$. In both cases the mixing layer rolls up with subsequent vortex pairing. The strength of Ω_z is apparently the same. In case of the small thickness $h_{TE} = 0.15$, rollup occurs at $x \approx 60$ and further

downstream ($x \approx 150$) two out of three vortices pair. The resulting vortex merges with the remaining third eddy at $x \approx 220$. Thereby it is almost random whether the single eddy pairs with the precedent or subsequent bigger vortex. In case of a thick splitter plate ($h_{TE} = 5.4$), a small separation zone exists behind the splitter plate. The dominant mixing layer originates from the edge of the fast stream and its roll up occurs earlier compared to case 5A. The dominant vortex pairing is located in the range of $150 < x < 200$. Additionally, single vortices can be observed which are generated randomly in the initial mixing layer. If these are generated pairwise, they merge at $x \approx 100$. A single vortex is absorbed by a large vortex further downstream ($x \approx 200$).

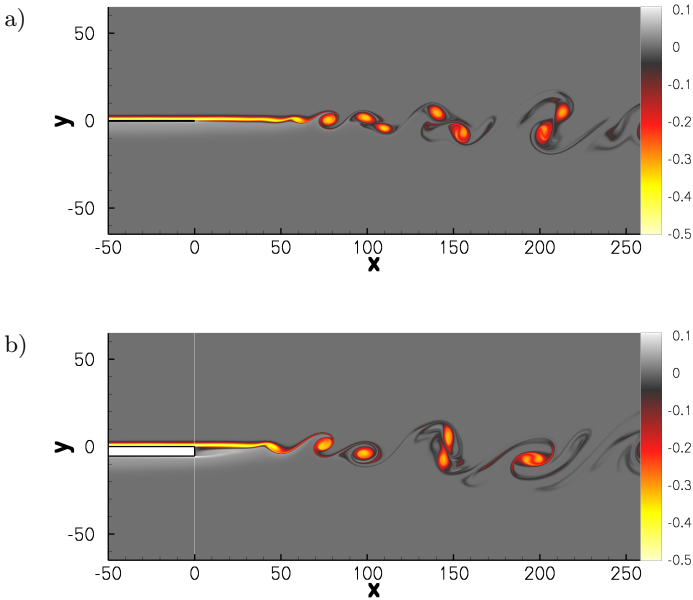


Figure 5.7: Spanwise vorticity Ω_z for different thicknesses of the trailing edge: a) case 5A with $h_{TE} = 0.15$, b) case 5B with $h_{TE} = 5.4$.

In the upper boundary layer, the TS wave grows independently of the thickness of the splitter plate. As shown in figures 5.8 a) and b), the mean growth rates of mode $(1,0)$ agree with the ones from linear stability theory. Near the trailing edge, a wave-like variation of α_i is visible. Its wavelength slightly decreases from $\lambda_x \approx 20$ in the middle of the splitter plate to $\lambda_x \approx 18.8$ near the trailing

edge. Its phase speeds are $|c_{ph}| = 0.22$ and $|c_{ph}| = 0.21$ which correspond to the upstream traveling acoustic wave with $c_{ph} = 1 - 1/Ma_I = -0.25$. Thus, the variation of α_i is caused by the noise generation of the mixing layer and is not due to the non-parallel flow field at the end of the splitter plate. Accordingly it is more visible for u than for v , given in [8]. For smaller values of x , shading of the flat plate successively reduces the upstream propagating sound to $\varphi = 180^\circ$. Hence, the variation of α_i is reduced and the wavelength increases in upstream direction. The same effect occurs for the first higher harmonic.

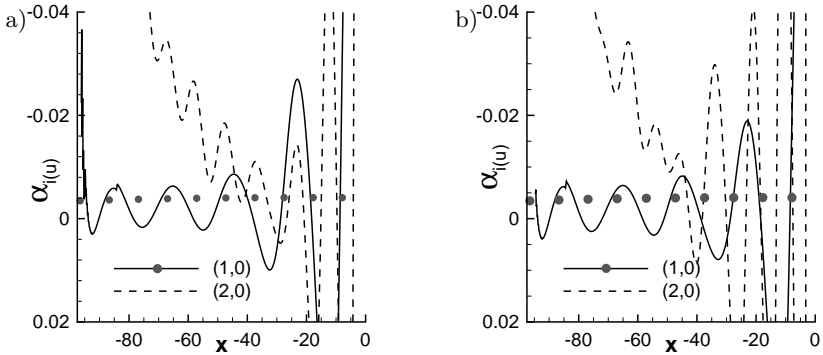


Figure 5.8: Spatial amplification rates in the upper boundary layer compared with LST (symbols): a) $h_{TE} = 0.15$, b) $h_{TE} = 5.4$.

Figure 5.9 a) shows the maximum amplitude of the streamwise velocity for case 5A. For $x < 0$, the data corresponds to the upper boundary layer; positive streamwise coordinates denote the mixing layer behind the splitter plate. Non-linear interaction of the TS wave generates higher harmonics in the upper boundary layer, where modes (2,0) and (3,0) reach a level of $|\hat{u}| = 5 \cdot 10^{-4}$ and $|\hat{u}| = 2 \cdot 10^{-5}$, respectively. Past the trailing edge, these modes are more amplified than the fundamental disturbance. As illustrated in figure 5.9 b), the initial growth of (1,0) and its higher harmonics is a linear mechanism. Except for the early stages of the mixing layer, amplification rates are in good agreement with LST. The higher harmonics (2,0) and (3,0) saturate at $x = 60$. There, the initial exponential growth of (1,0) is reduced before it grows again. The fundamental disturbance saturates at $x \approx 130$. In contrast to the pure mixing layer, the flow field is only quasi-deterministic. This appears as subharmonics in figure 5.9 a) which can not be generated non-linearly as it is the case for higher harmonics. With a simulated time of 139 periods of ω_0 (this

corresponds to 36 flow-through times), influences of the initial condition can be excluded. Hence, a feedback mechanism exists: upstream running acoustic waves which are emitted by the mixing layer impinge on the trailing edge and generate new instability waves there.

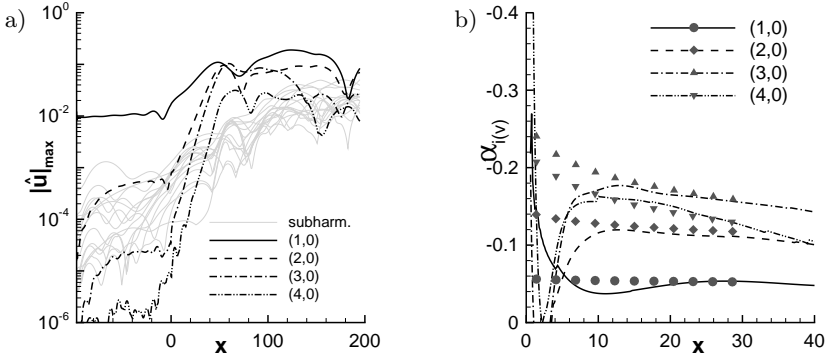


Figure 5.9: a) Maximum amplitude of the streamwise velocity u for the thin plate ($h_{TE} = 0.15$).

b) Spatial amplification rates behind the thin splitter plate. Results from LST are indicated by symbols.

In case 5B, the first higher harmonic saturates earlier at $x = 42$ as shown by figure 5.10 a). This is due to an increased growth rate in the mixing layer. Its spatial amplification rate in figure 5.10 b) shows good agreement with linear stability theory which is based on the time-averaged flow-field. The mean amplification of the fundamental disturbance is not affected by the thicker splitter plate. Directly behind the trailing edge, the amplitudes of disturbances (3,0), (4,0) and of the subharmonics are almost constant. With a level of $|\hat{u}| \approx 2 \cdot 10^{-4}$ the higher harmonics are of the same magnitude as the emitted sound (see figure 5.11). Besides these acoustic disturbances, low-frequency fluctuations exist within the separation bubble which are larger by one order of magnitude. According to the larger subharmonic fluctuations, the flow field shows a more random-like behavior compared to case 5A. From $x \approx 20$ onwards, the growth of the respective instability waves prevails.

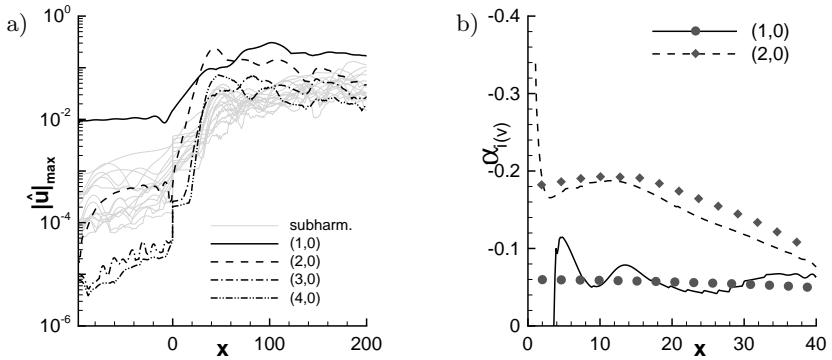


Figure 5.10: a) Maximum amplitude of the streamwise velocity u for the thick plate ($h_{TE} = 5.4$).
 b) Spatial amplification rates behind the flat plate (case 5B). Symbols denote results from LST.

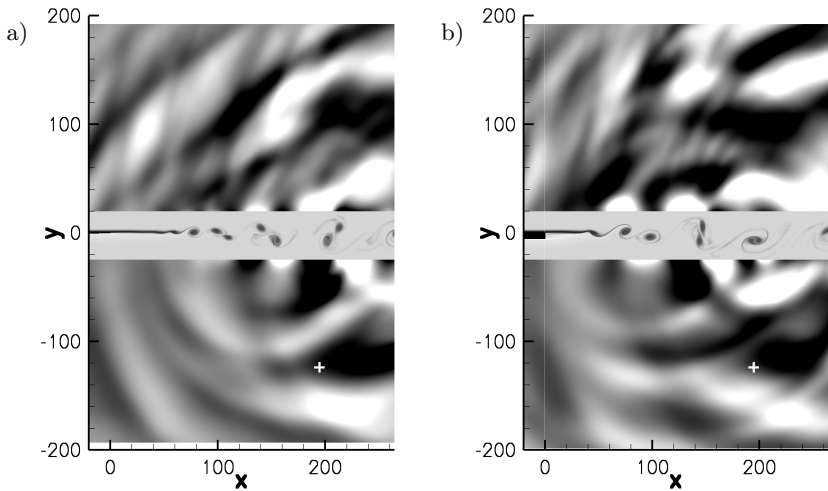


Figure 5.11: Snapshot of the emitted sound visualized by the dilatation $\nabla \mathbf{u}$ in the range of $\pm 3 \cdot 10^{-4}$. The position of the virtual microphone is indicated by a white cross: a) $h_{TE} = 0.15$ b) $h_{TE} = 5.4$.

A snapshot of the dilatation field is given for both cases in figures 5.11 a) and b). The emitted sound shows to be of the same magnitude. For the thin trailing edge, two acoustic sources can be detected. The first one is located at $x \approx 150$ which matches the position of the first vortex pairing. The main origin of sound can be found at the second position of vortex pairing ($x \approx 220$). Although the main emission is directed downstream, notable acoustic waves travel in upstream direction as well. In case of the thicker splitter plate ($h_{TE} = 5.4$), both acoustic sources are shifted slightly upstream to $x \approx 100$ and $x \approx 200$. Apart from an additional source at $x \approx 100$ in case 5B, both acoustic fields look similar.

For a more quantitative evaluation of the generated sound, a virtual microphone is placed at $(x = 195, y = -121.8)$. At this position, indicated by a white cross in figures 5.11 a) and b), a detailed time record is taken along 64 periods of the fundamental frequency. The temporal Fourier-analysis is given in figures 5.12 and 5.13 for the thin and thick splitter plate, respectively.

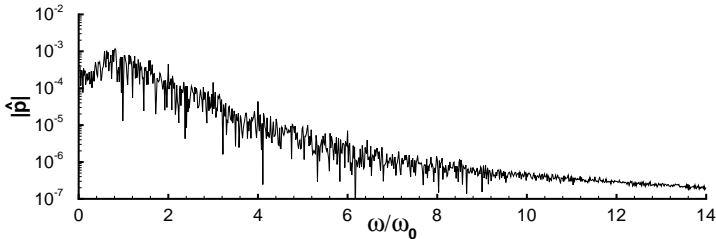


Figure 5.12: Spectrum of the pressure fluctuations at the virtual microphone ($x = 195, y = -121.8$) for the thin splitter plate of case 5A.

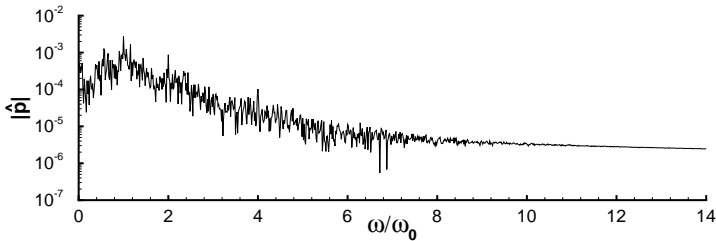


Figure 5.13: Same as figure 5.12 but for case 5B with $h_{TE} = 5.4$.

The main sound emission is in the frequency range up to $2 \cdot \omega_0$ for both cases. In case 5A, the amplitude decays, showing peaks for the first three higher harmonics. For the thick splitter plate, the fundamental frequency is more dominant with additional peaks of the first and third higher harmonic. The amplitude decay for higher frequencies is weaker compared to the thin splitter plate. From $\omega/\omega_0 = 8$ onwards, the spectrum is nearly constant with $|\hat{p}| \approx 10^{-6}$. The overall sound level is considered in terms of the rms-value of the pressure fluctuation:

$$p'_{rms} = \sqrt{\frac{1}{N} \sum_{j=j_1}^{j_2} (p - \bar{p})^2}, \quad (5.2)$$

computed along the considered time interval $[(j_2 - j_1) \cdot \Delta t] = 2\pi/(64 \cdot \omega_0)$. At the location of the microphone, it is $p'_{rms} = 0.0035$ and $p'_{rms} = 0.0042$ for cases 5A and 5B, respectively. Thus, the thicker trailing edge increases the sound pressure level by 1.5 dB, according to equation (1.1). Despite some minor differences, the fundamental mechanism of sound generation is apparently the same for both cases. Hence, the thin trailing edge is a reasonable assumption up to moderate values of h_{TE} and computational difficulties of the thicker splitter plate as described in appendix C.3 are avoided.

6 Serrated Trailing Edge

A passive means to influence the flow and the emitted sound is the adaptation of the geometry at the trailing edge. Although this is already applied to jets (figure 1.6), the underlying mechanisms are not well understood. In this context, two different shapes of the trailing edge are studied and compared with a reference solution. The parameters of the baseflow correspond to those from case 5A as is the case for the mesh in x - and y -direction. Apart from some varied parameters, the boundary conditions are the same as well. In addition to the two-dimensional TS-wave, an oblique disturbance is introduced in the upper boundary layer for a more realistic disturbance spectrum. With a spanwise wavenumber of $\gamma_0 = 0.2$, the oblique mode $(1, \pm 1)$ has a wave angle of 45° with respect to the streamwise direction. Accordingly, notable effects of the serrations are expected for one notch per $\lambda_{z,0}$. The reference case 6A is made of a straight trailing edge, ending at $x = 0$. The first modification of the geometry is a rectangular notch denoted as case 6B. As shown in figure 6.1 a), it covers half the spanwise extent of the domain. The influence of a non-symmetric geometry is investigated by the trailing edge of case 6C, sketched in figure 6.1 b). The depth of both serrations ranges back to $x = -10$.

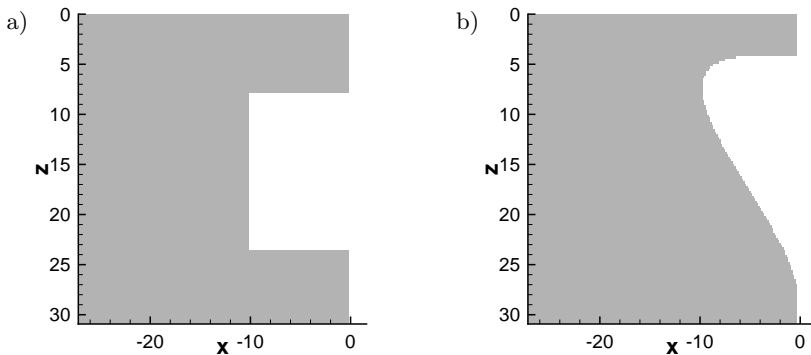


Figure 6.1: Top view on the two different engrailments of the trailing edge:
a) rectangular notch (case 6B),
b) curved non-symmetric shape (case 6C).

Due to the small amplitude of the oblique forcing, three-dimensional effects are expected to play a minor role in case 6A. Hence, a coarser resolution in z -direction of 10 modes is used, here. For the three-dimensional geometries, the spanwise direction is resolved with 42 modes which corresponds to $\Delta z = 0.245$. In physical space, the spanwise direction is resolved with 65 and 128 points for the symmetric case 6B and the non-symmetric case 6C, respectively. A total number of 105000 time steps, equivalent to 21 periods of the TS-wave, have been computed. Due to the simulated time and the huge amount of data, analysis is limited to eight periods of ω_0 . A detailed set of simulation parameters is given in table 6.1. With up to 283 million grid points, the computational effort strongly increases compared to chapter 5. Hence, the domain is decomposed into 16 subdomains (8 in streamwise and 2 in normal direction), allowing the usage of 128 processors.

case	6A	6B	6C
serration	none	rect.	aslope
total number of grid points	$37.6 \cdot 10^6$	$143 \cdot 10^6$	$283 \cdot 10^6$
number of spanwise modes	10	42	42
spanwise symmetry	yes	yes	no
Δx	0.15 - 14.738		
Δy	0.15 - 1.062		
Δz	0.9817	0.245	
fund. spanwise wave number γ_0	0.2		
fund. frequency ω_0	0.0688		
time step Δt	0.01826		
computed time steps	105000		
periods of ω_0 for analysis	8		
subsonic inflow:	$ \hat{u} _{max}$	$\Delta\Theta$	
(1, 0)	$5 \cdot 10^{-3}$	0.0	
(1, ± 1)	$5 \cdot 10^{-4}$	0.0	
characteristic freestream:			
damping parameter d	0.04		
grid points in damping zone	20		
subsonic outflow:			
beginning of filtering (x -position)	250		
filtering sequence (time steps)	20		
ramping of filter (grid points)	20		

Table 6.1: Simulation parameters for the investigation of different trailing edges ($Ma_I = 0.8$, $Ma_{II} = 0.2$, $Re = 1000$).

6.1 Reference Case

The reference case 6A is only slightly determined by three-dimensional effects as shown by the isosurface $\Lambda_2 = -0.005$ in figure 6.1. Up to $x = 100$, the spanwise Kelvin-Helmholtz vortices dominate the flow field. The following vortex pairing shows the first notable variation in z -direction. While the merged vortex at $x \approx 180$ is mainly two-dimensional, a stronger spanwise modulation of its small counterpart can be observed. The final vortex is again mainly two-dimensional. Hence, the minor spanwise resolution with 10 modes is justified for the reference case.

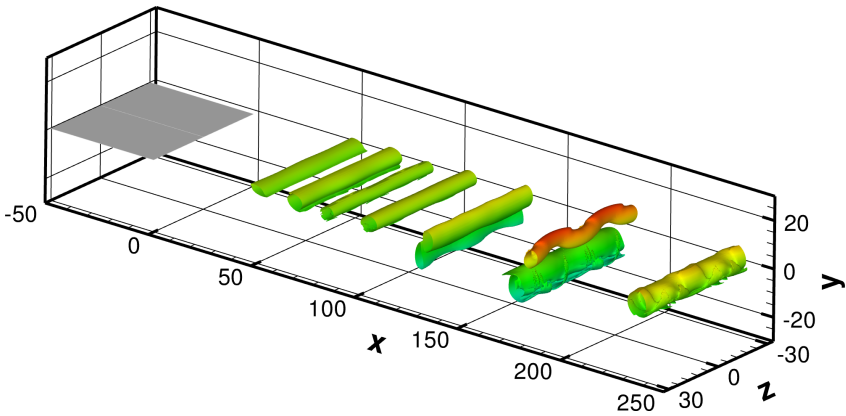


Figure 6.2: Instantaneous view of the vortical structures after 21 periods of the fundamental frequency, visualized by the isosurface $\Lambda_2 = -0.005$ along two spanwise wavelengths. The normal coordinate is colored from blue to red.

The maximum amplitudes of the normal velocity v are given in figure 6.3 a). In the upper boundary layer ($x < 0$), disturbances behave as in the corresponding two-dimensional case of chapter 5. According to the introduced disturbances, oblique modes are smaller than their 2-d counterparts by one order of magnitude. Behind the trailing edge, the disturbances grow according to linear stability theory as shown in figure 6.3 b). Having a two-dimensional baseflow, oblique waves are less amplified than those with $\gamma = 0$. Due to its high amplification, mode $(3, 0)$ saturates first at $x = 80$. From this point onwards, the growth of the oblique modes is interrupted. In this region, the phase speeds

of modes (1,0) and (2,0) are not able to adapt to the locally dominant disturbance (3,0). Hence, its growth can be observed as the dominant disturbance decays. A bit downstream the fundamental disturbance exceeds the amplitude of (3,0) and saturates at $x \approx 200$. Subharmonics grow rapidly behind the saturation of mode (3,0) reaching a level of up to 15%.

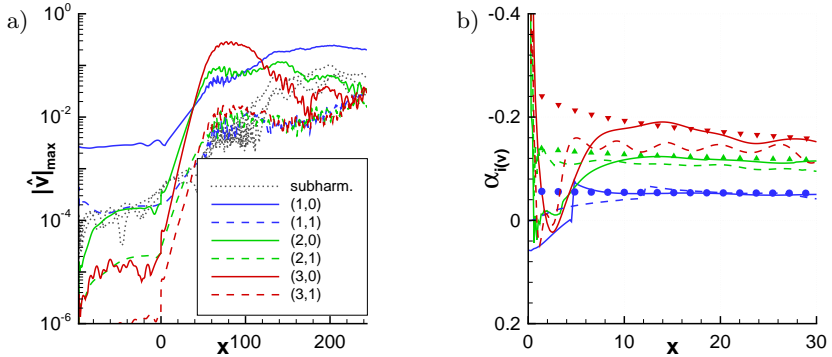


Figure 6.3: a) Maximum amplitude of the normal velocity component.
 b) Spatial amplification rates behind the straight trailing edge. Results from LST for $\gamma = 0$ are marked with symbols.

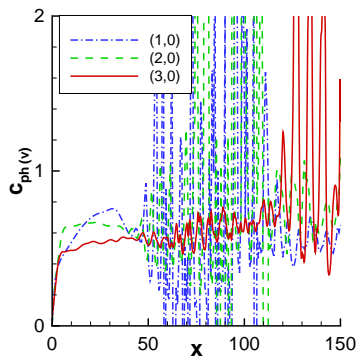


Figure 6.4: Phase velocities of two-dimensional disturbances, computed from the normal velocity v .

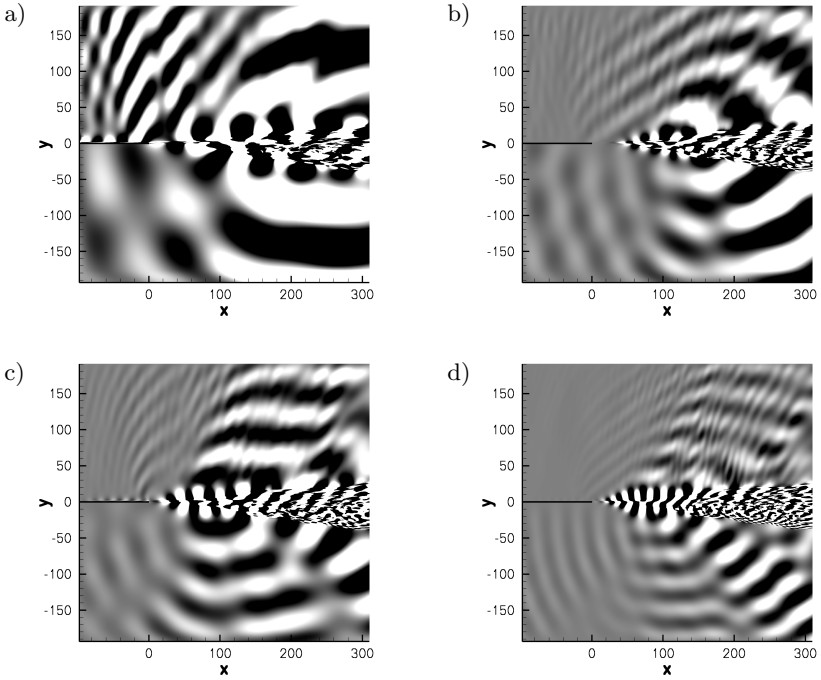


Figure 6.5: Real part of the Fourier-transformed dilatation field for the straight trailing edge at $z = 0$. Contour levels are in the range of $\nabla \mathbf{u} = \pm 3 \cdot 10^{-3}$: a) ω_0 , b) $7/4 \cdot \omega_0$, c) $2 \cdot \omega_0$, d) $3 \cdot \omega_0$

The spectral decomposition of the acoustic field is visualized by the real part of the Fourier-transformed dilatation field at the symmetry plane $z = 0$. This is shown in figure 6.5 a) - d) for the fundamental frequency, the undisturbed frequency $7/4 \cdot \omega_0$ and the first two higher harmonics, respectively. The acoustic emission is dominated by the frequency of the TS-wave. Upstream propagating sound with frequency ω_0 is generated at $x = 60$, where mode $(1, 0)$ tries to adapt to the phase speed of the dominating disturbance $(3, 0)$. Yet the major source is located at $x \approx 200$. Its directivity ranges from $\varphi \approx -110^\circ$ in the lower half to $\varphi \approx 100^\circ$ in the upper half of the domain. This region is also the source of sound with other frequencies as shown exemplarily for $7/4 \cdot \omega_0$ in figure 6.5 b). The emission of noise with frequencies of the first two higher harmonics originates from $x = 100$. Despite the second higher harmonic is the

first disturbance which saturates, its emission is relatively weak, compared to figures 6.5 a) - c).

6.2 Rectangular Serration

An instantaneous view of the flow field and the square-notched splitter plate is given in figure 6.6, showing the isosurface $\Lambda_2 = -0.005$ along two spanwise periods. At $x \approx 50$, a spanwise modulation of the Kelvin-Helmholtz vortices is visible. This croissant-shaped deformation is due to the earlier beginning of the mixing layer inside the notch. The strong spanwise gradients lead to streamwise vortices which are twisted around their spanwise counterparts. This can be seen in more detail in the top view of figure 6.7. Longitudinal vortices approach in spanwise direction while moving on top of the subsequent Kelvin-Helmholtz vortex. Thereby the position of the spanwise vortex alters along z . This is similar to the experimental results of Kit et al. [50] who found a spanwise modulation of vortex-strength (bulging) and -position (bending) of Kelvin-Helmholtz vortices. Further downstream, the interaction of streamwise and spanwise vortices leads to an early breakdown of the large-scale coherent structures. From $x \approx 130$ onwards, only small eddies are visible. Yet these are still accumulated in groups with a distance roughly corresponding to the Kelvin-Helmholtz vortices of the reference case. At $x \approx 200$, streamwise vortices are almost uniformly distributed along the spanwise direction. Longitudinal vortex tubes are also subject to instabilities as indicated by corkscrew vortices, e.g. at $x \approx 180$.

A spectral decomposition is shown in figures 6.8 a) and b), based on the maximum amplitude of the normal velocity along y . In the upper boundary layer ($x < 0$), the mean growth of the Tollmien-Schlichting wave is in good agreement with linear stability theory (figure 6.8 a)). Its non-linear interaction with $(1, 1)$ generates the steady mode $(0, 1)$ up to an amplitude of $|\hat{v}| = 2 \cdot 10^{-5}$. From $x = -25$ onwards, this is exceeded by the upstream effect of the engrailment. The serrated trailing edge ($-10 \leq x \leq 0$) generates steady spanwise disturbances $(0, k)$ up to $|\hat{v}| = 8 \cdot 10^{-3}$. In the notch, the combination of wake and mixing layer originates further upstream, which corresponds to the steady spanwise mode $(0, 1)$. Its amplitude decreases behind the trailing edge up to $x = 15$. Higher harmonics in spanwise direction $(0, 2)$ and $(0, 4)$ are generated at the notch as well, staying almost constant behind the splitter plate.

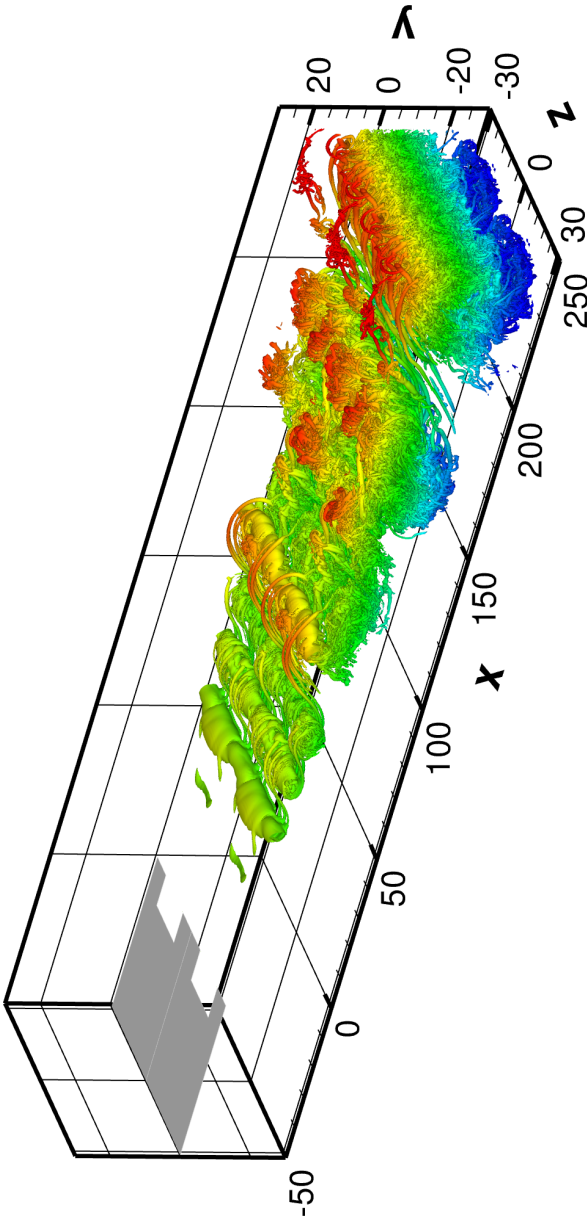


Figure 6.6: Perspective view of the engrailed trailing edge and the vortical structures at $t = 1917.8$, visualised by the isosurface $\Lambda_2 = -0.005$ along two spanwise periods. The colour denotes the wall-normal coordinate to increase the contrast.

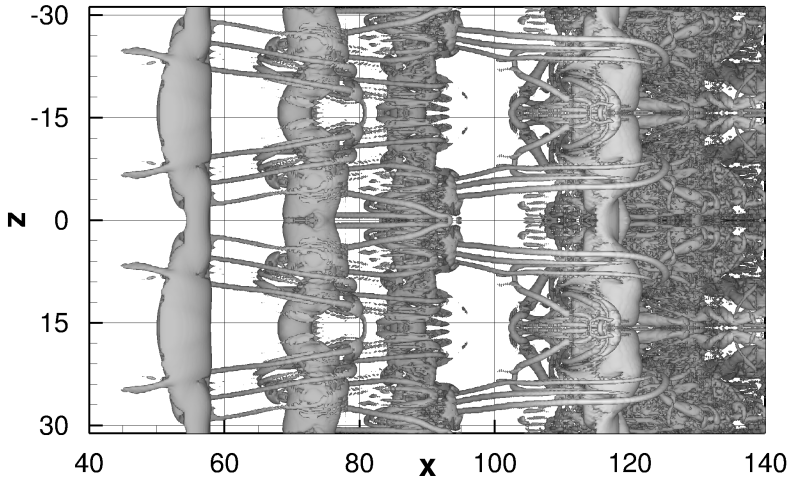


Figure 6.7: Top view on the mixing layer downstream of the square-notched trailing edge (detailed view of figure 6.6).

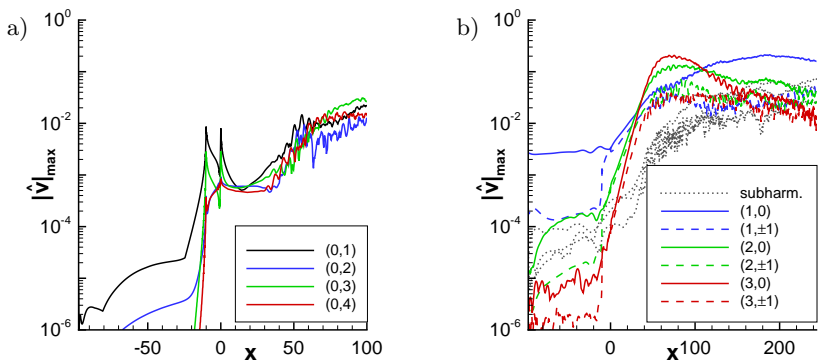


Figure 6.8: Maximum amplitude of the normal velocity component:
 a) steady modes $(0, k)$, b) unsteady modes (h, k)

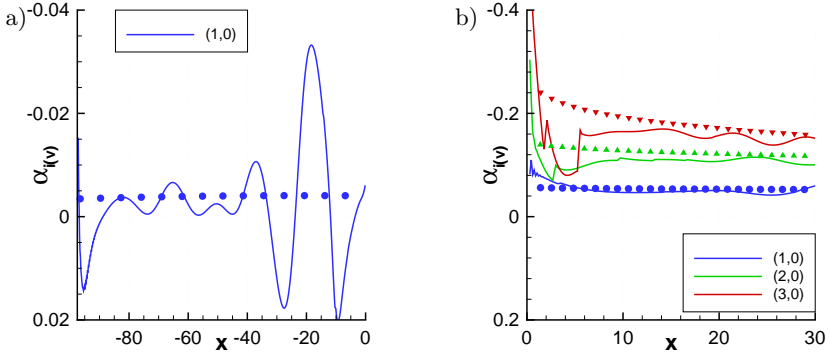


Figure 6.9: Spatial amplification rates compared with linear stability theory (symbols):
 a) upper boundary layer, b) behind the splitter plate

In the upper boundary layer, higher harmonics of the fundamental frequency are generated. With an amplitude of the driving TS-wave of $|\hat{v}| = 2 \cdot 10^{-3}$, modes $(2, 0)$, $(3, 0)$ reach amplitudes of $|\hat{v}| = 3 \cdot 10^{-4}$ and $|\hat{v}| = 2 \cdot 10^{-3}$, respectively. At the trailing edge, steady modes due to the serration interact with the two-dimensional waves, generating unsteady oblique modes $(h, 1)$. Unlike the stability results of Gudmundsson and Colonius [38] for high-Reynolds-number jets, amplification rates behind the trailing edge are only weakly affected by the modified geometry, here. As shown in figure 6.9 b), the growth of high-frequency, two-dimensional waves is only slightly reduced. Hence, the strongest growth is found again for mode $(3, 0)$ which saturates at $x \approx 70$. Despite having a slightly reduced amplification, its growth already starts inside the notch and thus, it saturates earlier compared to the simulation 6A. As in the reference case, the growth of the fundamental disturbance continues after the decay of $(3, 0)$ and reaches its maximum at $x \approx 200$. Oblique modes grow up to an amplitude of some 5%. Having a relevant amplitude now, oblique fluctuations affect the growth of two-dimensional subharmonics. They are reduced by a factor of roughly 3 compared to the reference case.

Figure 6.10 a) - d) shows the acoustic field for the same frequencies as in the reference case. The most significant difference is visible for the fundamental frequency where the dominant sound source at $x \approx 200$ is removed. This is also the case for the undisturbed frequency $7/4 \cdot \omega_0$ and the first higher harmonic whose acoustic emissions are reduced especially in the lower half of the domain.

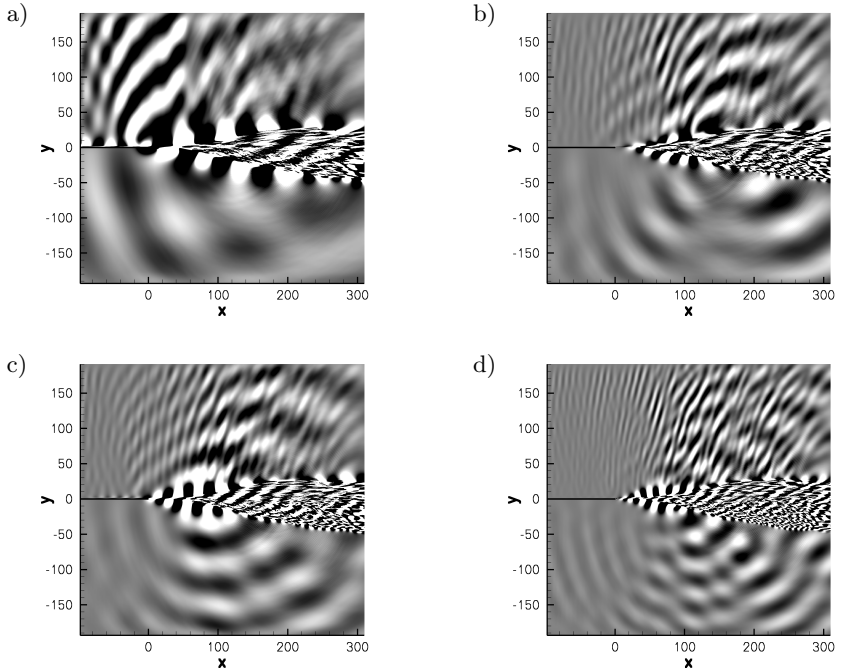


Figure 6.10: Real part of the Fourier-transformed dilatation field at the symmetry plane $z = 0$ for the rectangular engrailment (contour levels as in figure 6.5):
 a) ω_0 , b) $7/4 \cdot \omega_0$, c) $2 \cdot \omega_0$, d) $3 \cdot \omega_0$

For frequency $3 \cdot \omega_0$, a minor drop of the generated sound can be observed. The upstream-directed sound emission with frequency ω_0 ($x \approx 70$) is not affected by the serration since resonance of mode $(1, 0)$ is inhibited there as well. Despite the strong modification of the acoustic field, the position of the sources is not changed compared to the reference solution of case 6A.

6.3 Non-symmetric Serration

For the non-symmetric trailing edge, the vortical structures after 21 periods of the TS-wave are illustrated in figure 6.11 and 6.12.

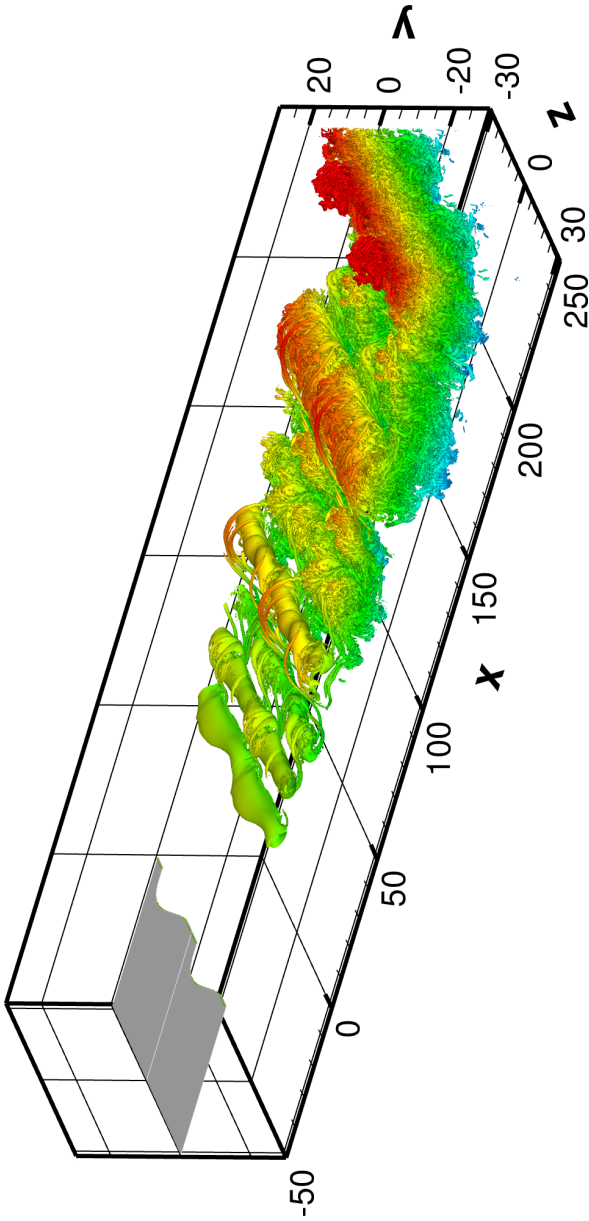


Figure 6.11: Perspective view of the vortices behind the non-symmetrically serrated trailing edge after 21 periods of ω_0 , visualization as in figure 6.6: isosurface $\Lambda_2 = -0.005$, color denotes normal coordinate.

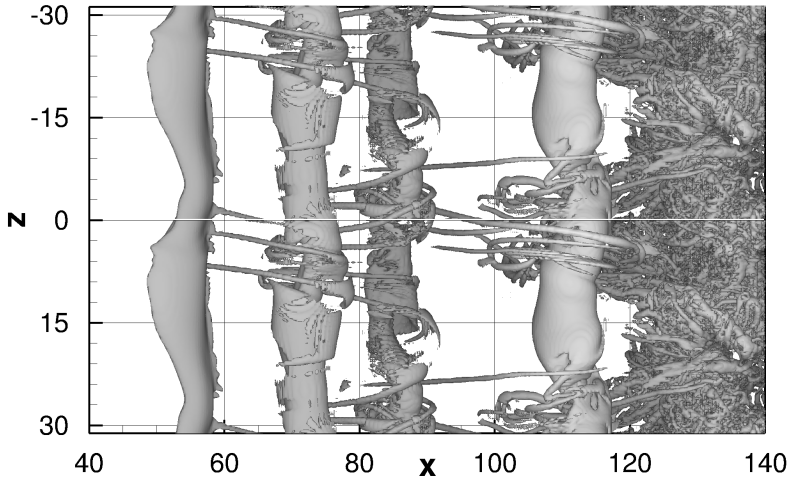


Figure 6.12: Top view on the mixing layer downstream of the non-symmetric serrated splitter plate (detailed view of figure 6.11).

Similar to the case 6B, the initial Kelvin-Helmholtz vortex at $x = 55$ is modulated along the spanwise direction. Yet this is no more symmetric. The strongest gradients occur behind the sharp edge, generating streamwise vortices which are directed towards the center of the notch (figure 6.12). The bending of the subsequent spanwise vortex at $x = 75$ is less intense than in the symmetric case. Despite less streamwise vortex tubes exist up to $x = 120$, a breakdown to small-scale structures occurs for $x > 125$. As shown in figure 6.11, streamwise vortices are already distributed equally along the span at $x \approx 170$. Since corkscrew vortices are not visible, longitudinal vortices seem to be less affected by additional instabilities. This might be due to their closer alignment to the accumulations of small-scale structures. Compared to the result for the symmetric serration, a more homogeneous distribution is visible at the end of the domain.

The non-symmetric serration generates steady disturbances $(0, k)$, shown in figure 6.13 a). With sustained amplitudes of up to $|\hat{v}| = 3 \cdot 10^{-3}$ inside the notch, it is more effective in generating a spanwise deformation. Similar to the symmetric case, its upstream effect is weak.

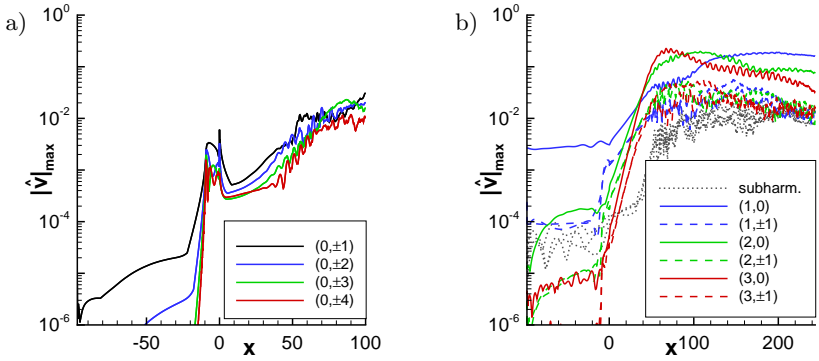


Figure 6.13: Maximum amplitudes of the normal velocity component:
 a) steady modes $(0, k)$, b) unsteady modes (h, k)

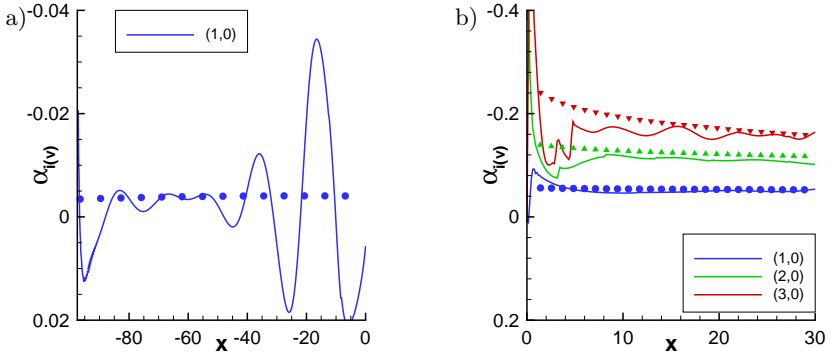


Figure 6.14: Spatial amplification rates compared with linear stability theory (symbols):
 a) upper boundary layer, b) behind the splitter plate

As shown in figure 6.13 b), the disturbance spectrum in the upper boundary layer is similar to the previous cases: the TS-wave grows according to linear stability theory (figure 6.14 a)), generating higher harmonics. At the trailing edge, oblique waves are generated by the interaction of two-dimensional instabilities with steady disturbances $(0, k)$. Keep in mind that amplitudes for left-

and right-running waves $((h, +k)$ and $(h, -k)$) are regarded separately in the non-symmetric simulation. Since figure 6.14 b) shows similar results as for the symmetric serration, the shape of the serration does not affect the linear growth of two-dimensional disturbances. Hence, mode $(3, 0)$ saturates at $x \approx 70$ like in case B. Three-dimensional disturbances reach an amplitude up to the one of $(1, 0)$, there. Compared to the rectangular notch, higher-harmonic oblique waves are larger by a factor of approximately 3. Subharmonics with $\gamma = 0$ are limited to $|\hat{v}| \approx 10^{-2}$ in the rest of the domain.

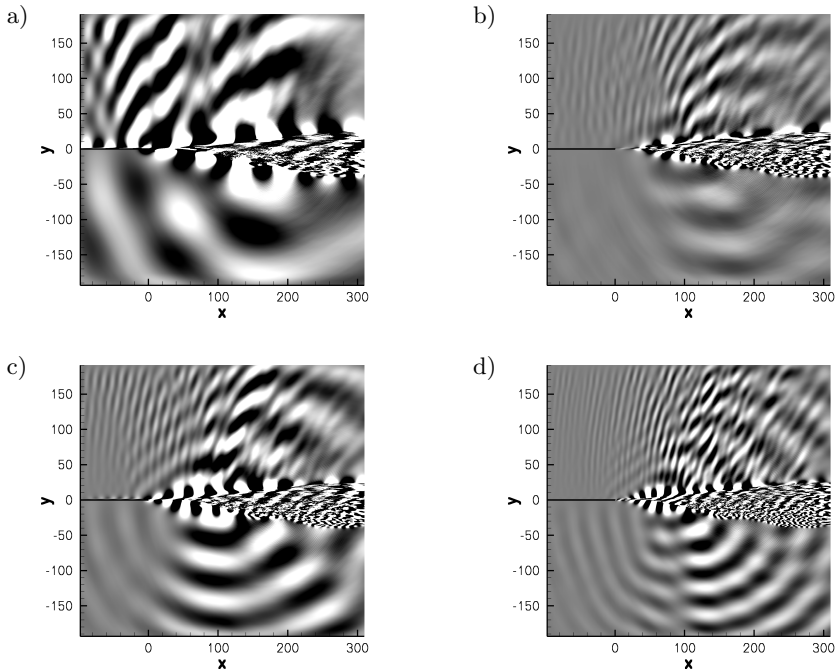


Figure 6.15: Real part of the Fourier-transformed dilatation field at the symmetry plane $z = 0$ (non-symmetric engrailment). Contour levels are in the range of $\nabla \mathbf{u} = \pm 3 \cdot 10^{-3}$:

a) ω_0 , b) $7/4 \cdot \omega_0$, c) $2 \cdot \omega_0$, d) $3 \cdot \omega_0$

The resulting acoustic field is shown by means of the real part of the Fourier-transformed dilatation field in figure 6.15 a) - d), again for frequencies ω_0 , $7/4 \cdot \omega_0$, $2 \cdot \omega_0$ and $3 \cdot \omega_0$, respectively. The dominant acoustic source for the

fundamental frequency is removed as found for the rectangular serration. The upstream propagating acoustic wave due to the scattering phase at $x \approx 60$ remains as well. For the undisturbed frequency $7/4 \cdot \omega_0$, noise reduction is more efficient than in case 6B. Yet this is not the case for the second higher harmonic whose emission in the range of $-100^\circ < \varphi < -45^\circ$ is not reduced compared to figure 6.5 c). The acoustic field for $3 \cdot \omega_0$ is basically the same as for the rectangular notch.

6.4 Comparison of Sound Emission

A direct comparison of the overall SPL is given in figures 6.16 a) - c) for cases 6A - 6C, respectively. Since all quantities are normalized, it is given only in increments of decibels. Yet if we assume the freestream pressure to be one bar, the contour levels are equivalent to 50 (black) to 100 dB (white). The acoustic field of the straight trailing edge is dominated by downstream directed sound which is substantially removed by both serrations. The rectangular notch generates less intense sound in the lower half of the domain, distributed more uniformly than in case 6C. This is in agreement to the experimental studies of Bridges and Brown [17] who found asymmetry to reduce the impact of chevrons slightly. On the other hand acoustic waves propagating inside the jet ($x < 0$, $y > 0$) are decreased most for the non-symmetric serration.

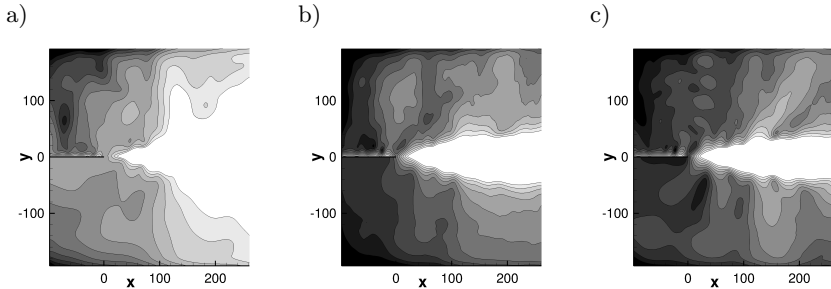


Figure 6.16: Overall sound pressure level L_p at $z = 0$, ranging from black to white with increments of 5 dB: a) straight, b) rectangular and c) non-symmetric trailing edge.

The actual noise reduction is illustrated in figures 6.17 a) and b), showing the difference of the SPL with respect to the reference case 6A. Due to additional oblique modes, hydrodynamic pressure variations in the mixing layer are in-

creased by some 5 dB directly behind the trailing edge for both cases. Yet missing large-scale structures lead to lower fluctuations further downstream.

The reduction of actual sound is determined by the difference in the farfield. In the lower freestream, the rectangular serration yields a noise reduction in the range of 6 to 10 dB with its distribution being relatively uniform along the streamwise direction. For positive values of y , downstream running acoustic waves are decreased by the same order of magnitude. Yet sound waves which propagate inside the jet are locally increased at $x \approx 0$, $y \approx 150$. For the non-symmetric serration, the sound emission in downstream direction is decreased locally by more than 10 dB in the lower half of the domain ($x > 200$, $y < 0$). On the other hand, the reduction of acoustic waves directed perpendicular to the flow speed is less distinct. This is due to the fact that sound with $2 \cdot \omega_0$ is not reduced substantially as revealed by figure 6.15 c).

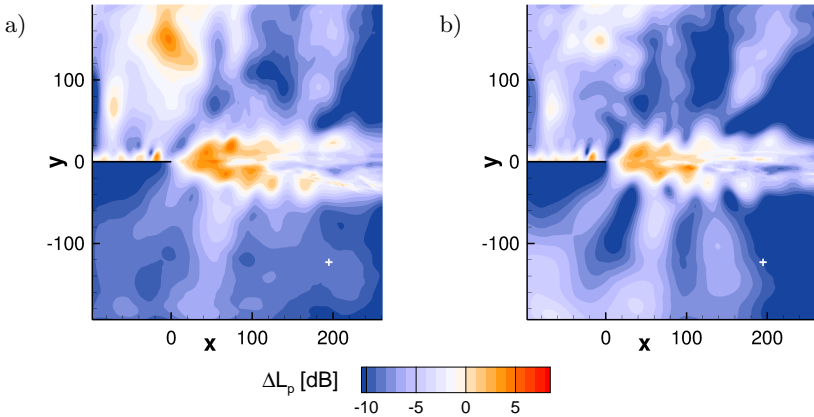


Figure 6.17: Difference of the sound pressure level ΔL_p in dB at $z = 0$ versus the reference case. The position of the virtual microphone is marked by a white cross. a) rectangular, b) non-symmetric notch.

The spectrum of the generated sound is compared in figure 6.18 for all three cases. It is based on a detailed time record at one location. The position ($x = 195$, $y = -121.8$, $z = 0$) of this virtual microphone is the same as for the two-dimensional case in chapter 5. Its location is indicated by a cross in figures 6.17 a) and b). The spectrum of the reference case is dominated by lower frequencies. The maximum amplitude $|\hat{p}| = 0.002$ is found for the fundamental frequency.

Furthermore, subharmonics contribute notably to the generated sound. Unlike the two-dimensional simulation, explicit peaks of higher harmonics can not be observed. For higher frequencies, amplitudes of the pressure decay down to $|\hat{p}| \approx 10^{-5}$. For both shapes of the splitter plate, the low-frequency noise is reduced. In the range of approximately $4 \cdot \omega_0$ to $20 \cdot \omega_0$, the emitted sound is partly increased. Comparing the pressure spectra of figures 6.18 ($z = 0$) and 6.19 ($z = \lambda_{z,0}/2$) shows that the sound emission is quite independent from the spanwise position for all three cases.

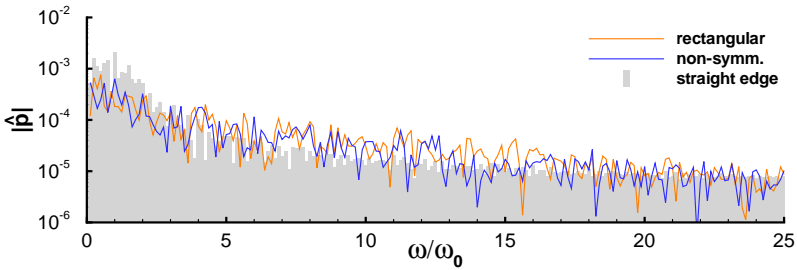


Figure 6.18: Amplitude spectrum of the pressure at the virtual microphone located at $x = 195$, $y = -121.8$, $z = 0$.

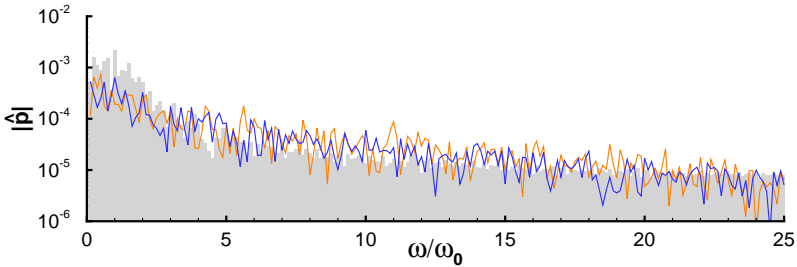


Figure 6.19: Pressure spectrum as in figure 6.18 but at spanwise location $z = \lambda_{z,0}/2 = 15.708$.

These results go with the experimental observations of Bridges and Brown [17] and Callender et al. [20]. Low-frequency noise is reduced since large-scale

Kelvin-Helmholtz vortices are destroyed. On the other hand, small eddies cause an increase of sound at higher frequencies. Considering the results for the pure mixing layer (chapter 4), noise reduction can be explained partially by lower amplitudes of the subharmonics.

7 Turbulent Mixing Layer

In the previous chapter, the two boundary layers upstream of the trailing edge were assumed to be laminar, containing only linear instability waves. However, the boundary layers in a real jet engine are typically turbulent, e.g. due to high-amplitude disturbances generated by the turbine. Therefore, the sound generation of a mixing layer with a turbulent boundary layer of the fast stream is investigated. The major flow parameters match those of chapters 5 and 6 with $Ma_I = 0.8$, $Ma_{II} = 0.2$ and $Re = 1000$. Using the Reynolds number of the previous cases, the reference length \tilde{L}_∞ stays the same. Yet the length scale corresponds no more to a specific boundary-layer thickness.

Before performing the actual simulation of the mixing layer, unsteady inflow data is required. Hence, laminar-turbulent transition of a flat-plate boundary layer is simulated first (section 7.1). The resulting time-dependent output is used as inflow condition for the actual simulation of the mixing layer given in section 7.2.

7.1 Generation of Inflow Data

Laminar-turbulent transition of a $Ma_\infty = 0.8$ boundary layer is simulated along the streamwise coordinates $x = 1400$ to 1707 , where $x = 0$ corresponds to the leading edge of the flat plate. Compared to previous cases, the inflow is shifted further downstream. This ensures that amplification is quite independent of the frequency along the streamwise coordinate. The fundamental frequency $\omega_0 = 0.03$ is given by the highest amplification rate of the TS-wave. The flow is forced at the inflow by eigenfunctions from linear stability theory with arbitrarily chosen phase shifts. The disturbance spectrum is selected according to a subharmonic transition scenario (H-Type) [40]. Beyond the first subharmonic $(1/2, k)$, oblique waves with $2/3 \cdot \omega_0$ are introduced as well providing an out-of-tune disturbance spectrum. Hence, the flow is periodic with respect to every sixth period of the TS-wave. Furthermore oblique waves are given for two spanwise wavenumbers. The fundamental spanwise wavenumber $\gamma_0 = 0.1$ yields wave angles of $\Psi = 68^\circ, 79^\circ, 62^\circ$ and 78° for modes $(1/2, 1)$, $(1/2, 2)$, $(2/3, 1)$ and $(2/3, 2)$, respectively. Relatively large amplitudes ($|\hat{u}|_{max} = 0.02$) and the variety of disturbances are intended to provide a rapid breakdown to turbulence.

In streamwise direction, the grid is uniform with a stepsize of $\Delta x = 0.14$ in the considered region. At $x = 1707$, the sponge zone begins and the mesh is stretched according to equation (3.106) by a factor of up to 100 at the end of the integration domain. In wall-normal direction, the step size is increased smoothly from $\Delta y = 0.06$ at the wall to $\Delta y = 1.21$ at the freestream, located at $y = 133$. With spanwise symmetry, 42 spanwise modes correspond to 65 grid points in z -direction and a stepsize of $\Delta z = 0.49$. The total number of 46.8 million grid points is distributed uniformly on eight subdomains. The number of computed time steps corresponds to 8.3 flow-through times. A detailed list of the simulation parameters is provided by table 7.1.

case	7A	
number of grid points ($N_x \times N_y \times N_z$)	2400 \times 300 \times 65	
Δx	0.14 - 13.9	
Δy	0.06 - 1.21	
Δz	0.49	
number of spanwise modes	42	
fund. spanwise wave number γ_0	0.1	
time step Δt	0.0157	
computed time steps	160000	
fundamental frequency ω_0	0.03	
periods of ω_0 for analysis	6	
subsonic inflow ($x_0 = 1400$):	$ \hat{u} _{max}$	$\Delta\Theta$
(1, 0)	0.02	0.0
(1/2, 1)	0.02	0.3
(1/2, 2)	0.02	0.6
(2/3, 1)	0.02	0.8
(2/3, 2)	0.02	0.4
characteristic free stream:		
damping parameter d	0.08	
grid points in damping zone	20	
subsonic outflow:		
beginning of filtering (x -position)	1707.1	
filtering sequence (time steps)	10	
ramping of filter (grid points)	20	

Table 7.1: Simulation parameters for the turbulent boundary layer with $Ma_\infty = 0.8$ and $Re = 1000$.

The resulting flow field at time instant $t = 2513.3$ is given in figure 7.1, showing the isosurface $\Lambda_2 = -0.01$. From $x \approx 1550$ on, first vortices emerge near the symmetry plane. Further downstream a turbulent spot around $z = \lambda_{z,0}/2$ is visible. They are followed by some Ω -vortices similar to the incompressible DNS of Meyer [67]. Unlike his symmetric simulation, the legs of the Ω -vortices have already disappeared. Downstream of $x \approx 1650$, breakdown along the complete spanwise direction can be observed. At the end of the physical domain ($x = 1707$), a relatively uniform distribution of vortices in the spanwise direction is reached.

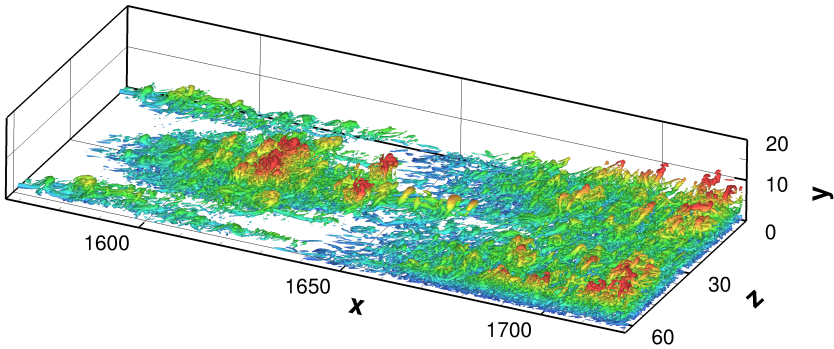


Figure 7.1: Isosurface $\Lambda_2 = -0.01$ of the turbulent boundary layer along one spanwise wavelength at $t = 2513.3$. Color denotes the wall-normal coordinate, ranging from blue to red.

Laminar-turbulent transition is known to increase wall friction [87, 106]. It is considered by the friction coefficient being the wall-normal shear stress normalized by the dynamic pressure:

$$c_f = \frac{\tau_w}{\frac{1}{2} \cdot \rho_\infty u_\infty^2} \tag{7.1}$$

$$\tau_w = \frac{\mu_w}{Re} \cdot \left. \frac{\partial u}{\partial y} \right|_w \tag{7.2}$$

The streamwise evolution of the time- and spanwise-averaged $\langle \bar{c}_f \rangle$ is shown in figure 7.2 a), with time and spanwise mean values being marked with $\bar{}$ and $\langle \rangle$, respectively. It is compared with the Blasius solution and the formula for turbulent boundary layers by Prandtl [87]. Near the inflow where the flow is dominated by single disturbances, $\langle \bar{c}_f \rangle$ corresponds to the laminar case. Further

downstream, it increases even above the empirical solution for turbulent flows, which is typical for laminar-turbulent transition. The inflection point of $\langle \bar{c}_f \rangle$ is found at $x \approx 1600$ where the first turbulent spot appears. Displacement thickness δ_1 according to equation (5.1) and momentum thickness

$$\delta_2 = \int_0^{\delta_{99}} \frac{\rho u}{\rho_\infty u_\infty} \left(1 - \frac{u^2}{u_\infty^2} \right) dy \quad (7.3)$$

describe the wall-normal extent of the boundary layer. Note that integration of δ_1 and δ_2 is done only within the boundary layer. Otherwise acoustic fluctuations in the freestream can distort the result. Their time- and spanwise average are given in figure 7.2 b). Since the streamwise-velocity profile of turbulent boundary layers is more bulbuous, the displacement thickness decreases during transition until it grows again ($x > 1670$). Yet growth of the momentum thickness is increased, reaching a value of $Re \cdot \delta_2 = 1220$ in front of the sponge zone. Figure 7.3 shows its spanwise dependency at $x = 1707$ together with the shape factor $H_{12} = \bar{\delta}_1 / \bar{\delta}_2$. Maximum values of $Re \cdot \bar{\delta}_2$ exist at the symmetry plane and at $z = \lambda_z / 2$. A spanwise variation of similar magnitude was also found by Meyer [67]. Like in his DNS, the shape factor H_{12} is quite constant along the spanwise direction.

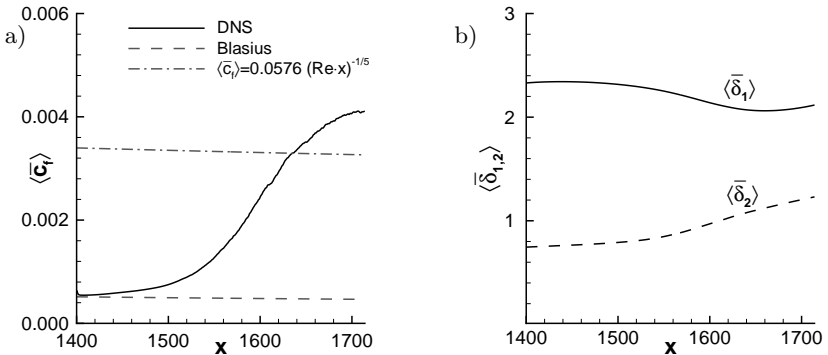


Figure 7.2: a) Streamwise distribution of friction coefficient $\langle \bar{c}_f \rangle$, compared with laminar solution and the friction formula of Prandtl for turbulent flows [87].

b) Streamwise evolution of time- and spanwise-averaged displacement- and momentum-thickness.

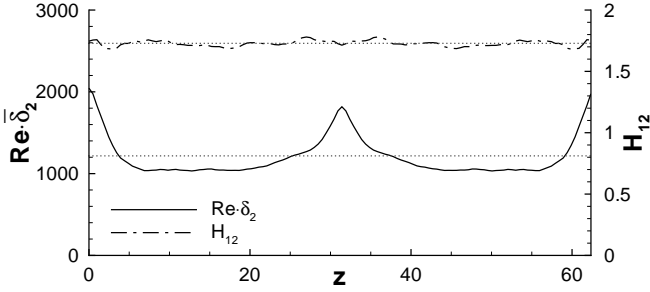


Figure 7.3: Reynolds number based on the momentum thickness $\bar{\delta}_2$ and shape factor H_{12} along spanwise direction at $x = 1707$. Dotted lines denote spanwise averaged values.

Velocity profiles are compared directly and by scaling them and the wall-normal coordinate with the wall-friction velocity u_τ , providing so-called wall units:

$$u_\tau = \sqrt{\frac{\langle \tau_w \rangle}{\rho}} \quad (7.4)$$

$$u^+ = \frac{\langle \bar{u} \rangle}{u_\tau} \quad (7.5)$$

$$y^+ = \frac{u_\tau \cdot \rho}{\mu} \cdot y \quad (7.6)$$

For $Ma_\infty = 0.8$, the wall-normal variation of density and temperature is weak. Thus, the freestream values of ρ_∞ and μ_∞ are used in equations (7.4) and (7.5) for simplicity.

The time- and spanwise-averaged velocity profile at $x = 1707$ is given in figure 7.4 a). Averaging is done within the simulation using every complete Runge-Kutta cycle within the last six periods of the TS wave. Despite having compressible flow and a lower Reynolds number $Re \cdot \bar{\delta}_2$, the result corresponds well to the incompressible DNS of Spalart [94]. Good agreement is also found for the mean profile in wall units shown in figure 7.4 b) together with the correlations for the viscous sublayer and the logarithmic range given by White [106]. For $y^+ < 10$, the u^+ -profile follows the slope of the viscous sublayer followed by the logarithmic range up to $y^+ \approx 150$. Before reaching its final value $u^+ = 22$,

the mean profile exceeds the log-law distribution. Similar postprocessing is shown in figure 7.5 for the root-mean-square values of the velocity fluctuations, based on the last 80000 time steps. For all quantities, the current simulation produces slightly larger fluctuations compared to the incompressible DNS of Spalart. Yet the location of the maximum of u_{rms}^+ and the overall trend of all three lines are the same in the compressible case.

In wall units, the stepsize in normal direction at the wall is $\Delta y^+ \approx 2.72$ at $x = 1707$. This is larger than $\Delta y^+ \approx 1$ proposed by Spalart. Yet the viscous sublayer is resolved sufficiently by the high-order compact scheme, providing good results on this mesh (figure 7.4). Since the time step limit is determined strongly by the wall-normal stepsize, a larger time step can be used and thus, the simulation is performed faster. Stream- and spanwise resolutions in wall units are $\Delta x^+ = 6.3$ and $\Delta z^+ = 22$, respectively.

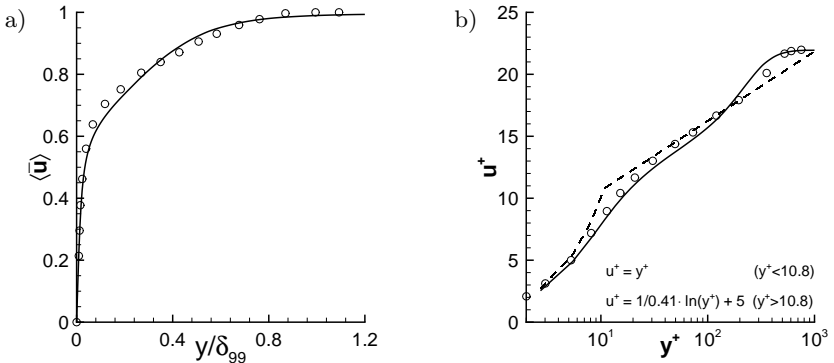


Figure 7.4: a) Time- and spanwise-averaged velocity profile at $x = 1707$ with $Re \cdot \langle \bar{\delta}_2 \rangle = 1220$.
 b) Averaged velocity profile, normalized with wall-friction velocity u_τ at the same position. Viscous sublayer and log-law are marked with dashed lines, see White [106]. In both plots, circles denote results from the incompressible simulation of Spalart [94] for $Re \cdot \langle \bar{\delta}_2 \rangle = 1400$.

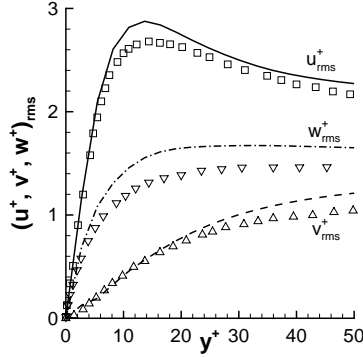


Figure 7.5: Spanwise averaged rms-values of the normalized velocity components at $x = 1707$ compared with the DNS of Spalart [94] marked with symbols.

Furthermore, spatial decay rates in x - and z -direction are compared with their theoretical values for turbulent flows in figures 7.6 a) and b). The energy spectra are computed by Fourier-transformation of u in the respective direction, squaring the amplitude and finally averaging it along all other directions including time, denoted by $\bar{\cdot}$. According to the $\langle \bar{e}_f \rangle$ -distribution in figure 7.2 a), the streamwise interval $1679 < x < 1707$ is limited to the turbulent region, providing wavenumbers down to $\alpha = 0.22$. Since the boundary layer grows in streamwise direction, a Hanning-window is required for the Fourier transformation along x , see Bonfigli [16] for details on windowing. The range of spanwise wavenumbers is given by $\gamma_0 = 0.1$ and the number of modes. Due to spanwise periodicity no windowing is required for the Fourier transformation along z . Averaging in normal direction and time is done for $0 < y < 10.13$ and along 40 time steps with an increment of $\Delta t = 31.42$, respectively.

The averaged energy spectrum in figure 7.6 a) shows a decay according to the slope $\alpha^{-5/3}$ up to $\alpha \approx 4.5$. For higher wavenumbers, the flow is dominated by viscous dissipation, hence following the slope α^{-7} . The results are in good agreement with the incompressible DNS of Bonfigli [16]. The steeper declining near the resolution limit is due to the inherent high-wavenumber damping of the numerical scheme (section 3.3.1). With multiple wavenumbers in the viscous range being included, the streamwise resolution is fine enough to capture all relevant turbulent scales. In figure 7.6 b), the initial decay in spanwise direction is again of shape $\alpha^{-5/3}$. Wavenumbers larger than $\alpha = 4.2$ are erased due to

dealiasing of the spectral ansatz (2/3 rule). Since the cut-off wavenumber corresponds quite well to the beginning of the viscous range found for the streamwise direction, the spanwise resolution is just sufficient for a DNS.

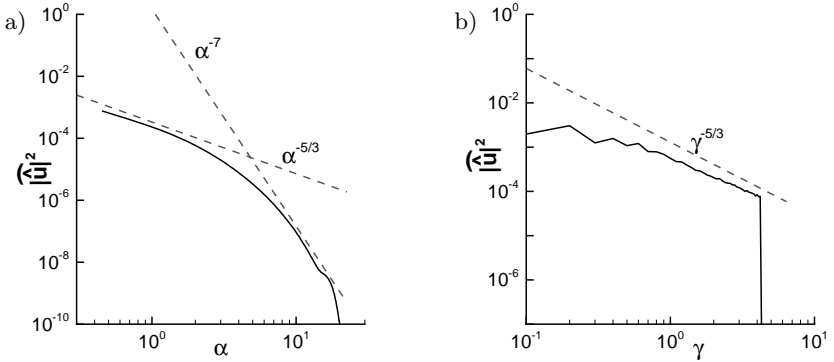


Figure 7.6: Averaged energy spectra of streamwise velocity component along a) x -direction and b) z -direction. Dashed lines show the slopes $\alpha^{-5/3}$, α^{-7} and $\gamma^{-5/3}$ (averaging along 40 time steps with increment $\Delta t = 31.42$, $1679 < x < 1707$, $0 < y < 10.13$, $0 < z < \lambda_{z,0}$).

Even if this simulation is intended primarily to provide unsteady inflow data for the turbulent mixing layer in section 7.2, it is worth to take a look at the acoustic field, too. Its temporal development is illustrated in figure 7.7 by snapshots of the dilatation $\nabla \mathbf{u}$. The sound emission is dominated by an acoustic source, emerging at $x \approx 1600$ where the first turbulent spot appears. It travels in streamwise direction with approximately 70% of the freestream velocity. Note that no acoustic disturbances are generated at the inflow despite high-amplitude disturbances which are introduced there.

With mean values, fluctuations and spectra showing the typical characteristics of turbulent flows, the numerical scheme is successfully validated for the turbulent flows and the resulting boundary layer is an appropriate inflow condition for the following DNS of a turbulent mixing layer.

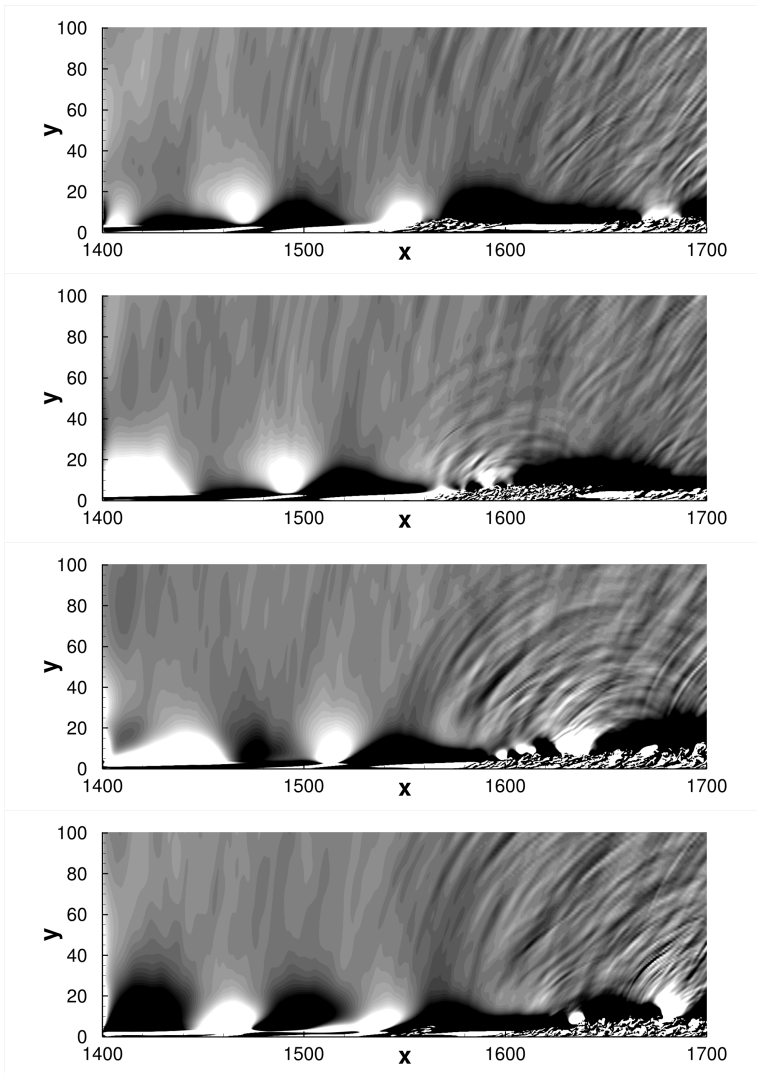


Figure 7.7: Snapshots of the transitional boundary layer's acoustic field up to time level $t = 2419$ with increment $\Delta t = 62.83$ (dilatation in the range of $\nabla \mathbf{u} = \pm 2 \cdot 10^{-4}$).

7.2 Results for the Turbulent Mixing Layer

The physical domain (without sponge zone) for the turbulent mixing layer covers a range of $-41.8 \leq x \leq 260$ and $-199 \leq y \leq 199$ in streamwise and normal direction, respectively. Compared to previous simulations (6A-6C), the length of the splitter plate is reduced. This allows to use more grid points past the trailing edge. The spanwise extent is given by the fundamental wavenumber $\gamma_0 = 0.1$ of the unsteady inflow data. The stepsize $\Delta x = 0.14$ of the previous boundary-layer simulation is kept until the sponge zone, where it is smoothly increased up to $\Delta x = 16.576$. In normal direction, the stepsize $\Delta y = 0.06$ at the wall is taken as well from case 7A. Yet the stretching ratio is decreased since a fine mesh is required over the whole mixing layer which is distinctly thicker than the introduced boundary layer. The spanwise symmetric flow is resolved with 42 modes (dealiased) and hence, 65 grid points along z are used in physical space. This yields a total number of 196.56 million grid points.

As mentioned above, freestream conditions are the ones of chapter 5 and again, the wall temperature is fixed to $\bar{T}_w = 296K$. The boundary layer thickness of the upper boundary layer at the inflow is given by the previous simulation and corresponds to a distance of 1693.17 from the leading edge. The thickness of the low-speed boundary layer is the one of the previous simulations. Thus, a moderate thickness of the mixing layer is achieved. This has the advantage of i) higher amplification rates and ii) a smaller region with fine resolution.

The total number of time steps is 144000 with $\Delta t = 0.01309$. This is equivalent to more than 6 flow-through times. The inflow data of the turbulent boundary layer is interpolated on the finer mesh up to $y \approx 25$. It contains 4000 time steps along six periods of the TS-wave of case 7A. Hence, the last six periods of the fundamental frequency are used for analysis. The simulation parameters are summarized in table 7.2.

Figure 7.8 shows a snapshot of the vortices above the splitter plate and in the mixing layer. Up to the trailing edge, flow structures are distributed quite uniformly in spanwise direction. Yet from $x \approx 50$ onwards, vortices protrude from the mixing layer in the symmetry planes $z = 0$ and $z = \lambda_{z,0}/2$. This is increased in streamwise direction, forming ring-like vortices along z . Below the mixing layer, the largest extent in normal direction is found only around the symmetry plane $z = 0$. Thus, the streamwise growth of the mixing layer mainly occurs in the symmetry planes, as shown by the color distribution in figure 7.8.

case	7B
number of grid points ($N_x \times N_y \times N_z$)	2400 \times 1260 \times 65
Δx	0.14 - 16.576
Δy	0.06 - 0.827
Δz	0.49
number of spanwise modes	42
fund. spanwise wave number γ_0	0.1
time step Δt	0.01309
computed time steps	144000
fundamental frequency ω_0	0.03
periods of ω_0 for analysis	6
turbulent inflow:	
number of time steps	4000
range in x	-41.888 .. -39.433
range in y	0 .. 24.944
characteristic free stream:	
damping parameter d	0.05
grid points in damping zone	20
subsonic outflow:	
beginning of filtering (x -position)	260
filtering sequence (time steps)	20
ramping of filter (grid points)	20

Table 7.2: Simulation parameters for the turbulent mixing layer with $Ma_I = 0.8$, $Ma_{II} = 0.2$ and $Re = 1000$.

The increasingly non-uniform spanwise distribution has its origin in the introduced turbulent boundary layer which shows an increased momentum thickness at $z = 0$ and $z = \lambda_{z,0}/2$ as well (see figure 7.3).

The mixing layer's temporal development is shown in figure 7.9 by a sequence of artificial shadow graphs. The time frame shown corresponds to 37.5% of the period of the fundamental frequency ω_0 . Along the splitter plate, the thickness of the upper boundary layer varies strongly with time. Thus, the introduced data corresponds to a rather early-turbulent boundary layer. The mixing layer grows mainly in the lower half of the domain. The spreading angle of approximately 10° is constant along the streamwise direction and hence, fluctuations are visible down to $y < -40$ in figure 7.9's last view. Along the fast stream, the growth of the mixing layer is much smaller.

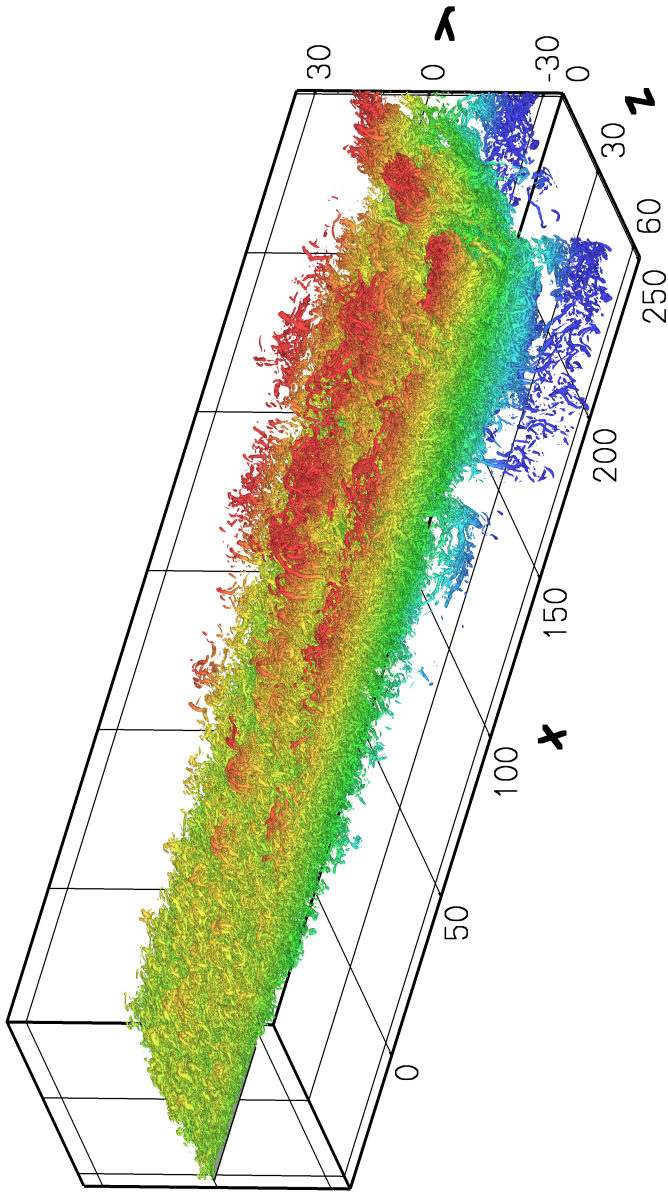


Figure 7.8: Perspective view of the isosurface $\Lambda_2 = -0.01$, showing the vortical structures in the turbulent mixing layer at time level $t = 1884.96$ with color denoting the normal coordinate.

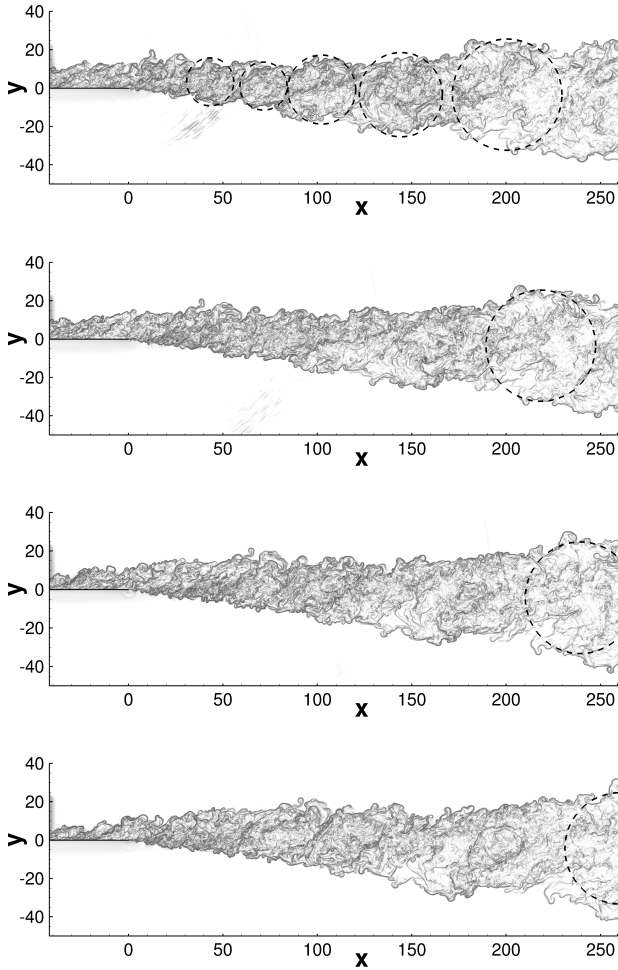


Figure 7.9: Artificial shadow graphs of the turbulent mixing layer, showing density gradients in the symmetry plane $z = 0$. The temporal development is shown by increments of $\Delta t = 26.18$, starting at $t = 1727.88$ (top to bottom). Coherent structures mentioned in the text are marked with circles.

The flow field is dominated by small-scale structures. Yet it is possible to detect accumulations of eddies. Especially in the first snapshot of figure 7.9, a row of circular structures is visible at $x \approx 45, 70, 100$ and 140 . Since they are superimposed with small-scale structures, it is hard to follow their position in time. Yet this is more clear for the big vortex located at $x \approx 200, 220, 240$ and 260 for the given time levels (top to bottom). Being quite large compared to the small eddies, one may speak of the first “real“ turbulent Kelvin-Helmholtz vortex here.

The time and spanwise averaged streamwise velocity is shown in figure 7.10 a) for an exemplary position $x = 150$. It corresponds to the S-shaped velocity profile, used in chapter 4. Fluctuations of the three velocity components are regarded by their rms-values at the same streamwise position in figure 7.10 b). Due to the absence of a wall, they are not normalized with a friction velocity as done for the turbulent boundary layer. The streamwise velocity shows the dominant disturbance with $\langle u_{rms} \rangle_{max} = 0.14$. Compared to figure 7.4 b) of the turbulent boundary layer, the spanwise velocity fluctuation $\langle w_{rms} \rangle_{max} = 0.1$ is only slightly larger than its counterpart in normal direction with $\langle v_{rms} \rangle_{max} = 0.096$. All quantities show a quite symmetric behavior with respect to the center of the mixing layer $y = 0$.

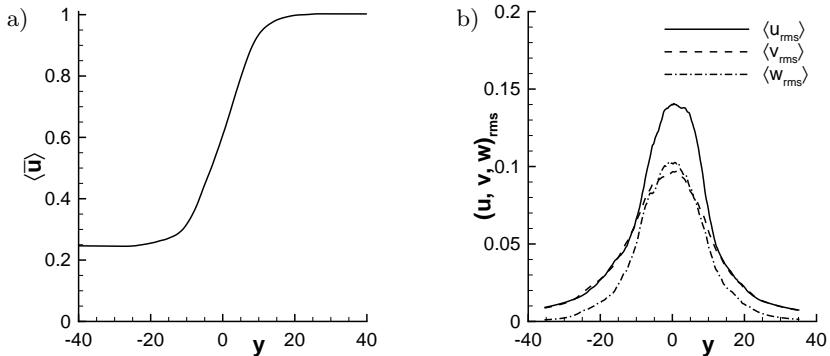


Figure 7.10: a) Temporal and spanwise averaged velocity profile at $x = 150$.
 b) Spanwise averaged rms-values of the three velocity fluctuations at the same x -position.

Figures 7.11 a) and b) show the averaged energy spectra in analogy to the turbulent boundary layer. They are based on the last six periods of the fundamental frequency and the spatial extent covers a region of $125.66 < x < 167.41$, $-20 < y < 20$, $0 < z < \lambda_{z,0}$. The Hanning window is applied in x - and y -direction to account for non-periodicity.

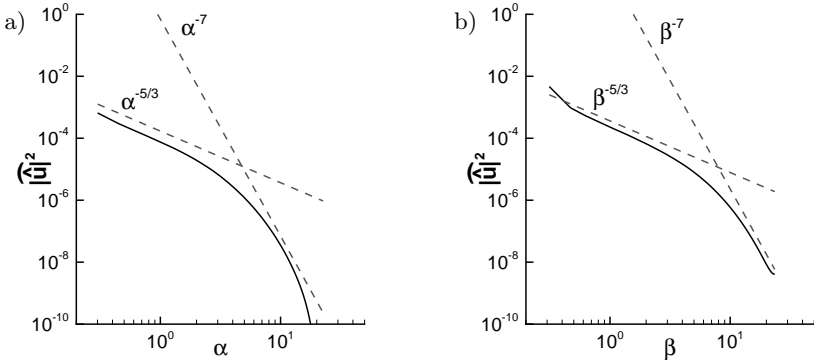


Figure 7.11: Averaged energy spectra of streamwise velocity component along a) x -direction and b) y -direction with dashed lines indicating decay rates $\alpha^{-5/3}$, α^{-7} and $\beta^{-5/3}$, β^{-7} , respectively (averaging along 120 time steps with increment $\Delta t = 10.47$, $125.66 < x < 167.41$, $-20 < y < 20$, $0 < z < \lambda_{z,0}$).

In both directions, the spectra follow the decay rates with the power of $-5/3$ and -7 . The streamwise spectrum is in the viscous range (α^{-7}) for wavenumbers larger than roughly 4.5 as found in figure 7.6 a). Near the cut-off wavenumber, the decline is again stronger than α^{-7} due to the dissipation of the numerical scheme. Yet in normal direction, the transfer to viscous decay occurs for $\beta > 8$. Thus, the mixing layer's turbulence is not isotropic and generally, the resolution in normal direction should be finer than in streamwise direction. Note that the cut-off wavenumber in figure 7.6 b) is somehow arbitrary since the data is interpolated on a mesh with constant $\Delta y = 0.133$ to enable the Fourier analysis.

The maximum amplitudes of the normal velocity component along y are shown in figure 7.12 a) for two-dimensional disturbances. Since the initial mixing layer is not laminar as in the cases considered before, the amplitude distribution is less distinct, showing short-wavenumber variations. In the turbulent boundary

layer, fluctuations are in the range of $|\hat{v}| = 10^{-3}$ to 10^{-2} . Behind the trailing edge, higher harmonics (3,0) and (4,0) grow strongly up to $50 < x < 60$ where they saturate. This position corresponds to the first accumulation of small eddies found in figure 7.9. Further downstream, the two-dimensional fundamental mode grows. The increase of its first higher harmonic is inhibited at a level of $|\hat{v}| \approx 10^{-2}$. Saturation of (1,0) occurs at $x \approx 200$ where the first vortex-like coherent structure is visible in figure 7.9.

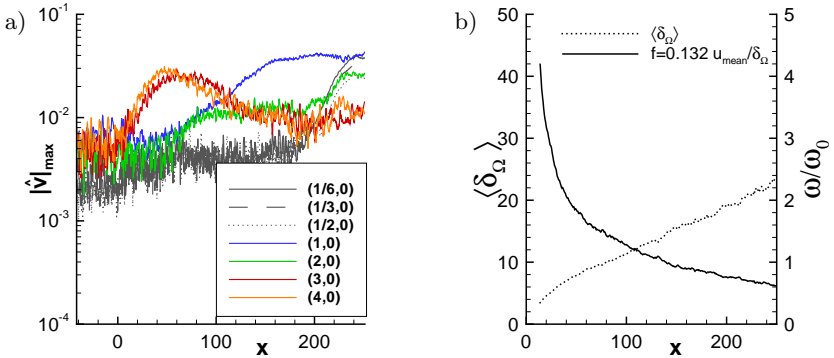


Figure 7.12: a) Maximum amplitude of the normal velocity along y for two-dimensional disturbances $(h, 0)$.

b) Vorticity thickness $\langle \delta_\Omega \rangle$ of the mean flow and resulting frequency of the most-amplified disturbance by Michalke [68].

For further understanding, the vorticity thickness of the time and spanwise averaged flow field according to equation (4.1) is considered. It is given in figure 7.12 b) together with the frequency of the most-unstable disturbance according to the inviscid linear analysis of Michalke [68]. At the beginning, disturbances in the range of $3\omega_0$ to $4\omega_0$ are most amplified as found in figure 7.12 a). Also the locations of the incipient growth of the fundamental disturbance at $x \approx 100$ and its first higher harmonic at $x \approx 60$ correspond to the findings of Michalke. Thus, the growth of two-dimensional modes $(h, 0)$ is due to the linear instability of the mean flow although no clearly separated scales exist. Near the end of the integration domain, the amplitudes of various subharmonics and the first higher harmonic increase rapidly. Despite the thicker mixing layer, growth rates are larger for the fundamental mode. Hence, this is no more due to the inflection point of the mean flow but rather some secondary instability mechanism.

The amplitudes of oblique modes are given for one and two times the fundamental spanwise wavenumber in figures 7.13 a) and b), respectively. In the turbulent boundary layer ($x < 0$), they are larger than their two-dimensional counterparts by a factor of approximately two. Behind the trailing edge, bumps of modes $(1, k)$ to $(4, k)$ exist at similar locations as for the corresponding two-dimensional disturbances. Since disturbances are less amplified for increasing spanwise wavenumbers (see e.g. figure 4.4 b), the growth of oblique modes is less intense than in figure 7.12 a). An exception is mode $(2, 1)$, reaching a maximum of $|\hat{v}| \approx 2.5 \cdot 10^{-2}$ around $x = 120$ before it decays again. The mean exponential growth of subharmonic oblique waves is quite constant along x .

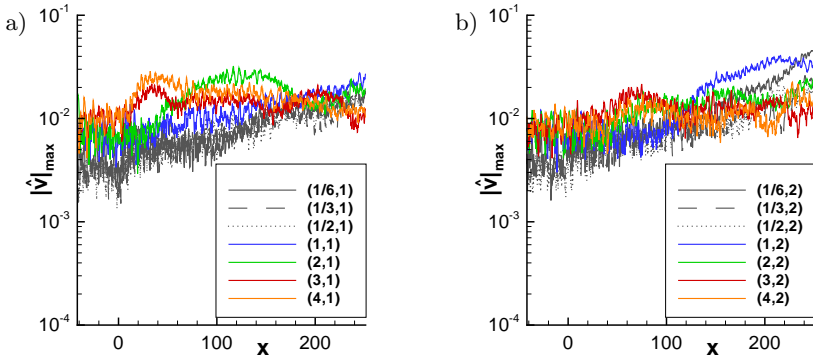


Figure 7.13: Maximum amplitude of v along the normal direction for oblique modes: a) $(h, 1)$ and b) $(h, 2)$

The resulting acoustic field at $z = 0$, visualized by dilatation in the range of $\nabla \mathbf{u} = \pm 5 \cdot 10^{-4}$ is given in figure 7.14 for four different time levels. Being part of the introduced perturbations, the downstream travelling acoustic source of the turbulent boundary layer (figure 7.7) appears as well with the fundamental frequency. It generates circular acoustic waves in the upper part of the domain. When reaching the trailing edge, a circular pulse with short-wavelength fluctuations is emitted towards the low-speed stream. Due to diffraction in the mixing layer, an additional wave front appears below the mixing layer. A uniform directivity is observed in the fast stream while acoustic waves in the lower half of the domain have a maximum for $\varphi \approx 45^\circ$. Sound running perpendicular to the flow speed is rapidly dissipated.

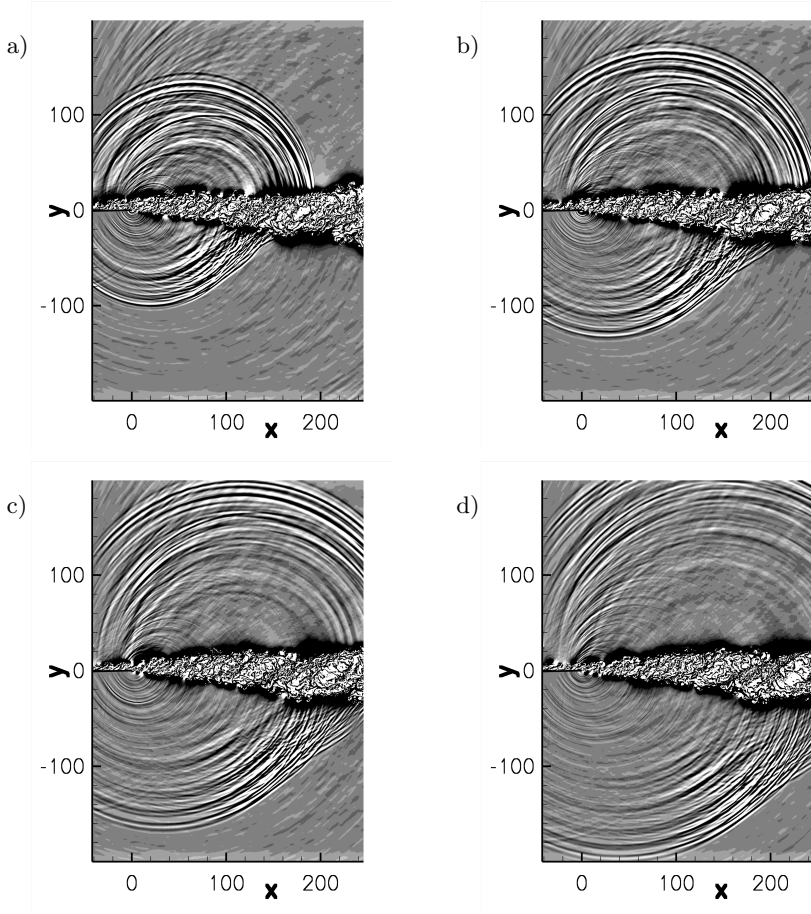


Figure 7.14: Acoustic field at $z = 0$, visualized by snapshots of the dilatation in the range of $\nabla \mathbf{u} = \pm 5 \cdot 10^{-4}$. Time levels are $t = 1780.2, 1806.4, 1832.6$ and 1858.8 for a) to d), respectively.

Between two dominant sources, less intense acoustic waves are also emitted from the trailing edge. Yet they are of smaller amplitudes and strongly dissipated due to their short wavelengths. The acoustic wave in the upper half of the domain travels faster than in the low-speed stream because of the different freestream velocities. Thus, the position of the upper wave front is further

downstream compared to the one below the mixing layer. With increasing x -coordinate, the streamwise traveling acoustic source is dissipated and finally, no relevant acoustic emissions are found in the fast-speed stream, see figure 7.14 d). Since no additional damping zone is applied to the one-dimensional, characteristic inflow boundary of the low-speed stream, some minor reflections are visible there, e.g. at $y = -90$ in figure 7.14 a). Yet these are relatively small and hence do not spoil the result. Note that artificial sound is generated neither by the turbulent inflow boundary condition nor by the sponge zone of the outflow.

The characteristic of the emitted sound is considered in figure 7.15 by the pressure fluctuations at an exemplary position in the low-speed stream. The coordinates of the virtual microphone are $x = 195$, $y = -121.8$, $z = 0$, being the same as for the temporal pressure spectrum in figure 6.18. Since the acoustic field is dominated rather by pulses than pure sinusoidal waves, the temporal pressure variation is given. Pressure peaks with a deflection of $p' \approx 0.006$ are visible at $t \approx 1230$, 1440, 1650 and 1860. Their interval is equivalent to the period of the fundamental frequency. The variation between two peaks is $p' \approx 0.0015$ and hence being quieter by 12 dB.

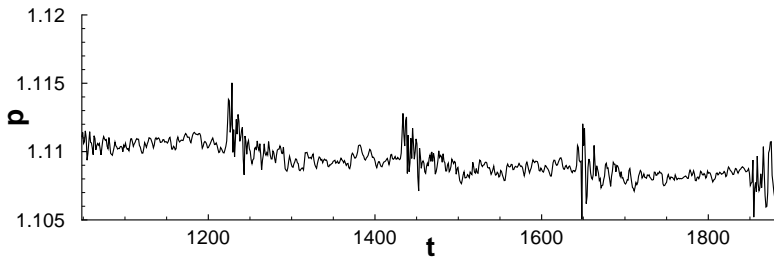


Figure 7.15: Time-dependent signal of the pressure fluctuations along 4 periods of the fundamental frequency. The virtual microphone is located at $x = 195$, $y = -121.8$, $z = 0$.

Apart from the downstream propagating noise source of the upper boundary layer, the turbulent mixing layer is remarkably quiet. Following the findings of chapter 4, this is due to the low amplitudes of the respective subharmonics, given in figure 7.12 a). This is the case for the maximum of high-frequency modes (3, 0) and (4, 0) as well as for the two-dimensional fundamental disturbance.

8 Conclusions and Outlook

The aim of the present work is the investigation of sound-generation mechanisms in the mixing layer of a jet with subsonic flow speeds. To avoid modeling of fluid-mechanic processes, direct numerical simulation (DNS) is applied for both, the flow field and the acoustic farfield. Since the amplitudes of the emitted sound are substantially smaller than hydromechanic fluctuations, a highly accurate numerical scheme with appropriate boundary conditions is mandatory.

The presented DNS-code is based on sixth-order compact finite differences and a spectral discretization in spanwise direction, allowing spanwise symmetric and non-symmetric simulations. Non-uniform grids are implemented to compute the acoustic farfield efficiently. The code can be run on multiple processors by means of shared-memory parallelization in spanwise direction and domain decomposition in streamwise and normal direction. Beyond increasing performance, the combination of domain decomposition and grid transformation allows to simulate a wide range of configurations. The method is verified by comparison with linear stability theory, reference cases including aeroacoustic problems, and statistical data for turbulent flows. The combination of DNS-code, linear stability theory, pre- and postprocessing provides a complete simulation framework for unsteady compressible flows. Despite DNS-code and linear-stability solver being new developments, it should not be forgotten that their successful implementation is also based on the work and experience of many others at the Institut für Aerodynamik und Gasdynamik throughout several years.

The core of this thesis is dedicated to aeroacoustic sound generation in mixing layers, which are a model for the initial part of a jet. The investigations are arranged such that the complexity of the simulations is successively increased, ranging from rather generic cases to more realistic configurations for “real-world” jets.

The fundamentals of aeroacoustic noise generation are investigated for a pure mixing layer which is forced with defined disturbances. Due to the inflection point of the velocity profile, disturbances are highly amplified, leading to a roll-up of the mixing layer with subsequent vortex pairing. The mechanism of vortex pairing can be explained by subharmonic resonance, meaning that the phase

speed of the respective subharmonic adapts to that of the currently dominant mode. Thus, the relative phase shifts of the introduced disturbances and not only their amplitudes are decisive for the modes' strength at a specific streamwise position. In case of an additional spanwise deformation, counter-rotating streamwise vortices occur and the growth of two-dimensional low-frequency modes is reduced. The interaction of streamwise vortex tubes and streamwise rollers yields a breakdown of the large-scale Kelvin-Helmholtz vortices. The main acoustic emission of a mixing layer is directed in downstream direction. It is caused not only by vortex pairing but requires the presence of notable subharmonics. Hence, it is possible to reduce the downstream directed sound by simply altering the phase of the corresponding low-frequency mode. Three-dimensional structures transform the originally tonal sound to broadband noise. In case of inhibited resonance, additional sound is generated in upstream direction.

By adding a splitter plate representing the nozzle end, a more realistic configuration is obtained which includes the initial region of the mixing layer. Furthermore, this setup allows the placement of wall-mounted actuators for flow control. Due to the thicknesses of the two different boundary layers on both sides of the flat plate, a combination of wake and mixing layer occurs. Further downstream, the flow field is dominated by vortex ejection and pairing similar to the Blasius mixing layer considered before. However, some random behavior can be observed and the flow is no longer completely periodic. This indicates that new instability waves are generated by upstream traveling acoustic waves impinging on the trailing edge of the splitter plate. Accordingly, a higher level of undisturbed subharmonics is found for an increased thickness of the splitter plate. Up to moderate thicknesses the process of sound generation stays the same. Hence, the computationally more convenient thin trailing edge is a justified approach.

A first attempt to reduce the noise emission is a spanwise deformation of the splitter plate's trailing edge. Two cases with a rectangular and a nonsymmetric notch are computed and compared with a straight trailing edge. The spanwise extent is the same for both serrations and chosen such that it corresponds approximately to a 45° waveangle for the introduced Tollmien-Schlichting wave. Inside the notch, the mixing layer begins earlier, resulting in a spanwise modulation of the Kelvin-Helmholtz vortices. Streamwise vortex tubes are generated at the sharp edge of the Kelvin-Helmholtz deformations and directed towards the spanwise position of the notch. Large structures which are observed for the straight trailing edge are replaced by small-scale eddies. These are still aligned in groups with a distance corresponding to the Kelvin-Helmholtz vortices of

the straight trailing edge. The sound emission of the dominant lower frequencies is reduced substantially. On the other hand, noise with higher frequencies is partly increased. Yet a sustained reduction of some 10 decibel can be observed for both serrations. An ostensive explanation is the replacement of the merging Kelvin-Helmholtz vortices by small scale structures. Alternatively, one may state decreased subharmonics to be responsible for the reduction of low-frequency noise, following the results of the pure mixing layer. For a constant spanwise extent, the actual shape seems to be of minor importance. Despite some major changes of the shape, symmetric to non-symmetric and rectangular to aslope, basically the same noise reduction can be observed.

In most “real-world” applications, jets are turbulent. In the simulation, this is realized by prescribing unsteady data at the inflow. The time-history of all flow quantities is extracted from a precursor DNS of laminar-turbulent transition in a flat-plate boundary layer. Due to the streamwise length of the integration domain, only the roll-up and not the pairing of turbulent Kelvin-Helmholtz vortices is captured by the simulation. Thus, the focus is set on trailing edge noise and the initial development of a turbulent mixing layer, here. It is dominated by small-scale turbulent structures forming larger Kelvin-Helmholtz-like structures. Despite no separate scales exist, the roll-up of the mixing layer is a linear mechanism, driven by the inflection point of the mean velocity profile. The simulation shows the dominant noise due to an acoustic source in the turbulent boundary layer. When reaching the trailing edge, it emits an acoustic pulse towards the low-speed stream. While traveling further downstream, the source is dissipated in the turbulent mixing layer.

The performed simulations allow to distinguish three types of sound generation mechanism in a mixing layer:

- vortex pairing:
In combination with notable subharmonics, vortex pairing is the strongest acoustic source in a mixing layer, generating downstream-directed sound
- suppressed resonance:
When adaptation of the phase speed is inhibited, upstream-directed sound is emitted into the fast stream, hence inside the jet. The actual directivity depends on the Mach number of the fast stream.
- trailing-edge noise:
This is mainly due to downstream traveling acoustic sources inside the jet. Apart from this, the sound generation at the trailing edge is weak and rapidly dissipated due to its short wavelength.

Outlook on Future Research

Of course, the DNS-code is not limited to jet noise. Future research may focus on simulating a complete airfoil as done by Sandberg et al. [84], Marsden et al. [64] and Jones et al. [47]. Thereby it is of special interest how disturbances are generated at the leading edge by upstream propagating acoustic waves. Direct numerical simulations may clarify whether freestream turbulence or self-induced disturbances trigger laminar-turbulent transition. Currently, first experience at IAG is gained in this field [88]. Generally, the code may be applied to the wide range of laminar-turbulent transition and flow control in sub-, trans- and supersonic regimes. When it comes to strong shocks, the implementation of a shock-capturing method will be necessary.

Future simulations of turbulent mixing layers may be extended to include the pairing of two turbulent vortices. Beyond an increased streamwise extent of the integration domain, a better spanwise resolution seems to be favorable. Furthermore, the influence of the spanwise extent of serrations should be investigated. This may yield some guidelines for the design of an optimally engrailed trailing edge. Beyond serrations, other active or passive actuators may be placed at the wall. With the current knowledge, fluid ejection or streamwise-vortex generators, either active or passive, seem to be methods for jet-noise reduction, worth to be investigated. Since instantaneous flow variables are available at each location, also some feedback control may be implemented where the actuator at the wall is triggered by some sensor, e.g. a microphone. Yet a useful realizable control law remains an open issue.

In principle, it might be possible to adapt the phase of subharmonics such that resonance is inhibited and their amplitude at the position of vortex pairing is reduced. According to the findings for the pure mixing layer, this seems to be a promising approach, having no penalty in terms of additional high frequency noise. Yet a wide range of low-frequency disturbances and not only the exact subharmonic of the merged vortex must be controlled in a practical implementation. This seems to be quite difficult because of i) the unknown disturbance spectrum and ii) the feedback mechanism which generates new instability waves. The reduction of trailing edge noise requires the elimination of acoustic sources in the boundary layer. Due to the presence of a wall, various actuators are conceivable for this.

A Finite Differences on Non-Uniform Grids

Some people may denote the investigation of numerical properties to be simple analysis. However, designing a numerical scheme without knowing the occurring discretization effects may cause unphysical results, hence querying the scientific outcome of such simulations. In this context, the effect of non-uniform grids is investigated theoretically and by means of numerical tests.

Three principal methods for finite difference discretization on non-uniform grids are considered. The first way is to use a biased stencil where the coefficients of the finite difference depend on the coordinates of the involved grid points, see e.g. Shukla & Zhong [90]. This has to be done once after the grid has been defined. The other two implementations are based on a transformation of the physical non-uniform grid to a computational equidistant grid. For the one-dimensional case, the transformation (3.9) for the first and second derivatives simplifies to

$$\frac{\partial}{\partial x} = \frac{1}{\left(\frac{\partial x}{\partial \xi}\right)} \cdot \frac{\partial}{\partial \xi} \quad (\text{A.1})$$

$$\frac{\partial^2}{\partial x^2} = \frac{1}{\left(\frac{\partial x}{\partial \xi}\right)^2} \cdot \frac{\partial^2}{\partial \xi^2} - \frac{\frac{\partial^2 x}{\partial \xi^2}}{\left(\frac{\partial x}{\partial \xi}\right)^3} \cdot \frac{\partial}{\partial \xi}, \quad (\text{A.2})$$

with the metric coefficients $\partial x/\partial \xi$ and $\partial^2 x/\partial \xi^2$ defined by the transformation $x = x(\xi)$. Being derivatives in computational space, the metric coefficients can be computed either numerically using the same procedure as for the flow variables or analytically if the transformation $x(\xi)$ is given analytically.

Visbal & Gaitonde [101] have shown the practical application of finite differences on deformed meshes using grid transformation with high-order schemes providing better results than a low-order discretization. The effect of skewed meshes was studied by You et al. [108]. They found large numerical dissipation on skewed grids which may negatively affect the stability of the computation. A special implementation of curvilinear meshes is proposed by Zhong & Tatieni [109]: the actual stretching is included in the coefficients of the stencil and grid transformation is used only for the bending of the mesh.

A.1 Modified-Wavenumber Analysis

The principles of different implementations of non-uniform grids are investigated theoretically using the classical wavenumber analysis [55, 58], There, one considers the one-dimensional advection-diffusion equation

$$\frac{\partial u}{\partial t} + c \cdot \frac{\partial u}{\partial x} = d \cdot \frac{\partial^2 u}{\partial x^2} \quad , \quad c, d \in \mathbb{R} \wedge \geq 0 \quad (\text{A.3})$$

on a periodic or infinite domain in x-direction with constant diffusion and convection speed. The evaluation of the spatial discretization is based on a wave with the wavenumber k , allowing an arbitrary phase Θ :

$$u(x) = \Re \left(e^{i(k \cdot x + \Theta)} \right) = \cos(k \cdot x + \Theta) . \quad (\text{A.4})$$

The dispersion/dissipation properties on uniform meshes can be found in section 3.3.1. To evaluate the properties of FDs on a non-uniform physical grid, the biased stencils or the metric coefficients need to be taken into account. Therefore, a specific grid stretching has to be defined with the analysis being only valid for this type of mesh. To achieve generally valid results, a generic function $x(\xi)$ is desirable. In contrast to the uniform grid, an analytical approach providing wavenumber diagrams as in figures 3.2 and 3.3 is now only possible for explicit finite differences. Due to the varying resolution, the quality of the computed derivative differs at the neighboring points. An analytical expression of the modified wavenumber is no more possible without specifying the mesh on the whole computational domain. Thus, the properties of compact FDs have to be investigated using a numerical experiment, as done in section A.2.

The probably most generic grid transformation is a continuous increase or decrease of the grid spacing Δx in physical space which can be expressed by an exponential function:

$$x(\xi) = e^{c \cdot \xi} \quad , \quad \frac{\partial x}{\partial \xi} = c \cdot x \quad , \quad \frac{\partial^2 x}{\partial \xi^2} = c^2 \cdot x \quad , \quad (\text{A.5})$$

where c determines the strength of the continuous stretching. Multiplication with the step size in computational space, $\Delta \xi$, gives the non-dimensional parameter $c^* = c \cdot \Delta \xi$. With the analytical grid stretching we can define a reference step size in physical space

$$\Delta x_{ref} = \left. \frac{\partial x}{\partial \xi} \right|_{an.} \cdot \Delta \xi = c^* \cdot x \quad (\text{A.6})$$

which is used to obtain the non-dimensional wavenumber $k^* = k \cdot \Delta x_{ref}$. Note that half the grid spacings of a “centered” stencil are smaller or larger than Δx_{ref} , respectively. With the coordinates based on equation (A.6), we obtain the values of the considered wave:

$$\begin{aligned} u_{j-2} &= e^{i\left(\frac{k^*}{c^*} \cdot e^{-2 \cdot c^*} + \Theta\right)}, & u_{j-1} &= e^{i\left(\frac{k^*}{c^*} \cdot e^{-c^*} + \Theta\right)}, & u_j &= e^{i\left(\frac{k^*}{c^*} + \Theta\right)}, \\ u_{j+1} &= e^{i\left(\frac{k^*}{c^*} \cdot e^{c^*} + \Theta\right)}, & u_{j+2} &= e^{i\left(\frac{k^*}{c^*} \cdot e^{2 \cdot c^*} + \Theta\right)}. \end{aligned} \quad (\text{A.7})$$

For biased finite differences, the spatial derivatives are computed directly in physical space

$$\frac{\partial u}{\partial x} \simeq \mathbf{a} \cdot u_{j-2} + \mathbf{b} \cdot u_{j-1} + \mathbf{c} \cdot u_j + \mathbf{d} \cdot u_{j+1} + \mathbf{e} \cdot u_{j+2} \quad (\text{A.8})$$

with the coordinates being included in the coefficients. Their derivation is based on a Taylor-series expansion at the considered point x_j . For simplicity we may define the local step sizes at

$$\begin{aligned} \Delta x_{m2} &= x_j - x_{j-2}, & \Delta x_{m1} &= x_j - x_{j-1}, \\ \Delta x_{p1} &= x_{j+1} - x_j, & \Delta x_{p2} &= x_{j+2} - x_j \end{aligned} \quad (\text{A.9})$$

to express the coefficients of the biased explicit finite differences for the first and second derivatives given in tables A.1 and A.2, respectively. For the particular case of an equidistant grid, the values of equation (A.9) are $\Delta x_{m2} = \Delta x_{p2} = 2 \cdot \Delta x$ and $\Delta x_{m1} = \Delta x_{p1} = \Delta x$. This results in the well-known standard FDs.

In case of grid transformation, the grid is considered in terms of metric coefficients and not by the stencil of the finite difference itself. For the evaluation of metric coefficients and spatial derivatives in computational ξ -space, standard finite differences are used. The resulting metric terms are provided by equations (A.10)-(A.11) and (A.12)-(A.13) for analytical and numerical grid transformation, respectively:

$$\frac{\partial x}{\partial \xi_{an.}} = c \cdot x = \frac{\Delta x_{ref}}{\Delta \xi} \quad (\text{A.10})$$

$$\frac{\partial^2 x}{\partial \xi^2_{an.}} = c^2 \cdot x = c^* \frac{\Delta x_{ref}}{\Delta \xi^2} \quad (\text{A.11})$$

$$\frac{\partial x}{\partial \xi_{num.}} = \Delta x_{ref} \left(\mathbf{a} \cdot e^{-2c^*} + \mathbf{b} \cdot e^{-c^*} + \mathbf{c} + \mathbf{d} \cdot e^{c^*} + \mathbf{e} \cdot e^{2c^*} \right) \quad (\text{A.12})$$

$$\frac{\partial^2 x}{\partial \xi^2_{num.}} = \Delta x_{ref} \left(\mathbf{a} \cdot e^{-2c^*} + \mathbf{b} \cdot e^{-c^*} + \mathbf{c} + \mathbf{d} \cdot e^{c^*} + \mathbf{e} \cdot e^{2c^*} \right) \quad (\text{A.13})$$

$\frac{\partial}{\partial x}$	$\mathcal{O}2$	$\mathcal{O}4$
a	0	$\frac{\Delta x_{m1} \Delta x_{p1} \Delta x_{p2}}{\Delta x_{m2} (\Delta x_{p2} + \Delta x_{m2}) (\Delta x_{p1} + \Delta x_{m2}) (\Delta x_{m2} - \Delta x_{m1})}$
b	$-\frac{\Delta x_{p1}}{\Delta x_{m1} (\Delta x_{p1} + \Delta x_{m1})}$	$-\frac{\Delta x_{m2} \Delta x_{p1} \Delta x_{p2}}{\Delta x_{m1} (\Delta x_{p2} + \Delta x_{m1}) (\Delta x_{p1} + \Delta x_{m1}) (\Delta x_{m2} - \Delta x_{m1})}$
c	$\frac{\Delta x_{p1} - \Delta x_{m1}}{\Delta x_{p1} \cdot \Delta x_{m1}}$	$-\frac{(\Delta x_{m1} \Delta x_{m2} \Delta x_{p1}) + (\Delta x_{m1} \Delta x_{m2} \Delta x_{p2}) - (\Delta x_{m1} \Delta x_{p1} \Delta x_{p2}) - (\Delta x_{m2} \Delta x_{p1} \Delta x_{p2})}{\Delta x_{m2} \Delta x_{m1} \Delta x_{p1} \Delta x_{p2}}$
d	$\frac{\Delta x_{m1}}{\Delta x_{p1} (\Delta x_{p1} + \Delta x_{m1})}$	$-\frac{\Delta x_{p1} (\Delta x_{p1} - \Delta x_{p2}) (\Delta x_{p1} + \Delta x_{m1}) (\Delta x_{p1} + \Delta x_{m2})}{\Delta x_{m2} \Delta x_{m1} \Delta x_{p1} (\Delta x_{p1} + \Delta x_{m1}) (\Delta x_{p1} + \Delta x_{m2})}$
e	0	$\frac{\Delta x_{p2} (\Delta x_{p2} + \Delta x_{m1}) (\Delta x_{p2} + \Delta x_{m2}) (\Delta x_{p1} - \Delta x_{p2})}{\Delta x_{p2} (\Delta x_{p2} + \Delta x_{m1}) (\Delta x_{p2} + \Delta x_{m2}) (\Delta x_{p1} - \Delta x_{p2})}$

Table A.1: Coefficients of explicit biased finite differences for the first derivative of 2^{nd} and 4^{th} order accuracy.

$\frac{\partial^2}{\partial x^2}$	$\mathcal{O}2$	$\mathcal{O}4$
a	0	$-2 \frac{\Delta x_{p1} \Delta x_{p2} - \Delta x_{m1} \Delta x_{p2} - \Delta x_{m1} \Delta x_{p1}}{\Delta x_{m2} (\Delta x_{m2} + \Delta x_{p2}) (\Delta x_{m1} - \Delta x_{m2}) (\Delta x_{p2} + \Delta x_{m2})}$
b	$\frac{2}{\Delta x_{m1} (\Delta x_{m1} + \Delta x_{p1})}$	$\frac{2 \Delta x_{p1} \Delta x_{p2} - \Delta x_{m2} \Delta x_{p2} - \Delta x_{m2} \Delta x_{p1}}{\Delta x_{m1} (\Delta x_{m1} + \Delta x_{p1}) (\Delta x_{m1} + \Delta x_{p2}) (\Delta x_{m1} - \Delta x_{m2})}$
c	$-\frac{2}{\Delta x_{m1} \Delta x_{p1}}$	$\frac{2 (\Delta x_{p1} \Delta x_{p2}) - (\Delta x_{m1} \Delta x_{p2}) - (\Delta x_{m2} \Delta x_{p2}) - (\Delta x_{m1} \Delta x_{p1}) - (\Delta x_{m2} \Delta x_{p1}) + (\Delta x_{m1} \Delta x_{m2})}{\Delta x_{m2} \Delta x_{m1} \Delta x_{p1} \Delta x_{p2}}$
d	$\frac{2}{\Delta x_{p1} (\Delta x_{m1} + \Delta x_{p1})}$	$\frac{2 \Delta x_{m1} \Delta x_{p2} + \Delta x_{m2} \Delta x_{p2} - \Delta x_{m1} \Delta x_{m2}}{\Delta x_{p1} (\Delta x_{m2} + \Delta x_{p2}) (\Delta x_{m2} + \Delta x_{p1}) (\Delta x_{p2} - \Delta x_{p2})}$
e	0	$-2 \frac{\Delta x_{m1} \Delta x_{p1} + \Delta x_{m2} \Delta x_{p1} - \Delta x_{m1} \Delta x_{m2}}{\Delta x_{p2} (\Delta x_{m2} + \Delta x_{p2}) (\Delta x_{p2} - \Delta x_{p1}) (\Delta x_{p2} + \Delta x_{m1})}$

Table A.2: Coefficients of explicit biased finite differences for the second derivative of 2^{nd} and 4^{th} order accuracy.

With the derivatives in physical space, the modified wavenumber and its square can be easily computed from equation (3.1) and (3.2). The real and imaginary parts of the modified wavenumber k_{mod}^* and the wave number square k_{mod}^{*2} are considered for two exemplary grid-stretching factors $c^* = 1$ and $c^* = 0.3$. They correspond to an increase of the physical step size Δx by a factor of $e = 2.718$ and 1.35, respectively. Thus, the resolution of a wave at the outer left and right grid points of a five-point stencil differs by a factor of 20 for $c^* = 1$. Despite one would not choose such a strong stretching for real applications, it clearly demonstrates the properties of the three different discretization methods on non-uniform grids.

The real and imaginary parts of the modified wavenumber k_{mod}^* of the first derivative based on three- and five-point stencils are shown in figure A.1 and A.2, respectively. The range of normalized wavenumber $0 \leq k^* \leq \pi$ in the plots is somewhat arbitrary. With the wavenumber k being normalized with Δx_{ref} , the value $k^* = \pi$ does not correspond to the least resolved wave as it is known from equidistant grids. Using the locally varying stepsize Δx , the resolution may be expressed in terms of points per wavelength λ_x :

$$\frac{n_{points}}{\lambda_x} = \frac{2\pi}{k \cdot \Delta x} = \frac{2\pi}{k^* \cdot \frac{\Delta x}{\Delta x_{ref}}} \quad . \quad (\text{A.14})$$

The value of $k^* = \pi$ being the abscissa's maximum value in the diagrams corresponds to a number of points per wavelength of 8.6, 3.2, 1.2 and 0.4 for the physical stepsizes $(x_{j-1} - x_{j-2})$, $(x_j - x_{j-1})$, $(x_{j+1} - x_j)$ and $(x_{j+2} - x_{j+1})$, respectively. For smaller values of c^* , the variation decreases. Independently of c^* , $\frac{n_{points}}{\lambda_x}$ for $k^* = \pi$ is larger than two for the first two points and smaller than two for the two right points of the stencil. Equation A.1 reveals that the first derivatives in physical space based on analytical and numerical metric coefficients simply differ by the factor of the differently computed metric terms. Thus, this is also the case for real and imaginary parts of the modified wavenumber.

First Derivative based on 3-Point Stencil

As one can see in figure A.1 a), the biased finite difference provides the best dispersion properties for the three-point stencil on the exponentially stretched grid with $c^* = 1$. Compared to analytically and numerically computed metric coefficients, the characteristic of the biased discretization differs less from the exact solution $k_{mod,r,exact}^* = k^*$. The analytical metric coefficients result in higher values for both real and imaginary parts of the modified wave number than the numerically computed metrics. In case of analytical metric coefficients,

the increase $\partial k_{mod,r}^*/\partial k^*$ of the modified wavenumber is slightly too large for well resolved waves. For numerically computed metric coefficients, good wave propagation properties are achieved up to $k^* \approx 0.6$. Aliasing occurs for both grid-transformation methods for values $k^* > 1$. If a biased FD is used, the imaginary part $k_{mod,i}^*$ of the modified wave number becomes negative (figure A.1 b). Thus, waves traveling in the direction of grid coarsening are successively damped. For the methods involving metric terms, these waves are amplified with increasing wave number up to $k^* \approx 2.7$. Less resolved waves ($k^* > 2.7$) are slightly damped.

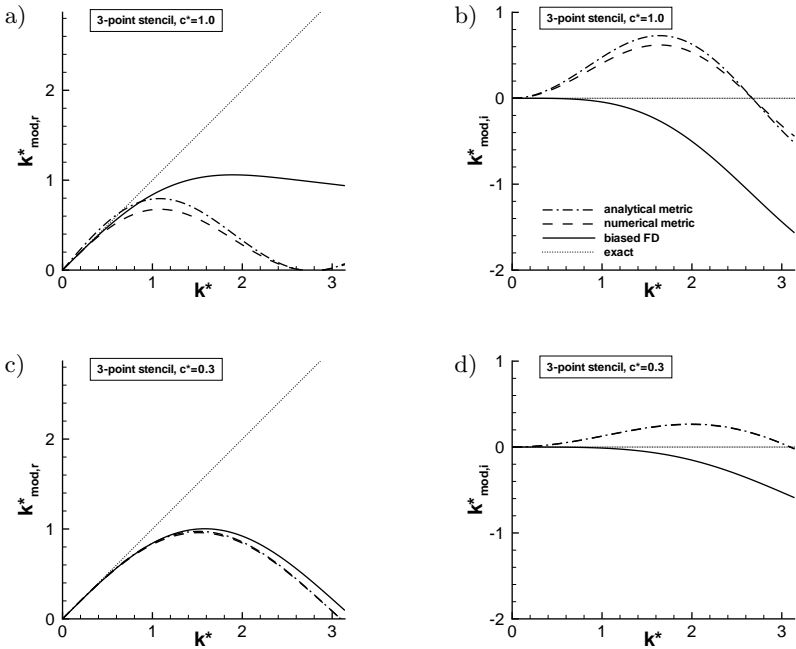


Figure A.1: Real and imaginary parts of the modified wave number k_{mod}^* for stretching factors $c^* = 1.0$ and $c^* = 0.3$ using explicit finite differences based on 3-point stencils.

For the weaker stretching $c^* = 0.3$, real and imaginary parts of the modified wave number are given in figures A.1 c) and d), respectively. Now, all three methods provide similar results for the real part $k_{mod,r}^*$ with the dispersion relation being almost equal to 2^{nd} -order FDs on a uniform mesh (see figure 3.2). The limiting factor for the accuracy is the imaginary part $k_{mod,i}^*$. In case of grid transformation, notable amplification for waves in the direction of grid coarsening exists. Also for smaller stretching ratios, this can not be neglected: e.g. a stepsize increase of 10% ($c^* = 0.1$) yields a maximum of $k_{mod,i}^* = 0.09$.

First Derivative based on 5-Point Stencil

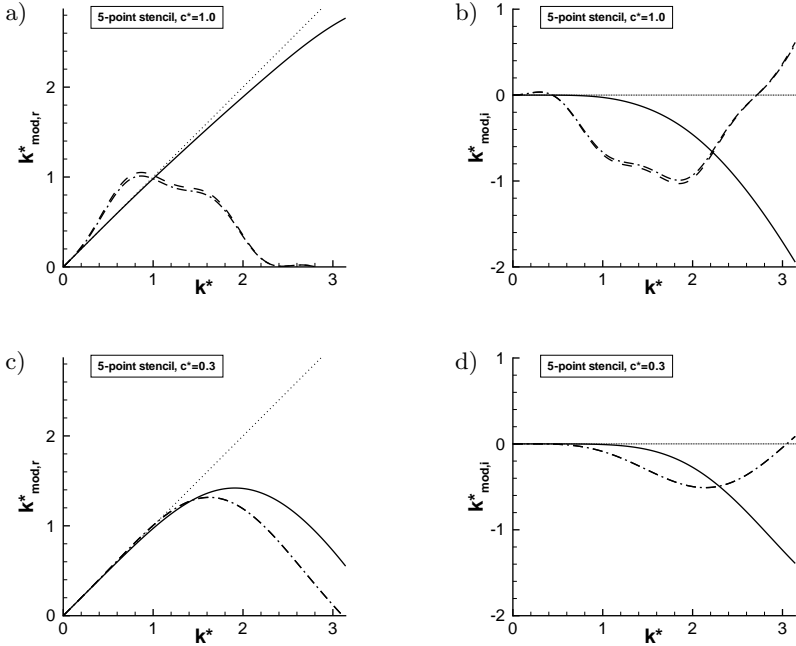


Figure A.2: Real and imaginary parts of the modified wave number k_{mod}^* for stretching factors $c^* = 1.0$ and $c^* = 0.3$ using explicit finite differences based on 5-point stencils.

For the larger stencils, again the biased FD gives the best results in terms of wave propagation, as shown in figure A.2 a) for $c^* = 1$. The difference between analytically and numerically evaluated metrics is less obvious than for the discretization based on second order FDs. The absolute values of the real and imaginary parts are slightly larger for the numerical grid transformation. Now, acceptable wave propagation properties are possible only up to $k^* \approx 0.3$. This smaller value compared to the three-point stencil is due to the fact that a stronger grid stretching is included in the stencil with the outer point x_{j+2} of the FD. Like for the three-point stencil, poorly resolved waves are damped for the 4th-order biased discretization as they propagate in the direction of coarsening since $k_{mod,i,bias}^* < 0$. This is also the case for grid-transformation methods in the range of $0.4 < k^* < 2.7$. Waves with smaller wave numbers are only slightly amplified compared to the least resolved waves exhibiting a distinct amplification.

The case of a weaker stretching ($c^* = 0.3$) is shown in figures A.2 c) and d). Now, the 5-point stencil provides a better result than the 3-point stencil in contrast to $c^* = 1$. The value $c^* \approx 0.4$ (50% increase of step size) was found to be the limit for the 5-point stencil to be more accurate than the 3-point stencil. Compared with figure 3.2 a), the dispersion properties for $c^* = 0.3$ are already quite similar to the equidistant spacing. With $k_{mod,i,min}^* = -0.52$ for biased FDs and $k_{mod,i,min}^* = -0.19$ for both grid-transformation methods, dissipation is still a relevant issue. Thus, damping is only weakly affected by coarsening of the grid. An acceptably low damping ($|k_{mod,i}^*| < 0.1$) for relatively well-resolved waves ($k^* < \pi/2$) is observed for $c^* \approx 0.1$ (step size increase by 10%).

Order of First Derivatives

The order of a scheme describes how the leading discretization error is reduced with increased resolution. The relative error of the first derivative can be expressed by the modified wave number to

$$\epsilon = \left| \frac{\sqrt{\left(k_{mod,r}^*\right)^2 + \left(k_{mod,i}^*\right)^2} - k^*}{k^*} \right|. \quad (\text{A.15})$$

Its dependence from the resolution, expressed by the number of grid points per wavelength ($= 2\pi/k^*$), is shown in figure A.3 a) for the 3-point stencil with $c^* = 0.3$. Increasing the resolution by a factor of four reduces the error to one fourth in case of biased FDs and numerical metric coefficients. Thus, these

methods are of second order as it is the case on equidistant grids. With its error being limited to $\epsilon = 0.015$, the method of analytically computed metric coefficients is of zeroth order.

Figure A.3 b) shows the corresponding results for the five-point stencil. Again, the biased FDs are of the same order ($\mathcal{O}4$) as on uniform grids. In case of numerically computed metrics, the error decays like for the 3-point FD. Thus, a larger stencil does not increase the order, rather the magnitude of the error is decreased. The error of analytical metric terms is bound to $\epsilon = 2 \cdot 10^{-4}$. Despite the error is reduced, it is still of $\mathcal{O}0$.

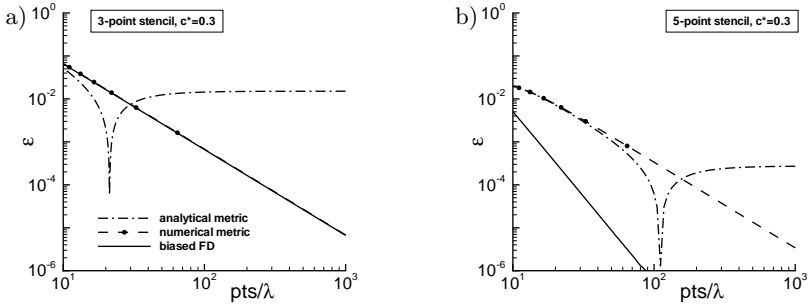


Figure A.3: Relative error of the first derivative versus the resolution for stretching factor $c^* = 0.3$): a) 3-point stencil, b) 5-point stencil.

The kink in the error for analytically computed metrics occurs where errors of the real and imaginary part cancel each other. Hence, considering only the order of a scheme provides less information compared to the modified wave number analysis. In general, the order is defined as

$$\mathcal{O} = -\frac{\partial \{\log(\epsilon)\}}{\partial \{\log(pts/\lambda)\}}. \tag{A.16}$$

Its dependence from the stretching factor is shown in figure A.4 for the 5-point stencil and $k^* = 0.311$ ($20pts/\lambda$). For vanishing grid stretching ($c^* \rightarrow 0$), numerical metric coefficients result in the fourth order known from the uniform mesh. At $c^* = 0.06$, a pole exists where amplitude and phase errors cancel each other. Then the scheme decreases to second order.

It is quite astonishing that the numerical metric coefficient provides a better result. Obviously, discretization errors of the derivative in computational space

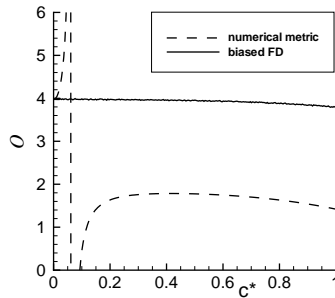


Figure A.4: Discretization order \mathcal{O} of the first derivative's 5-point stencil as a function of the stretching factor c^* ($20pts/\lambda$).

and of the metric coefficients cancel each other. A remarkable fact is also that an increased stencil does not increase the order on the non-uniform grid to more than two. However, the leading error is only in the imaginary part for numerically computed metrics, resulting in an exact group velocity of up to second spectral order.

Second Derivative based on 3-Point Stencil

The computation of the second derivative with a second-order biased FD gives the best accordance with the exact solution k^{*2} for the real part of the modified wave number square, given in figure A.5 a) for $c^* = 1$. Using numerical metric coefficients gives a similar result. However, deviation from the exact solution occurs for smaller values of k^* , and the maximum value of k_{mod}^{*2} is roughly 20% smaller than for the biased finite difference. The imaginary part is slightly smaller, thus less artificial convection is generated than is done by the biased FD. In the case of analytically computed metrics, the characteristics of k_{mod}^{*2} differs from the exact solution for the real and imaginary parts already for very small values of k^* . All three methods cause a positive value of $k_{mod,i}^{*2}$ (figure A.5 b) and thus an artificial advection in the direction of grid coarsening. For the weaker stretching $c^* = 0.3$, the real parts $k_{mod,r}^{*2}$ collapse for the three methods as shown in figure A.5 c). Similar to the stronger stretching, a positive value of $k_{mod,i}^{*2}$ is obtained for all methods (figure A.5 d). Biased FDs and numerical metric provide almost the same results, here. The value $c^* = 0.3$ is approximately the limit of acceptable accuracy for appropriately resolved waves ($k^* < \pi/2$) if biased FDs or numerically computed metric coefficients are used.

Analytical metrics are an exception here, since notable values of $k_{mod,i}^{*2}$ exist even for low stretching ratios and small values of k^* .

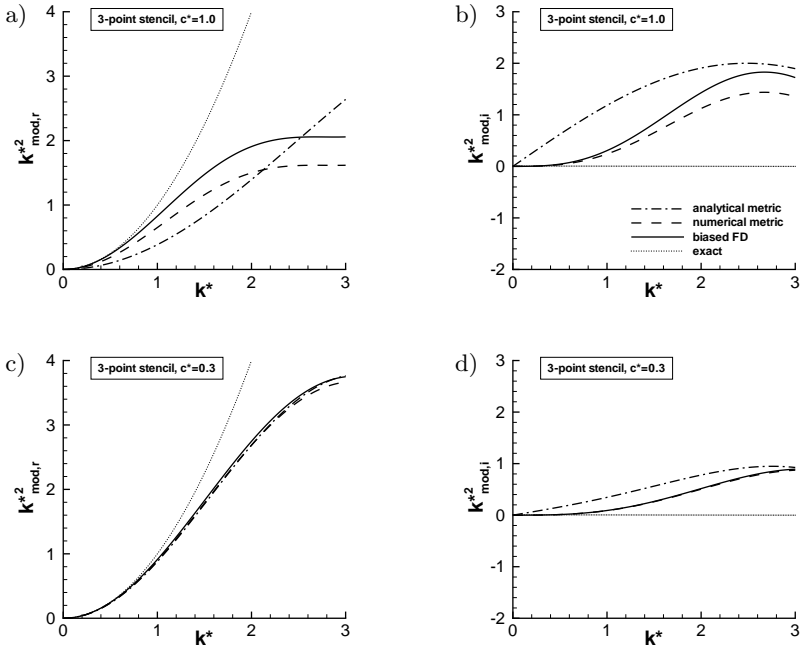


Figure A.5: Real and imaginary parts of the modified wave number square k_{mod}^{*2} for stretching factors $c^* = 1.0$ and $c^* = 0.3$ based on 3-point stencil.

Second Derivative based on 5-Point Stencil

For the 5-point stencils applied to the stretching factor $c^* = 1$, the real parts of the modified wave number square show a better agreement with the exact solution than the 3-point stencil for all three methods (figure A.6 a). At small values of k^* , the weakest deviation is given for the biased finite difference. Its value grows up to $k^* = 2.25$ and decreases above. For the two methods using grid transformation, higher values of $k_{mod,r}^{*2}$ are reached, remaining almost constant for poorly resolved waves. The imaginary part, given in figure A.6 b),

differs for biased FDs and grid transformation methods. For the latter, $k_{mod,i}^{*2}$ increases up to $k^* \approx 2.8$, meaning an artificial convection in the direction of grid coarsening.

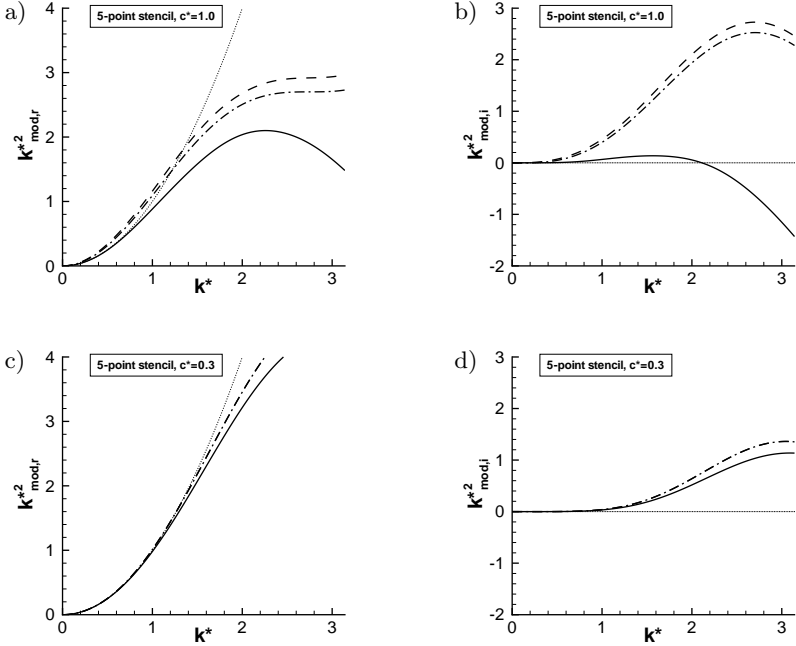


Figure A.6: Real and imaginary parts of the modified wave number square k_{mod}^{*2} for stretching factors $c^* = 1.0$ and $c^* = 0.3$ based on 5-point stencil.

If the biased FD is used, first, the imaginary part slightly increases. For higher wave numbers, $k_{mod,i}^{*2}$ declines to negative values for $k^* > 2.1$ meaning an artificial advection in the direction of grid refinement. Unlike the first derivative, the 3-point stencil does not provide better results than the 5-point stencil when grid transformation is applied to the strong stretching ratio $c^* = 1$.

The case of weaker grid coarsening ($c^* = 0.3$) is shown in figures A.6 c) and A.6 d) for the real and imaginary parts of the modified wavenumber square k_{mod}^{*2} , respectively. The real part is almost the same for all three methods. Unlike

for the stronger step-size ratio $c^* = 1$, biased FDs provide a positive value of $k_{mod,i}^{*2}$ similar to the grid-transformation methods. Thus, all three implementations of non-uniform grids induce an artificial advection in the direction of grid coarsening, here. Considering well-resolved waves ($k^* < \pi/2$), acceptable accuracy is achieved up to $c^* \approx 0.3$ as shown by figures A.6 c) and A.6 d).

Order of Second Derivatives

For the second derivatives, the relative error is given by

$$\epsilon = \left| \frac{\sqrt{\left(k_{mod,r}^{*2}\right)^2 + \left(k_{mod,i}^{*2}\right)^2} - k^{*2}}{k^{*2}} \right| \tag{A.17}$$

which is shown in figures A.7 a) and b) for the 3- and 5-point stencils, respectively. Plotted versus the number of grid points per wave length, it allows to determine the order as done for the first derivative.

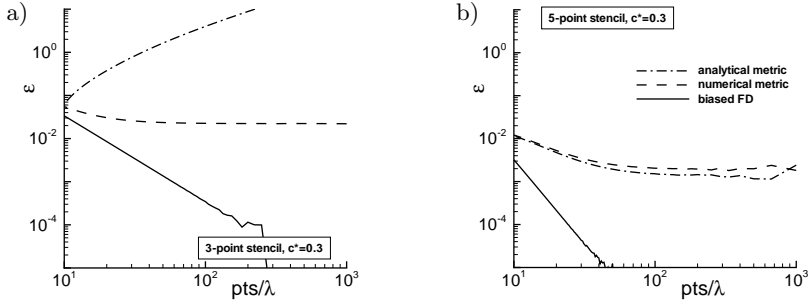


Figure A.7: Relative error of the second derivative versus the resolution for stretching factor $c^* = 0.3$): a) 3-point stencil, b) 5-point stencil.

For the 3- and 5-point stencils, the biased FDs are of second and fourth order, respectively. The error of numerical metric coefficients slightly reduces reaching its final level of $\epsilon = 2 \cdot 10^{-2}$ and $\epsilon = 2 \cdot 10^{-3}$ for the 3- and 5-point stencils, respectively. Hence, the increased stencil reduces the overall error by one magnitude. For well resolved problems, the order of the second derivative computed by numerical metric coefficients is of zeroth order independently of

the involved grid points. With an increasing error, the 3-point stencil provides inconsistent results. Yet this is not the case for the 5-point FD whose error behaves similar to one with the numerical metrics. The order according to equation (A.16) is shown in figure A.8 as a function of the stretching factor c^* for $k^* = 0.311$. On almost uniform grids ($c^* \rightarrow 0$), the order of all three methods is consistently four. For stretching factors $c^* > 0.2$ the order of both grid transformation methods reduces linearly with c^* .

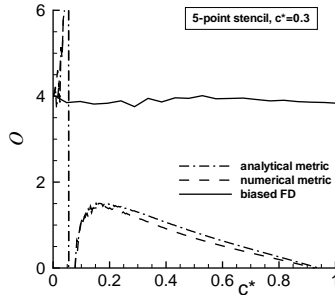


Figure A.8: Discretization order \mathcal{O} of the second derivative's 5-point stencil as a function of the stretching factor c^* ($20pts/\lambda$).

A.2 One-dimensional Numerical Investigation

Numerical Scheme

To investigate the effects of grid stretching for compact finite differences, we have to rely on numerical experiments. Therefore, the one-dimensional linear advection-diffusion equation (A.3) is solved in a periodic domain $x \in [0; x_{end}[$ with constant diffusion and advection speed. The initial condition and the resulting exact solution for this partial differential equation are given by equations (A.18) and (A.19), respectively, where $\alpha_0 = 2\pi/x_{end}$ is the fundamental wavenumber and $\alpha_k = \alpha/\alpha_0$ the number of wavelengths in the domain:

$$u_{(t=0)} = \cos(\alpha \cdot x) \quad (\text{A.18})$$

$$u_{exact} = e^{-d \cdot \alpha^2 \cdot t} \cdot \cos(\alpha[x - c \cdot t]) . \quad (\text{A.19})$$

Time integration is done using the classical 4th-order Runge-Kutta scheme (section 3.3.2). The spatial discretization is based on compact finite differences

of 4^{th} order. For the first and second derivatives, the coefficients of the biased compact scheme are given by Shukla & Zhong [90]. For equidistant grids, the stencils for first and second derivatives reduce to

$$u'_{j-1} + 4u'_j + u'_{j+1} = \frac{3}{\Delta\xi} (u_{j+1} - u_{j-1}) \quad (\text{A.20})$$

$$u''_{j-1} + 10 \cdot u''_j + u''_{j+1} = \frac{12}{\Delta\xi^2} (u_{j+1} - 2u_j + u_{j-1}) \quad , \quad (\text{A.21})$$

respectively. These stencils are the standard 4^{th} -order compact schemes with the constant step size $\Delta\xi$. The term “standard” means that the order is maximal for the stencil width. In case of grid transformation, the physical non-uniform grid is mapped on an equidistant computational grid. Spatial derivatives in physical space are then computed by equations (A.20) and (A.21) using the derivatives in computational space and multiplying them with the corresponding local metric coefficients at point x_j , given by equation (A.1) and (A.2). Additionally, explicit finite differences as discussed in section A.1 are implemented to see the difference between explicit and compact discretization on non-uniform grids.

Results

The used grid is stretched in the first half of the domain according to the transformation given below:

$$x(\xi) = \frac{1+s}{2} \cdot \xi + \frac{s-1}{2b} \cdot [\ln(\cosh(b(\xi - \xi_1))) - \ln(\cosh(-b\xi_1))] \quad (\text{A.22})$$

$$\frac{\partial x}{\partial \xi} = \frac{s-1}{b} \cdot \tanh(b(\xi - \xi_1)) + \frac{1+s}{2} \quad (\text{A.23})$$

$$\frac{\partial^2 x}{\partial \xi^2} = \frac{b(s-1)}{2} - \frac{b(s-1) \sinh(b(\xi - \xi_1))^2}{\cosh(b(\xi - \xi_1))^2} \quad (\text{A.24})$$

In order to have an almost sudden coarsening of the grid given by an analytical function, the metric coefficient $\partial x/\partial \xi$ is modelled by a tanh function. The grid stretching is defined by the ratio $s = \Delta x_{max}/\Delta x_0$. The mesh starts with the regular stepsize Δx_0 , increasing to the coarse Δx_{max} at the position ξ_1 . The parameter b defines how fast the stepsize is increased: large values of b compress the tanh profile of $\partial x/\partial \xi$ leading to a sharp switch from fine to coarse spacing. The following refinement of the grid is done accordingly.

For the current investigation a computational grid with 100 points and a regular spacing of $\Delta x_0 = \Delta\xi = 0.03141$ has been used. In half the domain, the spacing is $\Delta x = 4 \cdot \Delta x_0$ with $s = 4$. The stretched area is located in the

middle of the domain with $\xi_1 = 1/4\xi_{end}$ ($x_1 = 0.8$) and $\xi_2 = 3/4\xi_{end}$ ($x_2 = 7.0$) being the begin of coarsening and refinement, respectively. With $b = 100$, a rapid transition between the different stepizes is achieved. The total length of the domain is 7.8525, resulting in a fundamental wavenumber $\alpha_0 = 0.8$ of the domain. Figure A.9 shows the grid transformation $x(\xi)$ and the metric coefficients $x_\xi = \partial x / \partial \xi$ and $x_{\xi\xi} = \partial^2 x / \partial \xi^2$ for analytical and numerical evaluation.

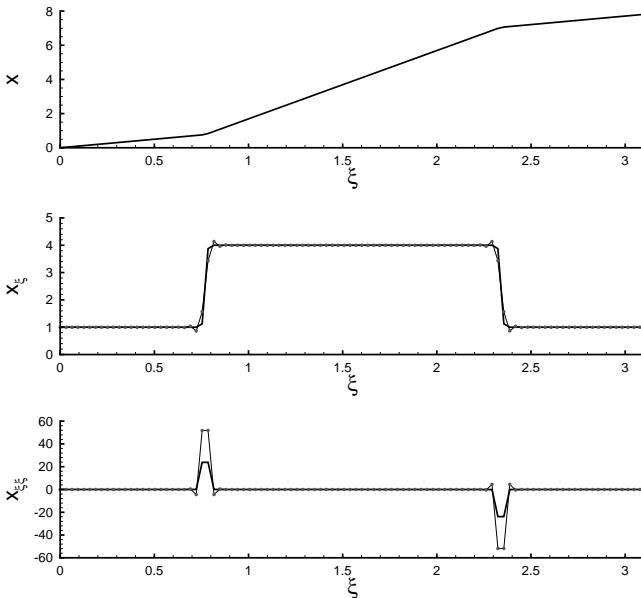


Figure A.9: Grid transformation $x(\xi)$ with the corresponding metric coefficients x_ξ and $x_{\xi\xi}$. The black solid line corresponds to the analytical metric coefficients. The numerically computed metric terms are given by the thin grey line with the discrete grid points indicated by dots.

The effect of different grid-stretching mechanisms is investigated by computing (i) a pure convection case ($c = 1, d = 0$) and (ii) a pure diffusion problem ($c = 0, d = 1$). The initial condition of both cases contains $n_\alpha = \alpha/\alpha_0 = 4$ wavelengths inside the domain. With the non-dimensional wave numbers $k^* = \alpha \cdot \Delta x = 0.025$ and $k^* = \alpha \cdot s \Delta x = 0.1$, the wave is well resolved with 250

and 62.5 points per wavelength in the fine and coarse regions, respectively. Therefore, the change of the grid and not the actual resolution mainly effects the accuracy of the result here. The time steps are $\Delta t = 0.015705$ and $\Delta t = 0.0001353$ for the advection and diffusion problem, respectively. In case of the pure advection, the wave of the initial condition is resolved with 125 time steps per period. With the high temporal resolution, effects due to the time-integration scheme can be neglected. For both cases, a total number of 500 time steps has been computed. The resulting computed time of the convection case corresponds to one flow-through time of the domain. For the diffusion problem, the amplitude is halved after the computed time steps. The exact solution is shown in figure A.10 for both cases after the corresponding computed time.

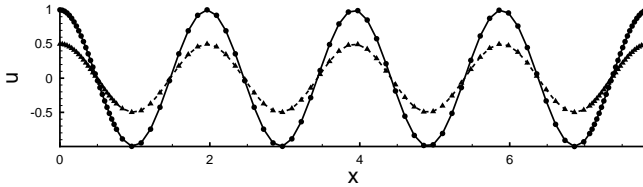


Figure A.10: Exact solutions for the advection problem (solid line with circles) and the diffusion problem (dashed line with triangles). The time corresponds to one flow-through time and one half-life period, respectively. The symbols refer to the grid points.

A.2.0.1 Advection Case

For the advection case, the quality of the computed first derivative is time dependent. As the wave travels through the domain, the largest error occurs when the maximum of the first derivative is located near positions of coarsening or refinement of the grid. Figure A.11 shows the temporal evolution of the solution for 2^{nd} -order explicit and 4^{th} -order compact FDs, both for analytical and numerical metric coefficients. During the temporal interval of 100 time steps, shown here, the wave travels along a distance of 1.57. The compact scheme provides an almost accurate solution with no observable differences between the two methods of grid transformation. The low-order methods show the same phase error increasing with time.

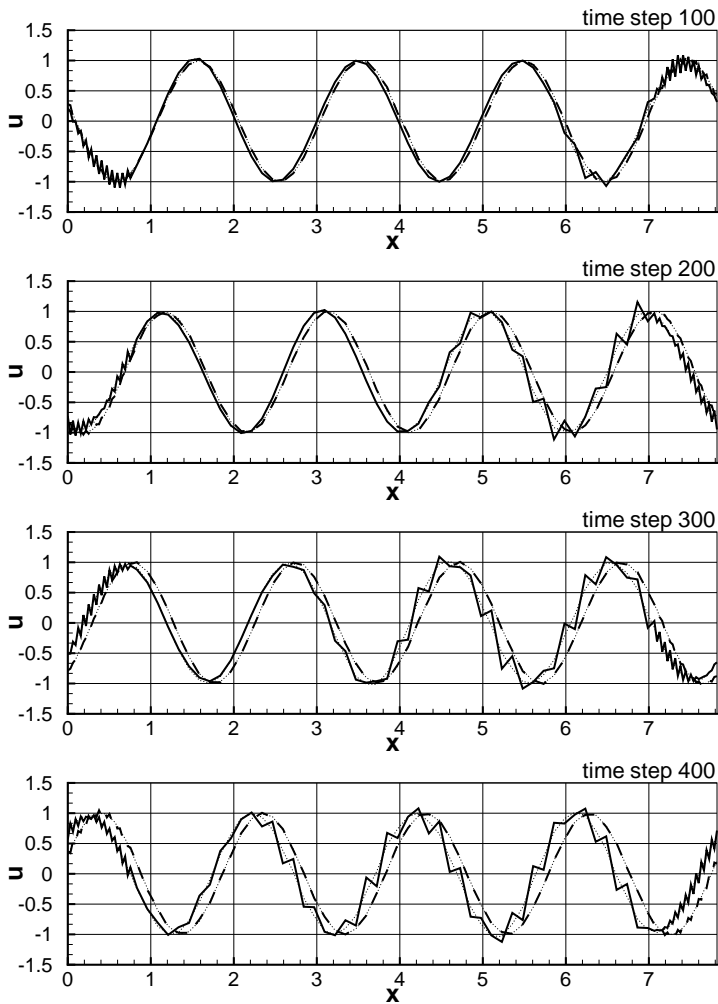


Figure A.11: Solution of the advection problem at various time steps. The dotted line corresponds to numerical metric coefficients. The solid and dashed lines refer to analytical metric coefficients based on 2nd-order explicit and 4th-order compact FDs, respectively.

The difference between the two grid-transformation methods is the strong generation of wiggles for analytical metrics. They are firstly generated at the coarsening of the mesh ($x = 0.8$). Having a negative group velocity, the wiggles move upstream and enter the domain at the right due to the periodicity of the problem. Between time step 100 and 200, the region of refinement ($x = 7.0$) is reached. Further on, the wiggles move into the coarse region and increase furthermore, spoiling the solution.

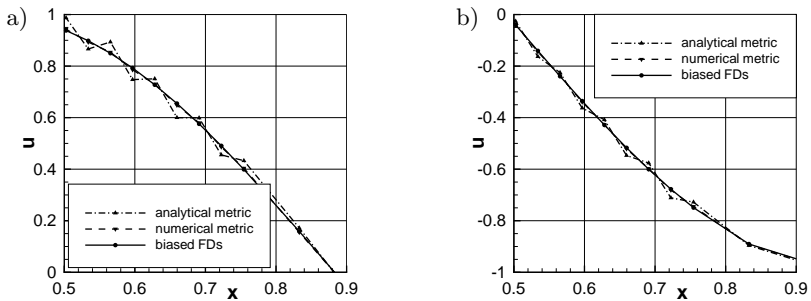


Figure A.12: Solution of the advection case based on 4th-order compact FDs: a) time step 400 (80% of flow-through time), b) time step 500 (one flow-through time).

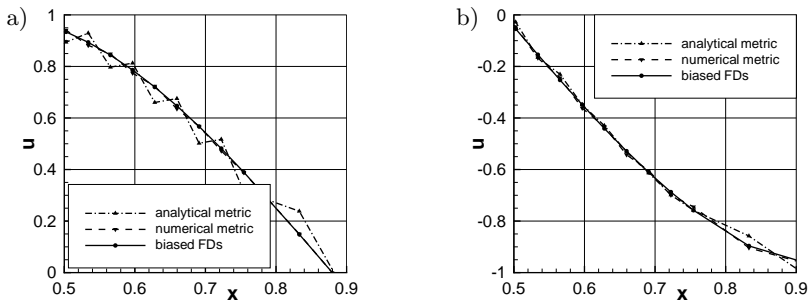


Figure A.13: Result as figure A.12 but for 4th-order explicit FDs: a) time step 400 (80% of flow-through time), b) time step 500 (one flow-through time).

For the compact 4th-order stencils, figures A.12 a) and b) show the different solutions in the region of grid stretching at time step 400 and 500, respectively. Time step 400 corresponds to $u \approx 0$ and thus the maximum of $|\partial u / \partial x|$ located at the beginning of grid stretching. At both time steps, the solution of the biased compact FDs and the numerical metric coefficients is similar. The computation using analytical metric coefficients shows the worst results resulting in wiggles in the area of fine grid spacing. For the computation using numerical metric coefficients, wiggles are also present but much smaller.

In order to evaluate the difference between explicit and compact stencils for this numerical example, equation (A.3) has been computed using the explicit five-point stencils as well. In figures A.13 a) and b), the solution is shown for time steps 400 and 500, respectively. The difference between the biased finite difference, the analytical and the numerical grid transformation is similar to the computation based on the compact scheme. The explicit stencils give a larger wobble mode which is most obvious at time step 400 for the analytical metric coefficients.

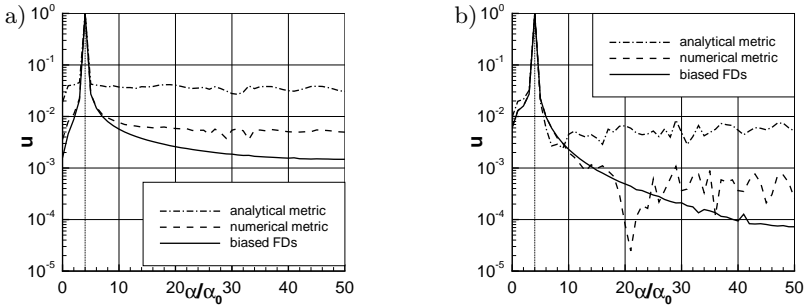


Figure A.14: Streamwise spectrum for the advection case, based on 4th-order compact FDs: a) time step 400, b) time step 500.

Having a periodic domain, a Fourier analysis in x -direction is applied to evaluate the dispersion properties of the three grid-stretching implementations. In figures A.14 a) and b), the streamwise spectrum is shown. The exact solution is a single amplitude of $u = 1$ at a spanwise wavenumber $\alpha/\alpha_0 = 4$, indicated by the dotted line in the spectra. At timestep 400, the analytical metric coefficients give an amplitude of $4 \cdot 10^{-2}$, almost constant along the whole spectrum. After one whole flow-through time (time step 500), the high-wavenumber amplitudes decrease to $5 \cdot 10^{-3}$. For the lower wavenumbers, only

a minor reduction occurs. The numerically computed metric coefficients lead to a spectrum approximately one magnitude smaller for both time steps considered here. The biased scheme provides a smooth decay for high wavenumbers. At low wavenumbers, the spectra of numerical metric coefficients and biased compact finite differences are almost identical.

A.2.0.2 Diffusion Case

Without convection speed ($c = 0$), the time dependence of the accuracy of the second derivative is only due to its decreasing amplitude. Thus, it is sufficient to consider only one time step. Figure A.15 a) compares the solutions for the compact scheme at time step 500, corresponding to one half-life period. Both numerical metric coefficients and biased FDs give a good approximation. For the analytical metric coefficients, the damping rate in the vicinity of the coarsening of the grid is too small. In the highly resolved part of the domain, shown in figure A.15 b), the damping rate is slightly too large. If the explicit five-point stencils are used, no relevant difference to the compact schemes can be observed.

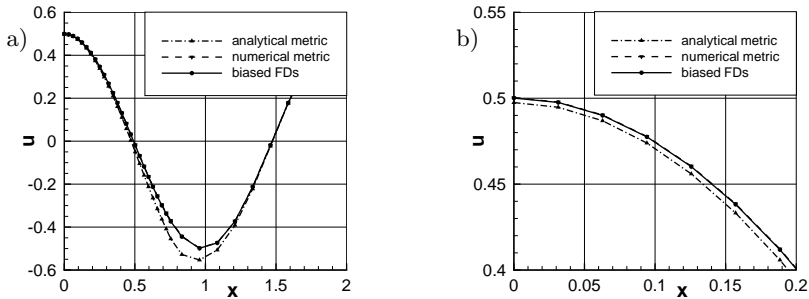


Figure A.15: a) Comparison of the three grid-stretching mechanisms (4^{th} -order compact FDs) for the diffusive case at time step 500 (one half-life period), b) detailed view.

The instantaneous error $|u - u_{exact}|$ of the compact schemes is plotted in figure A.16 a). The biased compact finite differences show the lowest error in the range of $4 \cdot 10^{-5}$ with the main derivation located in the stretched section of the grid. Both analytical and numerical metric coefficients have a maximum error of $8 \cdot 10^{-2}$ and $4 \cdot 10^{-3}$, respectively. The error peaks are at the locations of coarsening and refinement while in the coarse region, the error is similar to the

one of the biased FDs. The streamwise spectrum of the diffusion case is given in figure A.16 b) where the exact solution $u = 0.5$ at $\alpha/\alpha_0 = 4$ is indicated by a dotted line. The spectra of the biased FDs and the numerical metric coefficients show a smooth decay for the higher wavenumbers and the amplitudes of the lower wavenumbers decline to values of $3 \cdot 10^{-3}$. The numerically computed metric coefficients show an additional oscillation for the higher wave numbers. For the analytical metric coefficients, this oscillation is larger by almost one order of magnitude and the low-wavenumber amplitudes decrease less.

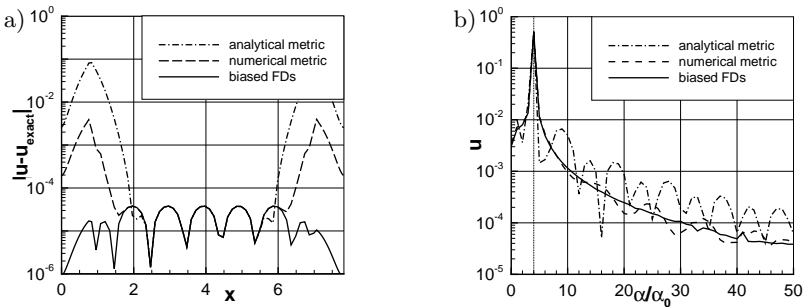


Figure A.16: a) Error of the three different grid stretching mechanisms at half-live level for the diffusion case.
b) Streamwise spectrum for the diffusive case at time step 500.

A.3 Summary

Although one might think analytically prescribed metric coefficients are the best choice, the theoretical analysis shows that this method is of zeroth order on the physical grid or may even cause inconsistent results. Furthermore it yields the wrong phase and group velocities even for arbitrarily resolved problems. In case of numerical metric terms, discretization errors of the derivatives in computational space and of the metric coefficients seem to cancel each other. The scheme is now of second and zeroth order on the non-uniform grid for first and second derivatives, respectively. It is notable that the order can not be increased but the magnitude of the error is decreased by a larger stencil. Biased finite differences show always the same order as on equidistant grids.

In the numerical investigation, a rapidly changing resolution creates a broad spectrum of artificial disturbances for all three methods. Numerical metric

coefficients show almost the same behavior as biased finite differences and the worst result is obtained for analytical metrics. Compact schemes are recommended since they reduce the error by almost one order of magnitude for the advection case. An additional numerical test for a transitional boundary layer can be found in [5].

B Coefficients of the LST Matrix Solver

In the following, the coefficients of the matrix solver for linear stability theory are listed. According to equation (3.96), coefficient matrices exist for the complex amplitude, its first and second y -derivative and terms containing the eigenvalue ω , being \mathbf{A}_0 , \mathbf{A}_1 , \mathbf{A}_2 and \mathbf{B} , respectively. The notation here corresponds to the one of Mack [63] where the pressure is normalized with the freestream pressure p_∞ instead of $\rho_\infty \cdot u_\infty^2$.

Note that the pressure distribution is only considered by its values and the wall-normal derivative of the pressure is neglected. However, using only $\partial p / \partial y = 0$ is a valid assumption for boundary layers.

Coefficients of matrix \mathbf{A}_0

$$a0_{11(j)} = I \cdot (\alpha U_{0(j)} + \gamma W_{0(j)}) \quad (\text{B.1})$$

$$a0_{12(j)} = I \cdot \alpha \rho_{0(j)} \quad (\text{B.2})$$

$$a0_{13(j)} = \frac{\partial \rho_{0(j)}}{\partial y} \quad (\text{B.3})$$

$$a0_{14(j)} = I \cdot \gamma \rho_{0(j)} \quad (\text{B.4})$$

$$a0_{15(j)} = 0 \quad (\text{B.5})$$

$$a0_{21(j)} = \frac{I \cdot \alpha}{\kappa Ma^2 \rho_{0(j)}} \cdot p_{0(j)} \quad (\text{B.6})$$

$$a0_{22(j)} = I \cdot \rho_{0(j)} (\alpha U_{0(j)} + \gamma W_{0(j)}) + \frac{\mu_{0(j)} (\frac{4}{3} \alpha^2 + \gamma^2) + \frac{2}{3} \mu_{B,0(j)} \alpha^2}{Re} \quad (\text{B.7})$$

$$a0_{23(j)} = \rho_{0(j)} \frac{\partial U_{0(j)}}{\partial y} - I \cdot \frac{(\frac{d\mu}{dT}) (\frac{\partial T_{0(j)}}{\partial y})}{Re} \alpha \quad (\text{B.8})$$

$$a0_{24(j)} = \frac{\alpha \gamma (2 \mu_{B,0(j)} + \mu_{0(j)})}{3Re} \quad (\text{B.9})$$

$$a0_{25(j)} = \frac{I \cdot \alpha}{\kappa Ma^2 T_{0(j)}} \cdot p_{0(j)} - \frac{\left(\frac{d^2 \mu}{dT^2}\right) \left(\frac{\partial T_{0(j)}}{\partial y}\right) \left(\frac{\partial U_{0(j)}}{\partial y}\right)}{Re} - \frac{\left(\frac{d\mu}{dT}\right) \left(\frac{\partial^2 U_{0(j)}}{\partial y^2}\right)}{Re} \quad (B.10)$$

$$a0_{31(j)} = -\frac{\left(\frac{\partial \rho_{0(j)}}{\partial y}\right)}{\kappa Ma^2 (\rho_{0(j)})^2} \cdot p_{0(j)} \quad (B.11)$$

$$a0_{32(j)} = \frac{2}{3} \cdot \frac{I \cdot \alpha \left(\frac{\partial T_{0(j)}}{\partial y}\right) \left(\frac{d\mu}{dT} - \frac{d\mu_B}{dT}\right)}{Re} \quad (B.12)$$

$$a0_{33(j)} = I \cdot \rho_{0(j)} (\alpha U_{0(j)} + \gamma W_{0(j)}) + \frac{\mu_{0(j)} (\alpha^2 + \gamma^2)}{Re} \quad (B.13)$$

$$a0_{34(j)} = \frac{2}{3} \cdot \frac{I \cdot \gamma \left(\frac{\partial T_{0(j)}}{\partial y}\right) \left(\frac{d\mu}{dT} - \frac{d\mu_B}{dT}\right)}{Re} \quad (B.14)$$

$$a0_{35(j)} = -\frac{\frac{\partial T_{0(j)}}{\partial y}}{\kappa Ma^2 (T_{0(j)})^2} \cdot p_{0(j)} - \frac{I \cdot \left(\frac{d\mu}{dT}\right) \left(\alpha \frac{\partial U_{0(j)}}{\partial y} + \gamma \frac{\partial W_{0(j)}}{\partial y}\right)}{Re} \quad (B.15)$$

$$a0_{41(j)} = \frac{I \cdot \gamma}{\kappa Ma^2 \rho_{0(j)}} \cdot p_{0(j)} \quad (B.16)$$

$$a0_{42(j)} = \frac{\alpha \gamma (2\mu_{B,0(j)} + \mu_{0(j)})}{3Re} \quad (B.17)$$

$$a0_{43(j)} = \rho_{0(j)} \frac{\partial W_{0(j)}}{\partial y} - I \cdot \frac{\left(\frac{d\mu}{dT}\right) \left(\frac{\partial T_{0(j)}}{\partial y}\right) \gamma}{Re} \quad (B.18)$$

$$a0_{44(j)} = I \cdot \rho_{0(j)} (\alpha U_{0(j)} + \gamma W_{0(j)}) + \frac{\mu_{0(j)} \left(\frac{1}{3}\gamma^2 + \alpha^2\right) + \frac{2}{3}\mu_{B,0(j)} \gamma^2}{Re} \quad (B.19)$$

$$a0_{45(j)} = \frac{I \cdot \gamma}{\kappa Ma^2 T_{0(j)}} \cdot p_{0(j)} - \frac{\left(\frac{d^2 \mu}{dT^2}\right) \left(\frac{\partial T_{0(j)}}{\partial y}\right) \left(\frac{\partial W_{0(j)}}{\partial y}\right)}{Re} - \frac{\left(\frac{d\mu}{dT}\right) \left(\frac{\partial^2 W_{0(j)}}{\partial y^2}\right)}{Re} \quad (B.20)$$

$$a0_{51(j)} = 0 \quad (B.21)$$

$$a0_{52(j)} = I \cdot \alpha p_{0(j)} (\kappa - 1) \quad (B.22)$$

$$a0_{53(j)} = \rho_{0(j)} \frac{\partial T_{0(j)}}{\partial y} - I \cdot \frac{2 \kappa (\kappa - 1) Ma^2 \mu \alpha \left(\frac{\partial U_{0(j)}}{\partial y}\right)}{Re} - I \cdot \frac{2 \kappa (\kappa - 1) Ma^2 \mu \gamma \left(\frac{\partial W_{0(j)}}{\partial y}\right)}{Re} \quad (B.23)$$

$$a0_{54(j)} = I \cdot \gamma p_{0(j)} (\kappa - 1) \quad (B.24)$$

$$a0_{55(j)} = +I \cdot \rho_{0(j)} (\alpha U_{0(j)} + \gamma W_{0(j)}) - \frac{\kappa (\kappa - 1) Ma^2 \left(\frac{d\mu}{dT}\right) \left(\left(\frac{\partial U_{0(j)}}{\partial y}\right)^2 + \left(\frac{\partial W_{0(j)}}{\partial y}\right)^2\right)}{Re} + \frac{\kappa \vartheta (\alpha^2 + \gamma^2) - \kappa \left(\frac{d^2 \vartheta}{dT^2}\right) \left(\frac{\partial T_{0(j)}}{\partial y}\right)^2 - \kappa \left(\frac{d\vartheta}{dT}\right) \frac{\partial^2 T_{0(j)}}{\partial y^2}}{Re Pr} \quad (B.25)$$

Coefficients of matrix \mathbf{A}_1

$$a1_{11(j)} = 0 \quad (B.26)$$

$$a1_{12(j)} = 0 \quad (B.27)$$

$$a1_{13(j)} = \rho_{0(j)} \quad (B.28)$$

$$a1_{14(j)} = 0 \quad (B.29)$$

$$a1_{15(j)} = 0 \quad (B.30)$$

$$a1_{21(j)} = 0 \quad (B.31)$$

$$a1_{22(j)} = -\frac{\left(\frac{d\mu}{dT}\right) \left(\frac{\partial T_{0(j)}}{\partial y}\right)}{Re} \quad (B.32)$$

$$a1_{23(j)} = -\frac{I \cdot \alpha (2 \mu_{B,0(j)} + \mu_{(j)})}{3 Re} \quad (B.33)$$

$$a1_{24(j)} = 0 \quad (B.34)$$

$$a1_{25(j)} = -\frac{\left(\frac{d\mu}{dT}\right) \left(\frac{\partial U_{0(j)}}{\partial y}\right)}{Re} \quad (B.35)$$

$$a1_{31(j)} = \frac{1}{\kappa Ma^2 \rho_{0(j)}} \cdot p_{0(j)} \quad (B.36)$$

$$a1_{32(j)} = -\frac{1}{3} \frac{I \cdot \alpha (2 \mu_{B,0(j)} + \mu_{(j)})}{Re} \quad (B.37)$$

$$a1_{33(j)} = -\frac{2}{3} \frac{\left(\frac{\partial T_{0(j)}}{\partial y}\right) \left(2 \frac{d\mu}{dT} + \frac{d\mu_B}{dT}\right)}{Re} \quad (B.38)$$

$$a1_{34(j)} = -\frac{1}{3} \frac{I \cdot \gamma (2 \mu_{B,0(j)} + \mu_{(j)})}{Re} \quad (B.39)$$

$$a1_{35(j)} = \frac{1}{\kappa Ma^2 T_{0(j)}(y)} \cdot p_{0(j)} \quad (B.40)$$

$$a1_{41(j)} = 0 \quad (B.41)$$

$$a1_{42(j)} = 0 \quad (B.42)$$

$$a1_{43(j)} = -\frac{I \cdot \gamma (2 \mu_{B,0(j)} + \mu_{0(j)})}{3 Re} \quad (B.43)$$

$$a1_{44(j)} = -\frac{\left(\frac{d\mu}{dT}\right) \left(\frac{\partial T_{0(j)}}{\partial y}\right)}{Re} \quad (B.44)$$

$$a1_{45(j)} = -\frac{\left(\frac{d\mu}{dT}\right) \left(\frac{\partial W_{0(j)}}{\partial y}\right)}{Re} \quad (B.45)$$

$$a1_{51(j)} = 0 \quad (B.46)$$

$$a1_{52(j)} = -2 \frac{\kappa (\kappa - 1) Ma^2 \mu_{0(j)} \left(\frac{\partial U_{0(j)}}{\partial y}\right)}{Re} \quad (B.47)$$

$$a1_{53(j)} = p_{0(j)} (\kappa - 1) \quad (B.48)$$

$$a1_{54(j)} = -2 \frac{\kappa (\kappa - 1) Ma^2 \mu_{0(j)} \left(\frac{\partial W_{0(j)}}{\partial y}\right)}{Re} \quad (B.49)$$

$$a1_{55(j)} = -2 \frac{\kappa \left(\frac{d\vartheta}{dT}\right) \left(\frac{\partial T_{0(j)}}{\partial y}\right)}{Re Pr} \quad (B.50)$$

Coefficients of matrix A_2

$$a_{211(j)} = 0 \quad (\text{B.51})$$

$$a_{222(j)} = -\frac{\mu_{0(j)}}{Re} \quad (\text{B.52})$$

$$a_{233(j)} = -\frac{2(\mu_{B,0(j)} + 2 \cdot \mu_{0(j)})}{3 \cdot Re} \quad (\text{B.53})$$

$$a_{244(j)} = -\frac{\mu_{0(j)}}{Re} \quad (\text{B.54})$$

$$a_{255(j)} = -\frac{\kappa \vartheta_{0(j)}}{Re \text{ Pr}} \quad (\text{B.55})$$

Coefficients of matrix B

$$b_{11(j)} = I \quad (\text{B.56})$$

$$b_{22(j)} = I \cdot \rho_{0(j)} \quad (\text{B.57})$$

$$b_{33(j)} = I \cdot \rho_{0(j)} \quad (\text{B.58})$$

$$b_{44(j)} = I \cdot \rho_{0(j)} \quad (\text{B.59})$$

$$b_{55(j)} = I \cdot \rho_{0(j)} \quad (\text{B.60})$$

C Computational Aspects

Besides applicability and accuracy, computational performance is a vital aspect for the DNS code. With the computational resources being limited, this factor determines which problems can be computed in reasonable time at all. The most important criterion for a user is the computational time in which a computation is performed. Since this depends on the size of the problem a specific CPU time is appropriate, being the computational time over the number of grid points and timesteps. Of course, performance data depends on the respective computer. Therefore, the number of floating-point operations per second can be compared with the theoretical peak performance to see how efficiently the hardware is used. When it comes to large simulations, multiple processors must be used to obtain the results in acceptable time. In this context scaling of the code is of interest, meaning how the computational speed increases with a growing number of processors.

C.1 Computational Performance

Performance on SX8 Vector Computer

The performance data is based on cases 6B and 6C of chapter 6, covering spanwise symmetric and non-symmetric computations, respectively. Both simulations were performed on 16 nodes of the NEC-SX8 vector machine of HLRS [12]. On each node, one MPI process was executed with eight tasks as shared-memory parallelization, respectively. This results in a total number of 128 processors. The performance data is summarized in table C.1.

Since the same number of spanwise modes are used, the non-symmetric simulation is larger than the symmetric case by a factor of roughly two. This is found for real time, CPU-time and the allocated memory. The vector operation ratio is 99.5% for both cases which is reflected in an efficient usage of the vector computer: on each CPU, 35% to 38% of the theoretical peak performance are reached. The specific CPU-times per grid point and complete Runge-Kutta time step are $1.7\mu\text{s}$ and $1.5\mu\text{s}$ for cases B and C, respectively. Compared to other codes, this is faster by a factor of 2.8 than the LES-code LESSOC [35] and 1.6 times slower than the incompressible code N3D of IAG [66]. Thereby one should keep in mind that more equations of higher complexity (e.g. com-

pressibility, non-linear viscous terms, grid transformation) are solved by this DNS-code than by the incompressible one. Furthermore, the incompressible code has been optimized for the current hardware, e.g. by using machine-dependent FFT routines.

Profiling reveals which subroutines are computationally most expensive. Most of the CPU-time (some 40%) is spent in the Fourier transformation, followed by the evaluation of the Navier-Stokes equation with 17%. Spatial derivatives in ξ - and η -direction require 10% and 16% of the CPU-time, respectively. The actual Runge-Kutta time integration is only a minor part with 1.7% CPU time.

case	6B	6C
number of CPUs	128	128
real time [h]	57.7	101.0
CPU-time [h]	7220.0	12830.0
memory [GB]	162.0	307
GFLOP/s per CPU	5.6	6.1
GFLOP/s (total)	707.0	783.0
spec. CPU-time [μ s]	1.7	1.5

Table C.1: Performance of the DNS-code NS3D on the NEC-SX8 vector computer, for cases 6B (spanwise symmetric) and 6C (non-symmetric).

Performance on SX9 Vector Computer

Computational performance on the latest vector computer at HLRS, the NEC-SX9, is given for simulation 7B. The simulation was run on 4 nodes, resulting in a total number of 64 processors. With 16 domains, each MPI process used 4 tasks as shared-memory parallelization. The same vector operation ratio (99.5%) as on the SX8 vector computer is observed. The number of floating-point operations per CPU is 14.467 GFLOP/s which is larger by a factor of 2.58 compared to the predecessor machine. The specific CPU-time is decreased by the same factor to 0.669 μ s per grid point and time step. This yields an overall computational performance of almost one teraflop. Since memory bandwidth is important for the computational speed, a factor of four is expected to be the maximum increase. Hence, there may be room for future optimizations. A list of computational parameters is provided by table C.2.

case	7B
number of CPUs	64
real time [h]	84.6
CPU-time [h]	5265.3
memory [GB]	264.8
GFLOP/s per CPU	14.47
GFLOP/s (total)	911.9
spec. CPU-time [μ s]	0.669

Table C.2: Performance on the NEC-SX9 vector computer, for the turbulent mixing layer (case 7B).

Performance on Scalar Machines

For comparison, the computational speed has been tested on scalar machines as well. This was done on one to four processors of a 2.6GHz Opteron and a 2.3GHz Intel Xeon cluster. For a simple two-dimensional test case, the specific CPU-times are in the range of 13 to 14.8 μ s for the Opteron cluster and 10.6 to 15.5 μ s for the Intel machine. This is slower by a factor of almost 10 than the SX8 vector machine and may become even worse for three-dimensional simulations. Yet this is not bad compared to other codes, see e.g. Denev et al. [26] and thus running NS3D on scalar machines remains an option.

C.2 Scaling

The performance data of a single simulation allows some theoretical estimation of the scaling [7]. This is done exemplarily for the symmetric simulation of case 6B, here. The spatial discretization by compact finite differences is made of 21 derivatives in ξ - and 25 derivatives in η -direction. According to equation (3.62) and the setup of the domains (eight subdomains in streamwise and two in normal direction), the speedup of the pipelined Thomas algorithm is $SU = 6$ for ξ - and $SU = 1.92$ for η -derivatives. This means that the efficiencies of the corresponding parts are 75% and 96%, respectively. Taking into account that all other computations are local for each domain, the theoretical efficiency of the MPI parallelization is 96%. This estimation does not consider communication times. Nevertheless, profiling shows that the time spent for data transfer is negligible.

Having a fast Fourier transformation, the number of grid points in z -direction is $(2^n + 1)$ for symmetric simulations. For 42 spanwise modes, the resolution

in physical space is 65 points ($n=6$). Distributing the spanwise grid points among eight processors of the shared-memory parallelization yields an uneven load balancing: seven processors pass a loop along z eight times and one processor nine times. Hence, the efficiency of the shared-memory parallelization decreases to 90%. This estimation corresponds to profiling results showing that some 10% of the CPU-time is spent in barriers, framing a Microtasking loop (e.g. subroutine `ex_lpmunit`, `ex_lpmterm`). Combining the losses of both types of parallelization, an overall parallel efficiency of 86% can be expected for 128 processors.

Real scaling of shared-memory and MPI parallelization are tested on the SX8 vector computer by one domain with 1 to 8 tasks and 1 to 16 domains with eight tasks each. The respective efficiencies of shared-memory and MPI parallelization are shown in figures C.1 a) and b), respectively. In case of one domain, the efficiency of the shared-memory parallelization decreases to 76% for eight processors. This differs distinctly from the theoretical prediction. Profiling reveals an increase of bank conflicts, meaning that multiple processes try to access one memory bank. Thus, there are still parts of the code which can be optimized. With 94%, the efficiency of the MPI parallelization closely matches the theoretical prediction. For both efficiencies, it does not matter whether they are based on the required time or the number of floating-point operations per second. This indicates that there are no relevant additional computations due to parallelization.

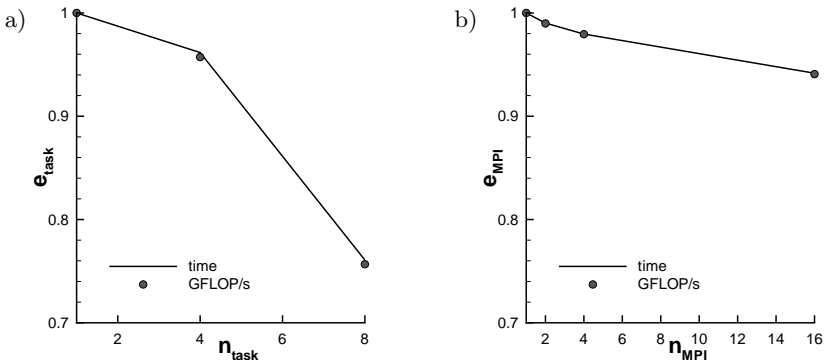


Figure C.1: Efficiency of the particular parallelization for case 6B, considered in terms of time and floating-point operations per second:

a) shared-memory, b) MPI

The overall speedup and efficiency are given in figure C.2. Within the first eight processors, the growth of the speedup is lowered which is reflected in the decreasing efficiency. When it comes to multiple MPI processes, the speedup grows almost linearly reaching a value of $SU = 92$ for 128 processes and the overall efficiency decreases only slightly for more than eight processors. Hence, it would be more favorable to use 32 domains with 4 tasks each, here.

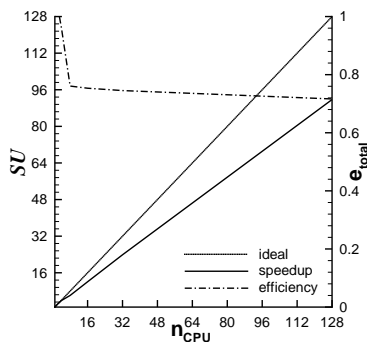


Figure C.2: Speedup and overall efficiency of the NS3D code in the range of 1 to 128 processors for simulation 6B.

C.3 Different Domain Sizes

It is also possible to have subdomains of different sizes as long as the interface between two subdomains contains the same number of grid points. This is the case for the thick splitter plate where the y -resolution of the subdomains behind the trailing edge is determined by the thickness of the splitter plate. For the configuration of chapter 5, the number of grid points is 35 and 425 behind the splitter plate and above/below, respectively. Hence, the load balancing is suboptimal, e.g. the computational performance on one processor of the SX-8 is 8.6 GFLOP/s in the large and only 0.7 GFLOP/s in the small subdomains. In case of three-dimensional simulations, the disproportionate distribution may be reduced by using less tasks for the small domain. Yet optimal load balancing is provided for an equal distribution of grid points. Thus, same array sizes should be used for all subdomains when possible.

Since fixed array sizes are used in the main part of the code, different executables are required for the two resolutions of the respective subdomains.

The parallel execution is achieved by a configuration file `mpirun.conf` for the `mpirun` command given exemplarily in figure C.3. With this configuration, the five processes of first executable `ns3d_grid_1.out` run on the first node and three of it on the second. The second executable `ns3d_grid_2.out` runs only on the second node with three MPI processes. This setup is started by the command `mpirun -f mpirun.conf`.

```
-h 0 -p 5 -e ./ns3d_grid_1.out
-h 1 -p 3 -e ./ns3d_grid_1.out
-h 1 -p 3 -e ./ns3d_grid_2.out
```

Figure C.3: Configuration file for the `mpirun` command to run eight processes of the first executable and three of the second executable on two different nodes.

D Coupling with Acoustic Solver

D.1 Numerical Example

The example which is chosen to test the coupling of DNS code and acoustic solver is a uniform mean flow in streamwise direction with $Ma_\infty = 0.5$ on a rectangular domain. The flow field is initialized with a constant temperature $\bar{T}_\infty = 280K$, except in the center of the domain. There, a disturbance of $0.001 \cdot T_\infty$ is located. This leads to a circular pressure pulse being emitted in all directions and a temperature spot which is convected with the streamwise mean flow. The initial temperature fluctuation is located at $x = 39.07$, $y = 0$ with its spatial extend being sketched in figure D.1. The Reynolds number is $Re = 500$ with the reference length L being the radius of the initial temperature disturbance.

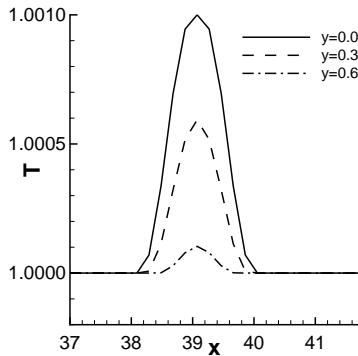


Figure D.1: Initial temperature distribution at several y -positions.

The DNS grid has a range of $-15 \leq y \leq 15$ and $0 \leq x \leq 115$ in normal and streamwise direction, respectively. A uniform stepsize of $\Delta y = 0.15$ is used in y -direction. In streamwise direction, the mesh is equidistant with $\Delta x = 0.196$ up to $x = 60$. Further downstream the stepsize is continuously stretched up to $\Delta x = 2.69$ at the outflow. The coarsening of the mesh is done accordingly

to equation (3.106) providing a damping zone for the subsonic outflow. At the left boundary of the domain, a subsonic inflow is used.

The DG code solves the linearized Euler equations above and below the integration domain of the DNS code. The unstructured grid ranges to $y = \pm 25$. The wave propagation is evaluated by comparing different discretization orders on different meshes, shown in figure D.2. The spanwise extent of DNS and acoustic domains is chosen with respect to favourable grid properties of the acoustic solver, being $0 \leq z \leq 0.5$ and $0 \leq z \leq 1.0$ for the fine and the coarse DG mesh, respectively.

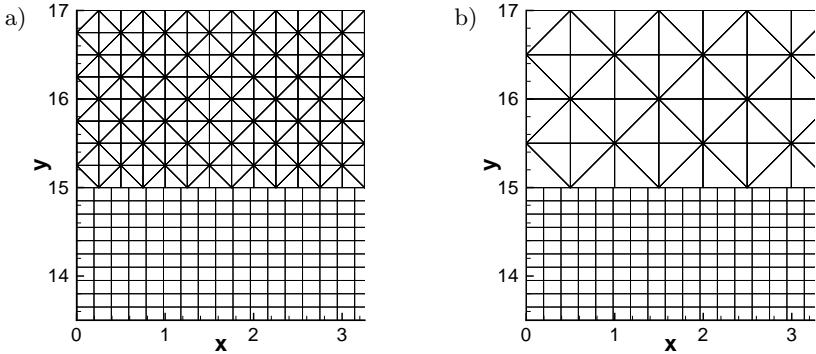


Figure D.2: Two-dimensional view of the Cartesian DNS- (bottom) and the tetrahedral DG-grid (top) at the upper coupling plane:
a) fine DG mesh, b) coarse DG mesh.

The functionality of the coupling is investigated by computing five configurations, listed in table D.1. The first two cases (A and B) are based on the fine unstructured grid with a discretization order of up to three. Case C and D are computed on the coarse grid with $\mathcal{O}4$ and $\mathcal{O}5$, respectively. A computation performed only by the DNS code is provided by case E. With a larger domain ($-45 \leq y \leq 45$), the emitted acoustic wave does not reach the free-stream boundary condition within the simulated time. As we can exclude errors due to boundary conditions, case E may serve as a reference solution.

case	DNS grid (x y z)	DG elements	\mathcal{O}_{DG}
A	401 x 201 x 5	368800	2
B	401 x 201 x 5	368800	3
C	401 x 201 x 5	92400	4
D	401 x 201 x 5	92400	5
E	401 x 603 x 5	-	-

Table D.1: Resolution given by number of grid points/elements and discretization order of the DG code (in space and time) for the computed test cases.

Figure D.3 shows the pressure field of the reference solution at time $t = 9.4247$. The fluctuation in the initial condition generates an omnidirectional circular acoustic pulse. At this time level, the pressure deflection is approximately $p' = 10^{-4}$ and parts of the acoustic wave have already crossed the location of the coupling plane.

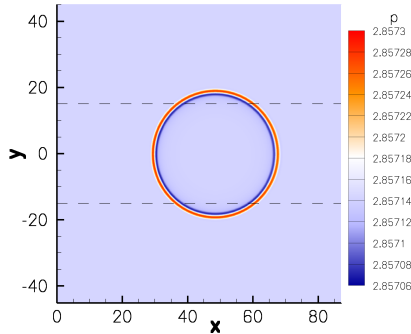


Figure D.3: Instantaneous pressure field at time $t = 9.4247$, obtained by DNS without coupling (case E). The location of the coupling plane for cases A-D is indicated by dashed lines.

The acoustic wave crossing the coupling interface is shown for case C in figure D.4 a). There, the polynomial ansatz of the DG elements is used to visualize the complete solution. In D.4 b), the grid configuration is illustrated, showing only the integral mean values of the DG elements. Despite using different equations on different grids, almost no reflection can be observed at the coupling plane.

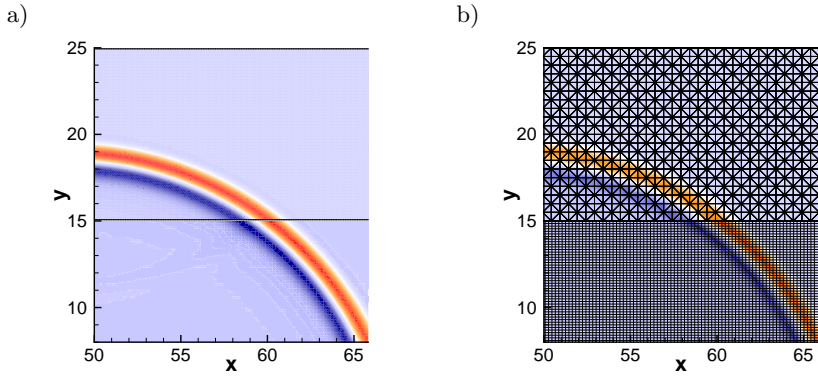


Figure D.4: Acoustic wave crossing the coupling plane at $t = 9.4247$ for 4^{th} -order DG scheme: a) visualization based on the polynomial ansatz of the DG elements, b) grid with integral values of the DG cells. Contour levels correspond to those of figure D.3.

The pressure distribution is compared quantitatively at the streamwise position $x = 52.03$, where the acoustic wave crosses the coupling plane at $t \approx 7.85$. This is shown in figure D.5 a) along the complete y -range. The detailed view in figure D.5 b) reveals that the amplitude is slightly underpredicted by the DG scheme. This error may correspond to small reflections at the interface. The solution at a later time level $t = 9.4247$ is given in figures D.6 a) and b) for the overall domain and the position of the amplitude maxima, respectively. While the 2^{nd} -order DG scheme shows a slightly smaller amplitude, no noticeable deviation is visible for $\mathcal{O}3$ and $\mathcal{O}4$.

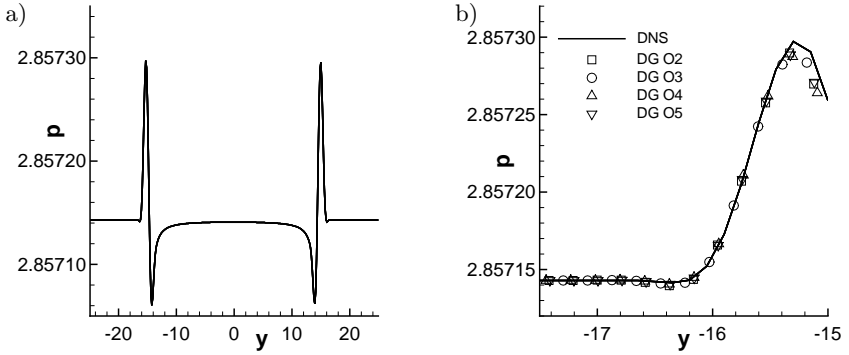


Figure D.5: a) Pressure distribution along the y -axis at $x = 52.03$, $t = 7.8539$.
 b) Detailed view of the pressure distribution comparing different discretization orders of the DG scheme with the reference solution.

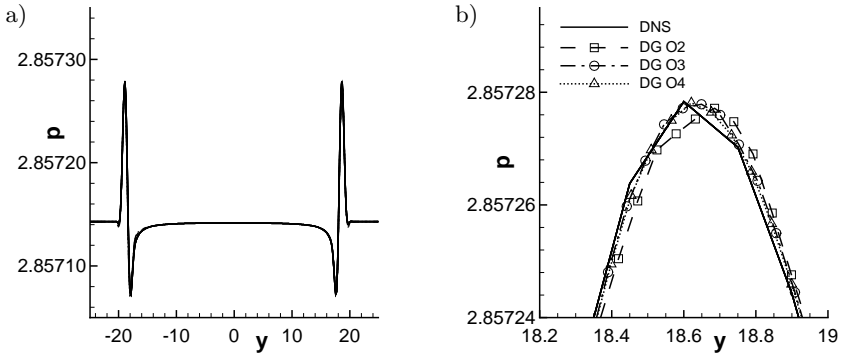


Figure D.6: a) Pressure distribution along the y -axis at $x = 52.03$, $t = 9.4247$.
 b) Detailed view of the pressure distribution comparing different discretization orders of the DG scheme with the reference solution.

D.2 Computational Performance

The basic idea of coupling two codes is to decrease the computational effort in the acoustic farfield where it is sufficient to solve linearized Euler equations instead of the full Navier-Stokes equations. Thus, computational performance needs to be considered as well. With the DNS code being fully vectorized, it was run on the NEC-SX8 installed at HLRS. The DG code is executed on an Itanium II computer with 1.5 GHz clock rate. Since the scalar machine is the frontend machine of the vector computer, good network connectivity is provided. The performance data for this hardware is listed in table D.2.

case	A	B	C	D	E
real time [s]	24079	60503	73869	195121	782
CPU time (DG) [s]	23560	59230	72869	193827	-
CPU time (DNS) [s]	576	571	507	503	2031
# CPU's DG	1	1	1	1	-
# CPU's DNS	1	1	1	1	3
Δt	0.00393	0.00393	0.00393	0.00196	0.01571
timesteps	800	800	800	800	800
DNS gridpoints	403005	403005	403005	403005	1209015
DG elements	368800	368800	92400	92400	-
comm. data [MB]/ Δt	3.99	3.99	4.82	4.82	-

Table D.2: Computational performance of the computed cases A to E, measured on the NEC-SX8 and 1.5 GHz Itanium II computer for the DNS and the DG code, respectively.

For the current configuration, the time step Δt is limited by the DG scheme, being four and eight times smaller than the DNS limit for cases A-C and D, respectively. Since the time step of the acoustic domain is allowed larger but not smaller than the one of the DNS domain, the time step ratio is set to one. However, the Runge-Kutta method requires values at intermediate time levels. Thus, the Taylor expansion in time is applied by the DG code despite the common time step.

The CPU time of the DNS code varies slightly between approximately 500 to 600 seconds. This is due to the fact, that the computation did not use one complete node explicitly. The CPU time of the DG method grows exponentially with the order of the scheme and ranges from 6.5 to 53 hours for 800 timesteps. The specific CPU time is $1.5\mu s$ to $2.1\mu s$ per grid point and time step for the DNS code. For the DG code, the specific computational time ranges from $20\mu s$

to $75\mu s$ per degree of freedom and time step. The total communication is less than five megabyte per timestep. Due to the good network connection between the SX8 and the Itanium II machine, the total communication per timestep takes less than one second.

With the DG code being 40 to 300 times slower than the DNS, the coupling mechanism does not yield the expected improvement for aeroacoustic simulations. However, the procedure has been validated with good results. The more severe timestep limitation for the DG scheme is a minor problem for *real-world* computations where the spatial resolution of the DNS is much higher than in the acoustic farfield. An alternative to the current implementation might be a two-dimensional discretization of the acoustic domain. This seems to be justified since the sound generation in a spanwise-periodic DNS domain is only weakly dependent on z if one is far enough from the acoustic source. Additionally, this would reduce communication overhead.

References

- [1] J. D. Anderson. *Computational Fluid Dynamics*. McGraw-Hill, 1995.
- [2] V. H. Arakeri, A. Krothapalli, V. Siddavaram, M. B. Alkisar, and L. M. Lourenco. On the use of microjets to suppress turbulence in a Mach 0.9 axisymmetric jet. *J. Fluid Mech.*, 490:75–98, 2003.
- [3] E. J. Avital, N. D. Sandham, and K. H. Luo. Calculation of basic sound radiation of axisymmetric jets by direct numerical simulations. *AIAA J.*, 37(2):161–168, 1999.
- [4] A. Babucke, M. Dumbser, and J. Uetzmann. A coupling scheme for direct numerical simulations with an acoustic solver. In *CEMRACS 2005 - Computational Aeroacoustics and Computational Fluid Dynamics in Turbulent Flows*, volume 16 of *ESAIM Proc.*, pages 1–15, 2007.
- [5] A. Babucke and M. J. Kloker. Accuracy analysis of finite-difference methods on non-uniform grids. *submitted to SIAM J. on Num. Analysis*, 2008.
- [6] A. Babucke, M. J. Kloker, and U. Rist. Numerical investigation of flow-induced noise generation at the nozzle end of jet engines. In *New Results in Numerical and Experimental Fluid Mechanics VI*, Contributions to the 15. STAB/DGLR Symposium Darmstadt, pages 413–420, 2007.
- [7] A. Babucke, M. J. Kloker, and U. Rist. Direct numerical simulation of a serrated nozzle end for jet-noise reduction. In *High Performance Computing in Science and Engineering '07*, pages 320–337. Springer Verlag Berlin, 2008.
- [8] A. Babucke, M. J. Kloker, and U. Rist. Direct numerical simulation of a square-notched trailing edge for jet-noise reduction. *AIAA Paper*, 2008-763, 2008.
- [9] A. Babucke, M. J. Kloker, and U. Rist. DNS of a plane mixing layer for the investigation of sound generation mechanisms. *Computers and Fluids*, 37(4):360–368, 2008.

- [10] A. Babucke, J. Linn, M. Kloker, and U. Rist. Direct numerical simulation of shear flow phenomena on parallel vector computers. In *High performance computing on vector systems: Proceedings of the High Performance Computing Center Stuttgart 2005*, pages 229–247. Springer Verlag Berlin, 2006.
- [11] J. P. Berenger. A perfectly matched layer for the absorption of electromagnetic waves. *J. Comp. Phys.*, 114(2):185–200, 1994.
- [12] H. Berger. Introduction to NEC SX-8. *Parallel Programming Workshop*, 2005.
- [13] L. P. Bernal and A. Roshko. Streamwise vortex structure in plane mixing layers. *J. Fluid Mech.*, 170:499–525, 1986.
- [14] S. F. Birch, D. A. Lyubimov, V. P. Maslov, and A. N. Secundov. Noise prediction for chevron nozzle flow. *AIAA Paper*, 2006-2600, 2006.
- [15] C. Bogey, C. Bailly, and D. Juvé. Numerical simulation of sound generated by vortex pairing in a mixing layer. *AIAA J.*, 38(12):2210–2218, 2000.
- [16] G. Bonfigli. Numerical simulation of transition and early turbulence in a 3-d boundary layer perturbed by superposed stationary and travelling crossflow vortices. *Dissertation, Insitut für Aerodynamik und Gasdynamik, Universität Stuttgart*, 2006.
- [17] J. Bridges and C. A. Brown. Parametric testing of chevrons on single flow hot jets. *AIAA Paper*, 2004-2824, 2004.
- [18] Bundesministerium für Umwelt, Naturschutz und Reaktorsicherheit. Gesetz zum Schutz gegen Fluglärm. *Bundesgesetzblatt*, 56, 2007.
- [19] E. Burkhardt. Numerische Untersuchung zum Strömungsumschlag in zweidimensionalen kompressiblen Plattengrenzschichten mit aufgeprägtem Druckgradient. *Studienarbeit, Insitut A für Mechanik, Universität Stuttgart*, 1991.
- [20] B. Callender, E. Gutmark, and S. Martens. Far-field acoustic investigation into chevron nozzle mechanisms and trends. *AIAA J.*, 43(1):87–95, 2005.
- [21] C. Canuto, M. Y. Hussaini, and A. Quarteroni. *Spectral methods in fluid dynamics*. Springer Series of Computational Physics. Springer-Verlag Berlin, 1988.

-
- [22] L. I. Cerviño, T. R. Bewley, J. B. Freund, and S. K. Lele. Perturbation and adjoint analyses of flow-acoustic interactions in an unsteady 2D jet. In *CTR Proceedings of the summer program*, pages 27–40, 2002.
- [23] T. Colonius. Modeling artificial boundary conditions for compressible flow. *Annu. Rev. Fluid Mech.*, 36:315–345, 2004.
- [24] T. Colonius, S. K. Lele, and P. Moin. Boundary conditions for direct computation of aerodynamic sound generation. *AIAA J.*, 31(9):1574–1582, Sept. 1993.
- [25] T. Colonius, S. K. Lele, and P. Moin. Sound generation in a mixing layer. *J. Fluid Mech.*, 330:375–409, 1997.
- [26] J. A. Denev, J. Fröhlich, and H. Bockhorn. Direct numerical simulation of a round jet into a crossflow - analysis and required resources. In *High Performance Computing in Science and Engineering '07*, pages 339–350. Springer Verlag Berlin, 2008.
- [27] W. Eissler. Numerische Untersuchung zum laminar-turbulenten Strömungsumschlag in Überschallgrenzschichten. *Dissertation, Insitut für Aerodynamik und Gasdynamik, Universität Stuttgart*, 1995.
- [28] W. Engblom and J. Bridges. Numerical prediction of chevron nozzle noise reduction using wind-mgbk methodology. *AIAA Paper*, 2004-2979, 2004.
- [29] R. Ewert and W. Schröder. Acoustic perturbation equations based on flow decomposition via source filtering. *J. Comp. Phys*, 188(2):365–398, 2003.
- [30] H. Fasel. Numerische Simulation inkompressibler viskoser Strömungen. *Habilitation, Fakultät für Verfahrenstechnik, Universität Stuttgart*, 1979.
- [31] Federal Aviation Administration. Noise standards: aircraft type and airworthiness certification. *Federal Aviation Regulations*, Sec. A36.4, 2002.
- [32] A. Fezer and M. J. Kloker. DNS of transition mechanisms at mach 6.8: flat plate vs. sharp cone. In *Proc. West-East High-Speed Flow Fields 2002.*, pages 434–441. CIMNE, Barcelona, Spain, 2003.
- [33] J. E. Ffowcs-Williams and D. L. Hawkings. Sound generation by turbulence and surfaces in arbitrary motion. *Phil. Trans. Royal Soc. A*, 264(1151):321–342, 1969.

- [34] J. B. Freund. Noise sources in a low-Reynolds-number turbulent jet at Mach 0.9. *J. Fluid Mech.*, 438:277–305, 2001.
- [35] M. García-Villalba and W. Rodi. Investigation of the turbulent flow separation from an axisymmetric hill. In *High Performance Computing in Science and Engineering '07*, pages 409–417. Springer Verlag Berlin, 2008.
- [36] M. B. Giles. Nonreflecting boundary conditions for Euler equation calculations. *AIAA J.*, 28(12):2050–2058, 1990.
- [37] E. Gröschel, P. Renze, W. Schröder, and M. Meinke. Towards noise reduction of coaxial jets. *AIAA Paper*, 2007-3646, 2007.
- [38] K. Gudmundsson and T. Colonius. Spatial stability analysis of chevron jet profiles. *AIAA Paper*, 2007-3599, 2007.
- [39] S. M. Harrison and E. J. Gutmark. Jet noise reduction by fluidic injection on a separate flow exhaust system. *AIAA Paper*, 2007-439, 2007.
- [40] T. Herbert. Secondary instability of boundary layers. *Annu. Rev. Fluid Mech.*, 20:487–526, 1988.
- [41] M. Herr. Design criteria for low-noise trailing edges. *AIAA Paper*, 2007-3470, 2007.
- [42] J. I. Hileman, Z. S. Spakovszky, M. Drela, and M. A. Sargeant. Airframe design for Silent Aircraft. *AIAA Paper*, 2007-453, 2007.
- [43] H. Hipp-Kalthoff. Numerische Untersuchung inkompressibler freier Scherschichten. *Dissertation, Institut für Aerodynamik und Gasdynamik, Universität Stuttgart*, 1992.
- [44] C. M. Ho and P. Huerre. Perturbed free shear layers. *Annu. Rev. Fluid Mech.*, 16:365–424, 1984.
- [45] F. Q. Hu. On absorbing boundary conditions for linearized euler equations by a perfectly matched layer. *J. Comp. Phys*, 129(1):201–219, 1996.
- [46] J. Jeong and F. Hussain. On the identification of a vortex. *J. Fluid Mech.*, 285:69–94, 1995.
- [47] L. E. Jones, R. D. Sandberg, and N. D. Sandham. Direct numerical simulations of forced and unforced separation bubbles on an airfoil at incidence. *J. Fluid Mech.*, 602:175–207, 2008.

-
- [48] H. Kamoun. Numerische Untersuchung einer Düsenströmung mit Schiebewinkel. *Studienarbeit, Institut für Aerodynamik und Gasdynamik, Universität Stuttgart*, 2008.
- [49] F. Keiderling and L. Kleiser. Influence of inflow forcing on jet flow and jet noise predicted by LES. *AIAA Paper*, 2007-3618, 2007.
- [50] E. Kit, I Wygnanski, D. Friedman, O. Krivonosova, and Z. Zhilenko. On the periodically excited plane turbulent mixing layer, emanating from a jagged partition. *J. Fluid Mech.*, 589:479–507, 2007.
- [51] V. Kleine. Influence of trailing-edge thickness on flow-induced airfoil noise investigated by DNS. *Trabalho de Graduação, Instituto Tecnológico de Aeronáutica, São José dos Campos, Brazil*, 2008.
- [52] M. Kloker. Direkte Numerische Simulation des laminar-turbulenten Strömungsumschlages in einer stark verzögerten Grenzschicht. *Dissertation, Institut für Aerodynamik und Gasdynamik, Universität Stuttgart*, 1993.
- [53] M. Kloker, U. Konzelmann, and H. Fasel. Outflow boundary conditions for spatial Navier-Stokes simulations of transitional boundary layers. *AIAA J.*, 31(4):620–628, 1993.
- [54] M. J. Kloker. private communication.
- [55] M. J. Kloker. A robust high-resolution split-type compact FD scheme for spatial DNS of boundary-layer transition. *Appl. Sci. Res.*, 59:353–377, 1998.
- [56] M. Kofler. *Maple V Release 2*. Addison-Wesley, 1994.
- [57] J. Laufer and T. Yen. Noise generation by a low-Mach-number jet. *J. Fluid Mech.*, 134:1–311, 1983.
- [58] S. K. Lele. Compact finite differences with spectral-like resolution. *J. Comput. Phys.*, 103(1):16–42, 1992.
- [59] M. J. Lighthill. On sound generated aerodynamically. I. General theory. *Royal Society of London Proceedings Series A*, 211:564–587, 1952.
- [60] M. J. Lighthill. On sound generated aerodynamically. II. Turbulence as a source of sound. *Royal Society of London Proceedings Series A*, 222:1–32, 1954.

- [61] G. M. Lilley. On the noise from jets. In *AGARD CP-131 Noise Mechanisms*, 1974.
- [62] J. Linn and M. J. Kloker. Numerical investigations of effusion cooling in hypersonic boundary-layer flow. In *New Results in Numerical and Experimental Fluid Mechanics VI*, Contributions to the 15. STAB/DGLR Symposium Darmstadt, pages 403–412, 2007.
- [63] L.M. Mack. Boundary-layer linear stability theory. In *AGARD R-709 Spec. Course on Stability and Transition of Laminar Flow*, 1984.
- [64] O. Marsden, C. Bogey, and C. Bailly. Direct noise computation of the turbulent flow around a zero-incidence airfoil. *AIAA J.*, 46(4):874–883, 2008.
- [65] K. Meister. Entwicklung einer instationären Einstromrandbedingung für Strömungssimulationen mit dem DNS-Code NS3D. *Studienarbeit, Insitut für Aerodynamik und Gasdynamik, Universität Stuttgart*, 2008.
- [66] R. Messing, U. Rist, and F. Svenson. Control of turbulent boundary-layer flow using slot actuators. In *High performance computing on vector systems: Proceedings of the High Performance Computing Center Stuttgart 2006*. Springer Verlag Berlin, 2007.
- [67] D. Meyer. Direkte numerische Simulation nichtlinearer Transitionsmechanismen in der Strömungsgrenzschicht einer ebenen Platte. *Dissertation, Institut für Aerodynamik und Gasdynamik, Universität Stuttgart*, 2003.
- [68] A. Michalke. On spatially growing disturbances in an inviscid shear layer. *J. Fluid Mech.*, 23:521–544, 1965.
- [69] A. Michalke. A note on spatially growing three-dimensional disturbances in a free shear layer. *J. Fluid Mech.*, 38:765–767, 1969.
- [70] Ulf Michel. Beitrag des Triebwerks zum Landegeräusch eines modernen Flugzeugs. *Innovationsforum Flugtriebwerkstechnik in Brandenburg*, Dezember 2004.
- [71] R. Miksad. Experiments on the nonlinear stages of free-shear-layer transition. *J. Fluid Mech.*, 56:695–719, 1972.
- [72] P. A. Monkewitz and P. Huerre. The influence of the velocity ratio on the spatial instability of mixing layers. *Phys. Fluids*, 25:1137–1143, 1982.

-
- [73] N. N. *ANSI/IEEE 754-1985, Standard for Binary Floating-Point Arithmetic*. IEEE, New York, 1985.
- [74] W. Neise. Lärmoptimierte An- und Abflugverfahren. *Zusammenfassender Schlussbericht, Forschungsverbund Leiser Verkehr*, 2007.
- [75] N.N. EAS3 (Ein-Ausgabe-System). <http://www.iag.uni-stuttgart.de/eas3>.
- [76] N.N. Lapack linear algebra package. <http://www.netlib.org/lapack>.
- [77] N.N. *MPI - A message-passing interface standard*. Technical Report CS-94-230, University of Tennessee, Knoxville, 1994.
- [78] N.N. Making future commercial aircrafts quieter. *NASA Facts, FS-1999-07-003-GRC, NASA Glenn-Research-Center, Cleveland, Ohio*, 1999.
- [79] A. Pagella, A. Babucke, and U. Rist. Two-dimensional numerical investigations of small-amplitude disturbances in a boundary layer at $Ma=4.8$: Compression corner versus impinging shock wave. *Physics of Fluids*, 16(7):2272–2281, 07 2004.
- [80] J. Postel. Transmission control protocol. *USC/Information Sciences Institute, Marina del Rey (CA), USA*, RFC-793, 1981.
- [81] A. Povitsky. Parallelization of the pipelined Thomas algorithm. *ICASE Report 98-48*, 1998.
- [82] L. Rayleigh. On the stability, or instability, of certain fluid motions. *Proc. London Math. Soc.*, 1879.
- [83] U. Rist and H. Fasel. Spatial three-dimensional numerical simulation of laminar-turbulent transition in a flat-plate boundary layer. In *Proc. Boundary Layer Transition and Control Conference*, The Royal Aeronautical Society, London, 1991.
- [84] R. D. Sandberg, L. E. Jones, N. D. Sandham, and P. F. Joseph. Direct numerical simulation of noise generated by airfoil trailing edges. *AIAA Paper*, 2007-3469, 2007.
- [85] R. D. Sandberg and N. D. Sandham. Nonreflecting zonal characteristic boundary condition for direct numerical simulation of aerodynamic sound. *AIAA J.*, 44(2):402–405, 2006.

- [86] N. D. Sandham and W. C. Reynolds. Three-dimensional simulations of large eddies in the compressible mixing layer. *J. Fluid Mech.*, 224:133–158, 1991.
- [87] H. Schlichting. *Boundary-Layer Theory*. McGraw-Hill, New York, 7. edition, 1979.
- [88] D. Schneider. Direkte Numerische Simulation eines Flügelprofils. *Studienarbeit, Insitut für Aerodynamik und Gasdynamik, Universität Stuttgart*, 2008.
- [89] J. Schulze, Ch. Schaupp, J. Sesterhenn, R. Friedrich, J. Berland, Ch. Bogey, and D. Juvé. Shock-induced noise in 2D sub- and supersonic mixing layers. In *CEMRACS 2005 - Computational Aeroacoustics and Computational Fluid Dynamics in Turbulent Flows*, volume 16 of *ESAIM Proc.*, pages 51–65, 2007.
- [90] R. K. Shukla and X. Zhong. Derivation of high-order compact finite difference schemes for non-uniform grid using polynomial interpolation. *J. Comp. Phys.*, 204:404–429, 2005.
- [91] M. Siegert. Numerische Untersuchung zum Einfluss von Machzahl und Temperatur auf das Stabilitätsverhalten einer freien Scherschicht. *Studienarbeit, Insitut für Aerodynamik und Gasdynamik, Universität Stuttgart*, 2006.
- [92] B. Spagnoli. Etude numérique de sensibilité et contrôle optimal du bruit aéroacoustique généré par une couche de mélange compressible bidimensionnelle. *Thèse de doctorat de l'Université Paul Sabatier, Toulouse*, 2006.
- [93] B. Spagnoli and C. Airiau. Adjoint analysis for noise control in a two-dimensional compressible mixing layer. *Computers and Fluids*, 37(4):475–486, 2008.
- [94] P. R. Spalart. Direct simulation of boundary layer up to $Re\theta=1410$. *J. Fluid Mech.*, 187:61–98, 1988.
- [95] W. Sutherland. The viscosity of gases and molecular force. *Phil. Mag.*, 36:507–531, 1893.
- [96] C.K. Tam. Supersonic jet noise. *Annu. Rev. Fluid Mech.*, 27:17–43, 1995.
- [97] C.K. Tam and L. Auriault. Jet mixing noise from fine-scale turbulence. *AIAA J.*, 37(2):145–153, 1999.

-
- [98] K.W. Thompson. Time-dependent boundary conditions for hyperbolic systems. *J. Comp. Phys.*, 68:1–24, 1987.
- [99] A. Thumm. Numerische Untersuchung zum laminar-turbulenten Strömungsumschlag in transsonischen Grenzschichtströmungen. *Dissertation, Institut für Aerodynamik und Gasdynamik, Universität Stuttgart*, 1991.
- [100] J. Utzmann, T. Schwartzkopff, M. Dumbser, and C.D. Munz. Heterogeneous domain decomposition for computational aeroacoustics. *AIAA J.*, 44(10):2231–2250, 2006.
- [101] M. R. Visbal and D. V. Gaitonde. On the use of higher-order finite-difference schemes on curvilinear and deforming meshes. *J. Comp. Phys.*, 181(1):155–185, September 2002.
- [102] A. W. Vreman, N. D. Sandham, and K. L. Luo. Compressible mixing layer growth rate and turbulent characteristics. *J. Fluid Mech.*, 320:235–258, 1996.
- [103] M. Wang, J.B. Freund, and S.K. Lele. Computational prediction of flow-generated sound. *Annu. Rev. Fluid Mech.*, 38:483–512, 2006.
- [104] P. Wassermann and M. J. Kloker. Mechanisms and passive control of crossflow-vortex-induced transition in a 3-d boundary layer. *J. Fluid Mech.*, 456:49–84, 2002.
- [105] M. Wei and J.B. Freund. A noise controlled free shear flow. *J. Fluid Mech.*, 546:123–152, 2006.
- [106] F. M. White. *Viscous Fluid Flow*. McGraw Hill, New-York, 2. edition, 1991.
- [107] H. Wielandt. Beiträge zur mathematischen Behandlung komplexer Eigenwertprobleme. In *Bericht B 44/J/37, Aerodynamische Versuchsanstalt Göttingen*, 1944.
- [108] D. You, R. Mittal, M. Weng, and P. Moin. Analysis of stability and accuracy of finite-difference schemes on a skewed mesh. *J. Comp. Phys.*, 213:184–204, 2006.
- [109] X. Zhong and M. Tatini. High-order non-uniform grid schemes for numerical simulation of hypersonic boundary-layer stability and transition. *J. Comput. Phys.*, 190:419–458, 2003.

- [110] M. Zhuang and P. E. Dimotakis. Instability of wake-dominated compressible mixing layers. *Physics of Fluids*, 7(10):2489–2495, 1995.